UNIVERSITY OF CALIFORNIA SAN DIEGO

SAN DIEGO STATE UNIVERSITY

Direct Numerical Simulations of a Cambered NACA 65(1)-412 Airfoil at Low Reynolds Numbers: Flow Separation, Instabilities and Lagrangian Aerodynamics

A dissertation submitted in partial satisfaction of the
requirements for the degree
Doctor of Philosophy

in

Engineering Science (Mechanical and Aerospace)

by

Bjoern Fabian Klose

Committee in charge:

University of California San Diego

Professor David Saintillan, Co-Chair
Professor Veronica Eliasson
Professor Qiang Zhu

San Diego State University

Professor Gustaaf B. Jacobs, Co-Chair
Professor Xiaofeng Liu

2021

The dissertation of Bjoern Fabian Klose is approved, and it is acceptable in quality and form for publication on microfilm:

_____

_____

_____

_____
Co-Chair

_____
Co-Chair

University of California San Diego

San Diego State University

2021

DEDICATION

To my wife.

EPIGRAPH

You miss 100% of the shots you don't take.

—Wayne Gretzky

TABLE OF CONTENTS

LIST OF FIGURES

LIST OF TABLES

ACKNOWLEDGEMENTS

I would like to express my gratitude to my advisor, Dr. Gustaaf Jacobs, for his continuous support, both on an academic and on a personal level as a mentor. A special thanks to Dr. David Kopriva for his comments, input, and support with the discontinuous Galerkin code.

I would like to thank Solar Turbines for their generous financial support of this research and acknowledge Dr. Douglas Smith and Dr. Gregg Abate from the Air Force Office of Scientific Research (AFOSR) for their funding (FA9550-16-1-0392 and FA9550-19-1-0387). I also would like to thank the Department of Defense for computational time on their high performance computing systems.

I would like to express my appreciation to my committee members for their contribution: Dr. Veronica Eliasson, Dr. Qiang Zhu, Dr. Xiaofeng Liu, and to my co-advisor, Dr. David Saintillan.

Thank you to Paul Fischer for the provision of subroutines for *gslib* and help with the implementation into our DG code.

Thank you to my labmates for support, academic stimulus, and many shared memories.

Finally, I want to thank my wife, my parents, and my friends for their unconditional support throughout these sometimes difficult times.

Chapter 3 and Sections 4.2 through 4.3, in full, are a reprint of the material as it appears in "Assessing standard and kinetic energy conserving volume fluxes in discontinuous Galerkin formulations for marginally resolved Navier-Stokes flows", B. F. Klose, G. B. Jacobs and D. A. Kopriva, *Computers & Fluids*, 2020. B. F. Klose: investigation, original draft preparation, visualization. G. B. Jacobs: supervision, review & editing. D. A. Kopriva: methodology review, supervision, editing.

Sections 2.1 through 2.2 and Chapter 5, in part, are currently being prepared

for submission for publication of the material, B. F. Klose, G. R. Spedding and G. B. Jacobs. B. F. Klose: investigation, original draft preparation, visualization. G. R. Spedding: minor contributions to supervision, review & editing. G. B. Jacobs: supervision, review & editing.

Sections 2.3 through 2.5 and Sections 6.2 through 6.4, in full, are a reprint of the material as it appears in "Kinematics of Lagrangian Flow Separation in External Aerodynamics", B. F. Klose, M. Serra and G. B. Jacobs, *AIAA Journal*, 2020. B. F. Klose: investigation, visualization, original draft preparation. M. Serra: support with theory and curvature routines, editing. G. B. Jacobs: supervision, review & editing.

Chapter 7, in full, is currently being prepared for submission for publication of the material, B. F. Klose, M. Serra and G. B. Jacobs. B. F. Klose: development of theory, data acquisition, original draft preparation. M. Serra: development of theory (Theorem 1), editing. G. B. Jacobs: development of theory, supervision, review & editing.

VITA

2010-2014	Bachelor of Science in Production Engineering, University of Bremen
2011-2012	Student Assistant at BIBA – Bremer Institut fuer Produktion und Logistik
2012-2014	Student Assistant at ZARM – Center of Applied Space Technology and Microgravity
2013-2014	Intern at Airbus Defense and Space
2014-2016	Master of Science in Production Engineering, University of Bremen
2017-2019	Teaching Associate at San Diego State University
2016-2021	Doctor of Philosophy in Engineering Sciences (Mechanical and Aerospace Engineering), Joint Doctoral Program, San Diego State University and University of California San Diego

PUBLICATIONS

B. F. Klose, G. R. Spedding and G. B. Jacobs, "The multitude of flow regimes in cambered airfoil aerodynamics at Re = 20,000: a two-sided story.", In Preparation, 2020.

B. F. Klose, M. Serra and G. B. Jacobs, "Objective early identification of kinematic instabilities in shear flows", In preparation, 2020.

B. F. Klose, G. B. Jacobs and D. A. Kopriva, "Assessing standard and kinetic energy conserving volume fluxes in discontinuous Galerkin formulations for marginally resolved Navier-Stokes flows", *Computers and Fluids*, 205, 2020.

B. F. Klose, M. Serra and G. B. Jacobs, "Kinematics of Lagrangian Flow Separation in External Aerodynamics", *AIAA Journal*, 58(5), 2020.

D. Bhattacharjee, B. Klose, G. B. Jacobs and M. S. Hemati, "Data-driven selection of actuators for optimal control of airfoil separation", *Theoretical and Computational Fluid Dynamics*, 2020.

B. F. Klose, G. B. Jacobs and D. A. Kopriva, "On the robustness and accuracy of marginally resolved discontinuous Galerkin schemes for two dimensional Navier-Stokes flows", *AIAA SciTech Conference, San Diego*, 2019.

B. F. Klose, G. B. Jacobs, J. Tank and G. R. Spedding, "Low Reynolds number airfoil aerodynamics: three different flow patterns within an angle of attack range of four degrees", *AIAA Aviation Forum, Atlanta*, 2018.

PRESENTATIONS

B. F. Klose, M. Serra and G. B. Jacobs, "Objective early identification of kinematic instabilities in shear flows", Presented at the APS Division of Fluid Dynamics Conference. Chicago, IL (Virtual). 2020.

B. F. Klose, M. Serra and G. B. Jacobs, "Lagrangian Flow Separation in External Aerodynamics", Presented at the APS Division of Fluid Dynamics Conference. Seattle, WA. 2019.

B. F. Klose, G. B. Jacobs and D. A. Kopriva, "Assessing standard and kinetic energy conserving discontinuous Galerkin formulations for marginally resolved two dimensional Navier-Stokes flows", Presented at the North American High Order Methods Conference. San Diego, CA. 2019.

B. F. Klose, G. B. Jacobs and D. A. Kopriva, "On the robustness and accuracy of marginally resolved discontinuous Galerkin schemes for two dimensional Navier-Stokes flows", Presented at the AIAA SciTech Conference. San Diego, CA. 2019.

B. F. Klose, G. B. Jacobs, J. Tank and G. R. Spedding, "Low Reynolds number airfoil aerodynamics: three different flow patterns within an angle of attack range of four degrees", Presented at the APS Division of Fluid Dynamics Conference. Atlanta, GA. 2018.

B. F. Klose, G. B. Jacobs, J. Tank and G. R. Spedding, "Low Reynolds number airfoil aerodynamics: three different flow patterns within an angle of attack range of four degrees", Presented at the AIAA AVIATION Forum. Atlanta, GA. 2018.

ABSTRACT OF THE DISSERTATION

Direct Numerical Simulations of a Cambered NACA 65(1)-412 Airfoil at Low Reynolds Numbers: Flow Separation, Instabilities and Lagrangian Aerodynamics

by

Bjoern Fabian Klose

Doctor of Philosophy in Engineering Science (Mechanical and Aerospace)

University of California San Diego, 2021
San Diego State University, 2021

Professor Gustaaf B. Jacobs, Co-Chair
Professor David Saintillan, Co-Chair

This dissertation is a comprehensive account of the low-Reynolds number (Re) flow over a cambered airfoil for a wide range of angles of attack with a focus on the dynamics of boundary layer separation and transition. The unsteady and complex phenomena of the transitional flow are analyzed through a combination of direct numerical simulations (DNS), large-eddy simulations (LES), experiments, and development of Lagrangian theory and methods.

A discontinuous Galerkin spectral element method (DGSEM) is used to model the compressible Navier-Stokes equations in two and three dimensions. The DGSEM generates high-order accurate results with low dispersion and diffusion errors and has

been developed to include kinetic-energy conserving volume fluxes, tools to efficiently track Lagrangian fluid tracers, and computation of higher wall-normal velocity derivatives. The code is benchmarked through a series of Navier-Stokes flows using different DG variants and polynomial orders.

High-fidelity DNS in three dimensions show that the transitional flow over a cambered NACA 65(1)-412 airfoil at $Re = 2{\times}10^4$ swiftly changes from a state of laminar separation at mid-chord without reattachment to a laminar separation bubble (LSB) at the leading edge with a turbulent boundary layer. The bifurcation occurs within an angle-of-attack change of two degrees and is accompanied by a rapid increase of the lift and decrease of the drag force, which is observed in computations and experiments likewise. Each flow regime is governed by different dynamics, instabilities, and wake structures that change with the transition location of the separated shear layer. The kinematic aspects of flow separation are further investigated in the Lagrangian frame, where the initial motion of upwelling fluid material from the wall is related to the long-term attracting manifolds in the flow field.

An objective finite-time diagnostic for instabilities in shear flows based on the curvature of Lagrangian material lines is introduced. By defining a flow instability in the Lagrangian frame as the increased folding of lines of fluid particles, subtle perturbations and unstable growth thereof are detected early based solely on the curvature change of material lines over finite time.

Chapter 1

Introduction

1.1 Motivation

As interest in practical small-scale flying devices, turbomachinery at various scales, and high-altitude unmanned aerial vehicles (UAV) proliferates, it becomes increasingly important to understand and characterize flows at moderate Reynolds number (Re). The aerodynamics of airfoils at low to intermediate Reynolds numbers in the range $10^4 \leq Re \leq 10^5$ are commonly characterized by an initially laminar boundary layer, its separation under an adverse pressure gradient, and transition to turbulence of the separated shear layer [2]. If the transition occurs upstream of the airfoil's trailing edge, the flow can reattach and form a laminar separation bubble (LSB). Because the transition from laminar to turbulent flow can yield significant and sudden changes in the flow topology (and forces) with minor changes in flow conditions, accurate prediction and control of such events are of interest for the operation of aerodynamic devices at moderate Reynolds numbers.

The control and prevention of flow separation can yield a substantial extension of the operating range of such aerodynamic devices, but the dynamics of flow separation

are highly non-linear and make the design of an effective passive and active flow control system challenging. While some flow control concepts work by completely removing or re-energizing the separated fluid through suction and blowing (see e.g. Schlichting and Gersten [3]), other techniques take advantage of instabilities and non-linearities in the flow by using more compact zero-net mass flux (ZNMF) devices such as synthetic jets [4, 5, 6]. Given the limited power of these ZNMF instruments, the design of an effective and efficient control strategy should not only focus on directly changing the global events in the flow, but rather on understanding and controlling the more subtle and unsteady features of separation.

To capture these unsteady events, highly accurate flow field data and tools to to extract the relevant structures are required. Direct numerical simulations (DNS) generate space and time-resolved flow field data without employing user-defined models and are therefore ideally suited to research the complex dynamics of flow separation. They are, however, computationally expensive and require highly accurate and efficient numerical schemes. The discontinuous Galerkin spectral element method (DGSEM) is such a scheme and combines high-order accuracy with adaptability to complex flow problems, which makes it ideally suited to tackle the dynamics of flow separation.

1.2 Simulation of low-Reynolds number airfoil flow

Modeling transitional flow is challenging and first-principle methods, such as *XFoil* [1], fail to accurately predict the transition and the aerodynamic forces [7]. Numerical methods based on the Reynolds-Averaged Navier-Stokes (RANS) equations are a widely used design tool for complex geometries and turbulent flow, but the solution is neither time nor space resolved, depends on the choice of turbulent closure models [8], and fails to predict transitional flow characteristics [9]. Large-eddy simulations

(LES) [10] or detached-eddy simulations (DES) [11] capture the larger structures of the unsteady flow, but similarly employ user-defined models to account for the the sub-grid scale fluid motions. In direct numerical simulations (DNS), the Navier-Stokes equations are computed without additional modeling terms and the fluid motion is resolved in space and time. The independence of user-defined models and the high accuracy make DNS the primary choice to model flow instabilities and transition [12].

Balancing the high accuracy required to create high-fidelity datasets with computational efficiency is demanding on numerical and computational methods. The DNS community generally agrees that high-order approximations are necessary to obtain accurate results with low diffusion and dissipation [12]. The high-order discontinuous Galerkin (DG) method is one of the high-order methods that has emerged as a discretization for DNS [13, 14]. DG combines high-order accuracy with grid complexity and parallel efficiency. A down-side of high-order methods is that they can be temperamental, i.e. they can be unstable or produce spurious oscillations if insufficient grid resolution is used. Filter functions and artificial viscosity have been successfully applied to remedy this problem [15] and much of the recent high-order method research has gone towards the development of provably stable schemes, that preserve kinetic energy and/or entropy [16, 17].

High-fidelity simulations of airfoils in the transitional flow regime have only been subject to research for the past decade and to date, only few DNS results in the Reynolds number range $10^4 \leq Re \leq 10^5$ are reported in literature, e.g. [18, 19, 20, 21]. The premier challenge of DNS is that it is computationally intensive to resolve all spatial and temporal scales of fluid motion, which limits their application to low and moderate Reynolds numbers and small computational domains [12]. Although airfoils are generally part of more complex flow systems, the high computational cost has restricted research to isolated configurations, e.g. a wing section in free stream or

a single blade section in a turbine cascade. These high-fidelity results are, however, fundamental to the understanding of complex flow phenomenons such as boundary layer separation, instability growth, or turbulent reattachment.

Airfoil simulations in free stream have been primarily carried out on the symmetric NACA 0012: Shan et al. [18] study the flow separation on a NACA 0012 airfoil at a chord-based Reynolds number of $Re = 1 \times 10^5$ through DNS and found that a three-dimensional instability emerges from the interaction of the vortices in the wake. For the same airfoil, Jones et al. [19] study the laminar separation bubble at $Re = 5 \times 10^4$ at 5° incidence with a span of $0.2c$ and report on self-sustaining turbulence from the LSB flow. The authors later elaborate on the receptivity of the LSB and found that acoustic feedback from instability waves originating from the vortex shedding at the trailing edge induce a global instability [20, 22]. Sandberg and Jones [23] further show that a serrated trailing edge does not significantly affect the upstream flow field but results in some variations of the structures within the separated shear layer. Almutairi et al. [24] study the intermittent bursting of a LSB on a NACA 0012 through LES and show that a spanwise domain size of 50% of the chord was necessary to capture the event. A sufficiently long span is therefore required to accurately capture the stability properties of LSBs on airfoils. Lee et al. [9] compare two- and three-dimensional simulations, as well as experiments, of the NACA 0012 at Reynolds numbers from $Re = 1 \times 10^4$ to $Re = 5 \times 10^4$ and show that the RANS method fails to accurately predict the aerodynamic characteristics. Aerodynamic statistics are also evaluated by Balakumar [25] for simulations at $Re = 5 \times 10^4$ and 1×10^6. The effect of a wavy leading edge configuration on a NACA 0012 for Reynolds numbers of $Re = 1 \times 10^4$ and 5×10^4 is studied by Serson et al. [26] and Visbal and Garmann [27] later reported on the deep stall dynamics of a pitching NACA 0012 at $Re = 2 \times 10^5$.

Despite the rich literature on the symmetric NACA 0012 airfoil, in engineering

applications one usually encounters cambered profiles that generate optimal performance for a given operating condition. The SD 7003 is a cambered airfoil designed for low-Reynolds number operations that has attracted attention in the last decade. The airfoil allows for a thin LSB under various conditions and performs well as the LSB forces the flow to transition and reattach. Several studies on implicit LES have been published on the transitional flow over this wing: Galbraith and Visbal [28] report on the bursting of a LSB at a Reynolds number of $Re = 6 \times 10^4$ and Visbal [29] later addresses the dynamic stall of a plunging SD 7003. For the same airfoil, Uranga et al. [7] show the shift from laminar, separated flow at $Re = 1 \times 10^4$ to transitional flow with turbulent reattachment past a LSB at $Re = 2.2 \times 10^4$ and $Re = 6 \times 10^4$. LES results on the SD 7003 by Beck et al. [30] are in overall good agreement with data in literature but show discrepancies in the skin friction coefficient distribution, which are attributed to the influence of the far-field boundaries and hence an insufficient domain size. Zhang et al. [21] compare the flows over the symmetric NACA 0012-64 and the cambered NACA 4412 at $Re = 1 \times 10^4$ and 10° incidence and report a significant delay of the laminar-turbulent transition for the cambered airfoil. DNS of a compressor section include the work by Zaki et al. [31], who investigate the effect of free-stream turbulence on the transition of a NACA-65 compressor cascade at $Re = 138{,}500$. Turbulent inflow conditions are also investigated by Sandberg et al. [32], who compute the flow in a LPT turbine cascade at a Reynolds number of 60,500.

Compressor blades owe their shape to the adverse pressure gradient against which they operate and their slender profile and small camber allows the flow to remain attached over most of the airfoil under operating conditions. In turbomachinery, for example, the blades in axial flow compressors are commonly selected from the NACA 65-series [33, 34] or Eppler series. The profile of the NACA 65(1)-412 differs from the canonical NACA 0012 or the SD 7003 in that it is intended to extend the region

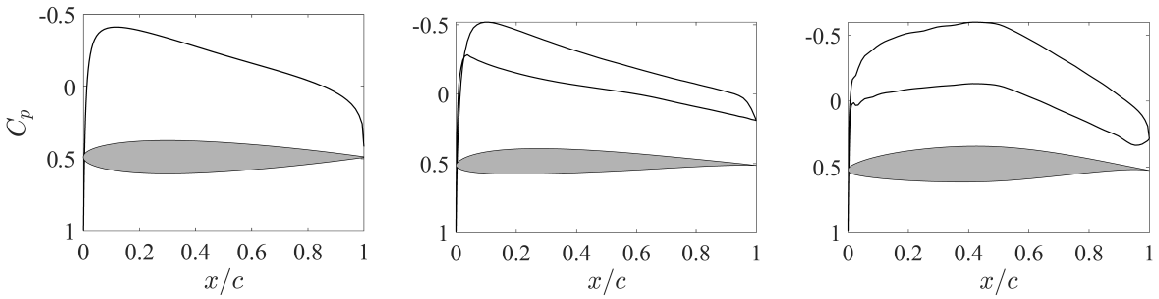

(a) NACA 0012 (b) SD 7003 (c) NACA 65(1)-412

Figure 1.1: Pressure coefficients (black) for inviscid flow over airfoils (grey) at 0° incidence. NACA 0012 (a), SD 7003 (b), and NACA 65(1)-412 (c) [1].

of laminar flow over the wing. Figure 1.1 summarizes the pressure coefficients for the NACA 0012, SD 7003, and NACA 65(1)-412 at 0° incidence. It is evident that the pressure distribution of the NACA 65(1)-412 differs significantly and features an extended favorable pressure gradient over half of the wing. While the boundary layer in airfoil flows with a Reynolds numbers larger than 10^6 generally transitions upstream of the location of the pressure minimum and is therefore likely to withstand the adverse pressure gradient, the laminar boundary layer in low-Reynolds number flow is prone to separate and thereby dictates the airfoil performance in this regime [2]. The airfoil shape is therefore central to the transition characteristics of the wing.

For the NACA 65(1)-412 airfoil at moderate Reynolds number, Tank et al. [35] show that laminar separated flow rapidly transitions and forms a LSB at the leading edge within one degree change of the flow angle. Although jumps in the aerodynamic forces are not unique to this airfoil (cf. Lee et al. [9]), its particular shape favors laminar flow over a long range of angles with a nearly linear lift trend until the transition of the boundary layer results in the sudden formation of a LSB at the leading edge. Because airfoils used in gas compressor and turbine configurations (e.g. as inlet guide vanes) are commonly assembled as arrays, they are directly impacted by the unsteady wake dynamics of the upstream assembly. The wake dynamics, however, are only sparsely

discussed in the literature discussed above.

1.3 The kinematics of flow separation

The aerodynamics of airfoils in the low to moderate Reynolds number regime are governed by the separation and transition of the laminar boundary layer. In steady flows, separation from a no-slip wall is well-known to be exactly identified by Prandtl's condition through a point of zero skin friction and a negative friction gradient in wall-tangential direction. For unsteady flows, similar first-principle criteria were only recently developed by Haller [36]. He proved that for time periodic flows, an objective Lagrangian separation point is located at the averaged zero-skin-friction location. Haller further showed that flow separation from a no-slip boundary starts with an upwelling of Lagrangian fluid tracers upstream of the separation point and that those particles are drawn towards an unstable manifold in the flow while they are ejected from the wall. This so-called asymptotic separation profile is anchored at the separation point and it guides fluid particles as they break away in the vicinity of the wall (see Haller [36] and Weldon et al. [37]).

To illustrate this Lagrangian separation behavior, we consider the time periodic flow over a circular cylinder in Figure 1.2. A set of fluid particle tracers is initialized in a layer parallel to the cylinder wall and is color-coded based on the linear approximation of the dividing asymptotic separation line. As the particles are advected, they undergo an upwelling motion, which is visible through an increasingly sharp spike in the material lines that are initially parallel to the wall. The spikes of particles are asymptotically drawn towards the attracting separation line. Mathematically, these attracting lines are interpreted as unstable manifolds.

In general, stable and unstable manifolds can be identified by extracting ridges

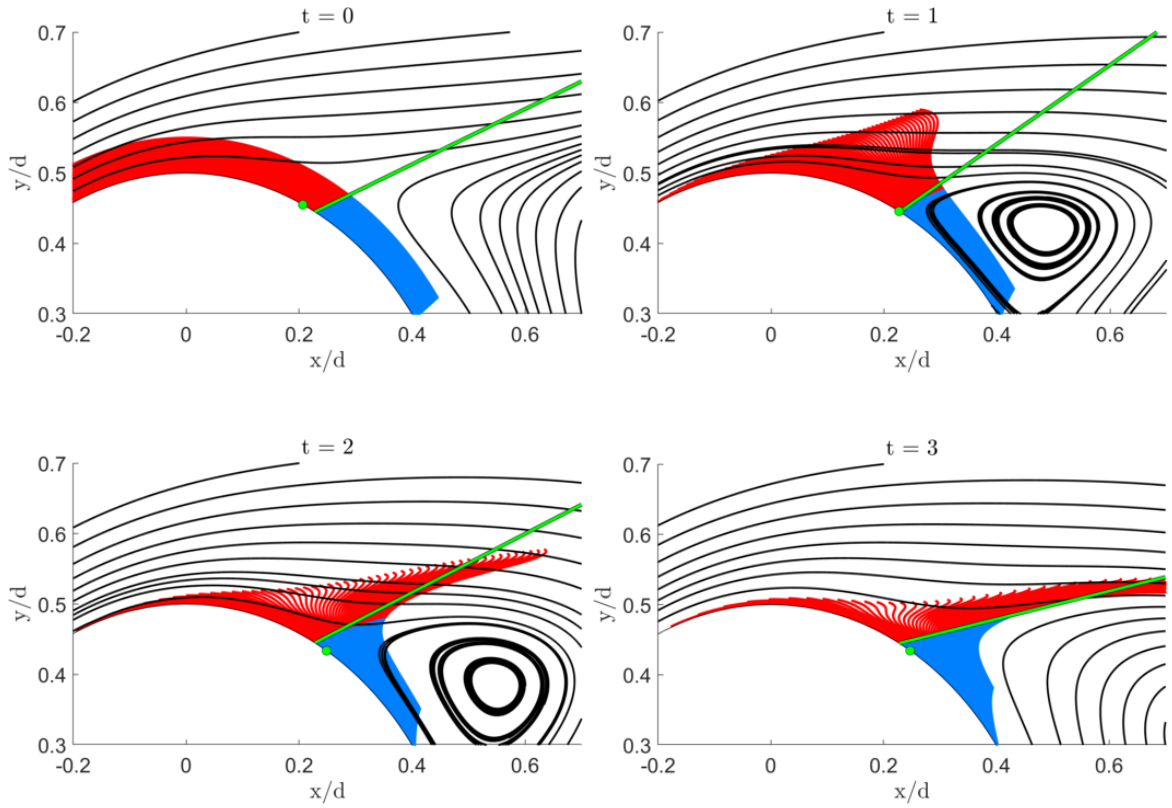

Figure 1.2: Snapshots of color coded particles advected over a circular cylinder near the separation point. Particles are divided in an upstream (red) and downstream (blue) group by the linear approximation of the separation line (green). Also visualized are the instantaneous zero-skin-friction point (green dot) and streamlines (black).

in the Finite-Time Lyapunov Exponent (FTLE) fields. These FTLE fields are determined from the maximum deformations in flow maps that are in turn constructed from integrated particle tracer fields in forward and backward time, respectively. The ridges usually demarcate a hyperbolic Lagrangian Coherent Structure (LCS) [38, 39]. Although a hyperbolic LCS can be identified through local maxima in the FTLE field, Haller [40] shows that the FTLE field has ridges in regions of high shear which are non-hyperbolic [41].

Even though hyperbolic LCS are mostly near zero-flux material lines [42], they fall short in the identification of the start of flow separation at the boundary wall. Because of the zero-velocity no-slip condition, the wall is naturally a set of *non*-hyperbolic fixed points. As a result, the backward time (attracting) FTLE cannot intersect the wall, but envelopes the aerodynamic body. The FTLE can, hence, only identify long-term attracting and repelling surfaces away from the wall rather than the onset of separation.

Based on the initial upwelling and subsequent spike formation described above, Serra et al. [43] developed a kinematic methodology to extract the *Lagrangian backbone of separation*, i.e. the theoretical centerpiece of the forming spike in wall-bounded flows from the analysis of the curvature of material lines. If the backbone connects to the wall, we call the separation on wall, and the intersection point the Lagrangian spiking point. This analysis therefore yields a criterion for determining the start of flow separation in the Lagrangian frame. The Lagrangian spiking point can also be directly related to higher-order derivatives of the normal velocity at the wall and therefore provides a criterion for the origin of flow separation in the kinematic sense using only wall-based quantities [43].

Historically, the control of flow separation has focused on techniques such as boundary layer suction and blowing [3] which, although very effective, require the

use of external pumps or compressors and can be very difficult to install, especially if the aerodynamic body is small. Alternative approaches include zero-net mass flux devices such as synthetic jets [4, 5, 6, 44], which use the working fluid itself by inducing instabilities in the shear layer. With the objective to design effective and efficient flow controllers, knowledge of the Lagrangian separation manifold (asymptotic separation line, attracting LCS and spiking point) might therefore inspire new control concepts or improve existing ones.

1.4 Objective identification of kinematic instabilities

The flow over airfoils at moderate Reynolds number is governed by the separation and possible transition and reattachment of the laminar boundary layer. Fundamental to the transition dynamics of the laminar shear layer is the is the development of instabilities and the question whether a local disturbance to an otherwise unperturbed base flow grows or recedes in space and time. In linear stability analysis (LSA), for example, a disturbance is assumed to have the form of complex waves. The stability of these waves can be determined by an eigenvalue problem that follows from substitution into linearized governing flow equations [45]. The theoretical treatment of instabilities has been subject of research for many decades (see Bayly et al. [46], Huerre and Monkewitz [45], Drazin and Reid [47], Schmid [48], and Theofilis [49], for a comprehensive overview).

Many flows, however, do not have a well-defined base flow. Either, there are multiple possible frame of references and/or a complex time dependency makes it impossible to define a base flow, preventing LSA. As stated in (Drazin and Reid [47], p. 354) "the meaning of instability is not clear when the magnitude of the basic flow

changes substantially with time" and "the method of normal modes is not applicable". Simple examples include the flow over a moving flat plate initially at rest [47] or the onset of vortex shedding in the wake behind a circular cylinder [50]. More complex examples are plentiful, such as the flow interaction of two flapping wings or maneuvering flying objects (see for example the flight mechanics of a dragonfly [51]).

Moreover, applying LSA to flows of general complexity can be challenging. While methods have been proposed to this end (Theofilis [49], Ranjan et al. [52]), they are recent and require significant computational resources and complicated algorithms whose limitations and by extension generality remain to be assessed. Even more importantly, perhaps, is that the stability properties of flows often vary in time and non-normal growth can drive the perturbations rather than the most unstable mode predicted by LSA [48]. The introduction of a finite-time horizon to the stability analysis and description of flow instabilities with a non-modal approach has been shown to reveal new perturbations dynamics [53, 48].

Since there is no limit to the complexity of flow problems, an instability should not depend on the frame of the observer. An analysis based on velocity components or the streamlines is inherently non-objective, as these are not invariant under coordinate transformations and always defined with respect to a reference frame. Velocity gradient based flow identifiers and visualizers, including vorticity and other Eulerian vortex identification criteria, such as the Q-criterion by Hunt et al. [54] or the λ_2-criterion by Jeong and Hussain [55], are frame-invariant in the Galilean sense, i.e. their values are consistent in coordinate systems moving at a constant relative speed. A quantity that remains invariant under *any* rotation or translation of the form

$$\mathbf{y} = \mathbf{Q}(t)\mathbf{x} + \mathbf{b}(t), \tag{1.1}$$

is called *objective*, where $\mathbf{Q}(t)$ is an orthogonal tensor and $\mathbf{b}(t)$ denotes a translation

vector. From this argument, Haller [56], Serra and Haller [57], Haller et al. [58] propose objective definitions of a vortex.

Material invariance is also the basis for the objective definition of hyperbolic Lagrangian Coherent Structures (LCS) [56] and Objective Eulerian Coherent Structures (OECSs) [57]. In general, hyperbolic LCS are manifolds that attract or repel fluid material and can be identified through ridges in the Finite-Time Lyapunov Exponent (FTLE) fields [39]. Although maxima in the FTLE identify potential LCS, it has been shown that non-hyperbolic ridges can occur in regions of high shear [40]. Haller [41] presents a methodology to resolve this inconsistency, but admits that the required computation is challenging and sensitive to noise. Babaee et al. [59] discuss the computation of reduced-order FTLEs based on the optimally time-dependent (OTD) modes associated with finite-time instabilities. The OTD modes were previously introduced by Babaee and Sapsis [60] and are shown to capture transient instabilities and their direction. For a more comprehensive literature overview of existing methods to identify transient instabilities and perform dimensionality reduction, we refer the reader to Babaee et al. [59] and the references therein.

Invariably, both the FTLE and the variational Coherent Structures [56, 57] are based solely on the stretching of fluid material. Divergence of particle trajectories, however, may require a long integration time to manifest. This is an undesired feature if one seeks to detect unstable modes in shear flows early. Only recently, Serra et al. [43, 61], Klose et al. [62] have focused on more subtle short-term events in Lagrangian fluid trajectories. Using the curvature of near-wall material lines, they identified the point early fluid upwelling from a no-slip boundary, and showed that such locations remain hidden to existing techniques. The material line curvature is independent of its parametrization, invariant to frame changes under (1.1) and naturally combines stretching- and rotation-based quantities [43]. The objective identification of early and

subtle changes in material lines naturally fits to the identification of instabilities, but a definition of instability based on this perspective has not been coined yet and is subject of this work.

1.5 Contributions and Outline

This dissertation is a comprehensive account of the low-Reynolds number flow over a cambered airfoil for a wide range of angles of attack with a focus on the dynamics of boundary layer separation. The unsteady and complex phenomena of the transitional flow are analyzed through a combination of DNS, LES, experiment, and development of Lagrangian theory and methods.

The main contributions of this thesis are summarized as follows:

- Two and three-dimensional direct numerical simulations of the compressible flow over NACA 65(1)-412 airfoil at Reynolds number $Re = 2 \times 10^4$ are analyzed for angles of attack ranging from zero to ten degrees. The three-dimensional flow topology, stability characteristics, wake structures, statistics, and aerodynamic forces show a rich and wide variety of flow regimes and dynamics that change rapidly with the location of the laminar separation bubble. Despite the extensive effort, a mismatch in the critical angle between computations and wind tunnel experiments remains.

- A comprehensive description of the kinematics of flow separation in the Lagrangian frame for general two-dimensional external aerodynamics including airfoils is presented. FTLE structures that identify coherent structures in the wake are connected to asymptotic Lagrangian separation lines and initial fluid upwelling. A method for extracting the initial location of fluid upwelling within the DGSEM framework is developed and tested. (Klose et al. [62])

- A Lagrangian definition of an instability in shear flows is coined as the wrinkling of material lines over a finite-time interval. The wrinkling is determined through the curvature change of material lines which is objective by definition. A theoretic relation between normal velocity modes in the Eulerian frame and the Lagrangian flow map is developed and links linear stability analysis to the curvature change of Lagrangian material lines.

- The stability and accuracy of marginally resolved DNS with a discontinuous Galerkin spectral element method in standard and kinetic energy conserving formulation is assessed. The study establishes the accuracy, robustness, and efficiency of the DG variants used for the three-dimensional airfoil DNS. (Klose et al. [17])

The following two chapters of this thesis describe the governing equations and the numerical method, including a review of the split-form DG formulation. The stability and accuracy of the DG scheme for marginally resolved Navier-Stokes flows is presented in Chapter 4. The next chapter discusses the three-dimensional flow over a NACA 65(1)-412 at $Re = 2 \times 10^4$ and various angles of attack. The analysis focuses on the rapidly changing flow regimes and the effect on the topology, wake structures, and statistics. Chapter 7 presents the kinematics of Lagrangian flow separation in external aerodynamics and the work on the objective identification of kinematic instabilities is discussed thereafter. A summary and outlook is listed in the final chapter of this thesis.

Chapter 2

Governing Equations

2.1 Conservation Laws

We compute solutions to the compressible Navier-Stokes equations, which can be written in non-dimensional form as the system of equations

$$\partial_t \mathbf{U} + \nabla \cdot \mathbf{F} = 0. \tag{2.1}$$

In (2.1), $\mathbf{U}$ represents the vector of the conserved variables,

$$\mathbf{U} = [\, \rho \quad \rho u \quad \rho v \quad \rho w \quad \rho e \,]^T . \tag{2.2}$$

The flux vector $\mathbf{F}$ is split into an advective (superscript a) and a viscous part (superscript v),

$$\nabla \cdot \mathbf{F} = \partial_x \mathbf{F}^a + \partial_y \mathbf{G}^a + \partial_z \mathbf{H}^a - \frac{1}{Re_f} \left(\partial_x \mathbf{F}^v + \partial_y \mathbf{G}^v + \partial_z \mathbf{H}^v \right), \tag{2.3}$$

where

$$\begin{aligned} \mathbf{F}^a &= \left[\rho u \quad p{+}\rho u^2 \quad \rho uv \quad \rho uw \quad u(\rho e{+}p) \right]^T, \\ \mathbf{G}^a &= \left[\rho v \quad \rho vu \quad p{+}\rho v^2 \quad \rho vw \quad v(\rho e{+}p) \right]^T, \\ \mathbf{H}^a &= \left[\rho w \quad \rho wu \quad \rho wv \quad p{+}\rho w^2 \quad w(\rho e{+}p) \right]^T, \end{aligned} \tag{2.4}$$

$$
\begin{aligned}
\mathbf{F}^v &= \begin{bmatrix} 0 & \tau_{xx} & \tau_{yx} & \tau_{zx} & u\tau_{xx}+v\tau_{yx}+w\tau_{zx}+\dfrac{\kappa}{(\gamma-1)\,PrM_f^2}T_x \end{bmatrix}^T, \\
\mathbf{G}^v &= \begin{bmatrix} 0 & \tau_{xy} & \tau_{yy} & \tau_{zy} & u\tau_{xy}+v\tau_{yy}+w\tau_{zy}+\dfrac{\kappa}{(\gamma-1)\,PrM_f^2}T_y \end{bmatrix}^T, \\
\mathbf{H}^v &= \begin{bmatrix} 0 & \tau_{xz} & \tau_{yz} & \tau_{zz} & u\tau_{xz}+v\tau_{yz}+w\tau_{zz}+\dfrac{\kappa}{(\gamma-1)\,PrM_f^2}T_z \end{bmatrix}^T.
\end{aligned} \tag{2.5}
$$

ρ, u, v, w, p, and T are the density, velocities, pressure, and temperature respectively. The specific total energy is $\rho e = p/(\gamma-1) + \frac{1}{2}\rho(u^2+v^2+w^2)$ and the system is closed by the equation of state,

$$
p = \frac{\rho T}{\gamma M_f^2}. \tag{2.6}
$$

All quantities are non-dimensionalized with respect to a problem specific reference length, velocity, density, and temperature yielding the non-dimensional Reynolds number, Re_f and Mach number, M_f.

We approximate the system, (2.1), with a discontinuous Galerkin spectral element method (DGSEM). Details can be found in [13, 17] and will not be discussed here.

2.2 Boundary layer relations

The boundary layer velocity profile is computed according to the methodology described by Alam and Sandham [63] and Uranga et al. [7], who use a pseudo-velocity profile inside the rotational boundary layer flow based on the spanwise vorticity

$$
\mathbf{u}^*(s,\eta) = \int_0^\eta \boldsymbol{\omega}(s,\tilde{\eta}) \times \mathbf{n}(s)\,\mathrm{d}\tilde{\eta}, \tag{2.7}
$$

where s and η refer to the wall-tangential and normal coordinates respectively and $\mathbf{n}(s)$ is the wall-normal unit vector. The boundary layer edge η_e is located at a distance where the vorticity magnitude and gradient are below a certain threshold and the

flow is assumed to be irrotational [7]. The displacement thickness δ^* and momentum thickness θ are compute by integrating the velocity profile across the boundary layer

$$\delta^*(s) = \int_0^{\eta_e} \left(1 - \frac{u_s(s,\eta)}{u_e(s)}\right) \mathrm{d}\eta, \tag{2.8}$$

$$\theta(s) = \int_0^{\eta_e} \frac{u_s(s,\eta)}{u_e(s)} \left(1 - \frac{u_s(s,\eta)}{u_e(s)}\right) \mathrm{d}\eta. \tag{2.9}$$

Here, u_s is the local, tangential velocity component and u_e the velocity magnitude evaluated at the boundary layer edge η_e. The shape factor is defined as the ratio of displacement to momentum thickness, $H = \delta^*/\theta$.

2.3 Finite-Time Lyapunov Exponent

We extract structures and patterns from flow field data using a Finite-Time Lyapunov Exponent contour field [42]. The FTLE, which characterizes the maximal stretching of infinitesimal fluid volumes over a given time interval, is determined by tracing fluid particles over time and subsequently computing the deformation tensor induced by the flow map.

We express the particle trajectories as

$$\mathbf{x}\left(\mathbf{x}_0, t_0; T\right) = \mathbf{x}_0 + \int_{t_0}^{t_0+T} \mathbf{v}\left(\mathbf{x}\left(\tau; \mathbf{x}_0, t_0\right), \tau\right) d\tau, \tag{2.10}$$

from which the flow map $\mathbf{\Phi}$ is defined:

$$\mathbf{\Phi}_{t_0}^{t}\left(\mathbf{x_0}, t_0; T\right) \equiv \mathbf{x}\left(\mathbf{x}_0, t_0; T\right). \tag{2.11}$$

From the deformation gradient tensor $\nabla\mathbf{\Phi}_{t_0}^{t}$, the right Cauchy-Green strain tensor $\mathbf{C}_{t_0}^{t} = [\nabla\mathbf{\Phi}_{t_0}^{t}]^* \nabla\mathbf{\Phi}_{t_0}^{t}$ can be used to compute the strain in the Lagrangian frame. With the largest eigenvalue of the strain tensor $\sigma_2\left(\mathbf{C}_{t_0}^{t}(\mathbf{x}_0)\right)$, the finite-time Lyapunov exponent field is defined as

$$\sigma_{t_0}^{t}(\mathbf{x}_0) = \frac{1}{|t - t_0|} \ln \sqrt{\sigma_2(\mathbf{x}_0)}. \tag{2.12}$$

This FTLE identifies the highest Lagrangian rate of stretching in the flow field. Tracing fluid particles forward or backward in time, ridges of the FTLE field can be used to identify hyperbolic repelling and attracting Lagrangian coherent structures (see Haller [38, 40], Nelson and Jacobs [64] for a more detailed description).

2.4 Separation Point and Angle

Haller [36] shows that for flows with an asymptotic mean, such as periodic flows, the asymptotic separation point γ is located at the integrated zero-skin-friction (c_f) point

$$\frac{1}{t_1 - t_0} \int_{t_0}^{t_1} c_f(\gamma, t)\, dt = 0. \tag{2.13}$$

Haller [36] further derives an analytic expression for the separation profile which is a wall-bounded unsteady manifold along which fluid particles are ejected from the wall into the free-stream. The slope, or separation angle, of this line can be computed just by evaluating integrated values of the pressure and skin friction data at the wall:

$$\tan(\alpha(t_0)) = -\lim_{T \to -\infty} \frac{3 \int_{t_0}^{T} \tau_x(\gamma, t)\, dt}{\int_{t_0}^{T} \left[p_x(\gamma, y_w, t) + 3\tau_x(\gamma, t) \int_{t_0}^{t} \frac{1}{\mu} \tau(\gamma, s)\, ds \right] dt}. \tag{2.14}$$

Here, the x coordinate refers to wall tangential direction and y points in wall-normal direction. The separation angle α is the angle to the tangent of the wall at the separation point. Using both, the separation point and the separation angle, a linear approximation of the separation profile can be constructed.

2.5 The Lagrangian Backbone of Separation and the Spiking Point

Flow separation is invariably characterized by the ejection of fluid particles from a no-slip wall. While the long-time (asymptotic) behavior of these particles are governed by attracting LCSs in the flow field, the onset of separation is not related to asymptotic structures. Serra et al. [43] show that the formation of a material spike is characterized by high folding induced by the flow on material lines close to the wall (Figure 6.1), which appears at a different location - generally upstream - compared to the asymptotic separation point (e.g., the zero-skin-friction point in the case of steady flows). This deformed spike, then, eventually converges to the breakaway from the wall along the corresponding long-term separation structure. The materially evolving set of points forming the centerpiece of the separation spike (magenta curve in Figure 6.1) is also referred to as the *backbone of separation* [43].

Following Serra et al. [43], separation is on-wall if the backbone has a transverse intersection with the non-slip boundary, off-wall otherwise. We note that such a distinction is not postulated a priori based on heuristic arguments, but rather is an outcome of the theory proposed in [43]. Using a coordinate system $[s, \eta]$ in direction tangential and normal to the wall respectively, we compute the Lagrangian curvature change relative to the initial curvature $\bar{\kappa}_{t_0}^{t_0+T} := \kappa_{t_0}^{t_0+T} - \kappa_0$ in a neighborhood of the no-slip boundary foliated by a set of material lines initially parallel to the wall, parametrized by $\mathbf{r}_\eta(s),\ s \in [s_1, s_2] \subset \mathbb{R},\ \eta \in [0, \eta_1] \subset \mathbb{R}$. Such a foliation enslaves the initial local tangent $\mathbf{r}'_\eta$ and curvature κ_{0_η} to the position $\mathbf{r}_\eta$, making therefore $\bar{\kappa}_{t_0}^{t_0+T}$ a function of t_0, T and of the initial configuration $\mathbf{r}_\eta$ only. Here $(\cdot)' := \frac{d}{ds}(\cdot)$. The $\bar{\kappa}_{t_0}^{t_0+T}$

field can be directly computed from the flow map $\mathbf{\Phi}_{t_0}^{t_0+T}$ using the relation

$$\bar{\kappa}_{t_0}^{t_0+T} = \frac{\left\langle \left(\nabla^2 \mathbf{\Phi}_{t_0}^{t_0+T}(\mathbf{r}_\eta)\mathbf{r}'_\eta\right)\mathbf{r}'_\eta, \mathbf{R}\nabla\mathbf{\Phi}_{t_0}^{t_0+T}(\mathbf{r}_\eta)\mathbf{r}'_\eta \right\rangle}{\left\langle \mathbf{r}'_\eta, \mathbf{C}_{t_0}^{t_0+T}(\mathbf{r}_\eta)\mathbf{r}'_\eta \right\rangle^{3/2}} + \kappa_{0_\eta}\left[\frac{\det\left(\nabla\mathbf{\Phi}_{t_0}^{t_0+T}(\mathbf{r}_\eta)\right)\left\langle \mathbf{r}'_\eta, \mathbf{r}'_\eta\right\rangle^{3/2}}{\left\langle \mathbf{r}'_\eta, \mathbf{C}_{t_0}^{t_0+T}(\mathbf{r}_\eta)\mathbf{r}'_\eta \right\rangle^{3/2}} - 1\right], \quad (2.15)$$

where $\langle\cdot,\cdot\rangle$ denotes the inner product; $(\nabla^2\mathbf{\Phi}_{t_0}^{t}(\mathbf{r}_\eta)\mathbf{r}'_\eta)_{ij} = \sum_{k=1}^{2}\partial_{jk}\Phi_{t_0 i}^{t}(\mathbf{r}_\eta)r'_{\eta_k}$, $i,j \in \{1,2\}$, and $\mathbf{R}$ is the rotation matrix defined as

$$\mathbf{R} := \begin{bmatrix} 0 & 1 \\ -1 & 0 \end{bmatrix}. \quad (2.16)$$

We note that with a clockwise parametrization of the no-slip boundary, $\mathbf{R}\mathbf{r}'_\eta$ is the vector normal to the initial material line, pointing towards the boundary. The initial position $\mathcal{B}(t_0)$ of the Lagrangian backbone of separation – i.e., the theoretical centerpiece of the material spike over $[t_0, t_0+T]$ – is then defined as a positive-valued wall-transverse ridge of the $\bar{\kappa}_{t_0}^{t_0+T}$ field (Serra et al. [43] for details). Later position of the backbone $\mathcal{B}(t)$ can be computed by materially advecting $\mathcal{B}(t_0)$, i.e., letting $\mathcal{B}(t) := \mathbf{\Phi}_{t_0}^{t}(\mathcal{B}(t_0))$, $t \in [t_0, t_0+T]$. If $\mathcal{B}(t_0)$ connects to the wall transversally, the intersection point is called the Lagrangian spiking point and is defined by

$$(s_p, 0) := \mathcal{B}(t_0) \cap \text{no-slip wall}. \quad (2.17)$$

Serra et al. [43] derived also alternative exact formulas for the Lagrangian spiking point using only on-wall Eulerian quantities in the case of steady, time periodic and generally aperiodic flows (cf. Table 2.1). Finally, in the instantaneous limit ($T = 0$), the Lagrangian backbone of separation and spiking point turns into their correspondent Eulerian versions (Serra et al. [43]).

In Table 2.1, $\hat{v}$ indicates the velocity in normal direction to the wall, and can be

Table 2.1: Equations determining the Lagrangian spiking point for generally aperiodic compressible (left) and incompressible (right) flows on a no-slip boundary in terms of on-wall Eulerian quantities. $\hat{v}$ indicates the velocity direction normal to the wall.

Lagrangian spiking point : $(s_p, 0)$

$\nabla \cdot \mathbf{v} \neq 0$	$\nabla \cdot \mathbf{v} = 0$
$\begin{cases} \int_{t_0}^{t_0+T} \partial_{sss\eta} \hat{v}\,(s_p,0,t) = 0, \\ \int_{t_0}^{t_0+T} \partial_{ssss\eta} \hat{v}\,(s_p,0,t) > 0, \\ \int_{t_0}^{t_0+T} \partial_{ss\eta} \hat{v}\,(s_p,0,t) < 0. \end{cases}$	$\begin{cases} \int_{t_0}^{t_0+T} \partial_{sss\eta\eta} \hat{v}\,(s_p,0,t) = 0, \\ \int_{t_0}^{t_0+T} \partial_{ssss\eta\eta} \hat{v}\,(s_p,0,t) > 0, \\ \int_{t_0}^{t_0+T} \partial_{ss\eta\eta} \hat{v}\,(s_p,0,t) < 0, \end{cases}$

computed from the inner product:

$$\hat{v} = \langle \mathbf{v}, \mathbf{n} \rangle = u n_x + v n_y, \quad \mathbf{n} := \mathbf{R} \frac{\mathbf{r}'_\eta}{|\mathbf{r}'_\eta|}, \quad |\mathbf{r}'_\eta| = \sqrt{\langle \mathbf{r}'_\eta, \mathbf{r}'_\eta \rangle}. \tag{2.18}$$

Assuming a curved, parametrized boundary $\mathcal{W}(s)$, the normal vector $\mathbf{n}$ at each collocation point $\mathbf{x}_i$ is the vector pointing to the closest intersection point with the boundary $\mathcal{W}$ and found by minimizing the distance function $d_i(s) = |\mathbf{x}_i - \mathcal{W}(s)|$. If we assume a continuous and sufficiently smooth function $\hat{v}$, we can switch the order of differentiation in Table 2.1 and compute the normal gradients first. Once the normal velocity is obtained at each collocation point, the gradient can be computed by multiplication with the derivative matrix $\mathcal{D}$. Using the spectral operator $\mathcal{D}$ gives the derivatives in x- and y-direction in the polynomial order of the scheme.

$$\nabla \hat{v} = \mathcal{D} \hat{v}. \tag{2.19}$$

The directional derivative of the normal velocity $\hat{v}$ in direction of the wall-normal vector $\mathbf{n}$ is computed as

$$\partial_\eta \hat{v} = \nabla_{\mathbf{n}} \hat{v} = \nabla \hat{v} \cdot \mathbf{n} = (\partial_x \hat{v})\, n_x + (\partial_y \hat{v})\, n_y. \tag{2.20}$$

This relation allows us to calculate the normal derivatives everywhere in the flow field from the velocity gradient and the normal vector at each point. Once $\partial_\eta \hat{v}$ or $\partial_{\eta\eta} \hat{v}$ are determined, they can be projected onto the boundary and the derivatives tangential to the wall can be computed subsequently as one-dimensional operations.

2.6 Acknowledgements

Sections 2.1 through 2.2 are currently being prepared for submission for publication of the material, B. F. Klose, G. R. Spedding and G. B. Jacobs. B. F. Klose: investigation, original draft preparation, visualization. G. R. Spedding: minor contributions to supervision, review & editing. G. B. Jacobs: supervision, review & editing.

Sections 2.3 through 2.5, in full, are a reprint of the material as it appears in "Kinematics of Lagrangian Flow Separation in External Aerodynamics", B. F. Klose, M. Serra and G. B. Jacobs, *AIAA Journal*, 2020. B. F. Klose: investigation, visualization, original draft preparation. M. Serra: support with theory and curvature routines, editing. G. B. Jacobs: supervision, review & editing.

Chapter 3

The Discontinuous Galerkin Spectral Element Method

We approximate the system, (2.1), with a discontinuous Galerkin spectral element method (DGSEM). Details can be found in [13, 65] and we only provide a short summary here.

The physical domain is subdivided into hexahedral elements, each of which is mapped from the reference element, $E = [-1, 1]^3$ by a transformation $\vec{x} = \vec{X}(\xi, \eta, \zeta)$. Under the transformation, the reference space equations become

$$\tilde{\mathbf{U}}_t + \nabla_\xi \cdot \tilde{\mathbf{F}} = 0, \tag{3.1}$$

where $\tilde{\mathbf{U}} = J\mathbf{U}$, J is the transformation Jacobian, and $\tilde{\mathbf{F}}$ is the contravariant flux.

The DGSEM approximates the conserved variables and the contravariant fluxes as polynomials of arbitrary order N within each element. We approximate the vector $\tilde{\mathbf{U}}$ as

$$\tilde{\mathbf{U}}_N = \sum_{i=0}^{N}\sum_{j=0}^{N}\sum_{k=0}^{N}\left(\tilde{\mathbf{U}}_N\right)_{i,j,k}\ell_i(\xi)\ell_j(\eta)\ell_k(\zeta), \tag{3.2}$$

where the Lagrange interpolating polynomials, $\ell_i(\xi)$ are

$$\ell_i(\xi) = \prod_{\substack{n=0 \\ n \neq i}}^{N} \frac{\xi - \xi_n}{\xi_i - \xi_n}, \tag{3.3}$$

and similarly for $\ell_j(\eta)$ and $\ell_k(\zeta)$. The nodes ξ_i, η_j, and ζ_k are chosen to be the nodes of a Gauss quadrature.

Weak Formulation

The approximation satisfies a weak form the conservation law, constructed by taking the inner product of (3.1) with a test function ϕ,

$$\int_E \left(\partial_t \tilde{\mathbf{U}} + \nabla \cdot \tilde{\mathbf{F}}\right) \phi \, \mathrm{d}\xi = 0, \tag{3.4}$$

and integrating by parts

$$\int_E \partial_t \tilde{\mathbf{U}} \phi \, \mathrm{d}\xi + \int_{\partial E} \tilde{\mathbf{F}} \cdot \mathbf{n} \phi \, \mathrm{d}S - \int_E \tilde{\mathbf{F}} \cdot \nabla \phi \, \mathrm{d}\xi = 0. \tag{3.5}$$

DG approximations do not require the solution to be continuous at the interface, and elements are coupled through the boundary flux in (3.5). We replace $\tilde{\mathbf{F}}$ with a numerical flux $\tilde{\mathbf{F}}^* \left(\tilde{\mathbf{U}}^L, \tilde{\mathbf{U}}^R\right)$, which depends only on the solutions on the left and right of the interface between two elements, and is computed through a Riemann solver, e.g. the upwinding scheme by Roe [66].

The integrals in (3.5) are approximated with a Gauss quadrature of $N+1$ nodes, and two choices have been commonly used. The first is the Legendre-Gauss (LG) quadrature, which approximates the integral exactly for polynomial integrands of order $2N+1$ or less, but whose nodes do not include endpoints. The second is the Legendre-Gauss-Lobatto (LGL) quadrature, whose nodes include endpoints, but is only exact for polynomial integrands of order $2N-1$ or less. For a more detailed discussion of the differences between LG and LGL quadrature we refer to Gassner and Kopriva [67].

By replacing the integrals in (3.5) with quadrature, and choosing $\phi = \ell_i(\xi)\ell_j(\eta)\ell_k(\zeta)$, the flux derivatives $\int_E \nabla \cdot \tilde{\mathbf{F}}\phi \mathrm{d}\xi$ for the Gauss-Lobatto version at the node $(i,\, j,\, k)$ become

$$\begin{aligned}
\partial_\xi \tilde{\mathbf{F}}\Big|_{ijk} &\approx \left(\delta_{iN}\tilde{\mathbf{F}}^*_{Njk} - \delta_{i0}\tilde{\mathbf{F}}^*_{0jk}\right) + \sum_{m=0}^{N} \hat{D}_{im}\tilde{\mathbf{F}}_{mjk}, \\
\partial_\eta \tilde{\mathbf{G}}\Big|_{ijk} &\approx \left(\delta_{jN}\tilde{\mathbf{G}}^*_{iNk} - \delta_{j0}\tilde{\mathbf{G}}^*_{i0k}\right) + \sum_{m=0}^{N} \hat{D}_{jm}\tilde{\mathbf{G}}_{imk}, \\
\partial_\zeta \tilde{\mathbf{H}}\Big|_{ijk} &\approx \left(\delta_{kN}\tilde{\mathbf{H}}^*_{ijN} - \delta_{k0}\tilde{\mathbf{H}}^*_{ij0}\right) + \sum_{m=0}^{N} \hat{D}_{km}\tilde{\mathbf{H}}_{ijm},
\end{aligned} \tag{3.6}$$

where $\hat{D}_{ij} = -D_{ji}w_j/w_i$, $D_{ij} = \ell'_j(\xi_i), i, j = 0, \ldots, N$ is the derivative matrix, and w_i is the quadrature weight at node i.

Formulations in strong and split form

Integrating (3.5) by parts one more time lets us rewrite (3.5) in what is known as the strong form

$$\int_E \partial_t \tilde{\mathbf{U}}\phi \, \mathrm{d}\xi + \int_{\partial E} \left(\tilde{\mathbf{F}}^* - \tilde{\mathbf{F}}\right) \cdot \mathbf{n}\phi \, \mathrm{d}S + \int_E \nabla \cdot \tilde{\mathbf{F}}\phi \, \mathrm{d}\xi = 0. \tag{3.7}$$

Again, we replace the integrals with quadrature and choose $\phi = \ell_i(\xi)\ell_j(\eta)\ell_k(\zeta)$, so that for the Gauss-Lobatto version the flux derivatives in (3.7) become [13]

$$\begin{aligned}
\partial_\xi \tilde{\mathbf{F}}\Big|_{ijk} &\approx \left(\delta_{iN}\left[\tilde{\mathbf{F}}^* - \tilde{\mathbf{F}}\right]_{Njk} - \delta_{i0}\left[\tilde{\mathbf{F}}^* - \tilde{\mathbf{F}}\right]_{0jk}\right) + \sum_{m=0}^{N} D_{im}\tilde{\mathbf{F}}_{mjk}, \\
\partial_\eta \tilde{\mathbf{G}}\Big|_{ijk} &\approx \left(\delta_{jN}\left[\tilde{\mathbf{G}}^* - \tilde{\mathbf{G}}\right]_{iNk} - \delta_{j0}\left[\tilde{\mathbf{G}}^* - \tilde{\mathbf{G}}\right]_{i0k}\right) + \sum_{m=0}^{N} D_{jm}\tilde{\mathbf{G}}_{imk}, \\
\partial_\zeta \tilde{\mathbf{H}}\Big|_{ijk} &\approx \left(\delta_{kN}\left[\tilde{\mathbf{H}}^* - \tilde{\mathbf{H}}\right]_{ijN} - \delta_{k0}\left[\tilde{\mathbf{H}}^* - \tilde{\mathbf{H}}\right]_{ij0}\right) + \sum_{m=0}^{N} D_{km}\tilde{\mathbf{H}}_{ijm},
\end{aligned} \tag{3.8}$$

where $D_{ij} = \ell'_j(\xi_i), i, j = 0, \ldots, N$ is the derivative matrix. Note that the forms (3.6) and (3.8) are algebraically equivalent [68].

The non-linearity of the inviscid Euler fluxes introduces aliasing errors when the fluxes are approximated by polynomials, which can lead to instability. Gassner et al.

[16, 65] showed that through the SPB property of the derivative operator when using the LGL points, the volume term contributions in (3.8) can be rewritten as

$$\begin{aligned}
\partial_\xi \tilde{\mathbf{F}}\big|_{ijk} &\approx \left(\delta_{iN}\left[\tilde{\mathbf{F}}^* - \tilde{\mathbf{F}}\right]_{Njk} - \delta_{i0}\left[\tilde{\mathbf{F}}^* - \tilde{\mathbf{F}}\right]_{0jk}\right) + 2\sum_{m=0}^{N} D_{im}\tilde{\mathbf{F}}^{\#}_{(i,m),j,k}, \\
\partial_\eta \tilde{\mathbf{G}}\big|_{ijk} &\approx \left(\delta_{jN}\left[\tilde{\mathbf{G}}^* - \tilde{\mathbf{G}}\right]_{iNk} - \delta_{j0}\left[\tilde{\mathbf{G}}^* - \tilde{\mathbf{G}}\right]_{i0k}\right) + 2\sum_{m=0}^{N} D_{jm}\tilde{\mathbf{G}}^{\#}_{i,(j,m),k}, \\
\partial_\eta \tilde{\mathbf{H}}\big|_{ijk} &\approx \left(\delta_{kN}\left[\tilde{\mathbf{H}}^* - \tilde{\mathbf{H}}\right]_{ijN} - \delta_{k0}\left[\tilde{\mathbf{H}}^* - \tilde{\mathbf{H}}\right]_{ij0}\right) + 2\sum_{m=0}^{N} D_{km}\tilde{\mathbf{H}}^{\#}_{i,j,(k,m)}.
\end{aligned} \tag{3.9}$$

so that the scheme becomes entropy or energy conserving, depending on the choice of the new two-point fluxes $\mathbf{F}^{a,\#}$, $\mathbf{G}^{a,\#}$, and $\mathbf{H}^{a,\#}$, and the numerical surface fluxes. The indices in parenthesis in (3.9) indicate the two nodes for the two-point fluxes. In this work, we choose the kinetic energy conserving split form by Pirozzoli [69]

$$\mathbf{F}^{a,\#} = \begin{bmatrix} \{\{\rho\}\}\{\{u\}\} \\ \{\{\rho\}\}\{\{u\}\}^2 + \{\{p\}\} \\ \{\{\rho\}\}\{\{u\}\}\{\{v\}\} \\ \{\{\rho\}\}\{\{u\}\}\{\{w\}\} \\ \{\{\rho\}\}\{\{u\}\}\{\{h\}\} \end{bmatrix}, \quad \mathbf{G}^{a,\#} = \begin{bmatrix} \{\{\rho\}\}\{\{v\}\} \\ \{\{\rho\}\}\{\{u\}\}\{\{v\}\} \\ \{\{\rho\}\}\{\{v\}\}^2 + \{\{p\}\} \\ \{\{\rho\}\}\{\{v\}\}\{\{w\}\} \\ \{\{\rho\}\}\{\{v\}\}\{\{h\}\} \end{bmatrix},$$
$$\mathbf{H}^{a,\#} = \begin{bmatrix} \{\{\rho\}\}\{\{w\}\} \\ \{\{\rho\}\}\{\{u\}\}\{\{w\}\} \\ \{\{\rho\}\}\{\{v\}\}\{\{w\}\} \\ \{\{\rho\}\}\{\{w\}\}^2 + \{\{p\}\} \\ \{\{\rho\}\}\{\{w\}\}\{\{h\}\} \end{bmatrix}, \tag{3.10}$$

with the notation $\{\{a\}\}_{im} := \frac{1}{2}(a_i + a_m)$.

The viscous stresses are computed in the standard formulation $\mathbf{F}^{v,\#} = \{\{\mathbf{F}^v\}\}$, $\mathbf{G}^{v,\#} = \{\{\mathbf{G}^v\}\}$, and $\mathbf{H}^{v,\#} = \{\{\mathbf{H}^v\}\}$ and the total fluxes are $\mathbf{F}^{\#} = \mathbf{F}^{a,\#} - \frac{1}{Re_f}\mathbf{F}^{v,\#}$, with the contravariant forms follow from $\tilde{\mathbf{F}}^{\#} = \left[\mathbf{F}^{\#}, \mathbf{G}^{\#}, \mathbf{H}^{\#}\right] \cdot \nabla\xi$, see [13, 65]. Formulations for $\tilde{\mathbf{G}}^{\#}$ and $\tilde{\mathbf{H}}^{\#}$ are obtained similarly.

It was also shown in [16] that the scheme is kinetic energy conserving only if a central Riemann solver, e.g. the Lax-Friedrichs numerical flux without additional stabilization terms, is chosen as the numerical flux. Additional dissipation can be added through the appropriate choice of Riemann solver to increase robustness or for implicit large eddy simulations [70].

Acknowledgements

Chapter 3, in full, is a reprint of the material as it appears in "Assessing standard and kinetic energy conserving volume fluxes in discontinuous Galerkin formulations for marginally resolved Navier-Stokes flows", B. F. Klose, G. B. Jacobs and D. A. Kopriva, *Computers & Fluids*, 2020. B. F. Klose: investigation, original draft preparation, visualization. G. B. Jacobs: supervision, review & editing. D. A. Kopriva: methodology review, supervision, editing.

Chapter 4

Assessing standard and kinetic energy conserving volume fluxes in discontinuous Galerkin formulations for marginally resolved Navier-Stokes flows

4.1 Overview and Summary

In this chapter, we asses the stability and accuracy of discontinuous Galerkin approximations in the standard conservation form and in a kinetic energy conserving split form for under-resolved computations. To this end, direct numerical simulations of a three dimensional inviscid Taylor-Green vortex, the viscous flows over a square cylinder, a plane jet, and an airfoil flow in two and three dimensions are conducted. Following Gassner et al. [16], we demonstrate the kinetic energy conservation of the

DG scheme on the inviscid Taylor-Green vortex and challenge the method's robustness and accuracy by computation of the turbulent break up of a plane jet (e.g. [71, 47]). The square cylinder is frequently used as a canonical test for numerical schemes and has been extensively studied in the past [72, 73, 74, 75], while the flow over a NACA 65(1)-412 cambered airfoil at incidence is a relevant case encountered in engineering applications, e.g. in turbomachinery [76].

On the basis of the examples introduced above, we show that the split form DGSEM produces numerically stable results of Navier-Stokes flows where the standard scheme fails. While the computations converge to the same solutions for high enough polynomial orders, the robustness of the kinetic energy conserving split form for simulations of marginally resolved flows makes it the primary choice for implicit LES computations.

The governing equations and the numerical model are outlined in Chapters 2 and 3. In Section 4.2, we present the setup and results of our computations. A summary and conclusion are presented at the end of this paper in Section 4.3.

4.2 Results and Discussion

In the this section, we present the setup and computed results for the Taylor-Green vortex, the square cylinder flow, the plane jet and the flow over a NACA 65(1)-412 airfoil. Each problem is simulated using the standard DGSEM, which supports both Gauss and Gauss-Lobatto nodes, and the kinetic energy conserving formulation of the split form (SF) with Gauss-Lobatto points. To advance the solution in time, the system of equations (2.1) is integrated with an explicit low-dispersion 6-stage 4th-order Runge-Kutta scheme [77].

4.2.1 Taylor-Green Vortex

The implementation of the kinetic-energy preserving inviscid fluxes into the DGSEM code is verified with the Taylor-Green vortex in three dimensions, as it has been done by Gassner et al. [16]. In addition to inviscid flow, we also consider the effect of viscosity and compute the Taylor-Green vortex at $Re = 1{,}000$. 16^3 elements in a $[0, 2\pi]^3$ box with periodic boundary conditions in all directions are used in combination with spatially uniform polynomial orders of $N = 3$, 6 and 9. A free-stream Mach number of $M = 0.1$ ensures low compressibility effects. Two DGSEM schemes are considered: the standard form using LG nodes and the split form with LGL nodes, where the interface fluxes are computed with an upwinding Roe solver (Roe), a central Lax-Friedrichs solver with a stabilization term (LxF), and a central Riemann solver without dissipation (Central). Note that the Pirozzoli flux splitting is also applied to the Lax-Friedrichs solver for cases using the split form. Based on the smallest node spacing, a Courant-Fridrichs-Lewy (CFL) number of 0.5 is used for computations with the standard Gauss DGSEM and 0.2 for the Gauss-Lobatto split-form variant to have similar time step sizes.

The kinetic energy $k = (u^2+v^2+w^2)/2$ is integrated over the domain at each time step and plotted in Figure 4.1 for inviscid flow and a polynomial order of $N = 3$. As expected, the standard form without dissipation at the interfaces is unstable. Upwinding or dissipative schemes are stable for this problem, but decrease the total kinetic energy with time (Fig. 4.1a). The split form approximation conserves the kinetic energy if a central Riemann solver without stabilization terms is used, while the Roe and Lax-Fiedrichs solvers add numerical viscosity and decrease the total kinetic energy (Fig. 4.1b), just as in the standard form. Consistent with [16], the Pirozzoli split form shows a marginal decrease in the kinetic energy over time (Fig. 4.1b), which can be attributed to the discretization of the pressure term.

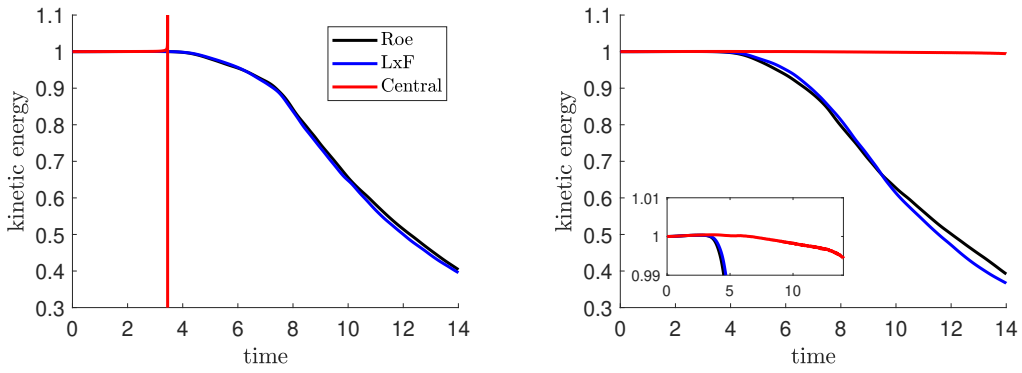

(a) Gauss nodes & standard DG (b) Gauss-Lobatto nodes & split form DG

Figure 4.1: Integrated kinetic energy over time of the Taylor-Green vortex in 3D with different Riemann solvers (Roe, Lax-Friedrichs (LxF), Central without dissipation) for polynomial order $N = 3$. (a) Standard form with LG nodes. (b) Split form with LGL nodes.

The numerical stability of the Taylor-Green vortex for different parameters is summarized in Table 4.1. For inviscid flow, the standard DGSEM scheme produces numerically stable results only at low order ($N = 3$) and with a dissipative Riemann solver, while the split form DG is numerically more robust and only fails for higher orders when the central Riemann solver is used. This result is consistent with the findings by Gassner et al. [16], who also report unstable results for polynomial orders $N > 3$. The introduction of viscosity stabilizes the simulations and the standard scheme fails only when run in conjunction with the non-dissipative central Riemann solver, while the split form DGSEM is now stable for all cases (Tab. 4.1).

Although the Roe and Lax-Friedrichs Riemann solvers both show the same stability properties here, it has been shown that the energy spectrum of the Roe solver follows the -5/3 law more closely than the Lax-Friedrichs scheme [78, 79]. Therefore, the upwinding Riemann solver of Roe is used in the following test problems.

Table 4.1: Numerical Stability of the Taylor-Green vortex. ✓= stable, x = unstable. DGSEM scheme: standard & Gauss nodes (LG) and split-form & Gauss-Lobatto nodes (LGL-SF). Riemann solver: upwinding Roe (Roe), central Lax-Friedrichs with stabilization (LxF) and central Riemann without dissipation (Cen).

	Inviscid						Re = 1,000					
	LG			LGL-SF			LG			LGL-SF		
N	Roe	LxF	Cen	Roe	LxF	Cen	Roe	LxF	Cen	Roe	LxF	Cen
3	✓	✓	x	✓	✓	✓	✓	✓	x	✓	✓	✓
6	x	x	x	✓	✓	x	✓	✓	x	✓	✓	✓
9	x	x	x	✓	✓	x	✓	✓	x	✓	✓	✓

4.2.2 Plane Jet

Fluid jets are naturally unstable shear flows that show exponential growth to perturbations and eventually transition to turbulence [47]. A high-order scheme can accurately capture these instabilities, but its numerical robustness might be challenged by the developing turbulence in this flow. We simulate the two-dimensional flow of a strong jet at a Reynolds number of Re_h = 27,300, based on the jet width h and the difference between centerline and coflow velocities, and a center flow Mach number of 0.3. The computational domain consists of 3,200 elements over -10h ≤ y ≤ 10h and 0 ≤ x ≤ 40h.

A top-hat inflow velocity profile is set at the left boundary, with the commonly used hyperbolic tangent function

$$u = \frac{U_1 + U_2}{2} + \frac{U_1 - U_2}{2} \tanh\left(\frac{y}{2\Theta}\right). \tag{4.1}$$

Here, U_1 is the centerline velocity and U_2 is the coflow velocity. We set $U_1 = 1$ and $U_2 = 0.09$, which results in a velocity ratio $\eta = \Delta U/(U_1 + U_2) = 0.83$ between the flows. The parameter Θ is the inflow momentum thickness and is set to $\Theta = h/20$, in accordance with the setup used by Stanley et al. [80]. At the other boundaries, a Riemannian free-stream pressure condition [81] is prescribed. A buffer layer of thickness 3h gradually damps the solution to the uniform free-stream value to avoid spurious reflections from

Table 4.2: Numerical Stability of the plane jet. ✓= stable, x = unstable.

Node type	Flux method	$N = 1$	$N = 3$	$N = 5$	$N = 7$	$N = 9$
LG	Standard	x	✓	✓	✓	✓
LGL	Standard	x	x	x	x	x
LGL	Split form	✓	✓	✓	✓	✓

the boundaries, as described by Stanescu et al. [82]. Similar approaches have been used by Jacobs et al. [81] and Rasetarinera et al. [83]. We compute the flow using polynomial orders of $N = [1, 3, 5, 7, 9]$ and a CFL number of 0.8. The velocity history and average flow field is recorded over 1,000 convective time units and the temporal spectrum of the turbulent kinetic energy is extracted at the center line and $x = 20h$.

Figure 4.2 shows instantaneous vorticity contours of the jet flow. Driven by the Kelvin-Helmholtz instability, vortices form in the shear layer and break up the jet.

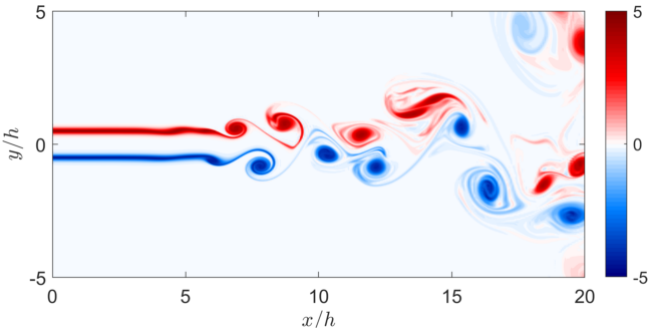

Figure 4.2: Instantaneous vorticity of the jet flow ($N = 9$).

Table 4.2 summarizes the numerical robustness of the approximations for this flow. The standard form with Gauss-Lobatto nodes is numerically unstable at all polynomial orders, while the split form remains stable for all cases. The standard form with Gauss nodes only crashes for this flow if a polynomial order of $N = 1$ is used.

Figure 4.3 shows the power spectra of the turbulent kinetic energy S_k computed from the velocity history at the center line at $x/h = 20$. Although the split form gives a result for a polynomial order of $N = 1$, the large deviation of the spectrum to the higher-

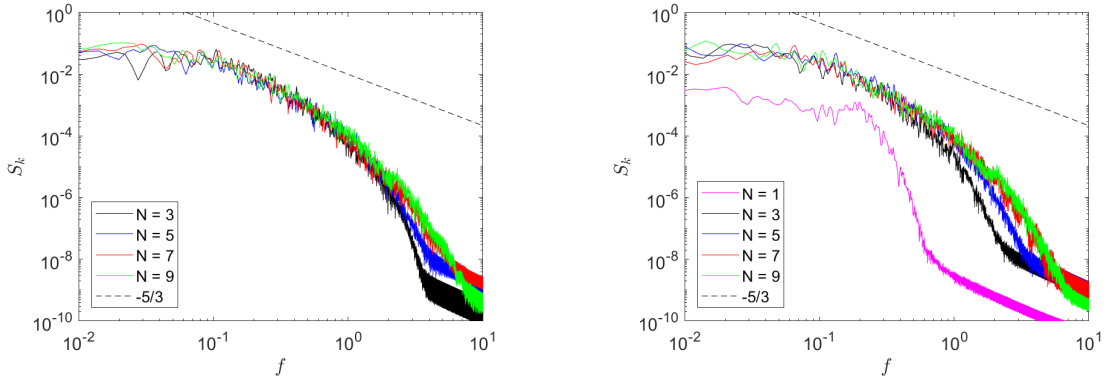

(a) Gauss nodes & standard DG (b) Gauss-Lobatto nodes & split form DG

Figure 4.3: Temporal power spectra of the turbulent kinetic energy for (a) standard form with LG nodes and (b) split form with LGL nodes.

order solutions renders the physical meaning of this solution irrelevant. All spectra obtained from higher-order simulations initially show a -5/3 decay, but an earlier start of the dissipation range at lower resolution indicates increased numerical dissipation at orders $N = 3$ and $N = 5$. Although the spectra for $N = 9$ are nearly identical for the standard and the split form, the lower-order results indicate higher accuracy when using the Gauss nodes, as the solution obtained with Gauss-Lobatto nodes is overly dissipated at higher frequencies. This result is the effect of underintegration when using Gauss-Lobatto nodes, which acts as a modal filter on the highest modes, as explained by Gassner and Kopriva [67].

Figure 4.4 shows the normalized velocity profile over the jet half-width for different streamwise locations for polynomial orders of $N = 3$ and $N = 5$. While the initial top-hat profile dominates close to the inlet, the well-known self-similar solution is obtained further away. The low-order approximation obtained with Gauss nodes shows a spurious oscillation in the velocity profile close to the inlet (Fig. 4.4a), while the result of the LGL solution does not. At higher order ($N = 5$), the profiles are similar and no spurious oscillations are present in the Gauss approximation.

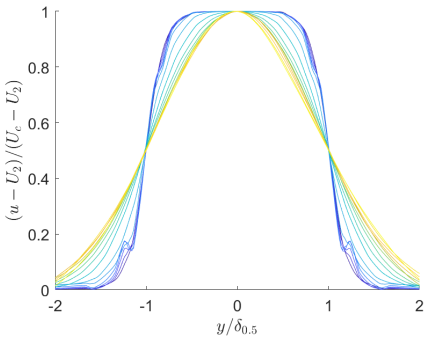

(a) LG, $N = 3$

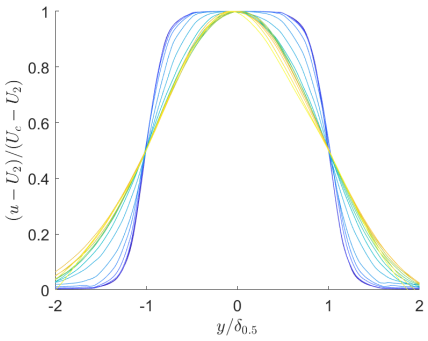

(b) LGL-SF, $N = 3$

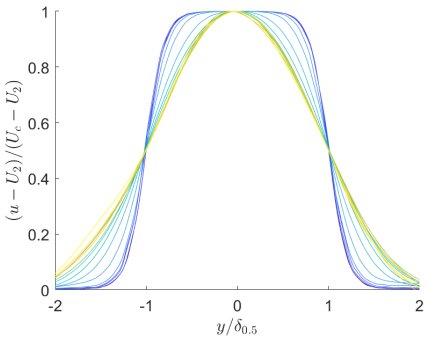

(c) LG, $N = 5$

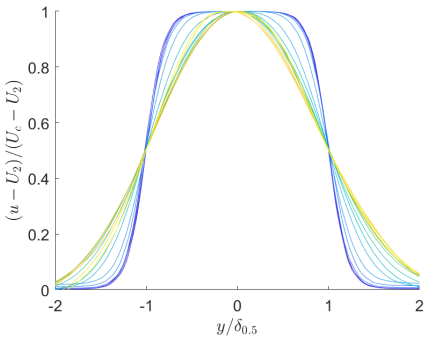

(d) LGL-SF, $N = 5$

Figure 4.4: Normalized velocity profiles at different streamwise locations. The color indicates the location from $x/h = 0$ (blue) to $x/h = 15$ (yellow). LG = Legendre-Gauss nodes (standard DG formulation). LGL-SF = Legendre-Gauss-Lobatto nodes & split form DG).

Table 4.3: Maximum stable convective time step size $\Delta t \cdot 10^{-3}$, x = unstable.

Node type	Flux method	$N = 5$	$N = 7$	$N = 9$
LG	Standard	2.8	1.9	1.2
LGL	Standard	x	x	x
LGL	Split form	4.7	2.6	1.6

As noted by Gassner and Kopriva [67], using Gauss-Lobatto nodes reduces the stiffness of the problem and can allow larger time steps. For the jet flow, we summarize the maximum stable time step sizes in Table 4.3 and show that simulations using the split form allow for a 66% ($N = 5$) to 32% ($N = 9$) increase in the step size Δt over the standard DG formulation. Although the leading order of operations for the computation of the advective flux derivatives is $(N+1)^{dim+1}$ for both the standard DGSEM and the split form, the total number of arithmetic operations required by the split form is approximately 3.9 ($N = 5$) to 4.5 ($N = 9$) times higher than with the standard scheme. For computations of viscous Navier-Stokes flows, this introduces an overhead of 64% ($N = 5$) to 150% ($N = 9$) per time step on the machine tested (Intel E5520), but has been observed to vary significantly between different computer systems.

Although the spectra indicate superior accuracy of the Gauss nodes for under-resolved computations, the results must be examined carefully, as spurious oscillations might be present. In such a case, the underintegrated solution of the Lobatto-Gauss nodes and its higher numerical diffusion might be beneficial, as such approximations should rather be considered implicit LES than DNS. This test case also highlights the effect of the kinetic energy conserving volume fluxes on the robustness of the scheme, as the standard form with LGL nodes crashes for all tested polynomial orders while the split form is numerically stable.

Table 4.4: Strouhal numbers of square cylinder flow at $Re = 100$ (literature).

Source	St
Okajima [72]	0.141-0.145
Sohankar et al. [73]	0.144-0.146
Darekar and Sherwin [74]	0.145
Shahbazi et al. [75]	0.145

4.2.3 Square Cylinder Flow

The canonical flow over a square cylinder at a Reynolds number of $Re = 100$ is chosen because of the numerous data sets available in the literature [81, 72, 73, 74, 75], which makes it a good candidate for the verification of the numerical method. The Strouhal numbers reported in the literature are summarized in Table 4.4.

The computational domain consists of 3,350 quadrilateral elements and has a blockage of 2.3%, matching previous computations in literature [74, 75]. Three polynomial orders of $N = [1, 2, 4]$ are used in the simulations and the time step size is based on a CFL number of 0.8. The cylinder walls are approximated with no-slip adiabatic walls and Riemannian free stream conditions [81] are applied at the outer boundaries at $x = [-15d, 26d]$ and $y = [-22d, 22d]$. A Mach number of $M = 0.1$ renders compressibility effects negligible. For all cases, the Strouhal number $St = fL/U$, based on the frequency of the lift coefficient, is computed over 400 convective time units after quasi-steady state is reached.

A plot of the instantaneous vorticity in Figure 4.5 shows the shedding of counter-rotating vortices from the square cylinder into a Von-Karman vortex street. This flow pattern is well known and has been observed in experiments, e.g. by Okajima [72].

The Strouhal numbers computed from spectral analysis of the lift coefficient are summarized in Table 4.5 and show convergence to $St = 0.145$ at a polynomial of $N = 2$, independent of the quadrature nodes or form of the advective fluxes. This value is in excellent agreement with the Strouhal numbers reported in literature (Tab. 4.4).

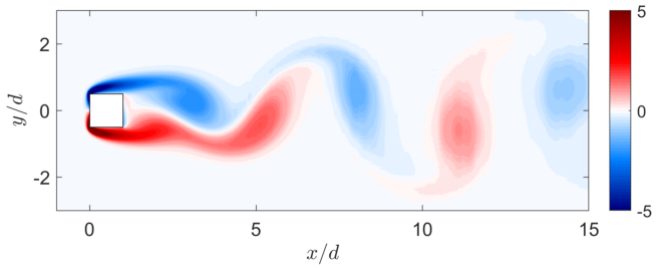

Figure 4.5: Instantaneous vorticity plot ($N = 4$).

All computations are numerically stable, but at a polynomial order of $N = 1$, the flows are under-resolved and differ from the converged solution by 4% for the Gauss and 7% - 8% for Gauss-Lobatto quadrature nodes. Given that the quadrature with Gauss-Lobatto nodes is only exact for polynomials of order $2N - 1$, Gassner and Kopriva [67] showed that underintegration with Gauss-Lobatto points can be interpreted as a modal filter and leads to damping of the highest modes. The higher accuracy of the Gauss quadrature translates to a smaller error of the Strouhal number for the under-resolved flow. Differences between the standard and the split form are minor, as the error for this problem appears to be dominated by the choice of quadrature nodes.

Table 4.5: Strouhal numbers of square cylinder flow at $Re = 100$ (present).

Node type	Flux method	N	St
LG	Standard	1	0.139
LGL	Standard	1	0.135
LGL	Split form	1	0.134
LG	Standard	2	0.145
LGL	Standard	2	0.145
LGL	Split form	2	0.145
LG	Standard	4	0.145
LGL	Standard	4	0.145
LGL	Split form	4	0.145

4.2.4 Two-Dimensional Airfoil Flow

The flow over a NACA 65(1)-412 airfoil is simulated at a Reynolds number based on the chord length of $Re_c = 20{,}000$ and a Mach number of $M = 0.3$. The airfoil is at 4° incidence.

The computational domain consists of 2,256 quadrilateral elements, where the boundaries are curved and fitted to a spline representing the airfoil's surface as described by Nelson et al. [76]. The mesh extends $15c$ (cord lengths) behind the airfoil and $5c$ in each vertical direction. The outer boundaries of the domain are defined as Riemannian free-stream boundaries while the airfoil surface is treated as a non-slip, adiabatic wall. Polynomial orders of $N = [3, 6, 12]$ are used in all elements, where $N = 12$ has been found to give a grid converged solution. A more detailed description of the base flow is given by Nelson et al. [76], Klose et al. [84]. The CFL number is set to 0.8 and all computations are run until quasi-steady state is reached. Statistics are subsequently computed over 10 convective time units.

The vorticity plot in Figure 4.6 shows that the boundary layer separates mid-cord, enclosing a recirculation region on the airfoil's upper side. Periodic shedding of vortices lead to the formation of a Von-Karmann type vortex street in the wake.

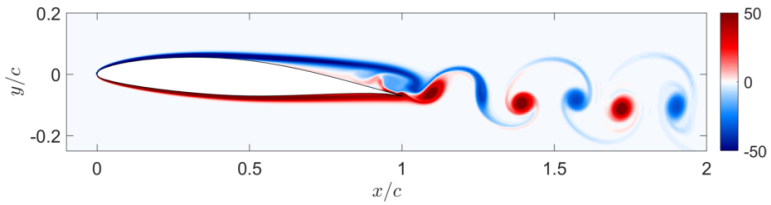

Figure 4.6: Instantaneous vorticity contours of flow over NACA 65(1)-412.

The averaged lift and drag coefficients, as well as the Strouhal numbers are summarized in Table 4.6. For a polynomial order of $N = 12$, the averaged lift and drag coefficients are $\bar{C}_l = 0.442$ for both LG and LGL-SF schemes and $\bar{C}_d = 0.0552$

Table 4.6: Aerodynamic data of airfoil flows at different polynomial orders.

Node type	Flux method	N	$\bar{C}_l$	$\bar{C}_d$	St
LG	Standard	3	0.457	0.0530	3.37
LGL	Standard	3	-	-	-
LGL	Split form	3	0.405	0.0732	2.30
LG	Standard	6	0.445	0.0561	2.69
LGL	Standard	6	0.415	0.0560	2.59
LGL	Split form	6	0.440	0.0565	2.75
LG	Standard	12	0.442	0.0552	2.78
LGL	Standard	12	0.442	0.0554	2.78
LGL	Split form	12	0.442	0.0554	2.78

for the standard form with Gauss points and $\bar{C}_d = 0.0554$ for the split form, resulting in a relative difference of <0.4%. The Strouhal number based on the frequency of the lift coefficient is consistently at $St = 2.78$ for all cases. The fact that no significant difference between the LG and LGL results are found is in accordance with the findings by Nelson *et al.*, who reported convergence for a polynomial order of $N = 12$ using LG points [76].

To evaluate the performance on under-resolved computations, we decrease the polynomial order to $N = 6$ and $N = 3$ and compare the results to the reference solution at $N = 12$. At a polynomial order of $N = 3$, the methods using Gauss-Lobatto quadrature nodes perform rather poorly, as the standard form is numerically unstable and the split form largely overestimates the drag (33%, Tab. 4.6). Results obtained from the standard LG form are closer to the converged solution (<4%), with the exception of the Strouhal number (21% over-estimated).

As expected, increasing the polynomial order to $N = 6$ considerably improves the quality of the results. The differences in the lift coefficient and Strouhal number of the split form are now below 1% and only the drag is slightly over-estimated by about 2%. The standard LG form matches lift and drag closely, but has a frequency error of 3% with a spurious low-frequency component in the lift and drag force (Fig. 4.7). The

standard form using LGL nodes gives the poorest results with larger errors in the lift and Strouhal number.

Overall, the results show that for the marginally resolved airfoil flow at $N = 6$, the split form yields the best results with the lift coefficient and Strouhal number matching the converged solution closely and only slightly larger deviations in the drag as compared to the standard DG scheme. For strongly under-resolved flows, the standard formulation with LG nodes is advantageous, as the errors in lift and drag coefficients are much smaller than for simulations using LGL nodes. Again, this result is expected, as the Gauss-Lobatto quadrature underintegrates and thus is less accurate. The favorable dispersion relation of the Gauss-Lobatto nodes, as shown by Gassner and Kopriva [67], also gives a reasonable explanation for the better representation of the Strouhal number for under-resolved cases when using the LGL split form.

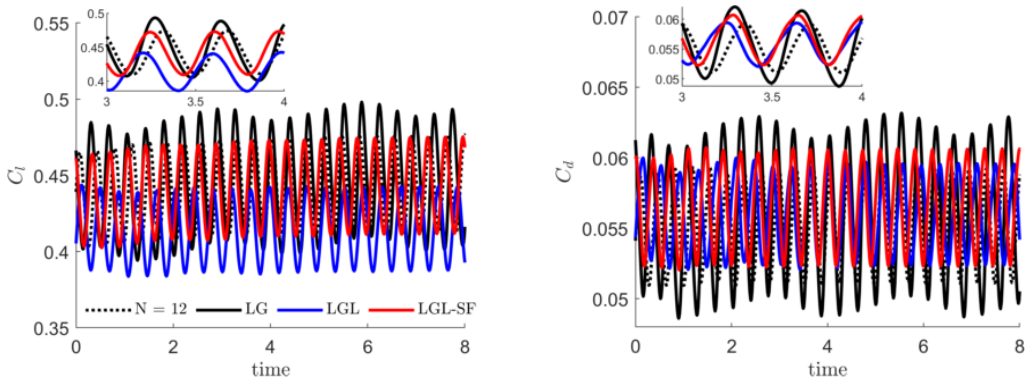

(a) Lift coefficient

(b) Drag coefficient

Figure 4.7: Lift (a) and drag (b) coefficients of underresolved flows for a polynomial orders of $N = 6$. LG = Legendre-Gauss nodes (standard DG formulation), LGL = Legendre-Gauss-Lobatto nodes (standard DG formulation), LGL-SF = Legendre-Gauss-Lobatto nodes & split form DG).

Table 4.7: Numerical Stability of the 3D airfoil simulations at 10° incidence. ✓= stable, x = unstable.

Node type	Flux method	$N = 10$	$N = 12$
LG	Standard	x	x
LGL	Split form	✓	✓

4.2.5 Three-Dimensional Airfoil Flow

Finally, we solve the three-dimensional flow over the NACA 65(1)-412 airfoil under an angle of attack of $\alpha = 10°$ at Reynolds number $Re_c = 20{,}000$. The flow is characterized by a laminar separation bubble at the leading edge and subsequent transition to turbulence [84]. Free-stream conditions are applied at the outer boundaries of the computational domain 30 cord lengths from the wing. The airfoil is extruded by half a cord length ($0.5c$) in the spanwise direction and periodic boundary conditions are used to approximate an infinite wing, resulting in a total of 33,660 hexahedral elements. The computations are initialized by mapping a two-dimensional flow field uniformly in the spanwise direction.

Two cases are considered: the standard DG scheme with Gauss nodes and the kinetic energy stable split form with Gauss-Lobatto nodes. Polynomial orders of $N = 10$ and $N = 12$ in the region close to the airfoil are chosen, but the order is gradually lowered in the far field to decrease the computational costs. To reduce spurious reflections from vortices entering lower order elements, a spectral filter [15] is applied to elements at least half a cord length away from the airfoil. A 5-stage 4th-order Runge-Kutta scheme [85] is used with a CFL number of 0.5.

Only the split form DG scheme has the numerical robustness to compute this flow and produce results past the initial start-up phase, as summarized in Table 4.7. Figure 4.8 (a) shows the lift coefficient over time for the different schemes and polynomial orders, where the dashed lines indicate the points of termination (crash). Figures 4.8 (b) – (d) show iso-surfaces of the vorticity at $t = 0.2$, $t = 1.6$, and $t = 18.1$ re-

spectively and illustrate the flow transition to three dimensional turbulent structures. The numerically unstable elements in the standard DG scheme are highlighted in red in Figure 4.8 (b).

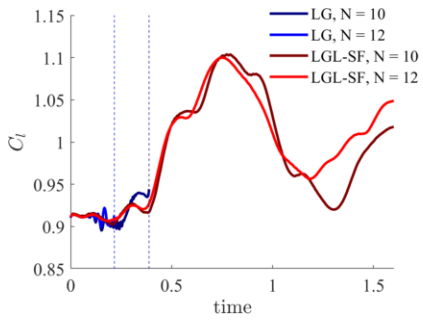

(a) Lift coefficient

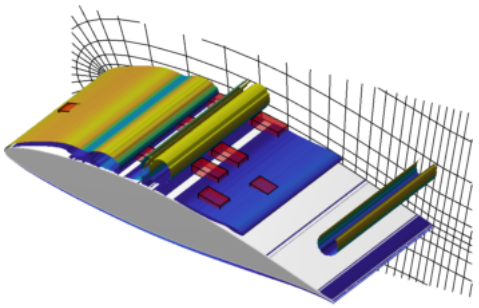

(b) Iso-vorticity, $t = 0.2$

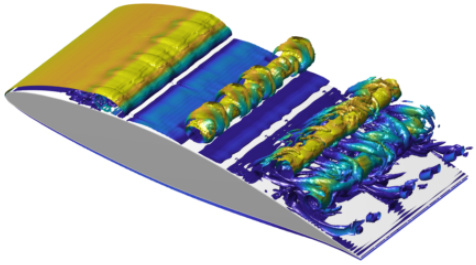

(c) Iso-vorticity, $t = 1.6$

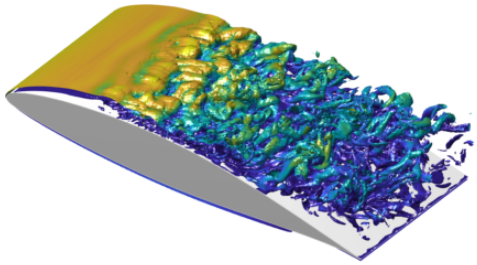

(d) Iso-vorticity, $t = 18.1$

Figure 4.8: (a) Lift coefficient for $N = 10$ & 12 and standard & split form DG. Times of termination indicated by dashed lines. (b) – (d): Iso-surfaces of the vorticity are presented for the LGL-SF computations ($N = 12$). Numerically unstable elements for the standard DG are highlighted in red.

Although the Reynolds number is moderate, the turbulent flow over the airfoil in Figure 4.8 (d) illustrates the small-scale vortical structures and the need for a numerically robust scheme to capture them without filtering. Because the standard DG formulation crashes – even with high-order approximations – we see that transitional flows with high velocity gradients greatly benefit from the enhanced robustness of the split form DG scheme.

4.3 Summary of Results

We have conducted a series of computations to evaluate the robustness and accuracy of the standard and a split form DG formulation for converged and marginally resolved viscous flows. The flows over a square cylinder, an airfoil and a plane jet are simulated for different polynomial orders, where each case is computed using the standard flux form with Legendre-Gauss and Legendre-Gauss-Lobatto quadrature nodes and the split form approximation of the advective fluxes with LGL nodes.

It is shown that the Gauss DG scheme has a higher accuracy per point and increased numerical robustness over the the standard Gauss-Lobatto formulation and matches the converged solution more closely for the marginally resolved cylinder and jet flow cases. This result is in accordance with the work by Gassner and Kopriva [67]. There is, however, no proof of numerical stability, and errors in the non-linear terms result in the termination of the computation for under-resolved simulations if the dissipation (physical or interface) is not large enough. This is demonstrated by the three-dimensional Taylor-Green vortex and the airfoil simulation, where the Gauss DGSEM crashes, even for high polynomial orders. Additionally, a spurious low frequency component in the lift and drag coefficient of the under-resolved two-dimensional airfoil simulation is present when using LG nodes.

The split form DGSEM, on the other hand, is provably stable in the sense that the kinetic energy is either conserved or dissipated, and generates solutions for marginally resolved flows that are inaccessible with the standard DG scheme. Although standard and split form DG approximations converge to the same solutions with increasing polynomial order, as shown for the two-dimensional cylinder, jet and airfoil flows, the split form DGSEM should be the primary choice for the computation of under-resolved flows, as it is robust and generates consistent results.

4.4 Acknowledgements

Sections 4.2 through 4.3, in full, are a reprint of the material as it appears in "Assessing standard and kinetic energy conserving volume fluxes in discontinuous Galerkin formulations for marginally resolved Navier-Stokes flows", B. F. Klose, G. B. Jacobs and D. A. Kopriva, *Computers & Fluids*, 2020. B. F. Klose: investigation, original draft preparation, visualization. G. B. Jacobs: supervision, review & editing. D. A. Kopriva: methodology review, supervision, editing.

Chapter 5

The multitude of flow regimes in cambered airfoil aerodynamics at Re = 20,000: a two-sided story

5.1 Overview and Summary

In this chapter, we analyze the flow over a cambered NACA 65(1)-412 airfoil at a chord-based Reynolds number of $Re = 2 \times 10^4$ for angles of attack (AOA, α) ranging from 0° to 10° using a combination of DNS and implicit LES. The results are obtained numerically with a high-order compressible discontinuous Galerkin spectral element method using a large span ($0.5c$) and domain ($30c$) to capture the significant spanwise instability modes and far field wake dynamics. The separation of the laminar boundary layer, transition to turbulence, and possible formation of a laminar separation bubble are studied in detail through analysis of the flow topology, statistics, and aerodynamic forces. The spatially and temporally resolved data sets are a comprehensive account of the transitional flow over a cambered airfoil at low Reynolds number, are generalizable

to other geometries and Reynolds numbers, and will serve as a baseline for future research in airfoil aerodynamics and flow control.

The governing equations used in this chapter are outlined in Chapter 2 and the numerical method is introduced subsequently in Chapter 3. In Section 5.2 we outline the setup of our computations and discuss the results of three-dimensional direct numerical simulations in Section 5.3. A summary and concluding remarks are given in Section 5.4. A parametric study based on two-dimensional DNS is given in appendix A.1, where we assess the effects of compressibility, resolution, and computational domain size.

5.2 Setup

The flow over a NACA 65(1)-412 airfoil is simulated in two and three dimensions at a chord-based Reynolds number of $Re_c = 2 \times 10^4$ and a free-stream Mach number of $M = 0.3$. At this Mach number, the compressibility effect on the pressure coefficient are expected to be of the order of 5% in relation to incompressible flow, according to the Prandtl-Glauert correction $C_{p,M}/C_{p,i} = 1/\sqrt{1-M^2}$. While the Mach number in comparable wind tunnel experiments is typically lower than 0.3, the increased stiffness of the explicit numerical scheme results in extremely small time step sizes that are unfeasible for three-dimensional simulations. A Prandtl number of $Pr = 0.72$, Sutherland constant $R_T = S/T_f = 110/200$, and ratio of specific heats $\gamma = 1.4$ are chosen in accordance with Nelson [86].

The Navier-Stokes equations are solved using a discontinuous Galerkin spectral element method (DGSEM) [13]. The conservative variables (2.2) are spatially approximated on a N^{th} order polynomial basis and collocated on Legendre-Gauss (G) or Legendre-Gauss-Lobatto (GL) nodes. The flux derivatives in (2.1) are either computed

using the standard DGSEM formulation with Gauss quadrature nodes or kinetic energy conserving flux splitting of the inviscid term and Gauss-Lobatto quadrature nodes (see Klose et al. [17] for details). An upwinding Roe scheme is used for the advective interface fluxes and a Bassy-Rebay formulation for the viscous part. A fouth-order explicit Runge-Kutta adaptive time-stepping scheme is used with time step sizes ranging between $2.3 \times 10^{-5} \leq \Delta t \leq 8.4 \times 10^{-6}$, depending on the choice of quadrature nodes and the resolution.

Consistent with the discontinuous Galerkin airfoil simulations by Uranga et al. [7] and Beck et al. [30], Riemannian free-stream conditions are applied at the outer boundaries of the domain. Spurious oscillations from exiting vortices are prevented through grid coarsening towards the outflow, as well as a damping layer on the energy term to reduce the reflected pressure waves [81]. The surface of the airfoil is treated as no-slip adiabatic wall and, to account for its curvature, we fit the neighboring boundary elements to a spline representing the profile of the wing according to Nelson et al. [76]. For 3D simulations, the spanwise boundaries are set to be periodic.

All simulations are run until the flow has fully transitioned to a three-dimensional state and the solution has reached quasi-steady state with the lift and drag coefficients fluctuating around a mean, typical after 10 to 20 convective time units. Flow statistics are recorded subsequently.

5.2.1 Domain Size

The impact of the outer boundaries on the numerical solution through blockage and spurious reflections is governed by the size of the computational domain. A compromise has to be found between a large-enough domain to minimize such boundary effects and the available computational resources limiting the number of grid points to be used. In figure 5.1(a), typical domain parameters such as the radius R and the

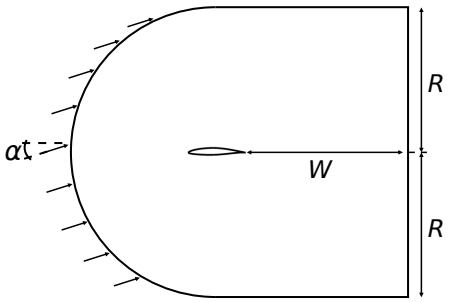

(a) Domain Parameters

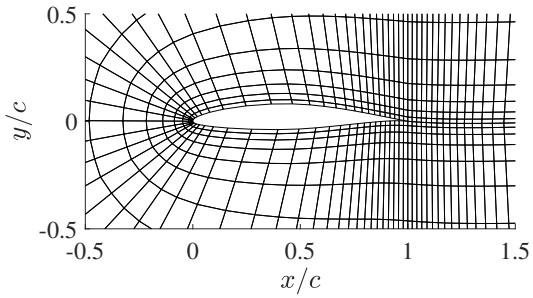

(b) Grid 1

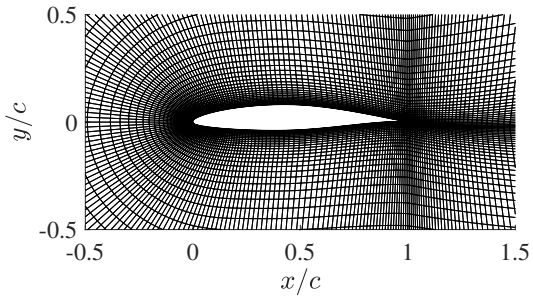

(c) Grid 2

Figure 5.1: (a) C-type computational domain with general parameters. Elements of 2D computational meshes *Grid 1* (b) and *Grid 2* (c) around the airfoil. Only elements without interior Gauss nodes are shown.

wake length W are shown.

Table 5.1 provides a selection of domain sizes used in selected airfoil simulations in literature. The domain radius of these airfoil DNS ranges from $4c$ [87] to $100c$ [29, 30].

In the present study, two different C-type meshes are applied, where each grid has a sharp trailing edge and a domain radius and wake length of 30 chord lengths. These values are higher than in most comparable studies (cf. table 5.1), but necessary to avoid spurious reflections from the outflow boundaries or changes in the separation bubble shape [30]. For three-dimensional computations with periodic boundaries, the domain is extruded in z-direction by $L_z = 0.5c$, as recommended by Almutairi et al.

Table 5.1: Domain sizes of selected airfoil studies.

Source	R/c	W/c	L_z/c
Deng et al. [87]	4	3	0.1
Jones et al. [19]	7.3	5	0.2
Uranga et al. [7]	6	6.4	0.2
Visbal [29]	100	100	0.1-0.8
Beck et al. [30]	100	100	0.2
Lee et al. [9]	25	25	0.2
Zhang et al. [21]	6	10	0.1-0.8
Balakumar [25]	15	15	0.2
Serson et al. [26]	15	10	0.5-2.0
present	30	30	0.5

[24] in their LES study of the NACA 0012.

5.2.2 Resolution - Is it DNS?

Two C-type meshes are employed in this study: *Grid 1* consists of 3,366 quadrilateral elements in the x-y plane and is extruded by 10 elements along the span for 3D simulations (see figure 5.1b). *Grid 2* is refined with 23,400 elements per 2D plane and 50 elements in spanwise direction (see figure 5.1c). For $Re = 2 \times 10^4$ and 4° incidence, Nelson et al. [76], Klose et al. [17] have reported a grid-converged solution at a polynomial of $N = 12$ for a mesh nearly identical to *Grid 1*, but limited to $R = 5c$ and $W = 15c$. Klose et al. [17], however, show that numerical instabilities occur at higher angles of attack (10°) if the standard DGSEM scheme is applied, but can be stabilized through a kinetic energy conserving formulation of the advective volume fluxes based on the split form by Pirozzoli [69]. While the coarse grid is proven to give a converged solution at $N = 12$ for lower angles of attack (0° and 4°), we use the refined *Grid 2* with a lower order of $N = 4$ and $N = 6$ for computations around the critical angle of attack at 7° and 8° respectively, which is more suitable for turbulent flow. At 8°

incidence, the maximum wall-normal height of the first element (*Grid 2*) at the leading edge is $\eta_e^+ = 8$ and places the first Gauss point at a wall coordinate of $\eta_g^+ = 0.2$. The maximum tangential grid spacing, based on the average spacing per element, is $\zeta^+ = 4$ and occurs at the reattachment point of the LSB at $x/c \approx 0.4$. These values are well within the limits accepted for DNS [88]. Resolution studies of selected cases have been conducted in two space dimensions and are presented in appendix A.1.

Only for the an angle of 10°, we abstain from resolving all scales of motion but use implicit LES computations and approximate the turbulent flow on *Grid 1* with twelfth order polynomials in the near field and reduced order elements in the outer field. A spectral filter reduces spurious oscillations from the decreasing order approximations away from the airfoil.

5.2.3 Overview of Simulations

Table 5.2 gives an overview of the three-dimensional simulations. The data has been collected over a long period of time and contains different meshes, polynomial orders and refinements. The cases are computationally very demanding and typically run on clusters of 1000 to 4000 processors. Consecutive entries in table 5.2 at the same flow angle and domain size are interpolated from the previous run. The results presented in this work are highlighted in bold font.

5.3 Results and Discussion

We start the discussion of the low-Reynolds number flow over the NACA 65(1)-412 with a summary of the lift and drag coefficients of DNS and experiments. An in-depth analysis of the flow topology, the statistics, and the aerodynamic forces based in on the DNS results follows in the subsequent sections.

Table 5.2: Overview of 3D simulations. Re = free-stream Reynolds number, α = angle of attack, R/c = domain radius, G = standard Gauss DGSEM (* = with spectral filter), GL-SF = split form DGSEM with Gauss-Lobatto nodes, T_{init}/T_{fin} = initial/final convective time of run, (2x) = h-refined, $N_i(N_o)$ = polynomial order inner (outer) region, DOF = degrees of freedom (number of high-order nodes).

Re	α	Mesh	R/c	Scheme	$N_i(N_o)$	T_{init}	T_{fin}	DOF ($\times 10^6$)
2×10^4	**0°**	**Grid 1**	**30**	**GL-SF**	**12**	**0**	**43.2**	**74.0**
2×10^4	0°	Grid 1	30	G	12(1)	24.2	40.0	30.7
2×10^4	4°	Grid 1	3.5	G	12(1)	0	12.0	9.1
2×10^4	**4°**	**Grid 1**	**30**	**GL-SF**	**12**	**0**	**46.7**	**74.0**
2×10^4	4°	Grid 1	30	G	14(1)	20	30.0	43.2
2×10^4	**7°**	**Grid 2**	**30**	**G**	**4**	**0**	**19.0**	**146.3**
2×10^4	8°	Grid 1 (2x)	3.5	G	4(1)	0	13.5	5.9
2×10^4	8°	Grid 1 (2x)	3.5	G	6(1)	13.5	16.8	15.0
2×10^4	8°	Grid 1	30	GL-SF	12(1)	0	25.8	30.7
2×10^4	**8°**	**Grid 2**	**30**	**G**	**6**	**25.8**	**39.0**	**401.3**
2×10^4	10°	Grid 1 (2x)	3.5	G	4(1)	0	11.5	5.9
2×10^4	10°	Grid 1 (2x)	3.5	G	6(1)	11.5	20.0	15.0
2×10^4	10°	Grid 1	30	GL-SF	10(1)	0	15.6	21.5
2×10^4	**10°**	**Grid 1**	**30**	**GL-SF**	**12(1)**	**15.6**	**36.1**	**30.7**

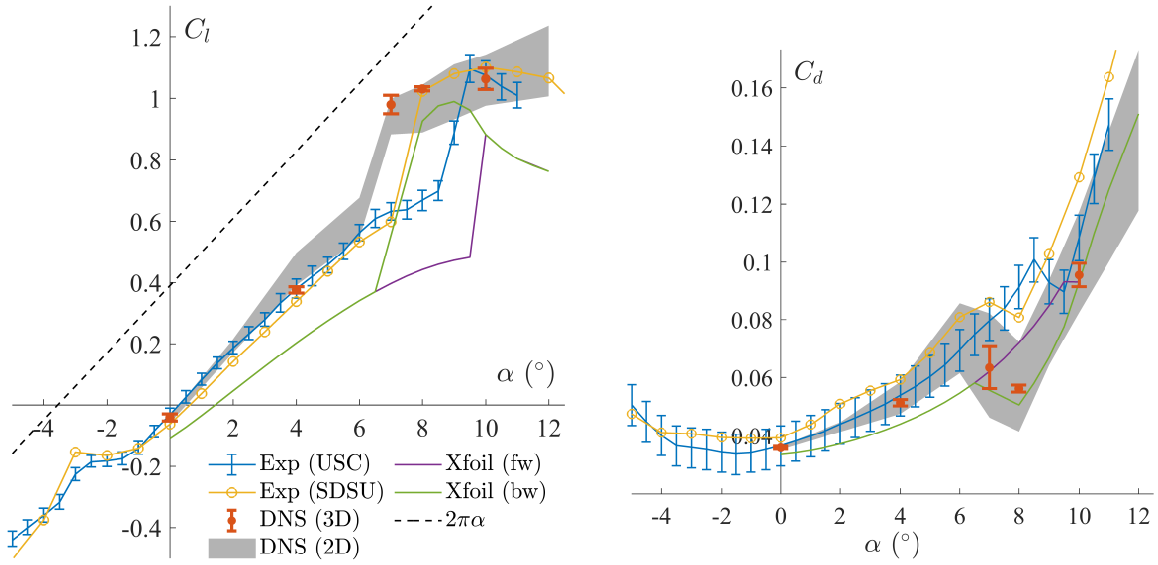

(a) Lift coefficient

(b) Drag coefficient

Figure 5.2: Lift (a) and drag (b) coefficients obtained from wind tunnel experiments at USC and SDSU, DNS data (2D & 3D), and Xfoil data (forward and backward sweep) for a NACA 65(1)-412 at $Re = 2 \times 10^4$. Error bars indicate RMS level of DNS. Gray area identifies the total lift and drag range of the parametric 2D study given by the averaged coefficient +/- standard deviation.

Figure 5.2 presents the lift (a) and drag (b) coefficients over the angle of attack α. The results include experiments conducted at the University of California, Los Angeles (USC) [35] and San Diego State University (SDSU) [89], DNS in two and three space dimensions, and data generated with *Xfoil* [1] for forward and backward angle sweeps. The $2\pi\alpha$-line of thin-airfoil theory [90] is included as a reference for ideal, inviscid flow. Despite some discrepancies between the computations and experiments, all result imply the existence of two flow regimes, between which the lift force changes rapidly. At this critical angle of attack α_{crit}, the flow transitions from a state of laminar separation without reattachment to turbulent reattachment and formation of a laminar separation bubble (LSB) at the leading edge [35].

5.3.1 Flow topology – separation, transition, and wake

In the following section, three-dimensional DNS results are presented for angles of attack of 0°, 4°, 7° and 8°, as well as results of implicit LES of the flow at 10°. This section is divided into the discussion of the flow topology, transition to turbulence, structures of the wake, and averaged velocity and boundary layer profiles. Given their similarity, the flow angles of 0° and 4°, as well as 8° and 10° are discussed together.

In this work, the asymptotic locations of flow separation and reattachment are based on the zero-crossings of the time and space-averaged skin friction coefficient. In accordance with Uranga et al. [7], the transition point indicates the location of a local maximum in the shape factor. We note, however, that the definition of the transition point is not unique and e.g. Alam and Sandham [63] use the point of maximum negative skin friction.

AOA = 0° and AOA = 4°

At an angle of 0° and 4°, the flow is characterized by a the separation of the boundary layer without reattachment to the airfoil surface and the formation of a regular vortex street in the wake. The lift coefficient (see figure 5.2) is well below the inviscid limit and implies that viscous forces deteriorate the aerodynamic performance. In the following section, we discuss the topology of the transitional flow and the wake.

Separation and transition At 0° incidence, the laminar boundary layer separates from the airfoil surface at the asymptotic (time-averaged) separation point at $x_s/c = 0.6$ and transitions to a three-dimensional flow in the wake. The temporal development of the separating shear layer and the formation of the vortex street behind the airfoil is outlined in figure 5.3 where contours of instantaneous vorticity ω_z are plotted along a slice at $z/c = 0.025$. The figure shows the separation of the laminar boundary layer

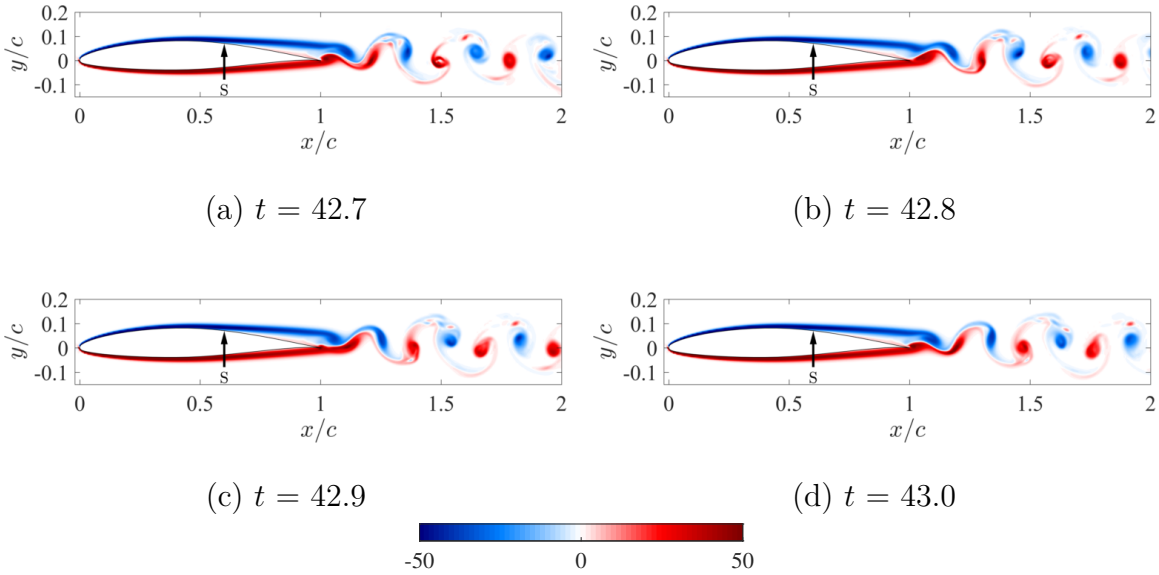

(a) $t = 42.7$ (b) $t = 42.8$

(c) $t = 42.9$ (d) $t = 43.0$

Figure 5.3: Snapshots of instantaneous vorticity ω_z along a slice $z/c = 0.025$ from $t = 42.7$ (a) to $t = 43.0$ (d). S indicates the mean locations of separation. AOA = 0°

(marked as location S) on the upper side of the wing and the alternate shedding of left-turning vortices from the bottom and right-turning vortices from the top. The boundary layer separation is induced by an adverse pressure gradient downstream of the maximum thickness of the profile caused by the convexly curved surface (cf. inviscid profile in figure 1.1c). The flow along the bottom surface remains attached until the shear layer sheds off the trailing edge of the airfoil. The formation of the vortices start with the roll-up of the bottom boundary layer at the sharp trailing edge (see figure 5.3b–d) and the generation of a strong, left turning eddy that forces the separated shear layer from the upper side to bend down and form a counter-rotating vortex. This pair of vortices then sheds off to form a Von-Karmann-type street behind the wing.

The three-dimensionality of the boundary layer separation and vortex formation process is outlined in figure 5.4: iso-surfaces of the vorticity magnitude $|\omega| = 30$ (a) and the second invariant of the velocity gradient $Q = 80$ visualize instantaneous, coherent vortical flow structures. Following Jeong and Hussain [55], positive contours of Q

$\equiv (u_{i,i}^2 - u_{i,j}u_{j,i})/2$ are commonly used to identify vortical structures, as it balances vorticity and shear strain, thereby revealing structures within region of high shear that remain hidden in the vorticity. In both plots, the iso-surfaces are colored according to the spanwise vorticity component, ω_z, and indicate the rotational direction of the vortices with respect to the axis aligned with the airfoil span. The vorticity surfaces in figure 5.4(a) show the separation of the laminar shear layer as a quasi two-dimensional vortex sheet, where the transition to three-dimensional structures occurs only in the wake once the bottom shear layer interacts with the separated flow from the top. The topology of the vortex shedding is characterized by spanwise rollers enveloped by longitudinal braid vortices that have their origin at the trailing edge and connect the spanwise eddies (braid region).

These spanwise rollers, also called 'Strouhal' or 'Karman' vortices, are the primary structures associated with the vortex shedding [91, 92], where elliptic flow within the vortex cores and hyperbolic flow along the braid shear layer can induce three-dimensional flow instabilities [92, 93, 94]. The elliptic instability is known to introduce a spanwise perturbation mode within rollers (called *mode A*) and scales with the length scales of the primary vortex. The braid region between the Karman vortices, on the other hand, is a hyperbolic shear flow and a three-dimensional instability along the braid shear layer results in the generation of the spanwise loop vortices at a wavelength that scales with the smaller braid shear layer (called *mode B*) [93, 94]. For the wake behind a circular cylinder, Williamson [93] show that the *mode A* has a wavelength $\lambda_z \approx 4D$ and *mode B* a wavelength of $\lambda_z \approx 1D$, where D is the cylinder diameter.

For the NACA 65(1)-412, the size of the Karman vortices are limited by the projected thickness of the profile, which is $0.12c$ and $0.126c$ at 0° and 4° incidence respectively and which we therefore assume a proper reference length scale for the

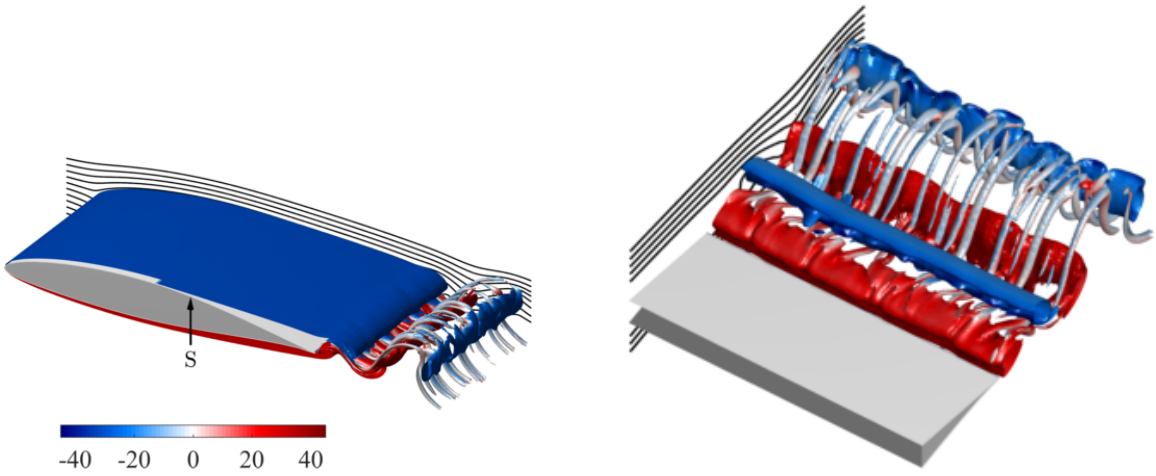

(a) Vorticity (b) Q-criterion

Figure 5.4: Iso-surfaces of vorticity $|\omega|$ (level 30) and Q-criterion (level 80) colored by vorticity ω_z at $t = 42.7$. AOA $= 0°$.

instability mode. The wavelength of *mode A* is therefore of the order of $0.48c$ and $0.12c$ for *mode B*. Figure 5.4(b) indicates that the primary rollers are subject to a mode that includes five waves over the span. This suggests that the streamwise loops correspond to an instability of *mode B* and are caused by the hyperbolic flow along the braid shear layer. In accordance with findings by Williamson [93], the generation of the streamwise vortices is self-sustaining and tied to the flow-recirculation region, where the braids induce perturbations to the upstream flow and induce the next set of loop vortices.

The topology of the flow at 4° incidence is similar to the previously discussed case at AOA $= 0°$ and we will therefore focus the discussion on the differences. Analogously, a laminar boundary layer develops over the wing, but separates further upstream at mid-chord ($x_s/c = 0.49$) as a result of the increased pressure gradient that is induced by the larger displacement of the flow at the higher angle of attack. Again, the shear layers from the top and bottom side of the wing shed off at the trailing edge and establish a vortex street in the wake (see figure 5.5). The vortex formation likewise

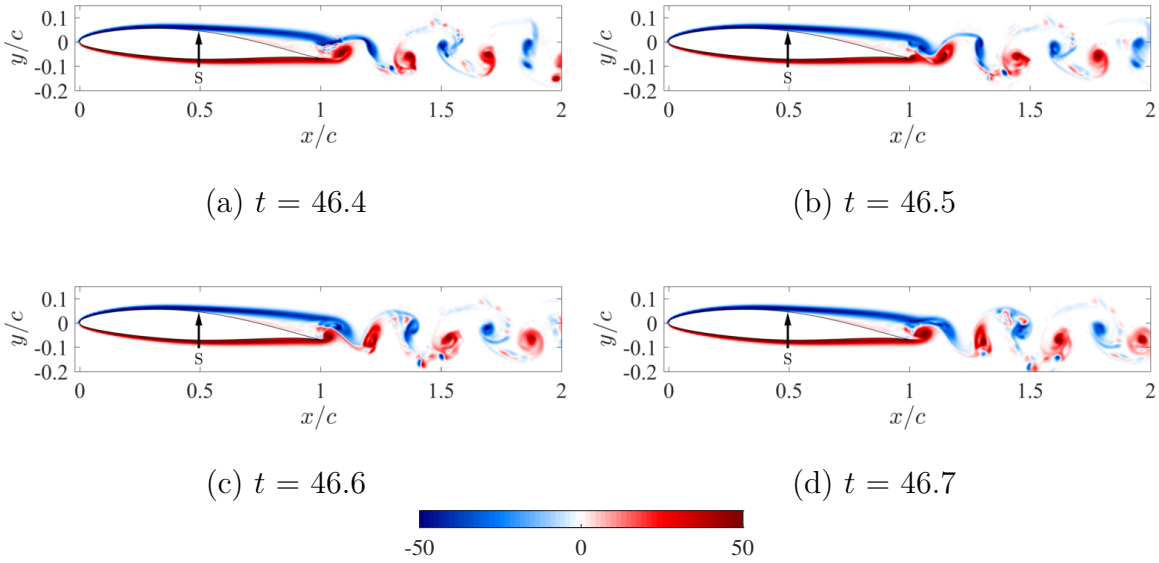

(a) $t = 46.4$ (b) $t = 46.5$

(c) $t = 46.6$ (d) $t = 46.7$

Figure 5.5: Snapshots of instantaneous vorticity ω_z along a slice $z/c = 0.025$ from $t = 31.4$ (a) to $t = 31.7$ (d). S indicates the mean locations of separation. AOA = 4°

starts from the roll-up of the bottom boundary layer but yields larger eddies compared to the case at 0° because the frontal area of the wing, which limits the vortex size, increases with the angle of attack. The resulting velocity gradients are higher and amplify perturbations more rapidly, therefore promoting the bursting of the spanwise rollers and transition to a turbulent wake flow.

Similar to the AOA = 0° case, the topology of the vortex shedding is characterized by spanwise Karman vortices and longitudinal braids that originate at the trailing edge of the airfoil within the recirculation region in a self-sustaining manner (see figure 5.6). Three-dimensional structures are also present within the recirculation region and stimulate the transition of the laminar flow by perturbing the formation of the trailing-edge vortex. The resulting vortical structures are less regular than at 0° incidence and interact directly upon shedding of the airfoil (see figure 5.6b). As discussed earlier, the high velocity gradient at the vortex edges promotes the rapid growth of such perturbations and accelerates the break-down of the large-scale vortices

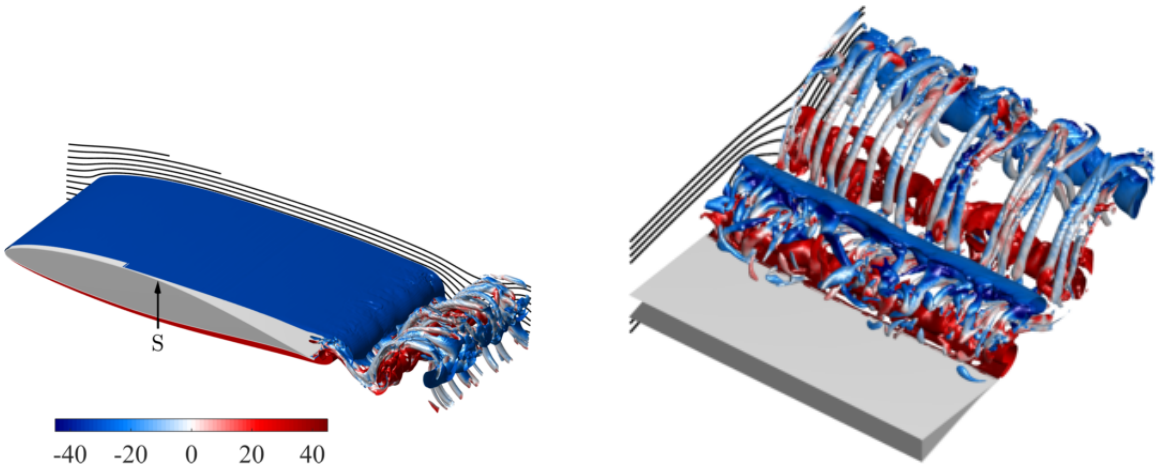

(a) Vorticity (b) Q-criterion

Figure 5.6: Iso-surfaces of vorticity $|\omega|$ (level 30) and Q-criterion (level 100) colored by vorticity ω_z at $t = 46.6$. AOA $= 4°$.

and the transition into turbulence in the wake early on.

The presence of three-dimensional flow is outlined in figure 5.7: instantaneous contours of the spanwise (w) velocity are plotted along a plane in x-y direction (a) and along a curved surfaces at a constant wall-normal distance $\Delta\eta = 0.02c$ (b), where, η is the wall-normal coordinate. Streamlines of the instantaneous u and v velocity components in (a) illustrate the separating flow at $x_s/c = 0.49$ (S) and show the roll-up of the bottom-side vortex at the trailing edge. The three-dimensional flow is strongly amplified at the edges of the trailing-edge vortex and along the streamwise braid vortices. Clock-wise rotating flow within the bubble transports the transverse (spanwise) momentum from the longitudinal vortex loops upstream, where it recirculates and is advected downstream with the separated shear layer flow on the upper side (see figure 5.6a and b). This perturbation facilitates the transition process in a self-sustaining manner and induces three-dimensional vortex loops upon the interaction of upper and lower shear layer.

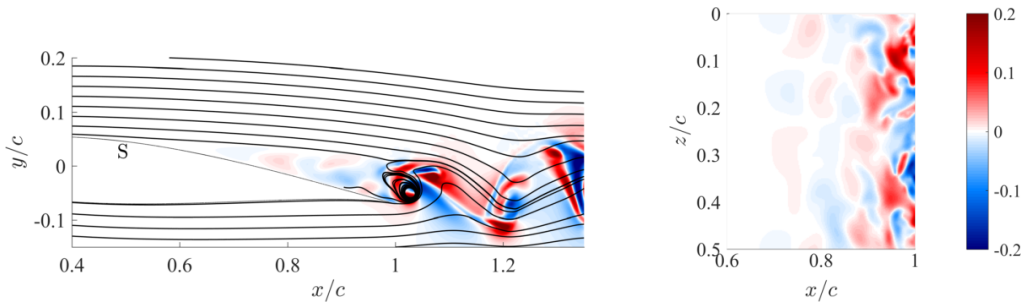

(a) x-y plane (b) x-z plane

Figure 5.7: Instantaneous transverse velocity w and streamlines along a x-y plane at $z/c = 0.025$ (a) and along a surface normal to the airfoil wall displaced by $\Delta\eta = 0.02c$ (b) at $t = 46.6$. S indicates the locations of asymptotic flow separation. AOA = 4°

Wake topology The spatial development of the vortex street in the airfoil wake is visualized in figure 5.8 for a flow angle of 0° and figure 5.9 for 4°, where contours of the instantaneous, spanwise vorticity component ω_z are plotted in (a) and contours of the specific entropy s in (b). Vorticity is generated at the airfoil wall and is transported away through convection and diffusion [95, 96, 97]. Stretching of vortex filaments, mixing, and diffusion results in the decay of the vorticity amplitude in the wake as an increasing amount of fluid is entrained by the swirling flow and causes the gradual spreading of the wake.

The transport of fluid from the airfoil into the wake is visualized by contours of specific entropy in figures 5.8(b) and 5.9(b). According to the second law of thermodynamics, irreversible processes, e.g. viscous dissipation at a no-slip boundary, generate entropy such that $Ds_{irr}/Dt > 0$ [98]. The specific entropy $s = \ln(p/\rho^\gamma)/(\gamma(\gamma-1)M_f^2)$ follows a scalar transport equation with a production term for such irreversible processes [98, 15]. Figure 5.8(b) shows that entropy is generated in the shear layer around the airfoil and within the separated flow region on the upper side, is then transported away and mixes with the surrounding fluid by diffusion and convection which results in its gradual decay far downstream from the wing. The mixing rate with the sur-

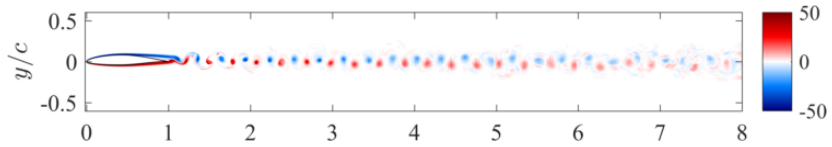

(a) Vorticity ω_z

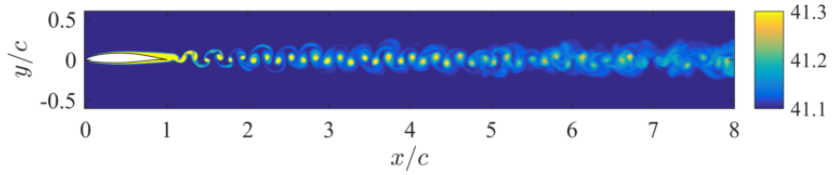

(b) Specific entropy s

Figure 5.8: Instantaneous snapshots of the vorticity ω_z (a) and the specific entropy $s = \ln(p/\rho^\gamma)/(\gamma(\gamma-1)M_f^2)$ (b) along a slice at $z/c = 0.025$ and $t = 42.7$. AOA $= 0°$.

rounding fluid is, however, low and local patches of high entropy indicate the presence of coherent structures in the wake flow several chord lengths behind the airfoil.

At 4° incidence, the vortex street in the airfoil wake looses its regularity shortly downstream of the trailing edge and transitions to a turbulent flow. The initial stages of the large-scale vortex break down are visualized by the iso-surface plots presented in figure 5.6, where the braid vortices induce significant transverse flow (see also figure 5.7a). The three-dimensional, transitional wake is characterized by an increased vorticity decay and chaotic entropy contours that spread at a higher rate than at 0° incidence.

Given that the NACA 65(1)-412 is designed to maximize the laminar flow region over the wing, it is not surprising that the flow remains laminar over the airfoil at low angels of attack of 0° and 4°, with transition occurring only in the wake at 4°. The absence of an early transition to turbulence, however, prevents the reattachment of the separated boundary layer on the airfoil's rear side and results in a significant loss of

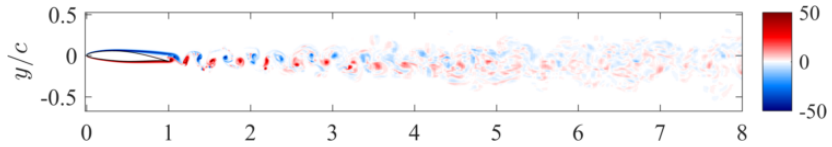

(a) Vorticity ω_z

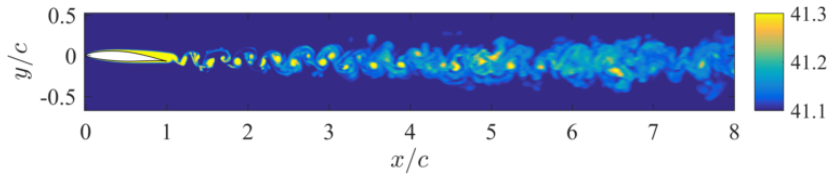

(b) Specific entropy s

Figure 5.9: Instantaneous snapshots of the vorticity ω_z (a) and the specific entropy $s = \ln(p/\rho^\gamma)/(\gamma(\gamma-1)M_f^2)$ (b) along a slice at $z/c = 0.025$ and $t = 46.6$. AOA $= 4°$.

the lifting force, which is even negative at AOA $= 0°$ (see figure 5.2). At low angles of attack, the operation of laminar airfoils in low-Reynolds number flow condition therefore obliges the use of flow controllers.

AOA $= 7°$

The flow at 7° incidence is characterized by a high lift and low drag force (see figure 5.2), which can be attributed to the collapse of the separated recirculation region that exists at lower angles of attack. In the following section, we discuss the temporal development and natural transition from two to three-dimensional flow and the formation of an absolute instability within a laminar separation bubble (LSB), as well as the flow topology of the turbulent vortex shedding.

Early temporal development and natural transition The early temporal development of the flow over the airfoil and the transition of the initial two-dimensional to three-dimensional structures is outlined in figure 5.10, where iso-surfaces of Q

are colored by the spanwise velocity component to visualize the emergence of three-dimensional modes within the vortices. Note that no perturbation or forcing is added to the flow and the transition occurs naturally. The flow is initially two-dimensional and characterized by the formation of spanwise Karman vortices from the separating shear layer at mid-chord (see figure 5.10a). A well-defined low-frequency perturbation mode develops along the spanwise rollers at the trailing edge, as highlighted by the transverse velocity coloring, and leads to the weak bending of the vortical structures downstream in the wake (see figure 5.10a). This perturbation is likely driven by an elliptic instability, which induces a three-dimensional mode along the vortex if the surrounding two-dimensional streamlines are elliptical [99]. A similar observation has been made by Jones et al. [19] for the LSB on a NACA 0012 and by Williamson [92] for the wake behind a circular cylinder. With time, the perturbation grows upstream and the vortex pairs deform into hairpin-like structures, also called horseshoe or loop vortices [100]. Because these loop vortices are initially formed at the rear side of the airfoil and therefore only grow over a short distance before shedding off the trailing edge, the hairpin-roller pairs are isolated at first and advect without the connecting braids to the upstream vortex pair (see figure 5.10b). Only at later times, when the flow becomes more turbulent and the perturbation has moved further upstream, a set of braid vortices link consecutive Karman rollers and establish a continuous wake of three-dimensional, turbulent motion (see figure 5.10d).

To monitor the development of the three-dimensional instability, we consider a time series of streamwise vorticity iso-surfaces $|\omega_x| = 1$ in figure 5.11. The vortical structures identified in this way only relate to rotating fluid along the streamwise axis and hence detect three-dimensional flow patterns without being obscured by the dominating two-dimensional topology. The ω_x surfaces in figure 5.11 are flat layers that are stacked on the airfoil surface and lifted off by passing spanwise vortices (cf. figure

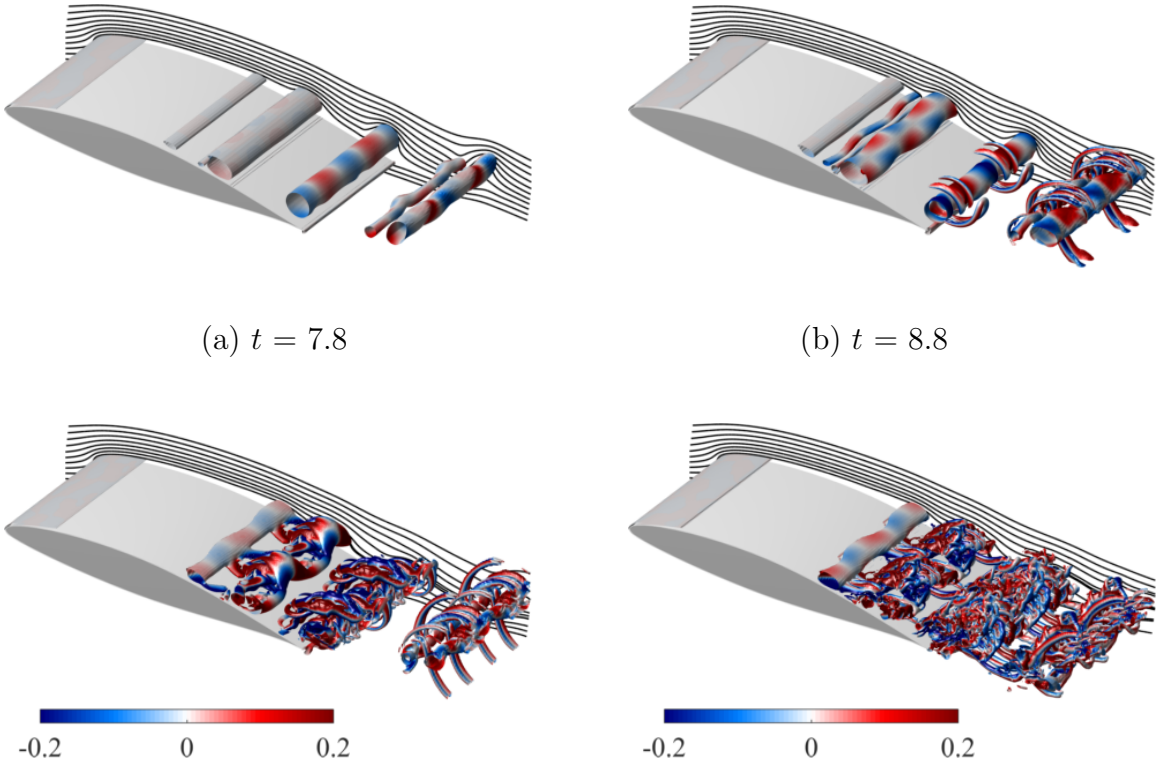

(a) $t = 7.8$ (b) $t = 8.8$

(c) $t = 9.8$ (d) $t = 10.8$

Figure 5.10: Iso-surfaces of Q-criterion (level: 100) colored by transverse velocity from $t = 7.8$ (a) to $t = 10.8$ (d). Instantaneous streamlines in black. AOA = 7°

5.10). A similar topology of streamwise vorticity surfaces has been reported by Sakai et al. [101] for the instability of a laminar separation bubble under a solitary wave. In the present case, a total of four patches of positive and negative vorticity reflect the same perturbation pattern observed in figure 5.10 and identifies a three-dimensional elliptic instability mode with wavelength $\lambda_z = 0.25c$, i.e. half the span. We note that, although this mode is imposed by the spanwise domain length $L_z = 0.5c$, the wavelength $\lambda_z = 0.25c$ confirms that L_z is sufficiently large to contain wavenumbers *smaller than* the naturally occurring minimum.

The time series in figure 5.11 illustrates that the streamwise vorticity is retained within a slender region of recirculating fluid at the airfoil surface after the vortices have moved downstream. As the next vortex forms, it is bent by the persisting three-dimensional mode at the airfoil surface and induces streamwise vorticity itself, thereby amplifying the three-dimensional instability. As shown in figure 5.11, the continuous repetition of this process gradually increases the bending of the spanwise vortices towards the trailing edge at a location where patches of positive and negative ω_x are in contact and therefore induce fluid movement in the same, upward direction. Figure 5.10(b-c) indicates that this asymmetric bending is associated with the generation of hairpin vortices that eventually grow into the enveloping braids at later times.

The upstream growth of the flow instability is therefore a result of the continuous amplification of three-dimensional flow within a slender region of recirculating fluid and verifies that the underlying instability mechanism is of absolute and not of convective nature.

Separation and transition As introduced above, the large recirculation zone existing at lower angles of attack has collapsed at 7° and the flow transitions over the rear side of the wing as the separated shear layer has become unstable. The transition

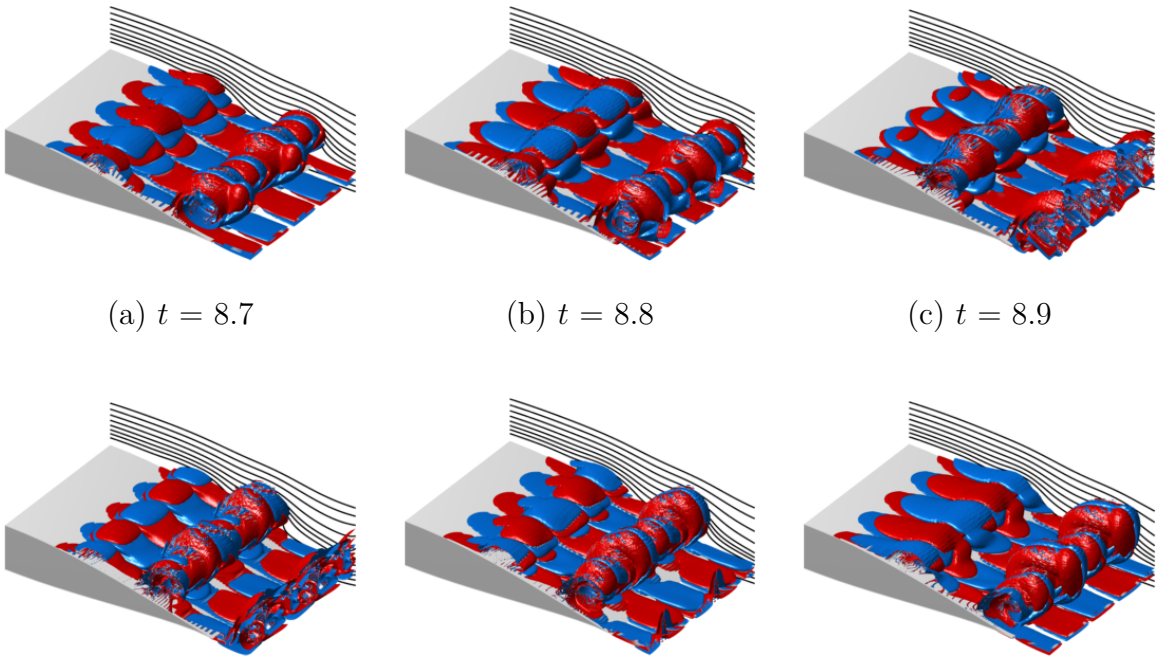

(a) $t = 8.7$ (b) $t = 8.8$ (c) $t = 8.9$

(d) $t = 9.0$ (e) $t = 9.1$ (f) $t = 9.2$

Figure 5.11: Iso-surfaces of the streamwise vorticity $+\omega_x$ (red) and $-\omega_x$ (blue) for a level $|\omega_x| = 1$. Rear section of the airfoil shown between $x/c = 0.4$ and $x/c = 1.1$ for $t = 8.7$ (a) to $t = 9.2$ (f). Instantaneous streamlines in black. AOA = 7°

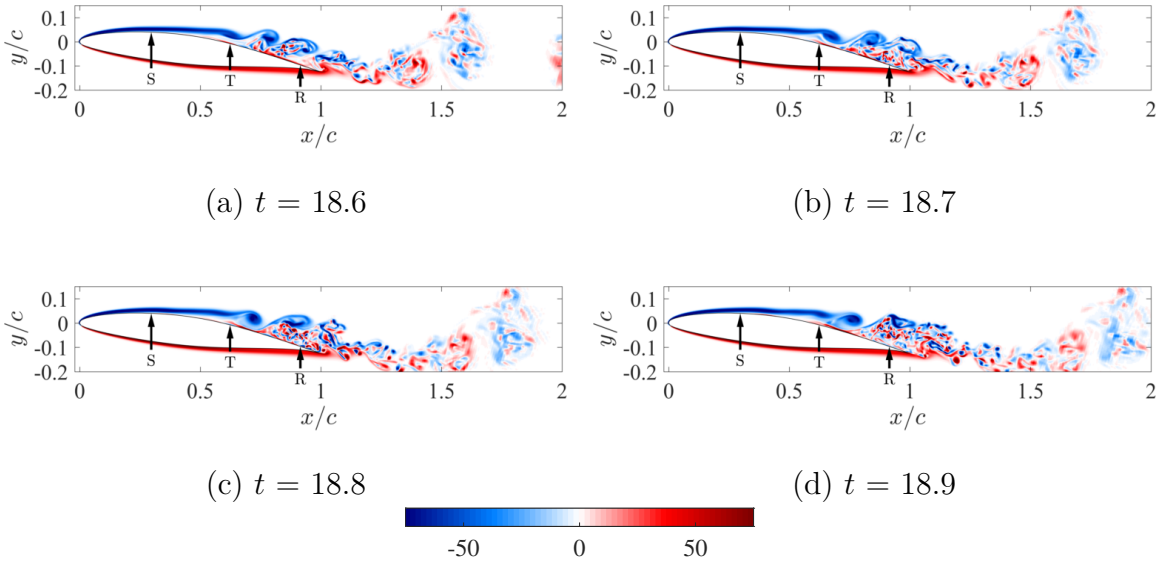

(a) $t = 18.6$ (b) $t = 18.7$

(c) $t = 18.8$ (d) $t = 18.9$

Figure 5.12: Snapshots of instantaneous vorticity ω_z along a slice $z/c = 0.025$ from $t = 18.6$ (a) to $t = 18.9$ (d). S, T, and R indicate the mean locations of separation, transition, and reattachment. AOA = 7°

process is visualized in figure 5.12, where the emergence and subsequent break-down of vortices along the upper shear layer is distinct. Because the large, low-speed recirculation zone is absent at 7° incidence, the bottom-side boundary layer can no longer roll-up into the strong trailing-edge vortex, but is carried downstream by the turbulent, reattached flow from the top.

The three-dimensional flow topology is outlined by plots of iso-Q surfaces in figure 5.13 and show that the vortex shedding at mid-chord is initially two-dimensional but promptly transitions into three-dimensional, chaotic vortical structures upon interacting with the instability retained within the slim recirculation region close to the airfoil surface (cf. figure 5.11). Given that the transition occurs upstream of the trailing edge, the vortices transport momentum from the outer flow into the boundary layer and cause the streamlines to reattach to the wall, thereby forming a slender laminar separation bubble (LSB) on the airfoil's rear side.

Compared to the lower flow angles shown in figure 5.4 and 5.6, the vortex

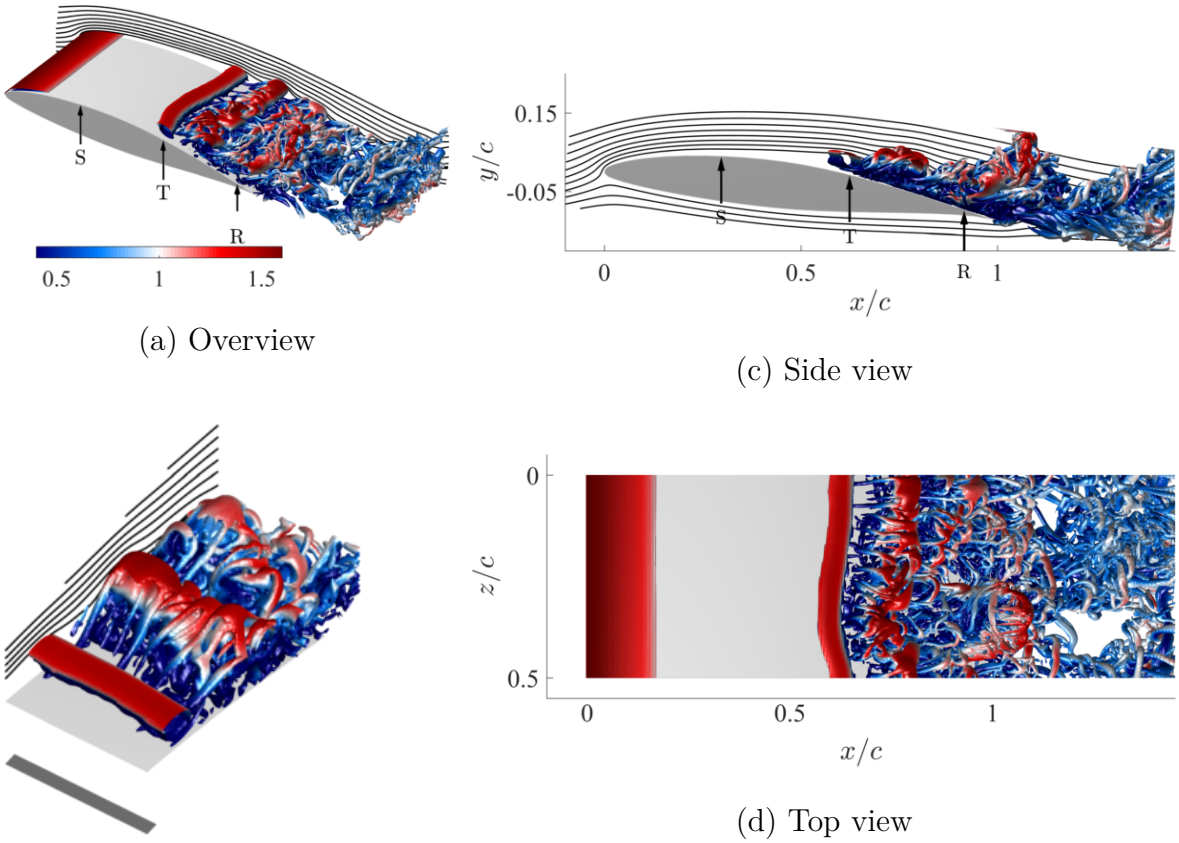

(a) Overview

(c) Side view

(b) Detailed view

(d) Top view

Figure 5.13: Iso-surfaces of Q-criterion (level: 100) colored by the velocity magnitude $|\mathbf{u}|$ at $t = 18.6$. Instantaneous streamlines at $z/c = 0$ in black. S, T, and R indicate the mean locations of separation, transition, and reattachment. Detailed view (b) of vortices in the region $0.55 < x/c < 1$ and $0 < z/c < 0.2$. AOA = 7°

bursting is more rapid and yield smaller length scales because (a) the flow has to work against a stronger adverse pressure gradient and (b) the vortices form upstream of the trailing edge and therefore interact with the recirculating, three-dimensional flow inside the LSB. The bursting vortices, however, retain their coherence on a large scale and can be identified in the continuous shedding of patches of turbulence, or "puffs", from the airfoil (see also figure 5.12).

We outline the transition from two to three-dimensional flow in figure 5.14,

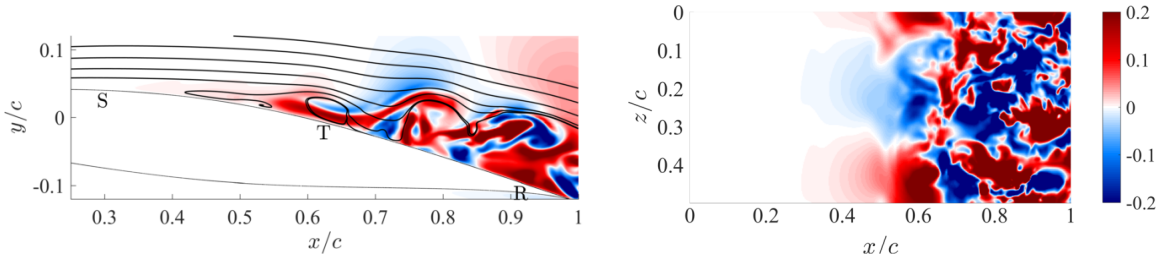

(a) x-y plane (b) x-z plane

Figure 5.14: Instantaneous transverse velocity w and streamlines along a x-y plane at $z/c = 0.025$ (a) and along a surface normal to the airfoil wall displaced by $\Delta\eta = 0.01c$ (b) at $t = 18.6$. S, T, and R indicate the mean locations of separation, transition, and reattachment. AOA = 7°

where instantaneous contours of the transverse (w) velocity are plotted along a plane in x-y direction (a) and a curved surfaces at a distance $\Delta\eta = 0.01c$ normal to the airfoil wall (b). The w-velocity contours show that three-dimensional flow is present within the entire LSB and forms a low-amplitude mode with a wavelength equal to the spanwise domain size. Around the transition point T, the transverse flow is strongly amplified as the shear layer rolls up and sheds.

The instantaneous streamlines shown in figure 5.14(a), the low-frequency mode of transverse velocity shown in (b), and the spanwise bending of the associated vortex tube at $x/c = 0.6$ (see figure 5.13) suggests that an elliptic instability causes the transition from two to three-dimensional flow. Similar observations in flows with LSBs have been made by Jones et al. [19] and Sakai et al. [101].

Wake topology The topology of the vortical structures within the airfoil wake is visualized in figure 5.15, where contours of instantaneous spanwise vorticy ω_z (a) and specific entropy s (b) are plotted. As introduced earlier, vorticity is generated at the airfoil wall and is transported away through convection and diffusion. Stretching of vortex filaments, mixing, and diffusion results in the decay of the vorticity amplitude

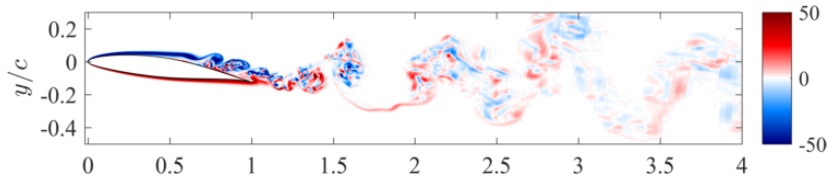

(a) Vorticity ω_z

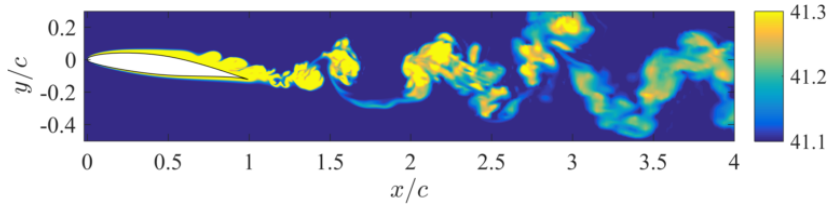

(b) Specific entropy s

Figure 5.15: Instantaneous snapshots of the vorticity ω_z (a) and the specific entropy $s = \ln(p/\rho^\gamma)/(\gamma(\gamma-1)M_f^2)$ (b) along a slice at $z/c = 0.025$ and $t = 18.6$. AOA $= 7°$.

in the wake as an increasing amount of fluid is entrained in the vortical motion. The entropy generated from dissipative processes within the transitioning flow over the wing is preserved within the eddies downstream and highlight the topology of the wake in figure 5.15(b). The scalar field shows that the vortices combine at the airfoil's trailing edge and form large-scale turbulent puffs as they shed downstream into the wake. These turbulent patches carry large amounts of specific entropy downstream and mix with the surrounding fluid which results in the gradual decay of entropy as the wake spreads.

As figure 5.15 shows, the vortices assemble into a low-frequency turbulent vortex street behind the wing, whose wavelength is of the order of the airfoil's chord. Compared to the flow at lower angles of attack without reattachment, the spread of the vortices is significantly increased and results in a much wider wake at AOA $= 7°$.

Velocity and boundary layer profiles The streamlines, wall-normal velocity profile, and the boundary layer displacement thickness of time and space-averaged flow field data are plotted in figure 5.16(a). Superposed are contours of the reverse flow magnitude normalized by the local velocity magnitude at the boundary layer edge within the LSB. In (b), the profiles of the displacement thickness δ^*, momentum thickness θ, and the shape factor H are plotted over the horizontal coordinate x/c.

The laminar boundary layer separates at location S and marks the leading edge of a long and slender LSB, which stretches over a large section of the airfoil from $x_s/c = 0.29$ to $x_r/c = 0.92$. The increase of the displacement thickness accelerates upon separation, whereas the momentum loss thickness abruptly grows at the center of the LSB where the flow transitions to turbulence. The delayed increase results in a local peak of the shape factor and marks the transition location T. As the flow becomes turbulent, The boundary layer reattaches at the trailing edge ($x_r/c = 0.92$) and the shape factor decreases below its upstream laminar level. Similar boundary layer profiles have been observed by Galbraith and Visbal [28] and Uranga et al. [7] for the formation of a LSB over a SD 7003.

The continuous breakdown of the separated, two-dimensional shear layer into three-dimensional turbulent structures suggests that an instability mode is established as a mechanism for self-sustaining turbulence. As noted by Jones et al. [19], three-dimensional fluctuations in a convectively unstable flow would be transported away from the LSB and revert the bubble into a two-dimensional state, whereas self-sustaining turbulence requires constant feeding of fluctuations from an existing instability. Following Alam and Sandham [63] and Jones et al. [19], laminar separation bubbles require a reverse flow velocity U_R of 15-20% of the local boundary layer edge velocity to develop an absolute stability. For values below this threshold, the instability is assumed to be of convective nature. We therefore evaluate the reverse flow within the

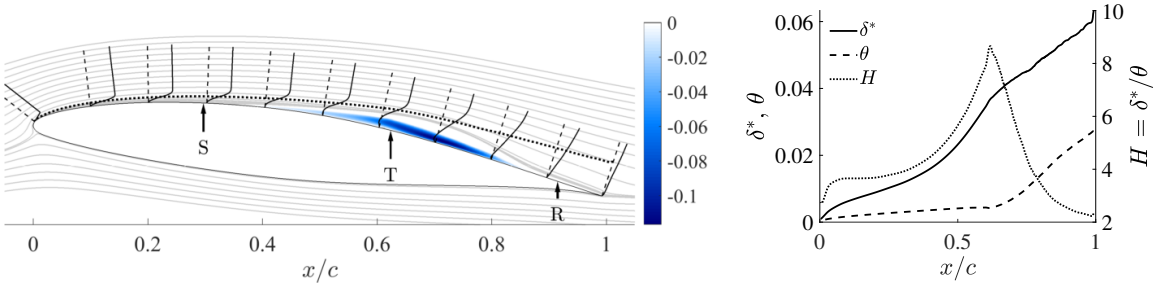

(a) Velocity profile (b) Boundary layer thickness

Figure 5.16: (a) Time and space (spanwise) averaged streamlines in gray, tangential velocity profiles at selected locations in black and displacement thickness δ^* as dotted, black line. Contours of reverse flow normalized by the local velocity at the boundary layer edge in blue. S, T, and R indicate the mean locations of separation, transition, and reattachment. (b) Displacement thickness, momentum thickness, and shape factor. AOA = 7°.

laminar separation bubble to quantify if an absolute instability has potentially been established within the bubble.

The maximum level of the reverse velocity component is $U_R = 11.7\%$, relative to the velocity magnitude at the boundary layer edge (see figure 5.16a). This value is lower than the 15.2% reported by Jones et al. [19] for the NACA 0012, and is below the threshold suggested by Alam and Sandham [63] of 15% to 20% to maintain an absolute instability. Although an absolute instability in the classical sense may not be the cause for the self-sustained turbulence here, the temporal and spatial growth of three-dimensional, turbulent flow suggests the presence of an instability mechanism not predicted by linear stability analysis based on the averaged velocity profile of the LSB [19]. Because three-dimensional vortical structures persist within the reverse flow region and grow upstream within the bubble over time, the presence of the self-exciting three-dimensional mode is likely the result of an elliptic instability combined with the reverse flow within the LSB.

AOA = 8° and AOA = 10°

At 8° and 10° incidence, the laminar boundary layer separates at the leading edge, transitions to turbulence at mid-chord and forms a laminar separation bubble over the airfoil's front surface.

Separation and transition The transition process is outlined in Figure 5.17: contours of instantaneous vorticity along a slice at $z/c = 0.025$ show that the flow is initially laminar and, under a strong, adverse pressure gradient, separates from the leading edge at $x_s/c = 0.016$ (marked as location S). A Kelvin-Helmholtz (K-H) instability drives the formation of large, spanwise vortices along the separated shear layer between $x/c = 0.3$ and 0.4. Upon their generation, these vortices have a clear outline but quickly burst as they roll up over the airfoil surface and transition to turbulence (marked as location T) by forming local turbulent clouds or "puffs". Because the transition process occurs far upstream of the trailing edge, the roll-up of the vortices over the wing transports momentum from the outer flow to the wall, which results to the reattachment of the flow in the time-averaged sense at $x_r/c = 0.48$ (marked as location R in figure 5.17).

The three-dimensionality of the transition process is outlined in figure 5.18, where iso-surfaces of the Q-criterion colored by the velocity magnitude visualize coherent vortical structures in the field. The separation of the boundary layer at location S and the subsequent shedding of laminar vortices correspond to the contours of the snapshot shown in figure 5.17(b). Three coherent, spanwise vortices (I – III) are identified around the transition point T and can be characterized as (I) formation of vortices within the separated shear layer, (II) growth and roll-up over the airfoil surface, and (III) bursting and loss of spanwise coherence. Upon formation along the separated shear layer, the spanwise vortices show an initial three-dimensional mode induced from

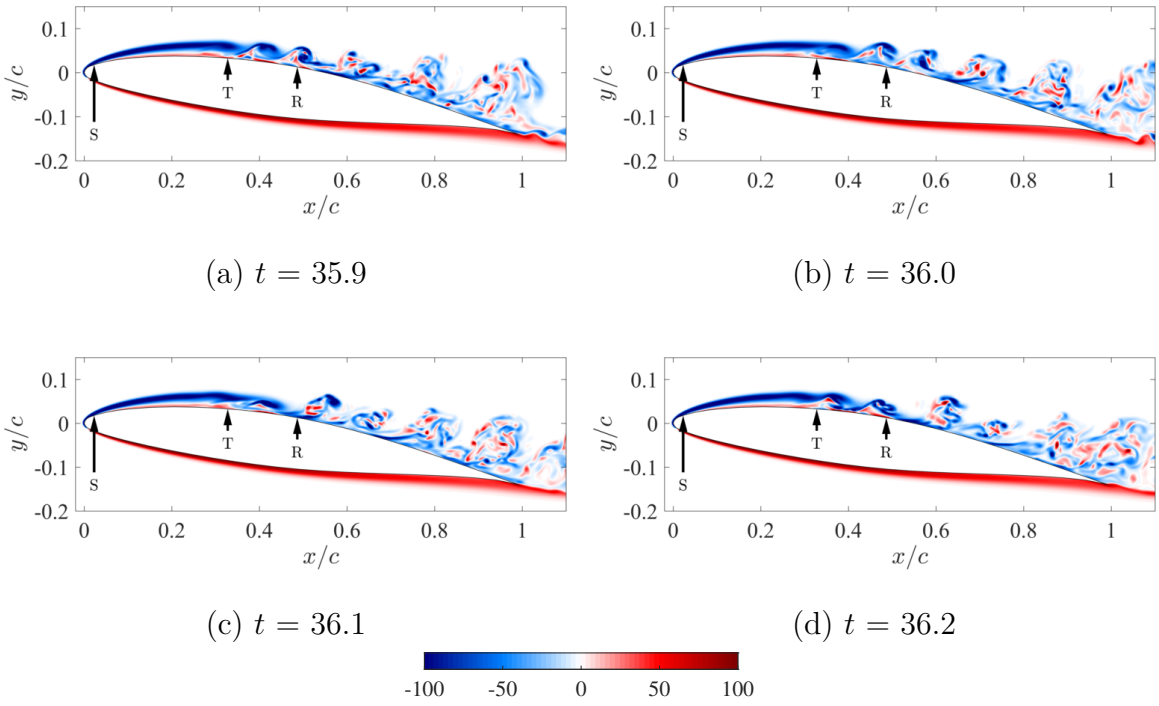

(a) $t = 35.9$ (b) $t = 36.0$

(c) $t = 36.1$ (d) $t = 36.2$

Figure 5.17: Snapshots of instantaneous vorticity ω_z along a slice $z/c = 0.025$ from $t = 35.9$ (a) to $t = 36.2$ (d). S, T, and R indicate the mean locations of separation, transition, and reattachment. AOA = 8°

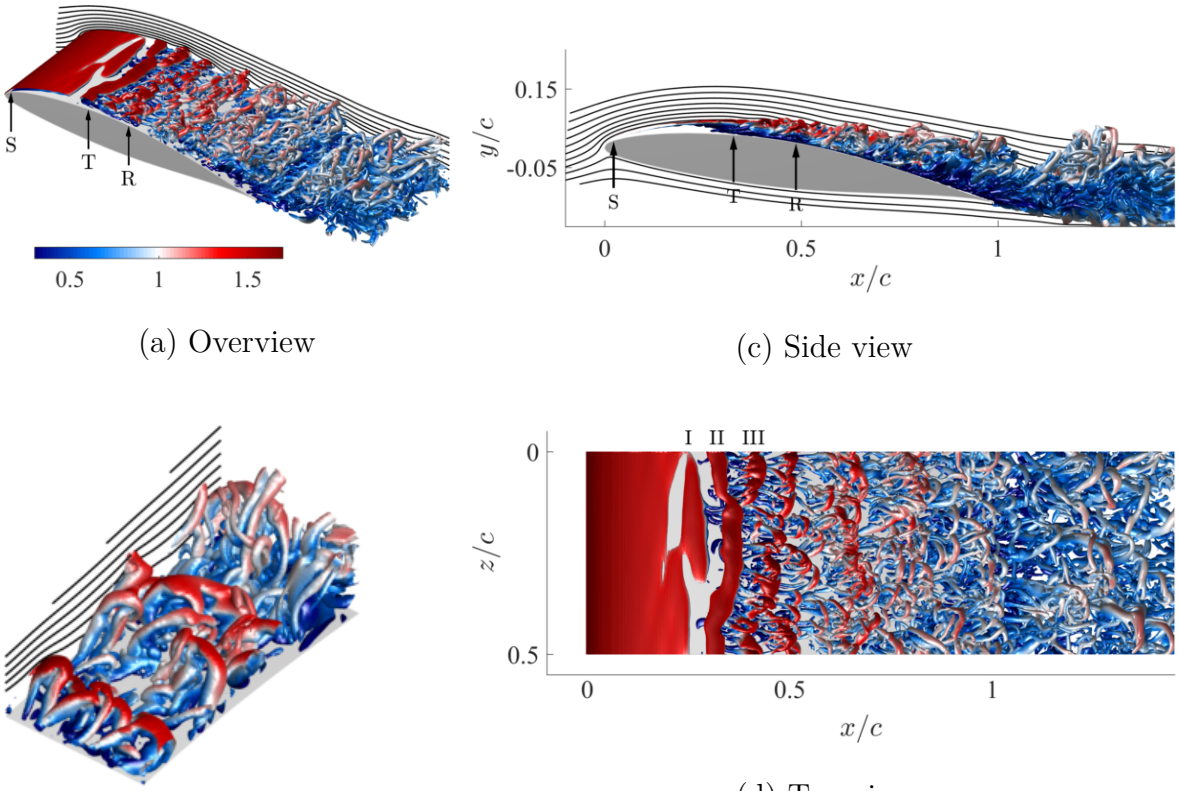

(a) Overview

(c) Side view

(b) Detailed view

(d) Top view

Figure 5.18: Iso-surfaces of Q-criterion (level: 100) colored by the velocity magnitude $|\mathbf{u}|$ at $t = 35.9$. S, T, and R indicate the mean locations of separation, transition, and reattachment. Vortices in separated shear layer (I–III). Detailed view (b) of hairpin vortices in the region $0.45 < x/c < 0.8$ and $0 < z/c < 0.15$. AOA $= 8°$

perturbing flow inside the LSB. As the vortices grow along the shear layer, they continue to bend until their interaction with the wall causes them to burst and loose their coherence. The resulting turbulent flow downstream of the LSB is governed by the formation of a series of wall-bounded hairpin vortices that emerge from the roll-up and bursting of vortex III over the airfoil surface at mid-chord. The coloring of the iso-surfaces by the velocity magnitude in figure 5.17(d) shows that the large-scale rollers are generated within a region of high momentum which they transfer into vortices of smaller scales and thereby into lateral and spanwise fluid motion.

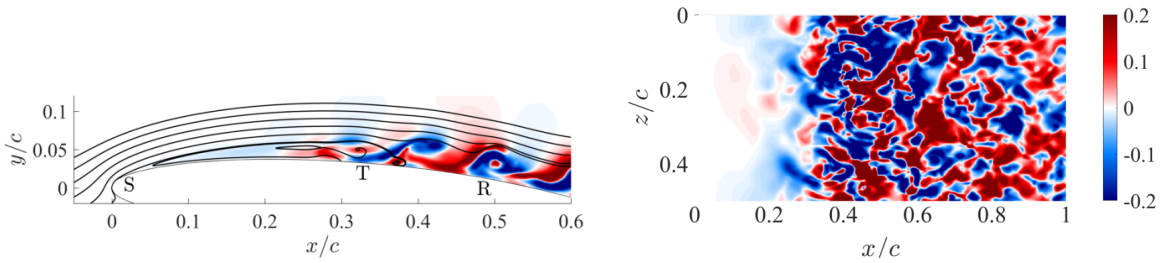

(a) x-y plane (b) x-z plane

Figure 5.19: Instantaneous transverse velocity w and streamlines along a x-y plane at $z/c = 0.025$ (a) and along a surface normal to the airfoil wall displaced by $\Delta\eta = 0.01c$ (b) at $t = 35.9$. S, T, and R indicate the mean locations of separation, transition, and reattachment. AOA = 8°

We outline the transition from two to three-dimensional flow in figure 5.19, where instantaneous contours of the transverse (w) velocity are plotted along a plane in x-y direction (a) and a curved surfaces at a distance $\Delta\eta = 0.01c$ normal to the airfoil wall (b). The instantaneous streamlines plotted in (a) illustrate the recirculating flow within the LSB and form spirals along the vortex cores that indicate fluid motion along the span. The w-velocity contours in (b) show that three-dimensional flow is present within the entire LSB and forms a low-amplitude mode with a wavelength equal to the spanwise domain size. At $x/c = 0.3$, the formation of the first eddy (see also figure 5.18 and 5.20) induces strong, three-dimensional flow associated with the streamwise tubes of hairpin vortices. These are generated in the high velocity gradient from the interaction of the perturbed span-wise rollers and the no-slip wall. The transport of transverse momentum into the LSB hints the presence of an absolute instability mode as a mechanism for self-sustaining turbulence.

The wall signature of the laminar separation bubble and subsequent transition to turbulence is visualized by skin-friction lines in figure 5.20. Friction lines, also called *surface streamlines*, are tangent lines in direction of the wall shear stress and provide information about the flow structure near the surface. Locations of flow separation and

reattachment, for example, can be identified through singular points in the friction line topology [102, 103]. As such critical points are characterized by vanishing wall shear stress, they either act as a source or a sink for surface streamlines [102].

In figure 5.20, the friction lines are superimposed onto contours of instantaneous wall shear stress magnitude (a) and the wall-pressure coefficient (b) to relate the flow topology to aerodynamic wall-based quantities. A straight, transverse shear line at the leading edge identifies the location of flow separation ($x_s = 0.016c$, highlighted in red). From the separation point, the shear lines have a streamwise, parallel orientation until singular lines in transverse direction at $x/c = 0.3$ indicate the change of direction of the wall shear stress along the edges of the first vortex (cf. figure 5.18d). This location agrees very well with the transition point $x_t/c = 0.32$, which is indicates by the second red line in figure 5.20. Downstream of the transition point x_t, the high magnitude of the wall shear stress between $0.4 < x/c < 0.5$ indicates that the vortices generated within the separated shear layer now roll up over the airfoil surface and induce a strong velocity gradient. Driven by upstream perturbation, the high velocity gradients at the vortex edges result in the rapid transition of the flow and a strongly increased transfer of momentum from the outer flow to the airfoil surface that leads to the reattachment of the streamlines in the time-averaged flow field at $x_r/c = 0.48$ (third red line).

Downstream of the reattachment point, the flow has transitioned to turbulence and the topology of the surface streamlines resembles patterns found in other turbulent wall-bounded flows [104, 97]. The highly increased momentum flux towards the airfoil surface in the turbulent region results in recovery of the wall pressure from the outer flow (cf. figure 5.20b), which directly translates into a reduced form drag. Note that the mechanism of pressure recovery is absent in the separated flow at lower angles of attack (0° and 4°).

Results of implicit LES show that the airfoil flow at 10° incidence is governed

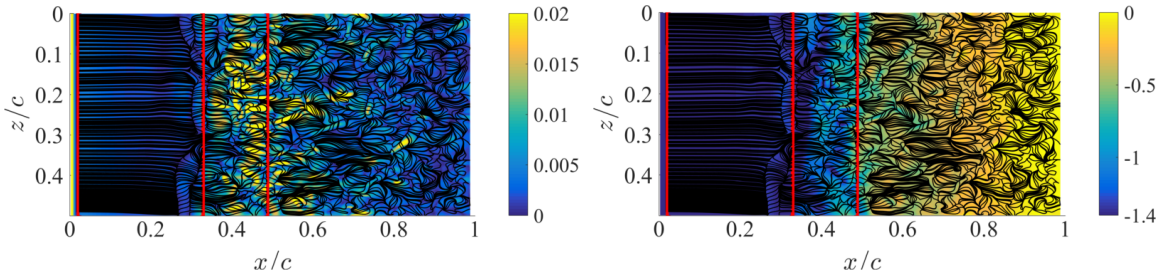

(a) Skin friction coefficient (b) Pressure coefficient

Figure 5.20: Skin friction and pressure coefficient contours on upper side of the airfoil at $t = 35.9$. Surface streamlines in black. Red lines indicate location of separation, transition, and reattachment (from left to right). AOA = 8°.

by a large, leading-edge LSB and transition to turbulence of the separated shear layer over the wing, similar to the case at 8° angle of attack. Contour plots of instantaneous vorticity (see figure 5.21), as well as iso-surfaces of the Q-criterion (see figure 5.22), illustrate how the spanwise vortices from the separated shear layer quickly burst and result in turbulent fluid motions downstream of the LSB. The strong, adverse pressure gradient at 10° incidence accelerates the flow transition and cause the vortices to loose their coherent shape earlier in comparison to the flow at 8° angle of attack. A larger, turbulent boundary layer downstream of the bubble results in higher viscous losses and lower performance as the airfoil moves closer to aerodynamic stall conditions (see figure 5.2).

Wake topology The subsequent break down of vortical structures from the separating shear layer over the airfoil into the turbulent wake is visualized for AOA = 8° in figure 5.23, which shows contours of instantaneous spanwise vorticy ω_z (a) and specific entropy s (b). As introduced earlier, vorticity is generated at the airfoil wall and is transported away through convection and diffusion. Stretching of vortex filaments, mixing, and diffusion results in the decay of the vorticity amplitude in the wake as an increasing amount of fluid is entrained in the vortical motion.

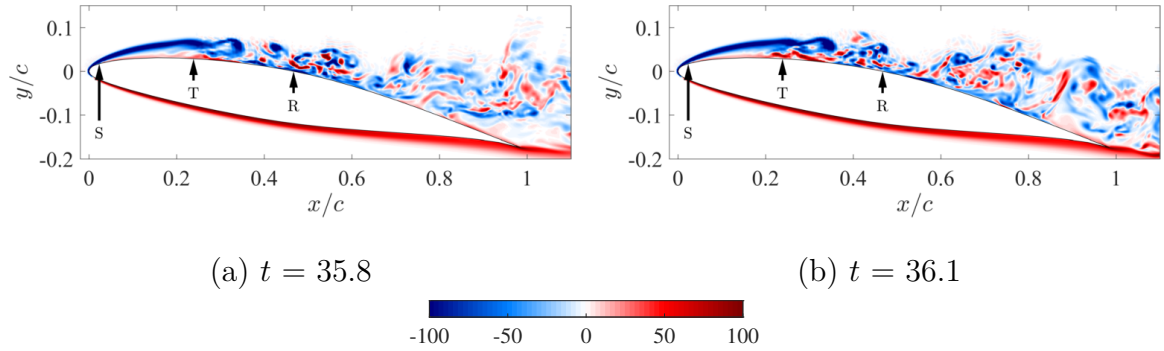

(a) $t = 35.8$ (b) $t = 36.1$

Figure 5.21: Snapshots of instantaneous vorticity ω_z along a slice $z/c = 0.025$ at $t = 35.8$ (a) and $t = 36.1$ (b). S, T, and R indicate the mean locations of separation, transition, and reattachment. AOA = 10°

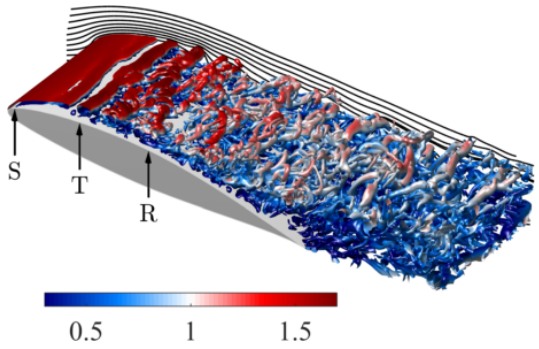

Figure 5.22: Iso-surfaces of Q-criterion (level: 100) colored by the velocity magnitude $|\mathbf{u}|$ at $t = 36.1$. S, T, and R indicate the mean locations of separation, transition, and reattachment. AOA = 10°

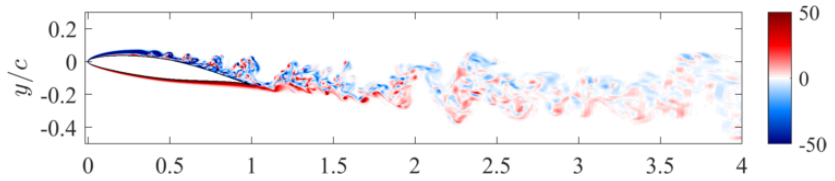

(a) Vorticity ω_z

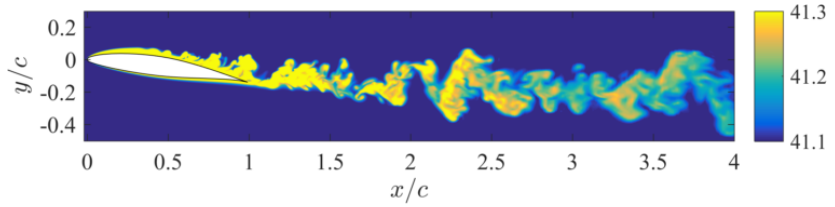

(b) Specific entropy s

Figure 5.23: Instantaneous snapshots of the vorticity ω_z (a) and the specific entropy $s = \ln(p/\rho^\gamma)/(\gamma(\gamma-1)M_f^2)$ (b) along a slice at $z/c = 0.025$ and $t = 35.9$. AOA $= 8°$.

The entropy generated from dissipative processes within the transitioning flow over the wing is preserved within the eddies downstream and highlight the topology of the wake in figure 5.23(b). The scalar field shows that the bursting vortices form large-scale turbulent puffs downstream in the wake as they merge with each other and the shear layer from the bottom side of the airfoil at the trailing edge. These turbulent structures carry large amounts of specific entropy downstream and mix with the surrounding fluid which results in the gradual decay of entropy as the wake spreads. The conservation of local patches with high entropy downstream in the wake indicate the existence of coherent structures.

Remarkably, the spread of the wake is smaller than for the flow at 7°, despite the higher angle of attack and larger projected frontal area. Because the turbulence develops over a longer distance before shedding off the airfoil, the vortices are less coherent at AOA $= 8°$ and the flow leaves the trailing edge more uniformly than at AOA $= 7°$.

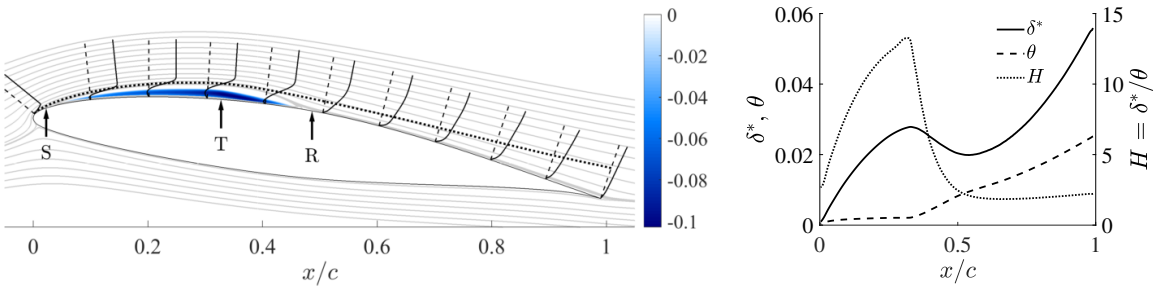

(a) Velocity profile (b) Boundary layer thickness

Figure 5.24: (a) Time and space (spanwise) averaged streamlines in gray, tangential velocity profiles at selected locations in black and displacement thickness δ^* as dotted, black line. Contours of reverse flow normalized by the local velocity at the boundary layer edge in blue. S, T, and R indicate the mean locations of separation, transition, and reattachment. (b) Displacement thickness, momentum thickness, and shape factor. AOA = 8°.

Velocity and boundary layer profiles The streamlines, wall-normal velocity profile, and the boundary layer displacement thickness of time and space-averaged flow field data are plotted in figure 5.24(a) for AOA = 8° and 5.25(a) for AOA = 10°. Superposed are contours of the reverse flow magnitude normalized by the local velocity magnitude at the boundary layer edge within the LSB. In (b), the profiles of the displacement thickness δ^*, momentum thickness θ, and the shape factor H are plotted over the horizontal coordinate x/c.

The flow separates at the leading edge (location S) and reattaches after transitioning to turbulence at approximately mid-chord, thereby forming a LSB over the first half of the wing. The displacement thickness increases strongly until the center of the LSB, where the momentum loss thickness starts to grow and results in a local peak of the shape factor, marking the transition point T. After the reattachment at $x_r/c = 0.48$ (AOA = 8°) and $x_r/c = 0.46$ (AOA = 10°), the flow transitions to a turbulent boundary layer and the shape factor levels out. Similar to the bubble dynamics at 7°, the turbulence is self-sustaining in case of the leading-edge LSB encountered at 8° and 10° incidence. Again, we evaluate the reverse flow within the separation bubble to

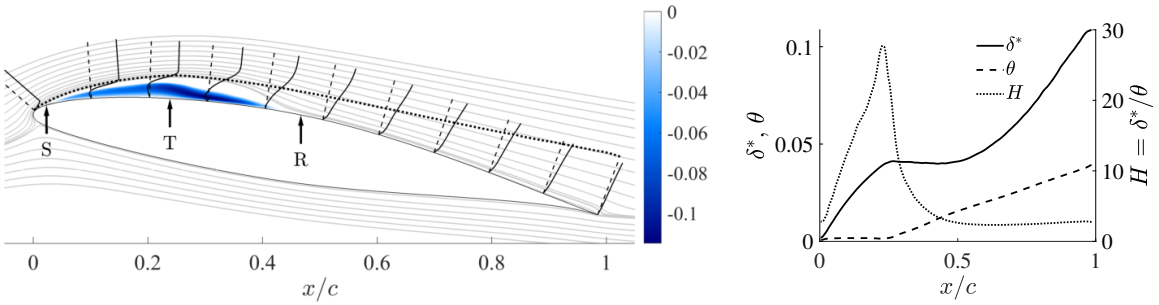

(a) Velocity profile (b) Boundary layer thickness

Figure 5.25: (a) Time and space (spanwise) averaged streamlines in gray, tangential velocity profiles at selected locations in black and displacement thickness δ^* as dotted, black line. Contours of reverse flow normalized by the local velocity at the boundary layer edge in blue. S, T, and R indicate the mean locations of separation, transition, and reattachment. (b) Displacement thickness, momentum thickness, and shape factor. AOA = 10°.

quantify if an absolute instability has potentially been established. At an angle of 8°, the maximum level of the reverse velocity component is $U_R = 10.3\%$, relative to the velocity magnitude at the boundary layer edge. This value is lower than the 11.7% at 7° or the 15.2% reported by Jones et al. [19] for the NACA 0012, and is clearly below the threshold suggested by Alam and Sandham [63] of 15% to 20% to maintain an absolute instability. At 10° incidence, the increased bubble height results in a higher reverse flow level with $U_R = 11.5\%$ of the local boundary-layer edge velocity, but still fails meet the criterion referenced by Alam and Sandham [63].

In both cases, the self-sustained turbulence within the leading-edge LSB is likely driven by a three-dimensional instability mode, where, similar to the previously discussed case at 7° incidence, the disturbance feeds from the upstream transport of streamwise vortical structures through the reverse flow region.

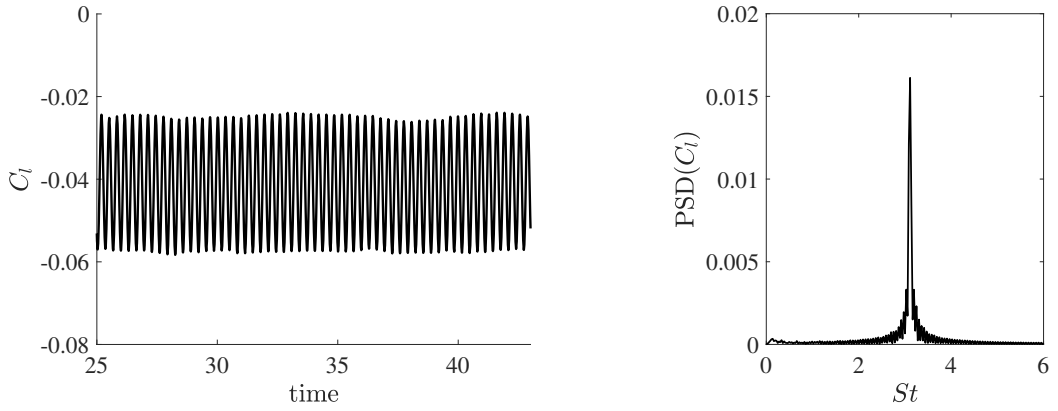

(a) Lift coefficient

(b) Lift spectrum

Figure 5.26: (a) Lift coefficients over time. (b) Frequency spectrum of the lift coefficient. AOA = 0°.

5.3.2 Aerodynamic forces

The following section addresses the aerodynamic forces on the wing and discusses time-averaged profiles of the pressure and skin friction coefficients as well as the time history of the integrated lift and drag forces and the associated frequency spectra. Note that the time unit is scaled with the free-stream velocity U_f and the chord-length of the airfoil c, such that the corresponding frequency identifies as the Strouhal number $St = fc/U_f$ of the flow.

AOA = 0°

Figure 5.26 shows the time-history of the lift coefficient and the corresponding frequency spectrum within the quasi-steady regime for the flow at AOA = 0°. The fluctuations of the forces are driven by the shedding of the laminar shear layers at the trailing edge and directly relate to the vortex street in the wake presented in figure 5.8. The forces steadily oscillate around a time-averaged mean of $\bar{C}_l$ = -0.041 and $\bar{C}_d$ = 0.036 and the frequency spectrum of the lift coefficient shows a single distinct peak at a Strouhal number of St = 3.1.

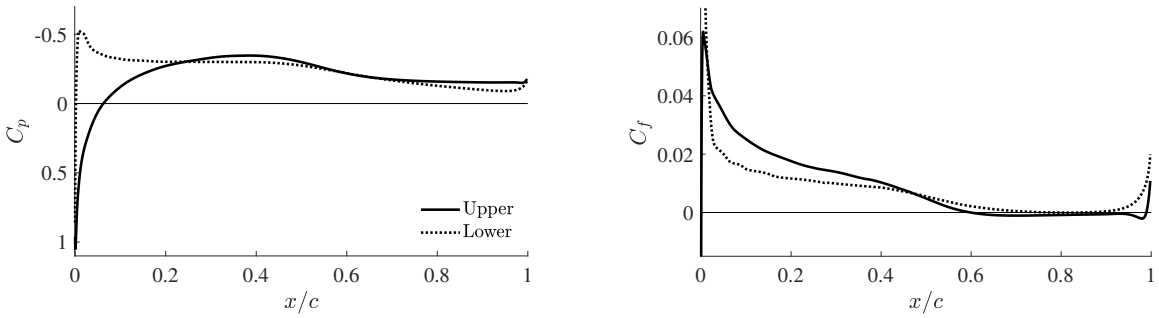

(a) Pressure coefficient

(b) Skin friction coefficient

Figure 5.27: Time and spanwise averaged pressure and skin friction coefficients. AOA = 0°

The time-averaged profiles of the pressure and skin friction coefficients are plotted over the chord length of the airfoil in figure 5.27. The pressure distribution differs significantly from the inviscid solution (see figure 1.1c) and shows an overall higher pressure on the upper side that results in the negative lifting force. At the leading edge, the positive peak of the pressure coefficient on the upper side is caused by the stagnation point flow ($C_p \approx 1$), whereas the negative peak is related to the fluid turning around the leading edge from the upper to the bottom side, causing a low pressure region and negative lift. The separation point of the boundary layer on the upper side is indicated by negative skin friction at $x_s/c = 0.6$, while the flow stays attached on the bottom side. Downstream of the separation point, the pressure remains nearly constant as the flow has separated and the free-stream pressure is not recovered towards the trailing edge.

AOA = 4°

At 4°, the flow topology is similar to 0° and is governed by the boundary layer separation at mid-chord. The lift and drag forces still oscillate in a quasi-steady manner (see figure 5.28), but contain additional low-frequency components. The time-averaged

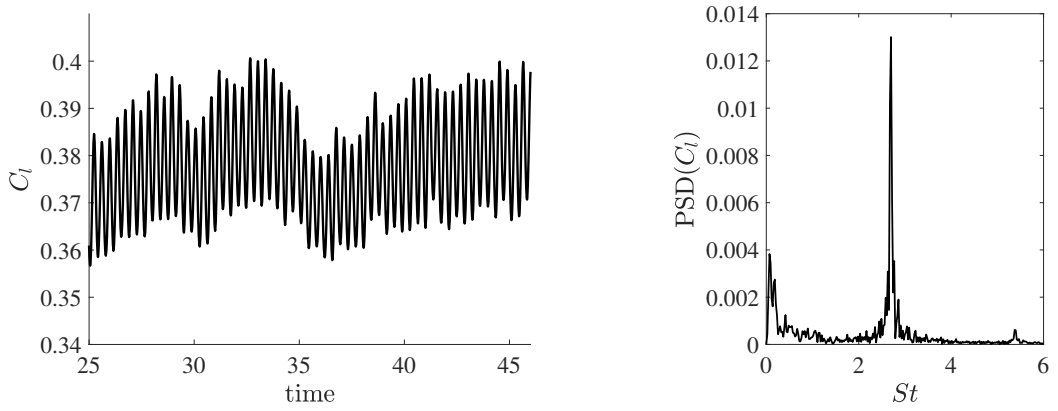

(a) Lift coefficient

(b) Lift spectrum

Figure 5.28: (a) Lift coefficients over time. (b) Frequency spectrum of the lift coefficient. AOA = 4°.

forces are $\bar{C}_l = 0.378$ and $\bar{C}_d = 0.051$ at a Strouhal number of $St = fc/U_f = 2.7$, where we take f to be the most energetic frequency of the lift coefficient. The change in the vortex-shedding frequency is driven by the larger size of vortices generated at the trailing edge. The vortex size is limited by the projected height of the wing area onto the free-stream plane and therefore increases with the angle of attack, allowing for the generation of larger vortices.

Figure 5.29 shows the pressure and skin friction coefficients plotted over the airfoil chord. The upper (suction) side shows a moderate adverse pressure gradient until the flow separates at $x_s/c = 0.49$, where again the pressure remains constant throughout the recirculation region and is not recovered towards the trailing edge. The skin friction coefficient gradually decreases after the leading-edge spike as the boundary layer thickens and turns negative at the separation point at $x_s/c = 0.49$ on the upper side.

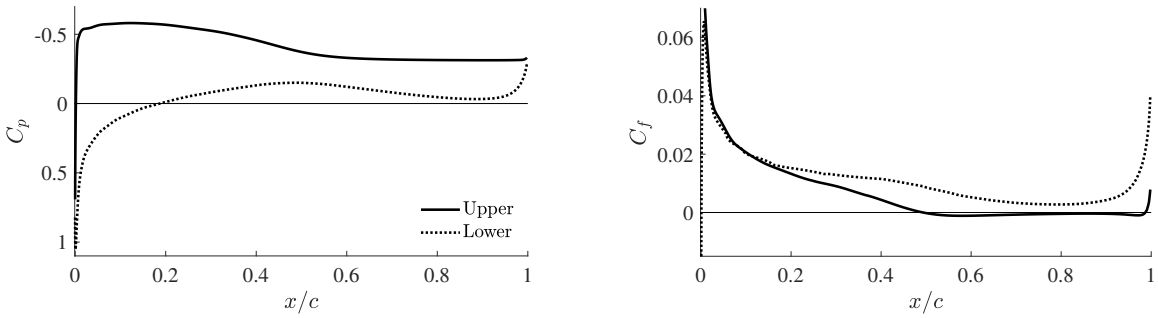

(a) Pressure coefficient (b) Skin friction coefficient

Figure 5.29: Time and spanwise averaged pressure and skin friction coefficients. AOA = 4°

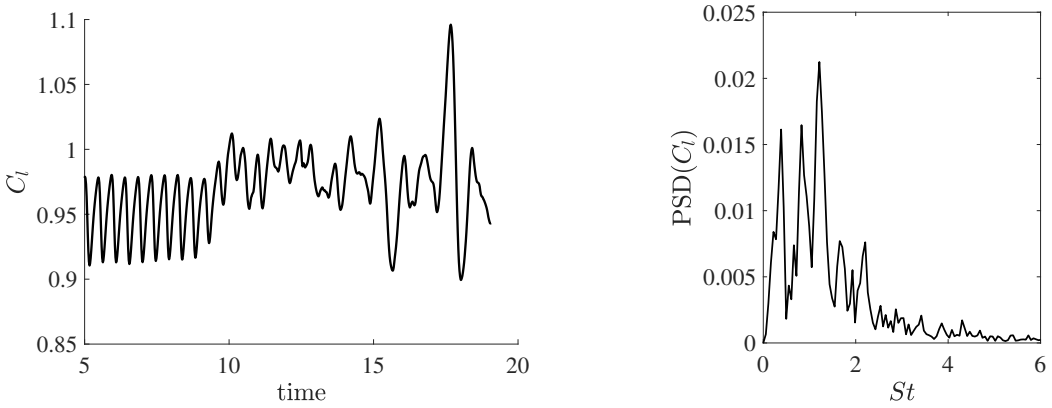

(a) Lift coefficient (b) Lift spectrum

Figure 5.30: (a) Lift coefficients over time. (b) Frequency spectrum of the lift coefficient. AOA = 7°.

AOA = 7°

The lift history and the associated frequencies are given in figure 5.30. The trend is highly irregular and shows a clear transition from two-dimensional ($t < 10$) to three-dimensional ($t > 10$) flow. The time-averaged forces are $\bar{C}_l = 0.98$ and $\bar{C}_d = 0.063$ at a Strouhal number of $St = fc/U_f = 1.2$, where, again, we take f to be the most energetic frequency of the lift coefficient.

Figure 5.31 shows the pressure and skin friction coefficients plotted over the

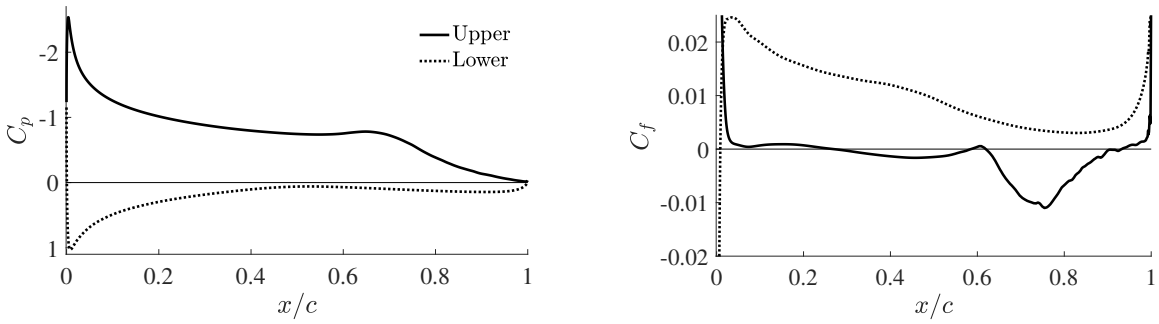

(a) Pressure coefficient

(b) Skin friction coefficient

Figure 5.31: Time and spanwise averaged pressure and skin friction coefficients. AOA = 7°

airfoil chord. The upper (suction) side shows a strong adverse pressure gradient at the leading edge which levels out downstream until the flow transitions at $x_t/c = 0.62$ where the pressure shows a local minimum. The skin friction distribution over the wing is rather unique: downstream of the leading edge spike, the shear stress at the wall drops to near zero and remains low until the flow transitions and turbulence causes high shear gradients for $x/c > 0.6$. Although the time-averaged zero-skin friction point is at $x_s/c = 0.29$, the skin friction periodically becomes negative at the trailing edge (not shown), thus making the exact determination of the separation point challenging.

AOA = 8°

The transition to a flow with a LSB at the leading edge and subsequent turbulent boundary layer over the rear side of the airfoil results in a chaotic pattern of the lift and drag forces. As discussed in Section 5.2, the simulation is initially run with at low spatial resolution and interpolated onto the finer grid with higher wall resolution at $t \approx 26$ to better account for the small-scale turbulent structures, resulting in a transition period from $t \approx 26$ to $t \approx 30$, which is the taken to be the starting point for

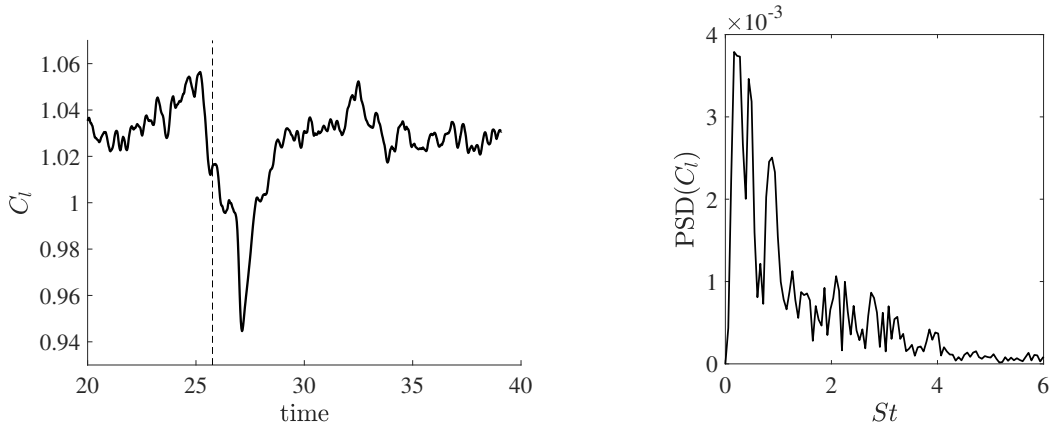

(a) Lift coefficient (b) Lift spectrum

Figure 5.32: (a) Lift coefficients over time. Dashed line indicates interpolation from *Grid 1* to *Grid 2*. (b) Frequency spectrum of the lift coefficient. AOA = 8°.

the temporal statistics in this computation. The time-averaged mean of the lift and drag coefficients are $\bar{C}_l = 1.03$ and $\bar{C}_d = 0.056$. Contrary to the flows at sub-critical angles of attack, the lift spectrum does not yield a single, dominant frequency peak in the spectrum, but indicates an exponential decay of the energy content typical for turbulent flows.

Figure 5.33 presents plots of the time and space-averaged pressure and skin friction profiles of the flow at AOA = 8° (compare to instantaneous results in figure 5.20). As shown in the previous section, the laminar boundary layer separates at the leading edge ($x_s/c = 0.02$), transitions ($x_t/c = 0.32$), and reattaches ($x_r/c = 0.48$), thereby forming a laminar separation bubble over the upper front side of the wing. Figure 5.33(a) shows that the pressure coefficient strongly increases at the leading edge, causing a local adverse pressure gradient and separation of the laminar boundary layer. Downstream of the separation point, the pressure remains constant across the LSB before it abruptly increases at the reattachment point and then gradually approaches towards the free-stream pressure at the trailing edge, resulting in low form drag. The

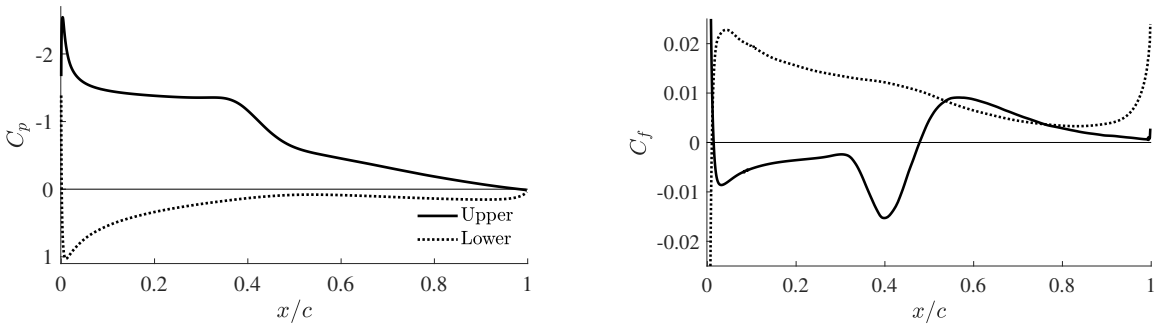

(a) Pressure coefficient

(b) Skin friction coefficient

Figure 5.33: Time and spanwise averaged pressure and skin friction coefficients. AOA = 8°

reverse flow region inside the LSB induces a negative skin friction until the shear layer transitions ($x_t/c = 0.32$) and reattaches at $x_r/c = 0.48$. Between the transition and the reattachment point, the skin friction shows a prominent negative peak caused by the clock-wise rotating flow as the growing vortex rolls up over the airfoil surface. The subsequent bursting results in highly increased transport of momentum from the outer flow to the wing surface and in the recovery of the pressure over the rear side of the wing, as shown in figure 5.33(a).

AOA = 10°

Figure 5.34 presents the lift coefficient history and the corresponding frequency spectrum of the implicit LES simulations at 10° incidence. The time-averaged mean of the lift and drag coefficients are $\bar{C}_l = 1.06$ and $\bar{C}_d = 0.095$. Similar to the flow at 8°, the lift spectrum does not yield a single dominant frequency, but shows several peaks of decreasing amplitude with Strouhal number caused by the turbulent boundary layer that develops downstream of the LSB. The time and space-averaged pressure and skin friction coefficients in figure 5.35 are similar to the profiles at 8° angle of attack, but show a decreased length of constant pressure across the LSB and a broader peak of

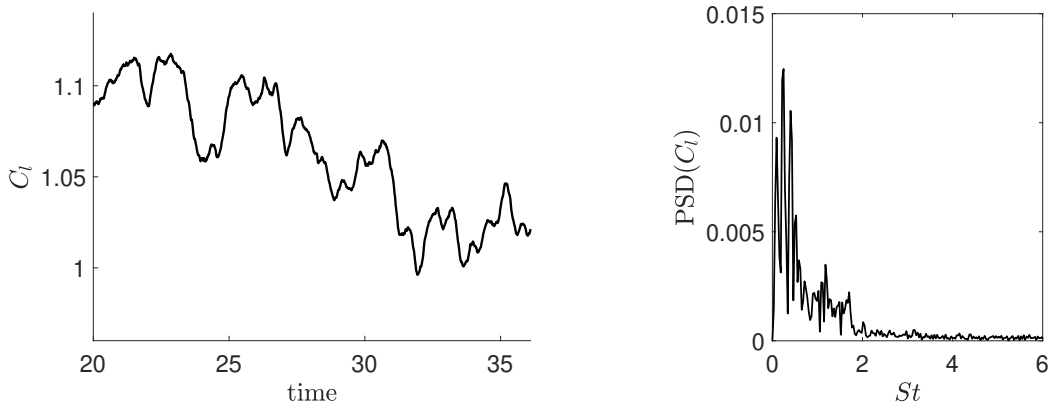

(a) Lift coefficient (b) Lift spectrum

Figure 5.34: (a) Lift coefficients over time. (b) Frequency spectrum of the lift coefficient. AOA = 10°.

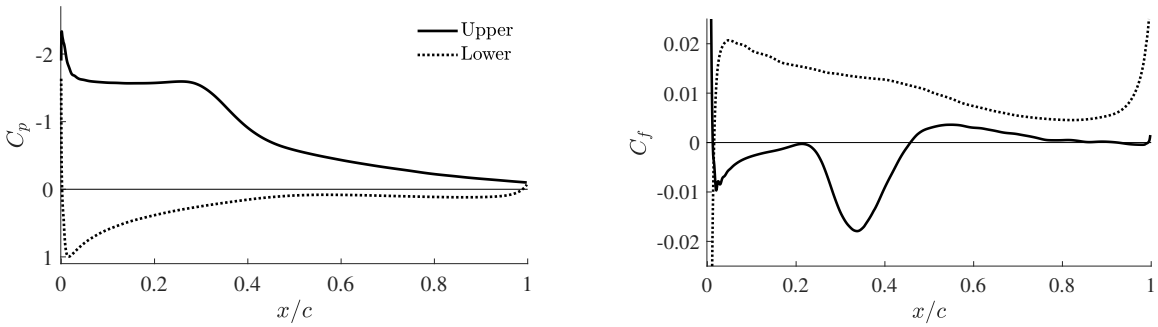

(a) Pressure coefficient (b) Skin friction coefficient

Figure 5.35: Time and spanwise averaged pressure and skin friction coefficients. LES results are filtered to increase smoothness. AOA = 10°

negative shear stress at the transition point.

5.3.3 Temporal and spatial statistics

For compressible flows, the transfer of energy between the mean flow, turbulent fluctuations, and internal energy is described by a set of transport equations that derive from the decomposition of the Favre-averaged Navier-Stokes equations, as shown by Huang et al. [105]. The terms in these equations are relevant for the testing and development of turbulence models [12]. The decomposition results in three separate equations for the transport of mean-flow, turbulent, and internal energy, where shared terms represent the energy transfer between these quantities. In the following, $\langle u_i \rangle = T^{-1} \int_T u_i(t) \mathrm{d}t$ refers to Reynolds-averaged variables and $\{u_i\} = \langle \rho u_i \rangle / \langle \rho \rangle$ refers to Favre-averages. The decomposition into mean and fluctuating components is such that $u_i = \langle u_i \rangle + u_i'$ and $u_i = \{u_i\} + u_i''$.

The turbulent kinetic energy (TKE) $\{k\} = \{u_i'' u_i''\}/2$ is governed by the transport equation

$$\frac{\partial \langle \rho \rangle \{u_k\} \{k\}}{\partial x_k} = -\langle \rho \rangle \{u_i'' u_k''\} \frac{\partial \{u_i\}}{\partial x_k} - \frac{\partial \langle \rho \rangle \{u_k'' k''\}}{\partial x_k} - \frac{\partial \langle p' u_k' \rangle}{\partial x_k} + \frac{1}{Re_f} \frac{\partial \langle \tau_{ik}' u_i' \rangle}{\partial x_k} - \frac{1}{Re_f} \left\langle \tau_{ik}' \frac{\partial u_i'}{\partial x_k} \right\rangle - \langle u_k'' \rangle \frac{\partial \langle p \rangle}{\partial x_k} + \frac{1}{Re_f} \langle u_i'' \rangle \frac{\partial \langle \tau_{ik} \rangle}{\partial x_k} + \left\langle p' \frac{\partial u_k'}{\partial x_k} \right\rangle . \quad (5.1)$$

In (5.1), the advection of the TKE is balanced by several terms on the right-hand side that represent the transfer to the mean-flow and the internal energy. The first right-hand side term describes the energy production, the second is the turbulence transport, the third describes transport related to the velocity-pressure gradient, the fourth is viscous diffusion, and the fifth is the viscous energy dissipation. The last three terms in (5.1) are energy transport associated with compressibility effects.

In this section, we evaluate the energy budget of the turbulent kinetic energy for the transitional airfoil flow. Additionally, we determine the frequency content and spatial coherence of the turbulent structures within the separated flow region by assessing the energy spectrum of the turbulent kinetic energy $\langle k \rangle = \langle u_i' u_i' \rangle / 2$ along the

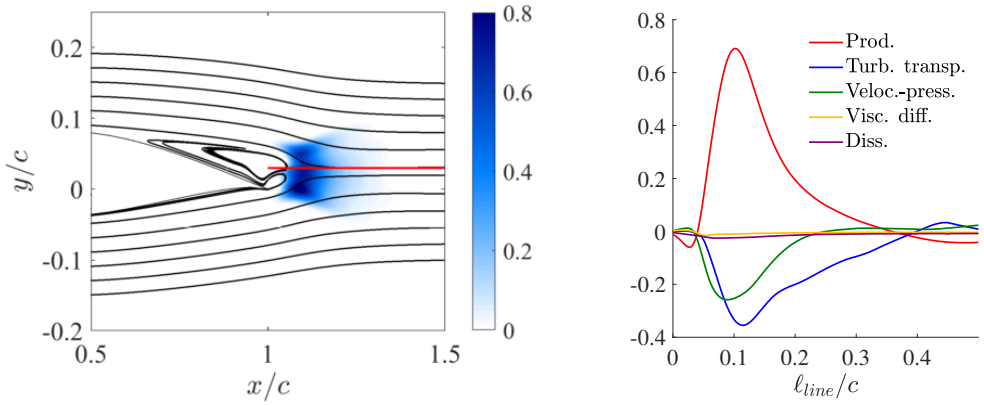

(a) TKE production (b) TKE budget

Figure 5.36: (a) Production of the TKE in the airfoil wake (Y-axis stretched). (b) TKE budgets plotted along a line shown in (a). AOA = 0°.

span at selected locations based on the averaged flow pattern.

AOA = 0° and AOA = 4°

We evaluate the production, transport, and dissipation of the turbulent kinetic energy for the flow at 0° incidence in figure 5.36. In (a), contours of the production term $-\langle\rho\rangle\{u_i''u_k''\}\partial\{u_i\}/\partial x_k$ are overlayed by streamlines from time-averaged flow field data. The plot shows that turbulent kinetic energy is produced in a short region at the downstream edge of the recirculation bubble. At this location, the separated bottom and top shear layer meet and form vortex pairs, as shown in the instantaneous vorticity plots in figure 5.3.

Figure 5.36(b) evaluates the first five terms on the right-hand side of (5.1) along a line in the wake (see figure 5.36a). The turbulent production dominates the TKE budget and is mainly balanced by turbulent transport $-\partial(\langle\rho\rangle\{u_k''k''\})\partial x_k$ and velocity-pressure gradient diffusion $-\partial(\langle p'u_k'\rangle)\partial x_k$. The contribution of the viscous diffusion and viscous dissipation is small compared to the other terms, as the flow is no longer wall-bounded at this location which highly reduces the contribution of viscous forces.

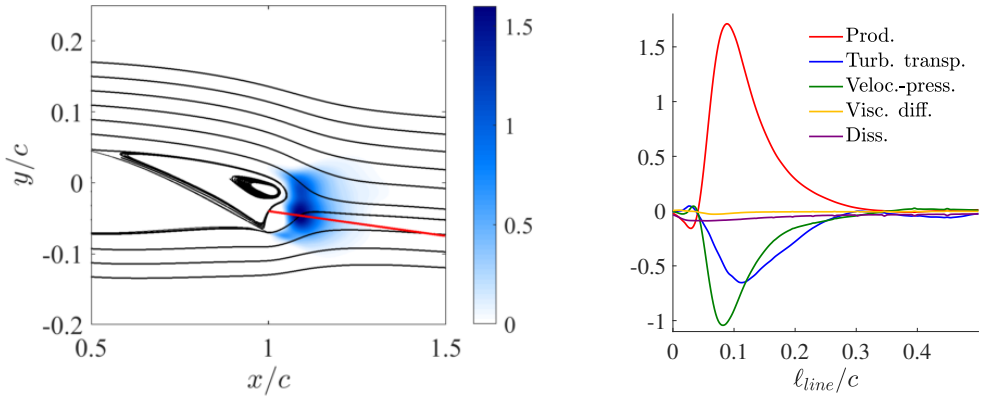

(a) TKE production (b) TKE budget

Figure 5.37: (a) Production of the TKE in the airfoil wake (Y-axis stretched). (b) TKE budgets plotted along a line shown in (a). AOA = 4°.

At 4° incidence, the turbulent kinetic energy production approximately doubles over the values reported at 0° and spans a slightly larger region that is consistent with the increase in the size of the separation bubble (see figure 5.37). Again, the TKE production is strictly limited to the outside of the recirculation zone where the bottom and top vortex meet. Figure 5.37(b) shows that the first five right-hand side terms of (5.1) follow the pattern found at 0°, with the production being balanced by turbulent and velocity-pressure diffusion.

It should be noted that at both flow angles the TKE production is negative at the separation bubble edge and indicate a local region of reverse energy transfer, i.e. from energy of turbulent fluctuations to the mean flow.

Spectra of the velocity fluctuations are recorded at three locations along spanwise lines. The probe locations are selected such that location 1 lies within the recirculation zone, location 2 at the edge, and location 3 in the wake $0.3c$ behind the trailing edge, as shown in figures 5.38(a) and 5.39(a) for 0° and 4° respectively. Both velocity spectra are similar in shape and approximately follow the -5/3 decay for wavenumbers between $10 < k_z < 30$, but deviate in their smoothness. Despite averaging the spectra

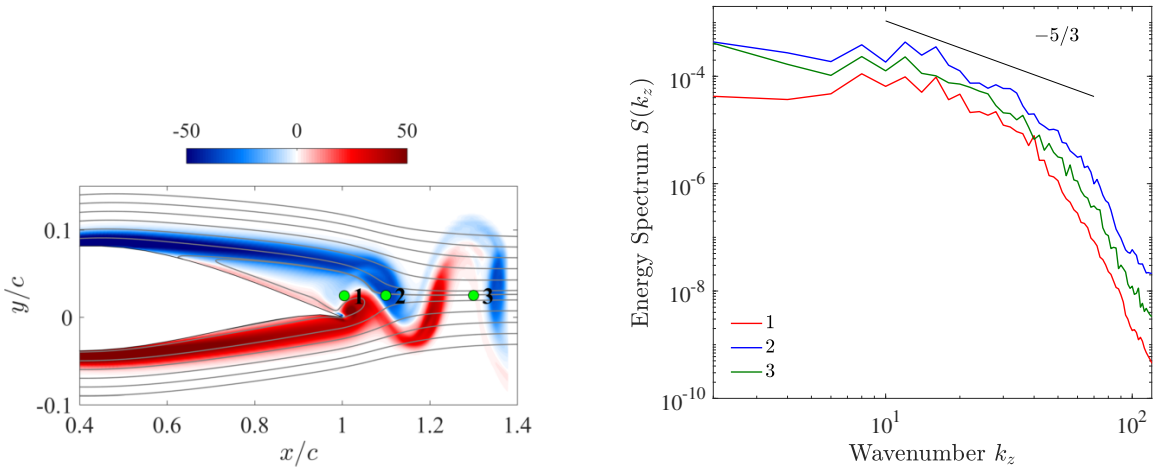

(a) Locations (b) Spectra

Figure 5.38: (a) Spanwise-averaged vorticity at $t = 42.7$ and time-averaged streamlines. Green markers indicate probe locations for spanwise velocity spectra. Y-axis stretched. (b) Spanwise velocity spectra (power spectral density) at locations marked in (a). Spectra are averaged over 99 samples. AOA = 0°.

over ten convective time units, figure 5.38(b) shows several low-wavenumber peaks at $k_z = 8$, 12, and 16. These peaks correspond to the well-defined longitudinal braid-vortices that emerge from the vortex roll-up at the trailing edge (see figure 5.4). The lack of smoothness indicates that the flow remains laminar at the probed locations and does not transition to turbulence, as is the case at 4°, where a much smoother velocity spectrum in figure 5.39(b) results from the onset of turbulent motion at the trailing edge (see figure 5.6).

AOA = 8°

Because the laminar flow transitions upstream of the trailing edge at higher angles of attack and forms a separation bubble at the leading edge, the generation of turbulence is wall-bounded and no longer limited to the wake. Figure 5.40(a) shows that the TKE production peaks towards the rear end of the LSB, right between the

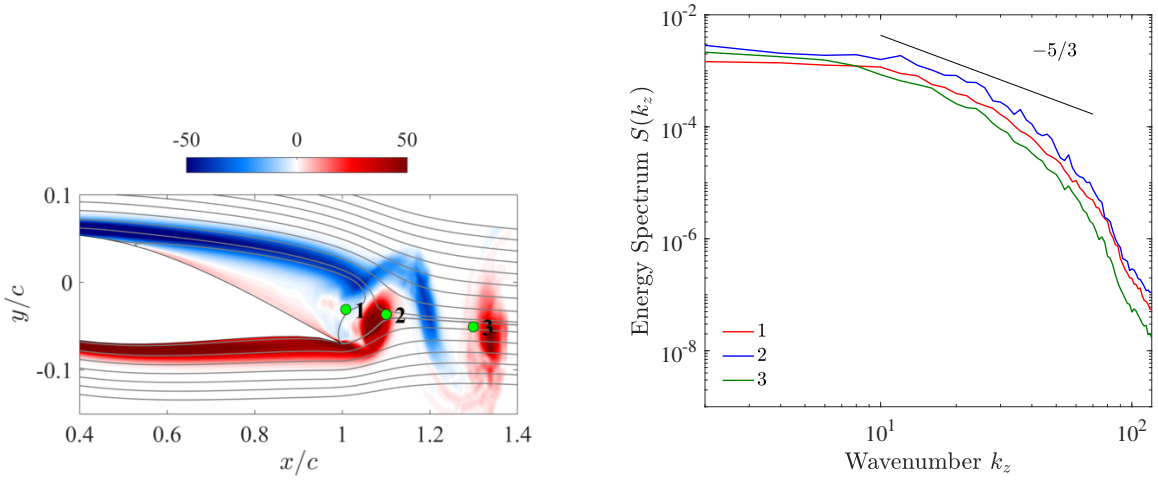

(a) Locations

(b) Spectra

Figure 5.39: (a) Spanwise-averaged vorticity at $t = 46.0$ and time-averaged streamlines. Green markers indicate probe locations for spanwise velocity spectra. Y-axis stretched. (b) Spanwise velocity spectra (power spectral density) at locations marked in (a). Spectra are averaged over 102 samples. AOA = 4°.

transition point at $x_t/c = 0.32$ and the reattachment point of the time-averaged flow at $x_r/c = 0.48$. This location is consistent with the bursting of the spanwise vortices (see figure 5.18d), local maxima in the skin friction (see figure 5.20a), and rapid increase of the spanwise velocity component (see figure 5.19b).

We evaluate the TKE production, transport, and dissipation in the vicinity of the reattachment point ($x_r/c = 0.48$) along wall-normal lines at 40% and 55% chord length in figure 5.40(b). The first line is within the LSB at a location of high reverse flow (see figure 5.24) and the second measurement is taken downstream of the reattachment point, such that the measurements are approximately symmetric around x_r. The change in the profiles of the TKE budget between the two locations is remarkable, as the prominent peak in the production term at $x/c = 0.4$ is reduced by 78% at the downstream location ($x/c = 0.55$). Accordingly, the balancing turbulent and velocity-pressure transport terms show similar decays in amplitude and only the

viscous diffusion and dissipation preserve their shape.

The profiles observed in figure 5.40(b) are in accordance with the data reported by Alam and Sandham [63] for a laminar separation bubble on a flat plate. Specifically, the measurements downstream of the LSB reattachment point show a nearly identical shape of the production, dissipation, turbulent transport, and viscous diffusion. Only the transport through the pressure-velocity gradient is considerably larger in the airfoil flow, with compressibility effects and the complex geometry of the wing being likely responsible for the deviation.

The dominant peak in the TKE production within the separation bubble is consistent with the finding that the LSB is subject an absolute instability and self-sustaining turbulence. The viscous diffusion and dissipation terms, while nearly zero for flow angles 0° and 4°, have high contributions of opposite sign close to the wall, but decrease rapidly outside the viscous sublayer. Besides the peak at the wall, the dissipation has a local maximum at a wall-normal distance of $\Delta\eta_{0.4c} = 0.016c$ and $\Delta\eta_{0.55c} = 0.014c$. Compared to the peak production in the shear layer, the magnitude of the local dissipation maxima accounts only to 23% ($x/c = 0.4$) and 76% ($x/c = 0.55$) of the production and is clearly balanced by the other transport terms.

We evaluate the velocity spectrum at four locations over the airfoil for the turbulent flow at 8° incidence. The first two probes are located at the transition point x_t and the reattachment point x_r respectively, while the other two locations are selected to lie downstream within the turbulent boundary layer ($x/c = 0.7$ and $x/c = 0.9$). All probes have a wall-normal distance of $\Delta\eta/c = 0.03$, such that the first points lies within the separated shear layer (see figure 5.41a). The velocity spectrum in figure 5.41(b) shows that the energy of the velocity fluctuations follows the -5/3 decay over a short frequency range for probe locations downstream of the transition point (location 1). The absence of an extended region with -5/3 slope is like related to

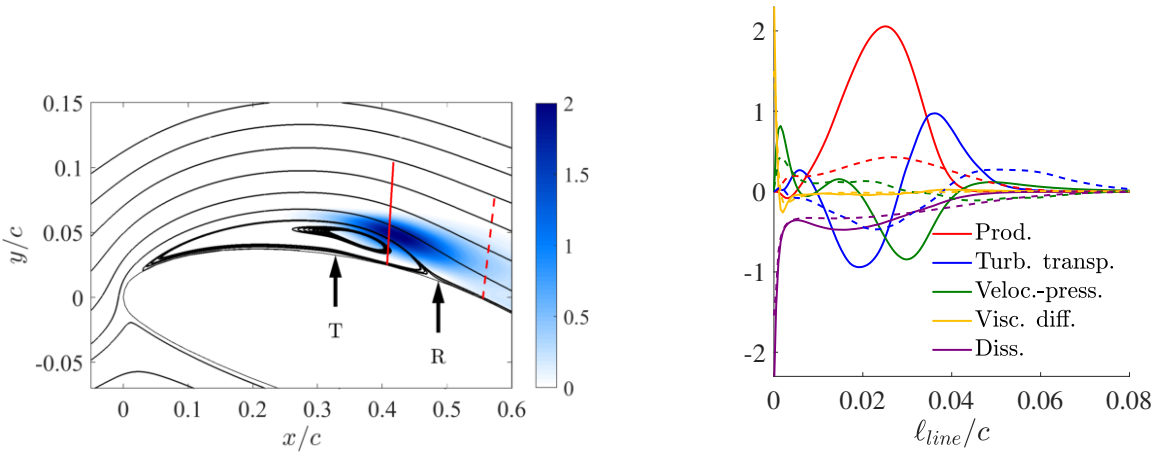

(a) TKE Production

(b) TKE budget

Figure 5.40: (a) Production of the TKE over the airfoil (Y-axis stretched). T and R indicate the mean locations of transition and reattachment. (b) TKE budgets plotted along the lines shown in (a). Solid line: $x/c = 0.4$, dashed line: $x/c = 0.55$. AOA = 8°.

the low Reynolds number of this airfoil flow. At location 4, the high-frequency content decays according to the -7 slope and matches the result for turbulent flow over a flat plate by Wu and Moin [106], thereby confirming that a fully turbulent boundary layer develops at the airfoil's trailing edge. At location 1 (transition point x_t), the energy contained in the velocity fluctuations is distinctly lower than at the downstream probes because the flow has only started to transition and involves fewer scales of motion. The spectrum, however, shows a distinct local peak at a wavenumber of $k_z = 18$, indicated by the dashed line in figure 5.41(b), that refers to a spanwise mode with 9 waves over the span and a wavelength $\lambda = 0.056c$ at the trailing edge of the laminar separation bubble. Figure 5.18(d) hints that this mode corresponds to the number of hairpin vortices that emerge from the breaking vortex roller at the reattachment point.

The characteristic energy decay within the turbulent boundary layer at the airfoil's trailing edge is confirmed by the analysis of the u-velocity component's time history and corresponding frequency spectrum in figure 5.42. The velocity is recorded

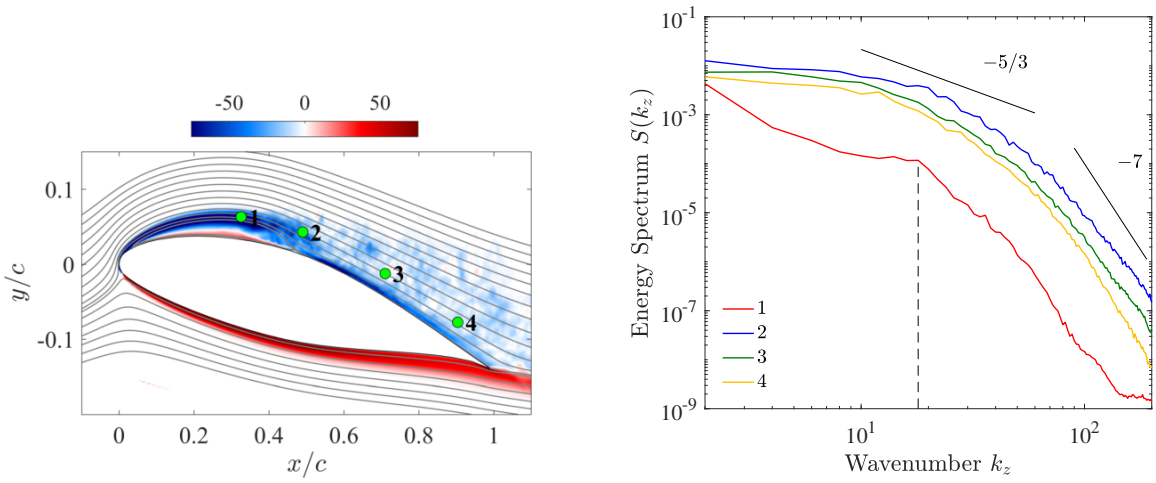

(a) Locations (b) Spectra

Figure 5.41: (a) Spanwise-averaged vorticity at $t = 35.9$ and time-averaged streamlines. Green markers indicate probe locations for spanwise velocity spectra. Y-axis stretched. (b) Spanwise velocity spectra (power spectral density) at locations marked in (a). Spectra are averaged over 69 samples. Dashed line indicates local peak at $k_z = 18$. AOA = 8°.

at $[x, y, z] = [0.85, -0.044, 0.25]$ (for a rotated coordinate system with horizontal inflow) and is close to location 4 plotted in figure 5.41(a). Similar to the spatial frequency spectrum at location 4, the temporal spectrum follows the -5/3 and -7 slopes, where the -5/3 decay is more pronounced than in the spatial analysis. Because the time-history is recorded at every time step, the temporal spectrum has a significantly higher resolution than the spatial analysis, which is based on samples extracted every one-tenth convective time units.

5.4 Summary of Results

The laminar separation and transition of the low-Reynolds number flow over a cambered NACA 65(1)-412 airfoil is analyzed for flow angles from 0° to 10° through a series of high-fidelity DNS and implicit LES. The NACA 65(1)-412 is designed to extend

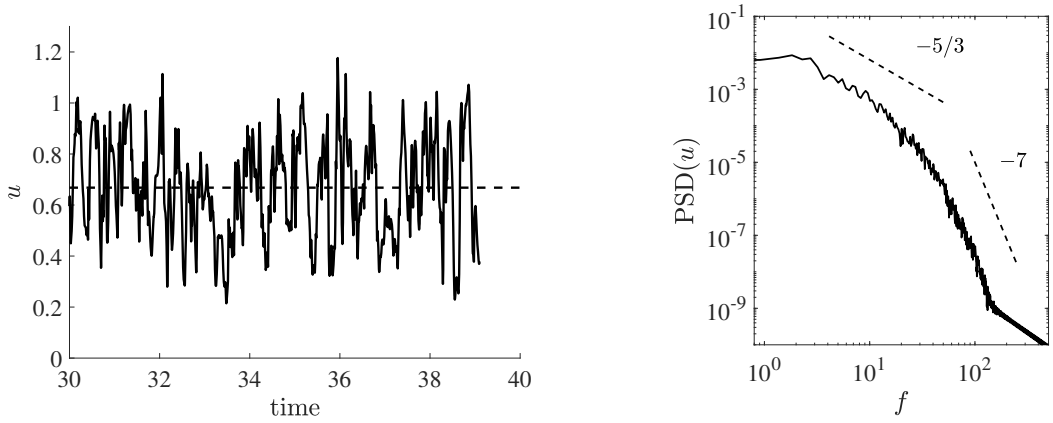

(a) $u(t)$ history

(b) Frequency spectrum of $u(t)$

Figure 5.42: (a) History of the u-velocity component at probe location $[x, y, z] = [0.85, -0.044, 0.25]$ and the mean indicated by the dashed line. (b) Power spectral density estimate of $u(t)$, where the dashed lines indicate -5/3 and -7 slopes. AOA = 8°.

the laminar flow regime under operating conditions and has its maximum thickness at $x/c = 0.4$. The flow topology, wake structure, aerodynamic forces, and statistics are shown to be governed by the transition location of the separated shear layer on the airfoil's suction side, which divides the flow into two regimes: at angles of attack smaller than 7°, the upper boundary layer separates around mid-chord and remains laminar until it interacts with the trailing edge vortex, which forms from the roll-up of the bottom-side boundary layer. For angles larger than 7°, the separation point moves to the leading edge of the airfoil and the shear layer transitions to turbulence and reattaches, resulting in a laminar separation bubble at the leading edge. The bifurcation of the flow is accompanied by a rapid increase of the aerodynamic lift and decrease of drag, which is attributed to the recovery of the free-stream pressure at the trailing edge. An intermediate state is shown to exist at 7° incidence, where a LSB forms at the rear side of the airfoil. Here, the flow reattachment occurs just upstream of the trailing edge ($0.92c$) such that the development of turbulent structures is not wall-bounded but shed off in large patches or "puffs".

It is further shown that the change in flow regimes over the airfoil directly affects the topology of the wake: at angles smaller than 7°, the vortices are shed in a fairly regular manner and form a distinct, narrow street in the wake. Transition of the laminar flow occurs after a few chord lengths behind the trailing edge where the street looses its coherence. At an angle of attack larger than 7°, the wake is highly irregular and governed by the turbulent structures that shed from the leading-edge LSB, resulting in a wide range of scales of motion. Remarkably, the intermediate state at 7° is characterized by fast spreading vortices that form in low-frequency vortex street. Although the shear layer becomes unstable shortly after mid-chord, the wall interaction of the generated vortices is limited in this case and they shed off in the form of turbulent clouds or "puffs" while retaining their coherence.

The results of the low-Reynolds number flow over an airfoil designed for laminar flow can be summarized as follows:

(i) At lower angles of attack, the flow separates shortly downstream of the airfoil's maximum thickness without reattaching and forms a transitional, narrow wake with a regular vortex street. The free-stream pressure is not recovered at the trailing edge resulting in losses of the lift force.

(ii) At higher angles of attack, the sharp leading edge induces flow separation and promotes the formation of a leading-edge separation bubble with subsequent wall-bounded turbulent flow. Flow reattachment results in the recovery of the ambient pressure at the trailing edge and therefore high lift forces. The airfoil is close to aerodynamic stall.

(iii) An intermediate state can exist if the boundary layer separates downstream of the leading edge but transitions upstream of the trailing edge. The result is a long and slender LSB that strongly reduces the form drag. The limited wall interaction

of the vortices results in large-scale turbulent patches that shed off the airfoil.

Because the NACA 65(1)-412 is designed to maximize the laminar flow region over the wing, the absence of an early transition to turbulence at low Reynolds number prevents the reattachment of the separated boundary layer on the airfoil's rear side at lower angles of attack and results in a significant loss of the lifting force, which is even negative at AOA = 0°. With the rapid increase in the lifting force upon bifurcation of the flow, the efficient operation of laminar airfoils in low-Reynolds number flow conditions can be challenging and difficult to predict. The use of active or passive flow controllers to induce transition early should therefore be considered in order to alleviate these drawbacks.

5.5 Acknowledgements

Chapter 5, in part, is currently being prepared for submission for publication of the material, B. F. Klose, G. R. Spedding and G. B. Jacobs. B. F. Klose: investigation, original draft preparation, visualization. G. R. Spedding: minor contributions to supervision, review & editing. G. B. Jacobs: supervision, review & editing.

Chapter 6

The Kinematics of Lagrangian Flow Separation in External Aerodynamics

6.1 Overview and Summary

In this chapter, we present a comprehensive kinematic study of Lagrangian flow separation in external aerodynamics by connecting FTLE dynamics, the asymptotic separation line and spike formation. Using direct numerical simulations of a circular cylinder flow and the flow over a cambered NACA 65(1)-412 airfoil, we show that while the motion of fluid particles in the vicinity of the no-slip wall is governed by the spike formation theory (Serra et al. [43]) over short times, and over long times by the asymptotic separation profile (Haller [36]), the off-wall kinematics are governed by long-term attracting LCSs in the flow field that can be extracted from ridges in the backward-time FTLE. We find that the shape of the Lagrangian backbone of separation attains strong bends along the boundary layer heights identified through momentum and displace-

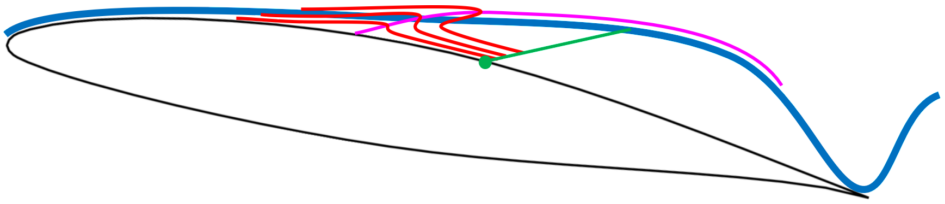

Figure 6.1: Schematic of the manifolds involved in Lagrangian flow separation: backward-time FTLE (blue), upwelling material lines (red) and associated Lagrangian backbone (magenta), linear separation profile and asymptotic separation point (green). Schematic is not to scale.

ment thickness. These boundary layers thickness approximations are based on kinetics arguments and typically involve a threshold value. The purely kinematic Lagrangian backbone of separation, in contrast, is threshold free and consistently distinguishes on- and off-wall regions characterized by different dynamics.

A schematic of the principal mechanisms of separation in steady or periodic flows with an asymptotic mean is presented in Figure 6.1. The attracting LCS, which is identified from the backward-time FTLE ridge (blue), attracts the upwelling fluid material (red) from the wall. This ridge does not intersect with the wall, but rather develops along the separated shear layer. The Lagrangian backbone of separation (magenta) is the theoretical centerpiece of the spike and intersects the boundary at the so-called spiking point. Attracted by the hyperbolic LCS, the backbone then aligns with the FTLE ridge once the Lagrangian fluid tracers have left the vicinity of the wall. Downstream of the spiking point, the asymptotic separation profile (green) is anchored at the location of averaged zero skin friction and oriented in the direction of particle break-away.

We further identify the wall signature of upwelling material lines, i.e. the spiking point [43], from Lagrangian quantities and, for the first time, from high-order wall-based velocity derivatives. By matching the spiking points extracted from the Lagrangian curvature change of material lines and Eulerian on-wall velocity derivatives of

the circular cylinder, we verify the criterion proposed by Serra et al. [43]. The cylinder case benefits from an analytically known boundary with constant curvature. To extend the test to a non-analytic wall representations, the flow around the airfoil with a cubic-spline based boundary is analyzed. Although the material lines show the formation of a single spike at mid-cord characterized by a severe curvature change, very weak curvature ridges occur upstream of the asymptotic location of separation. The higher-order on-wall derivatives reflect these ridges and show their relation to the piece-wise linear curvature of the wall. Applying a filter with a kernel based on the distance between supporting points of the spline, we recover the spiking point of the principal separation event from the on-wall velocity derivatives and match the wall intersection of the Lagrangian backbone of separation. The robustness of this method to local oscillations or noise is an important result that will benefit future applications, given that many engineering applications rely on surface representations through splines.

We further show that singular points, such as the stagnation point at the leading edge, must be excluded from the analysis of material spike formation, as they can induce fluid upwelling without separation. Barring this limitation, the material spike formation provides wall-based and short-term information that remains hidden in the backward-time FTLE and the asymptotic separation profile. The new information about the material spike adds a valuable piece to the picture of Lagrangian flow separation and is a promising tool in the design of flow controllers.

The governing equations and the numerical model are defined in Chapter 2 and 3. In Section 6.2 we outline the setup of our computations and the results are discussed in the subsequent part. A summary and conclusion is given in Section 6.4.

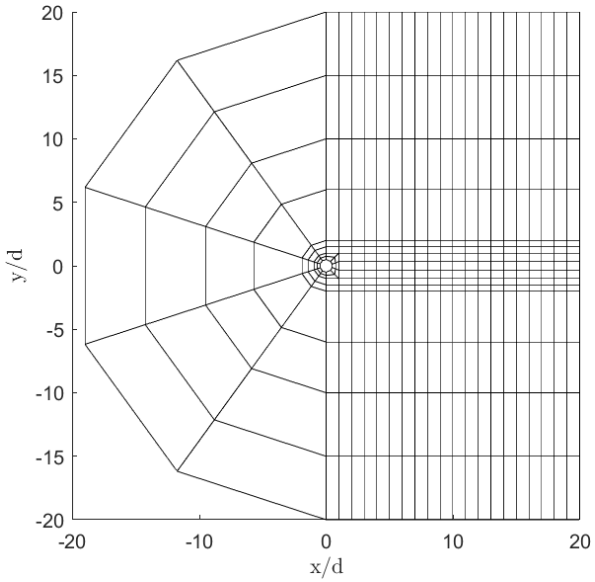

Figure 6.2: 2D computational domain for circular cylinder.

6.2 Problem Setup

The canonical circular cylinder flow is computed at a Reynolds number of $Re_d = 100$ based on a cylinder diameter of unity and Mach number of 0.1, rendering compressibility effects negligible. The computational domain is divided into 347 quadrilateral elements and the solution is approximated with a 16^{th} order polynomial. This accounts to a total of 100,283 collocation points. At the outer boundaries, a free stream condition is applied while the cylinder is approximated with curved element faces and an adiabatic no-slip wall. A Riemann solver is used to sort out the characteristic relations at the boundaries [107, 81]. 402,201 Lagrangian particles are initialized in 201 wall-parallel lines around the cylinder with a spacing of $\Delta/d = 0.001$ between each line.

The flow over a NACA 65(1)-412 airfoil is simulated at a Reynolds number based on the chord length of $Re_c = 20,000$ and a Mach number of $M = 0.3$. The Mach number is relatively low ensuring a nominally incompressible flow, but it is high

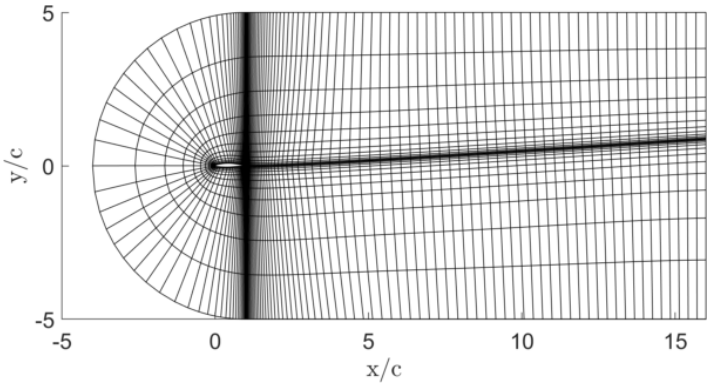

Figure 6.3: 2D computational domain for NACA 65(1)-412. Only elements without interior Gauss-Lobatto nodes are shown.

enough to prevent stability issues pertaining to the explicit time integration we use. The computational domain is given in Figure 6.3 and consists of 2,256 quadrilateral elements, with the dimensions of the domain being adopted from Nelson et al. [76], who show that the solution is not significantly affected by the domain size. Boundary conditions at outer edges of the computational domain are specified as free-stream boundaries while the airfoil surface is treated as a non-slip, adiabatic wall. The wall-boundary elements are curved and fitted to a spline representing the airfoil's surface according to Nelson et al. [76]. Again, the characteristic relations at the boundaries are sorted out by using a Riemann solver. The solution vector is approximated with a 16^{th} order polynomial, giving a total of 651,984 collocation points in the domain. 1,005,201 Lagrangian particles are initialized in 201 wall-parallel lines around the airfoil with a spacing of $\Delta/c = 0.0002$ between each line.

In both simulations, Lagrangian particles are tracked by spectrally interpolating the velocity field for each particle and numerically integrating $\dot{\mathbf{x}}(\mathbf{x}, t) = \mathbf{v}(\mathbf{x}(t), t)$ using a 3^{rd} order Adam-Bashfort scheme. The *gslib* library is used for efficient particle tracking and velocity interpolation, as described by Mittal et al. [108]. Once the Lagrangian curvature change field (Eq. 2.15) is calculated, a basic smoothing operation

is performed to filter out numerical noise.

The wall-normal derivatives in Table 2.1 are computed within the DGSEM solver. With Equations 2.18 and 2.20, the quantities $\hat{v}_\eta$ and $\hat{v}_{\eta\eta}$ can be spectrally computed in each element using the operators available in the DGSEM framework and subsequently projected onto the wall using Lagrange interpolating polynomials. The derivatives in wall-tangential direction can either be computed within the DGSEM solver or as part of the post-processing work. Given the sensitive nature to numerical noise of second and higher derivatives, a smoothing filter is applied to the DNS output data as a post-processing step.

6.3 Results and Discussion

6.3.1 Cylinder Flow

To study the kinematics of flow separation, we consider a cylinder flow at $Re_d = 100$. Ridges in the FTLE field show a flow pattern that is well-known to be dominated by a pair of counter-rotating vortices alternately shedding in a regular manner from the top and bottom of the cylinder with a period of approximately six convective time units [92, 109]. A snapshot of the backward-time FTLE (Figure 6.4) reveals the long-term attracting LCSs in the wake, which highlight the edges of the advected vortices. Although this LCS is associated with separation (see Mohseni et al. [110]) and with early vortex formation and shedding [109], the FTLE ridge cannot intersect with the cylinder wall but rather envelopes the body. This is a direct consequence of the no-slip condition at the wall and non-hyperbolicity, as was explained in the introduction. The exact on-wall origin of separation can hence not be identified solely based on a strain-based FTLE field. A more rigorous analysis of the near-wall flow field is required. To this end, we first determine the asymptotic separation point and line

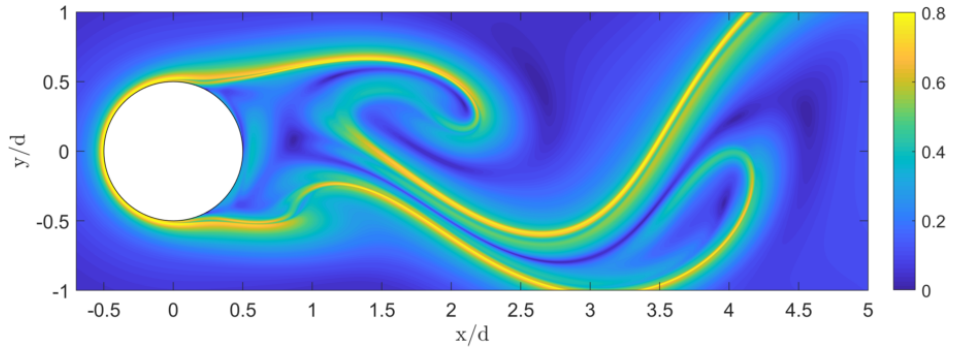

Figure 6.4: Backward-time FTLE from integration over one vortex shedding period.

[36] and then compute the Lagrangian curvature change $\bar{\kappa}_{t_0}^{t_0+T}$ and associated spiking dynamics. Later, we will relate the material spiking and the FTLE.

The averaged zero-skin-friction point is determined according to Eq. 2.13 with the temporal mean of the skin friction coefficient over one vortex shedding period. It is located at $x/d = 0.23$, approximately half way between center and the rear end of the cylinder. The angle of the separation line with respect to the tangent of the cylinder surface at the separation point is determined with Eq. 2.14. It oscillates periodically between 34° and 57°. We use the angle and separation point to create a linear approximation of the unstable manifold to which fluid particles that eject from the wall are asymptotically attracted.

The near-wall dynamics are visualized in Figure 6.5, where color-coded fluid tracers, the linear separation profile and instantaneous streamlines are plotted for different integration times, T. Particles up- and downstream of the line undergo an initial upwelling (spiking) and are drawn towards the unstable manifold.

To identify the onset of flow separation, i.e. the origin of material spiking, we extract a backbone from the evolution of the material lines through ridges in the corresponding advected curvature field $\bar{\kappa}_{t_0}^{t_0+T}$. We plot the curvature field for integration times of $T = [0.1,\ 0.4,\ 0.7,\ 1.0]$, and $t_0 = 0$ in Figure 6.6. Note that

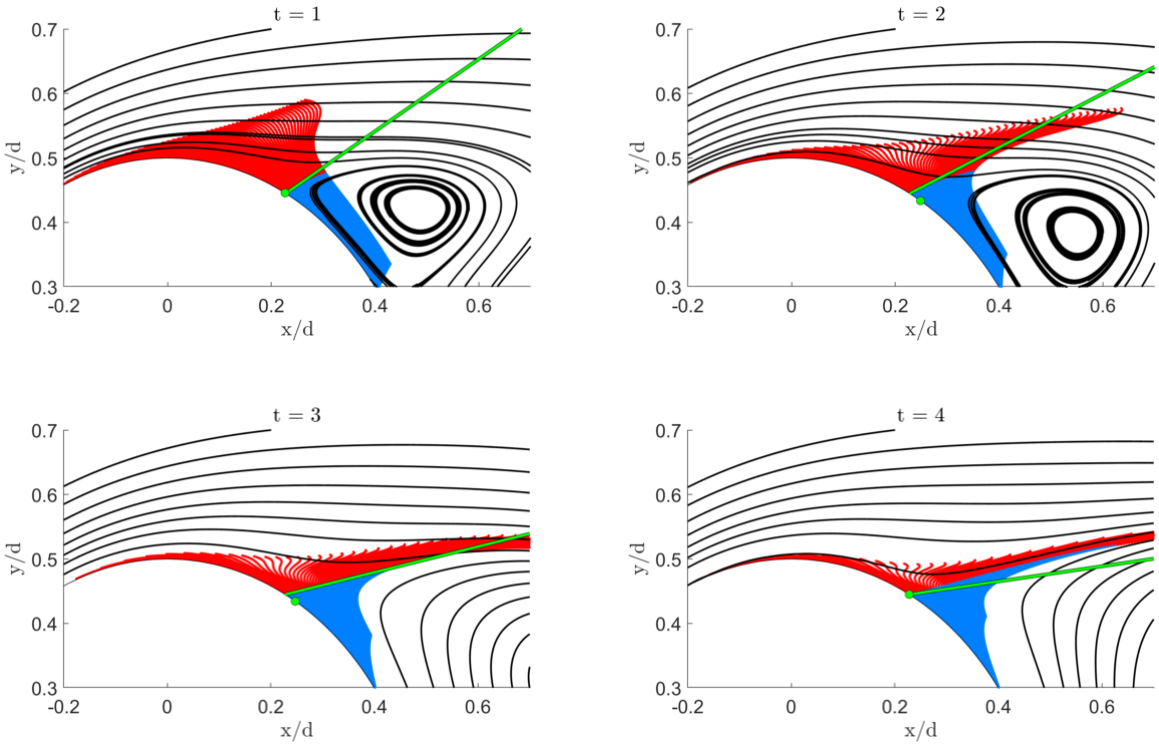

Figure 6.5: Snapshots of color coded particles advected over a circular cylinder near the separation point. Particles are divided in an upstream (red) and downstream (blue) group by the linear approximation of the separation line (green). Also visualized are the instantaneous zero-skin-friction point (green dot) and streamlines (black).

we first compute $\bar{\kappa}_{t_0}^{t_0+T}$, which is a scalar field based at t_0, and then advect it with $\mathbf{\Phi}_{t_0}^{t_0+T}$. The latter operation reflects the material property of lines and the backbone, $\mathcal{B}(t_0+T) := \mathbf{\Phi}_{t_0}^{t_0+T}(\mathcal{B}(t_0))$. The backbone, $\mathcal{B}(t)$, shown in magenta. For reference, we also plot the instantaneous zero-skin-friction point and the linear approximation of the separation profile in green.

The evolution of material lines in Figure 6.6 show that the backbone profile $\mathcal{B}(t)$ is correctly placed along the local spikes of material lines and intersects with the wall shortly upstream of the center of the cylinder. The separated fluid tracers then follow the direction of the linearly approximated separation profile. While the asymptotic separation profile provides information about the long-term behavior of separating fluid tracers, the initial material spike formation remains hidden and can only be extracted from analysis of the curvature scalar field.

The curvature change field $\bar{\kappa}_{t_0}^{t_0+T}$ for integration time intervals of $T = 0.4$ and 1.0 in Figure 6.7 reveal a total number of four Lagrangian backbones. Two originate from the top and the bottom of the cylinder and evolve along a dominant, growing ridge in the curvature field driven by the separation of the boundary layer. The two other backbones are located within the recirculation region in the separated cylinder wake. They are based on much weaker curvature ridges and we therefore deem them of secondary interest in the onset of separation.

Spiking phenomenon and FTLE

The spike formation, which occurs over short time, is hidden to the FTLE field [43]. For longer integration times, however, the material spike, governed by off-wall dynamics, converge to the attracting backward-time FTLE ridge (Fig. 6.1). For the cylinder case, we visualize the spatial relation between the backbone, material lines and the backward-time FTLE field at different time instances in Figure 6.8. In this

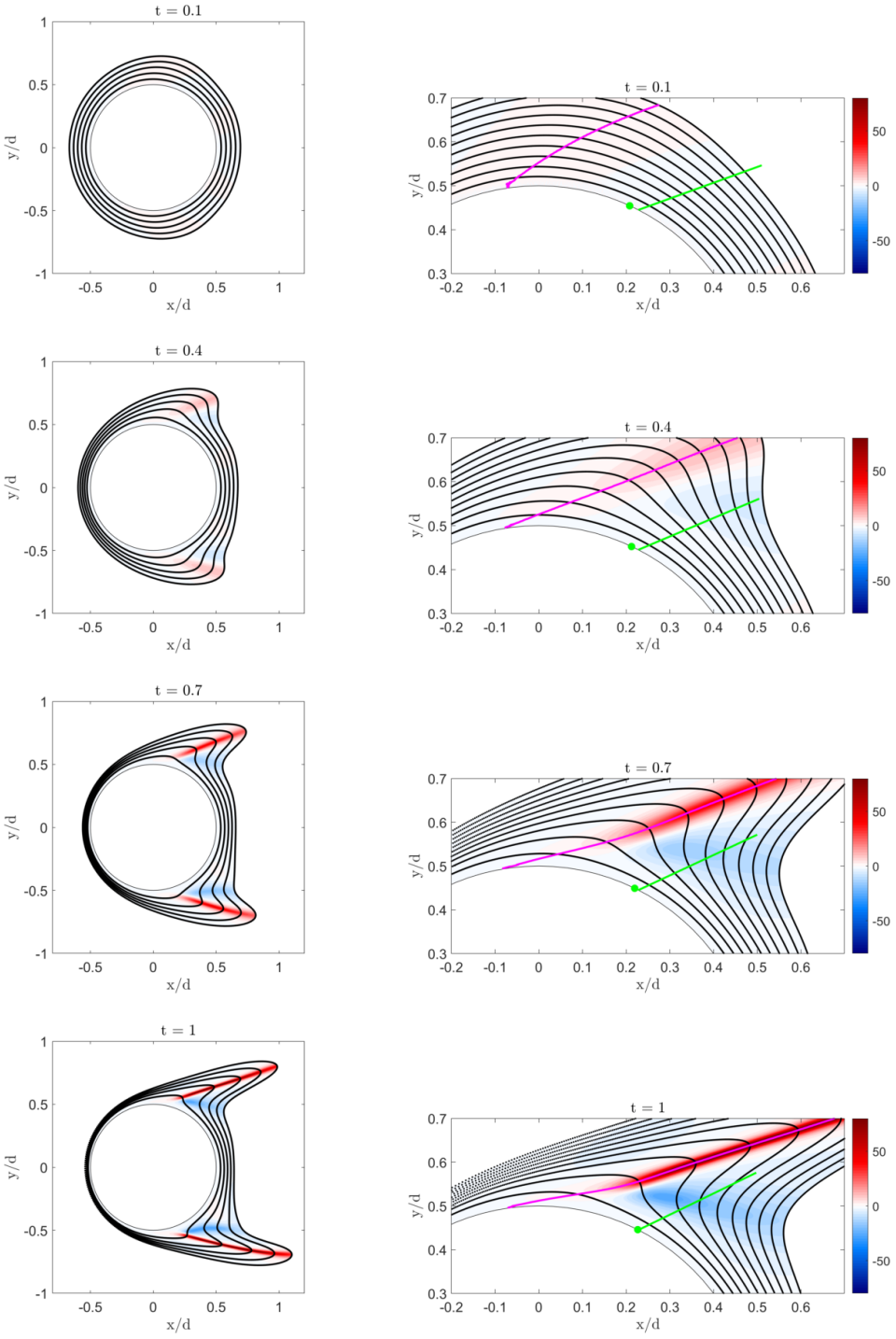

Figure 6.6: Advection of material lines and the curvature field $\bar{\kappa}^t_{t_0}$, $t = t_0 + T$ around a cylinder for different integration times. The backbone $\mathcal{B}(t)$ is highlighted in magenta. Linear separation line and zero-skin-friction point in green.

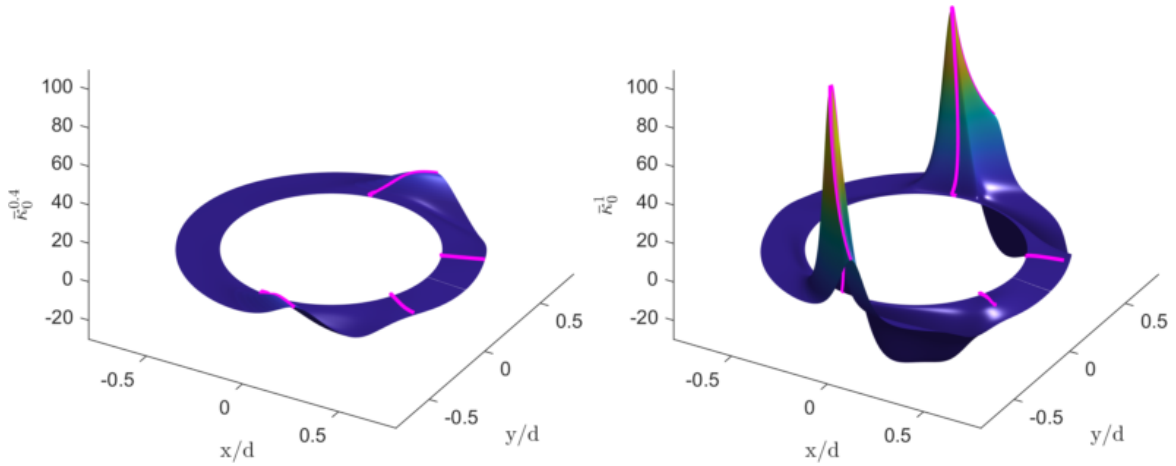

Figure 6.7: Surface plot of the curvature scalar fields $\bar{\kappa}_0^{0.4}$ and $\bar{\kappa}_0^1$. Backbone of separation in magenta.

figure, a time interval of one vortex shedding period, $T = 6$, is used to compute the FTLE field. Material lines and the backbone are advected from $t = 0$ to $t = 1$, 2, 3, and 4 (black).

Initially, the fluid tracers undergo an upward motion in transverse direction to the cylinder and the backbone along the material spike crosses the FTLE ridge ($t = 1$). As the integration time increases, however, the material lines bend downwards ($t = 2$) and gradually align with the unstable manifold for $t \geq 3$. The long-term manifold identified through the backward-time FTLE ridge attracts the separating fluid material and gradually aligns with the material backbone. The trace of the separated fluid in the wake follows the same pattern and shows long-term sharp spikes along dominant FTLE ridges, as illustrated in Figure 6.9.

The above results highlight that the Lagrangian backbones of separation and the FTLE provide critical complementary structures in the analysis of Lagrangian flow separation. While the initial motion through upwelling of fluid material can only be determined through the analysis of the curvature change field [43], the long-term off-wall dynamics are governed by the FTLE. A combination of both methodologies

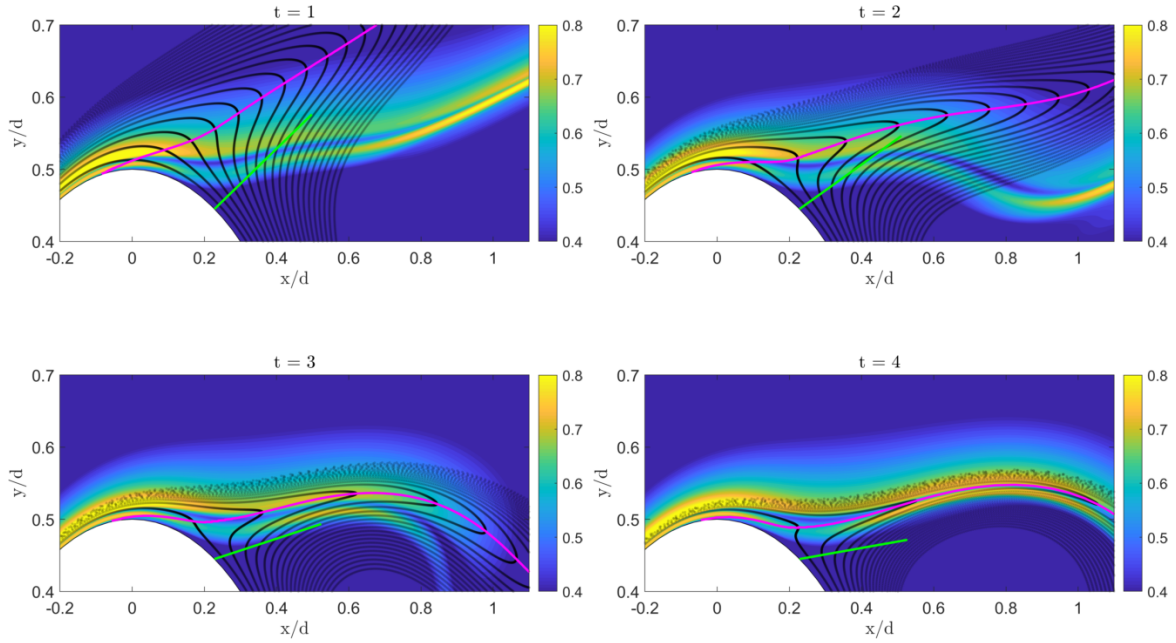

Figure 6.8: Backward-time FTLE field (contour plot) computed from t to $t - T$ over $T = 6$. Advected material lines from 0 to t in black and the Lagrangian backbone of separation in magenta. Asymptotic separation profile in green. Y-axis stretched.

therefore, together with the asymptotic separation line, gives a complete picture of the kinematics of separation (see Figure 6.1).

Extraction of Spiking Points

The spiking points, s_p, are the wall signatures of material upwelling and can either be identified from the intersection of a wall-transverse curvature change ridge with the boundary (Eq. (2.17)) or from on-wall Eulerian derivatives of the wall-normal velocity (Table 2.1). Here, we extract s_p using the criterion for incompressible flows, since the flow with a free-stream Mach number of $M = 0.1$ is nearly incompressible.

From the condition specified in Table 2.1, the spiking points are located at minima of the integrated derivatives of the normal velocity in normal and tangential direction, $\int_{t_0}^{t_0+T} \partial_{\eta\eta ss}\hat{v}dt$. We plot this function in Figure 6.10 (a) for the upper half of

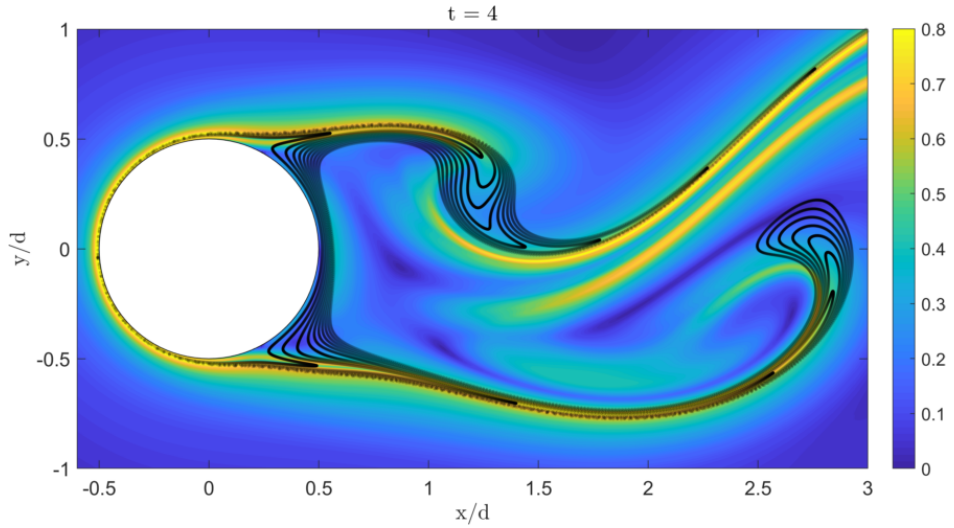

Figure 6.9: Backward-time FTLE and material lines in the wake.

the cylinder and an interval of $T = 1$. The resulting spiking points are indicated with red circles. Figure 6.10 (b) shows the curvature change field $\bar{\kappa}_0^1$ and the Lagrangian backbones of separation $\mathcal{B}(t_0)$ in magenta. The spiking points identified from the normal velocity derivatives are plotted as red dots at the boundary and match exactly with the intersection of the backbones and the wall. Through the agreement of the spiking points determined from Eulerian on-wall quantities and the alternative Lagrangian definition (Eq. (2.17)), here, we verify the theory by Serra et al. [43] *for the first time*, i.e. we confirm the theory that material upwelling in the Lagrangian frame can be captured also by using wall-based Eulerian quantities only.

Figure 6.11 shows the curvature change field, based at the initial time, on the upper side of the cylinder for increasing integration times, together with the Lagrangian spiking points from on-wall quantities (red), backbones of separation (magenta), and boundary layer approximations based on the momentum and displacement thickness in grey and black respectively. These plots are based on the same particle trace that is used in the previous Figures 6.6, 6.7, and 6.10 (b). The Lagrangian spiking point s_p

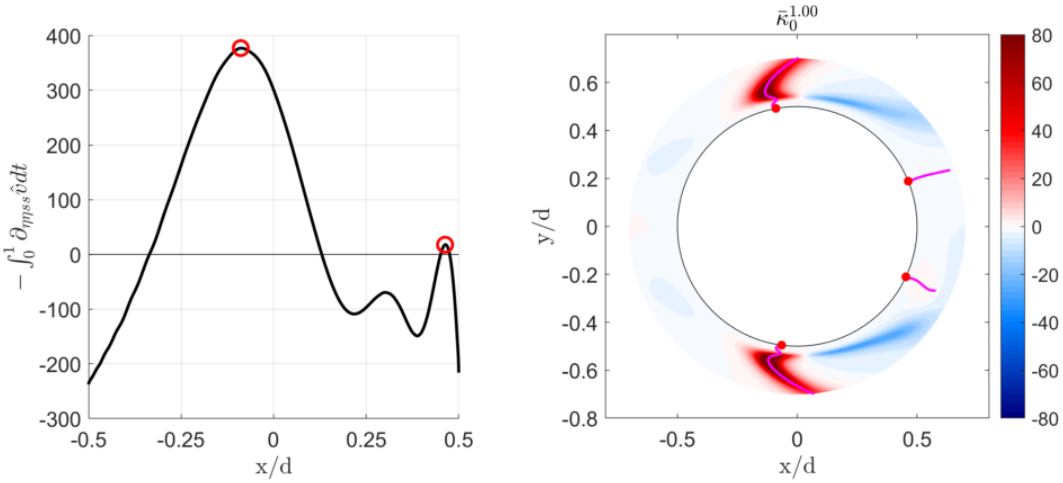

(a) (b)

Figure 6.10: (a) $-\int_0^1 \partial_{\eta\eta ss}\hat{v}dt$ with spiking points in red. (b) Curvature change field $\bar{\kappa}_0^1$ with backbones (magenta) and Lagrangian spiking points (red) identified from Eulerian on-wall quantities.

is located at x/d = -0.09, which places it far upstream of the asymptotic separation point ($x/d = 0.23$) and, remarkably, even upstream from the cylinder center.

We find that there is a strong correlation between the curvature change field and the boundary layer scaling thicknesses, such as the displacement thickness and momentum loss thickness [3]. Figure 6.11 shows that, as the integration time increases, ridges of $\bar{\kappa}_{t_0}^{t_0+T}$ form and develop a peak at the intersection with the displacement thickness (black line). Within the momentum thickness layer (grey line), the curvature of the ridge abruptly decreases. The dependence of the backbone of separation on the displacement and momentum thickness is a remarkable result, as boundary layer thicknesses follow kinetic arguments and typically involve thresholds parameters. Inflection of the backbone of separation, in contrast, despite being threshold free and purely kinematic, accurately separate on- and off-wall regions characterized by different dynamics. We are currently exploring this correlation in material and plan to report on this in the near future.

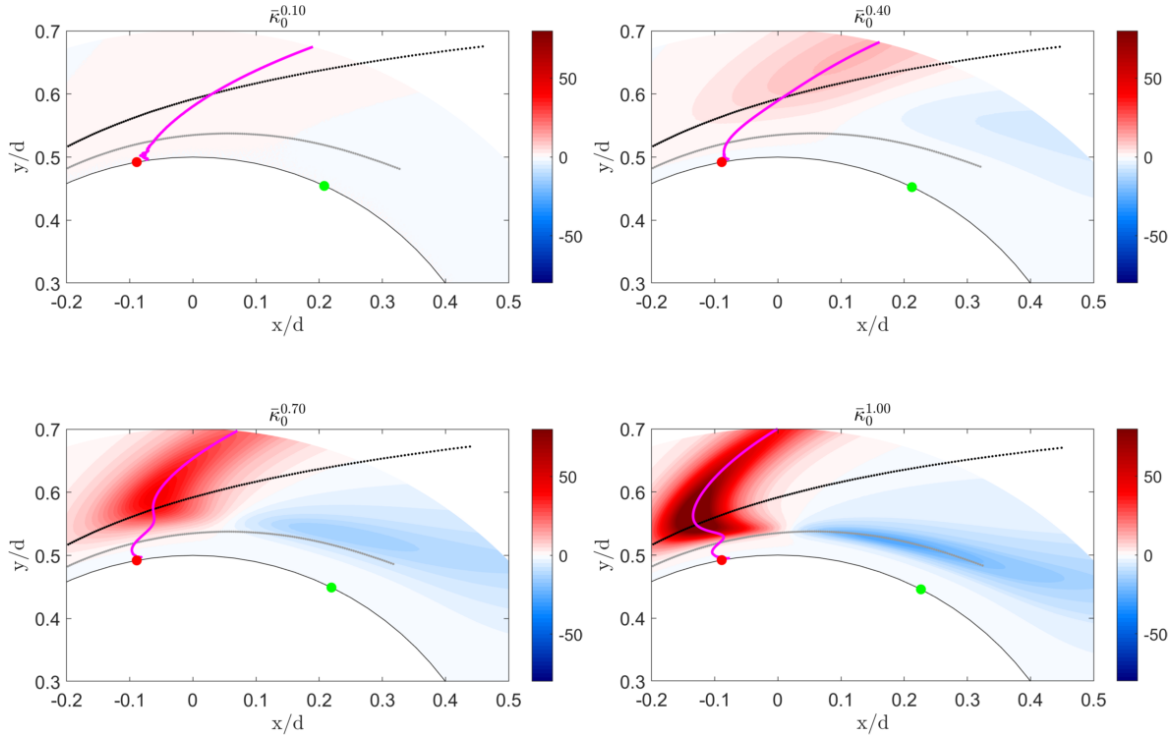

Figure 6.11: Lagrangian curvature change field with the corresponding backbone of separation (magenta) and Lagrangian spiking points (red) identified from Eulerian on-wall quantities for different integration times. Zero-skin-friction point in green, boundary layer displacement thickness in black and momentum thickness in grey.

We note that even though the curvature change ridge develops a 'nose' and moves upstream with increasing integration time, the backbone $\mathcal{B}(t_0)$ maintains its original on-wall signature and intersects the wall at the spiking points identified by the criteria in Table 2.1.

6.3.2 Airfoil Flow

For a more complex and encompassing external aerodynamics test case, we study the kinematics of flow separation on a cambered NACA 65(1)-412 airfoil at a chord-based Reynolds number of $Re_c = 20,000$ and 4° angle of attack. The low Reynolds airfoil flow is characterized by boundary layer separation at mid-cord, a

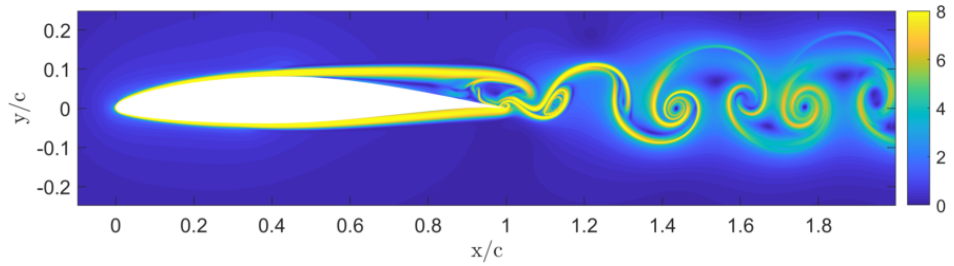

Figure 6.12: Backward-time FTLE from integration over one vortex shedding period.

recirculation region downstream of the separation location and a Von-Karmann-type vortex shedding in the wake, resulting in a time-periodic flow pattern with a period of $T = 0.36$ convective time units.

A snapshot of the backward-time FTLE (Figure 6.12) visualizes the separated shear layer and the edges of the shedded and advected vortices.

The asymptotic separation point is computing using the mean over one vortex shedding period, and is located at the averaged zero-skin-friction point at $x/c = 0.50$, i.e. exactly at mid-cord, slightly behind the maximum thickness location of the airfoil ($x/c = 0.4$). This is in accordance with the result reported in Nelson et al. [76] and Kamphuis et al. [111]. The angle of the separation line with respect to the tangent of the airfoil surface periodically oscillates between 7.05° and 7.5°. These near-wall dynamics are summarized in Figure 6.13, where color-coded fluid tracers, the asymptotic separation profile and instantaneous streamlines are plotted for different integration times. Similar to the cylinder flow, the particles upstream of the asymptotic separation point undergo an upwelling motion and form a sharp spike that will be later guided by an attracting LCS in the flow.

The advected curvature change field at the final time, together with a set of material lines, is shown in Figure 6.14 for different integration times. Multiple spikes emerge on the suction side of the airfoil: a dominant ridge evolves along the separating

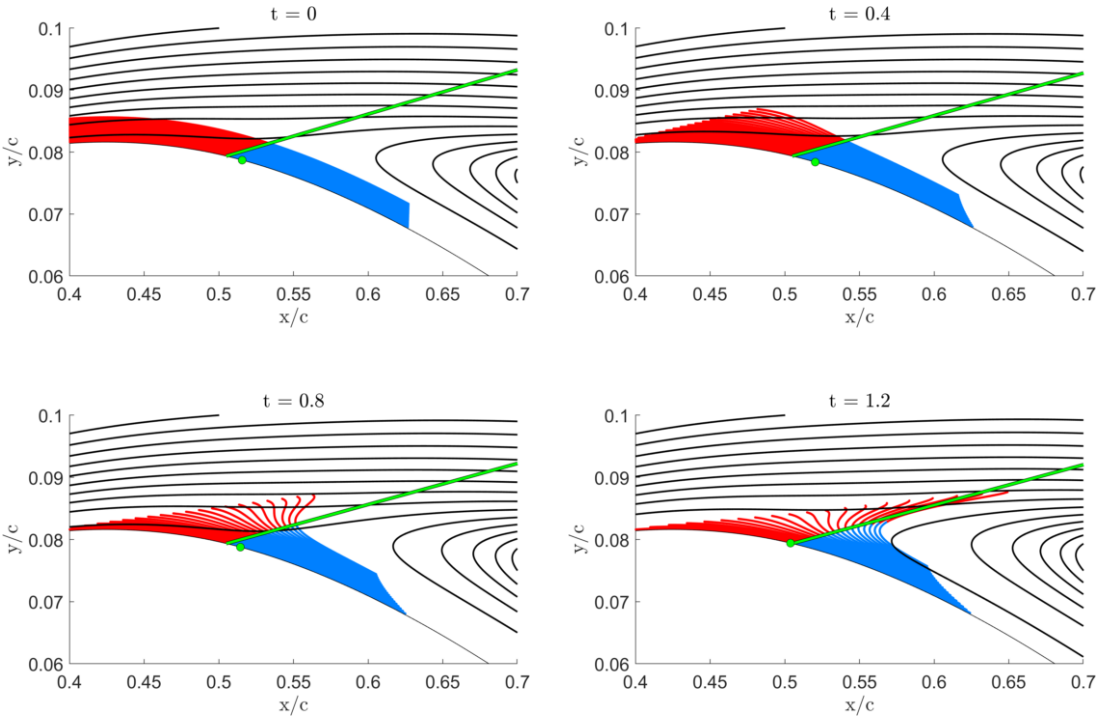

Figure 6.13: Snapshots of particles advected over the airfoil near the asymptotic separation point. Particles are divided by the asymptotic linear separation line (green) in an upstream (red) and downstream (blue) grouped. Also visualized the instantaneous zero-skin-friction point (green dot) and streamlines (black).

shear layer and several smaller spikes appear within the separated recirculation region. On the pressure (bottom) side, the flow remains attached and the fluid tracers are advected without breaking away from the boundary until the trailing edge is reached. Given that global separation occurs only on the suction side of the airfoil, we focus our analysis on the upper section of the profile. A magnified view of the curvature scalar field introduced in Figure 6.14, together with the backbone of separation $\mathcal{B}(t)$ and the asymptotic separation profile is given in Figure 6.15. Note that the y-axis is stretched to aid visibility of subtle features.

The backbone emerging at mid-cord is based on the upwelling of separating material lines in the vicinity of the asymptotic separation line and intersects the no-slip wall at $s_p/c = 0.46$. This location is slightly upstream of the asymptotic separation point at $x/c = 0.5$. Additional curvature ridges are detected within the separated recirculation region, but, given that the boundary layer has already separated, are of little interest for determining the start of Lagrangian flow separation.

Spiking phenomenon and FTLE

The relation between the Lagrangian backbone of separation, material lines, and the backward-time FTLE field is illustrated in Figure 6.16 at different snapshots in time. To determine the backward-time FTLE field, again, we use an integration time interval equal to one vortex shedding period ($T = 0.36$). Material lines (black) and backbones (magenta) are advected forward in time from $t = 0$ to $t = 0.05$, 0.1, 0.2, 0.3, 0.4, and 0.5.

Similar to our findings for the cylinder flow, the material spike starts from the no-slip wall, crossing the FTLE ridge at short time scales. As the integration time increases, the material spike, along with the backbone of separation, aligns to the attracting FTLE ridge, which again governs the off-wall dynamics of the separated

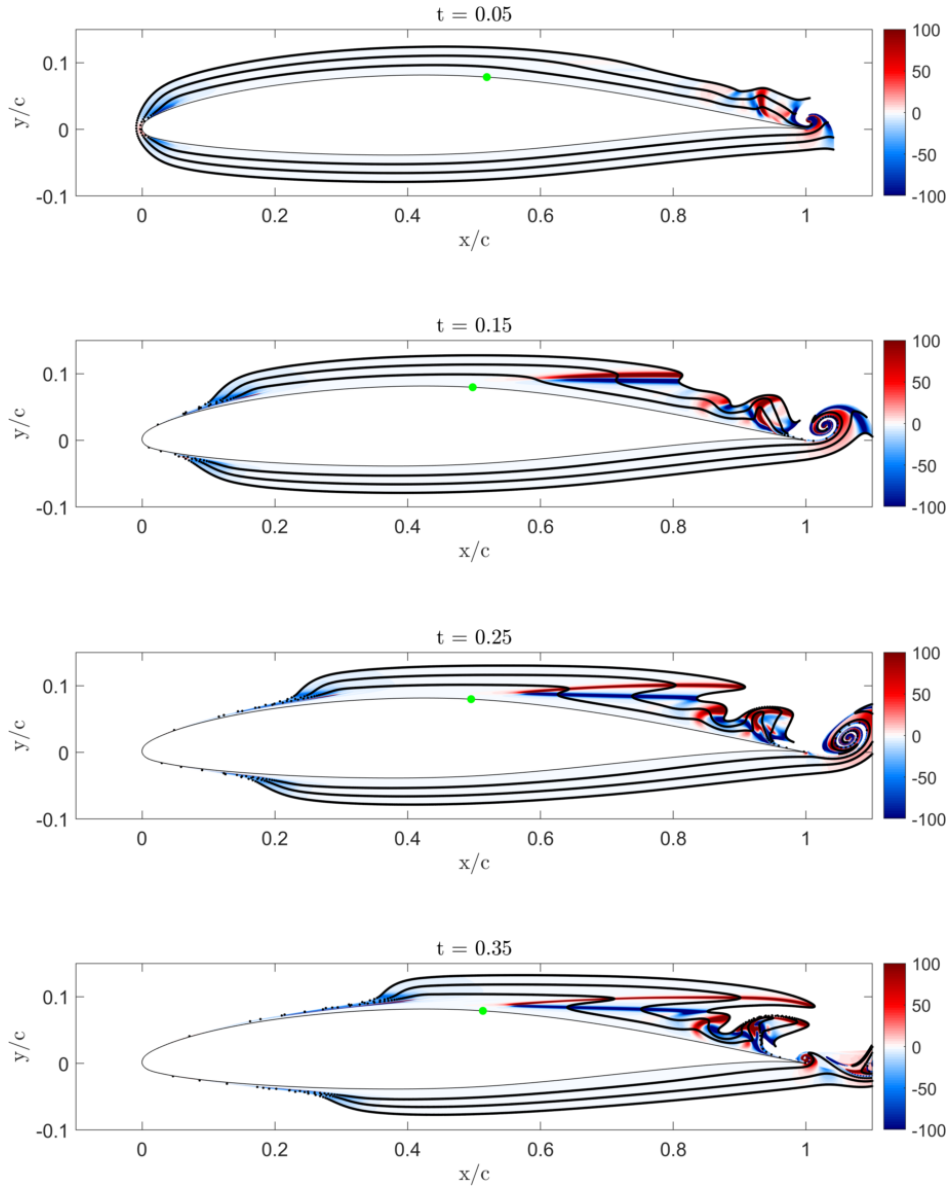

Figure 6.14: Advection of material lines and the curvature field $\bar{\kappa}_{t_0}^{t_0+T}$ around the airfoil for different integration times. Zero-skin-friction point in green.

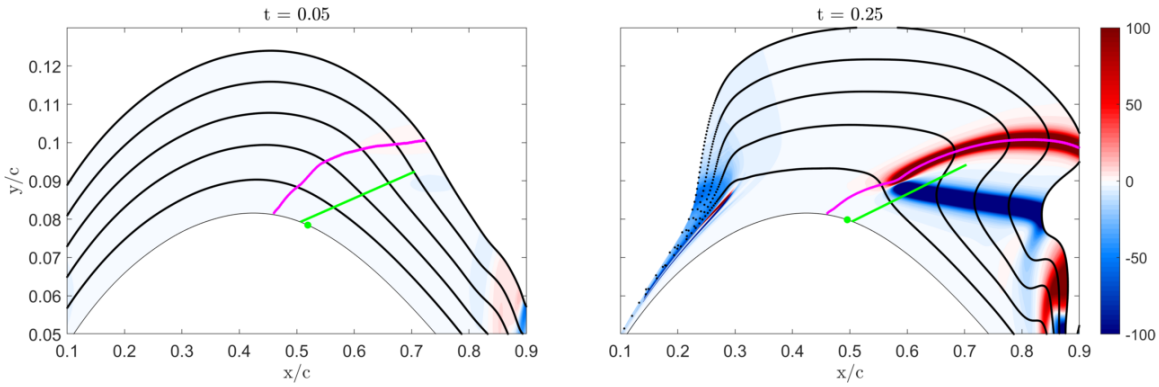

Figure 6.15: Advected curvature scalar field with material lines (black) and the Lagrangian backbone of separation $\mathcal{B}(t)$ (magenta). Zero-skin-friction point and linear separation line in green. Y-axis stretched.

fluid tracers. The separation picture is then completed by the asymptotic separation line (green) and its connection to backward-time FTLE ridge (see Figure 6.16).

Extraction of Spiking Points

We extract the spiking points of the separating airfoil flow from both their Lagrangian and wall-based Eulerian definitions. The curvature change field $\bar{\kappa}_{t_0}^{t_0+T}$ is given in Figure 6.17 for three different integration intervals in x and η coordinates, where η is the wall-normal distance. Besides the large ridges at mid-cord and at $x/c \approx 0.75$, a weak waviness in the curvature field exists upstream of the asymptotic separation point ($x/c = 0.5$). This oscillatory pattern is recovered in the Eulerian wall derivative $\int_0^{0.25} \partial_{\eta\eta ss}\hat{v}dt$, shown on left of Figure 6.18.

According to the conditions specified in Table 2.1, spiking points are located at local maxima of the function $-\int_{t_0}^{t_0+T} \partial_{\eta\eta ss}\hat{v}dt$, which identifies three locations upstream of the separation point in Figure 6.18 (a). Weak curvature ridges are present at these locations that we found are not contributing to material spiking and fluid break away in the context of flow separation. The oscillatory curvature field and associated ridges correlate directly with the piece-wise linear curvature κ_0 of the airfoil surface represen-

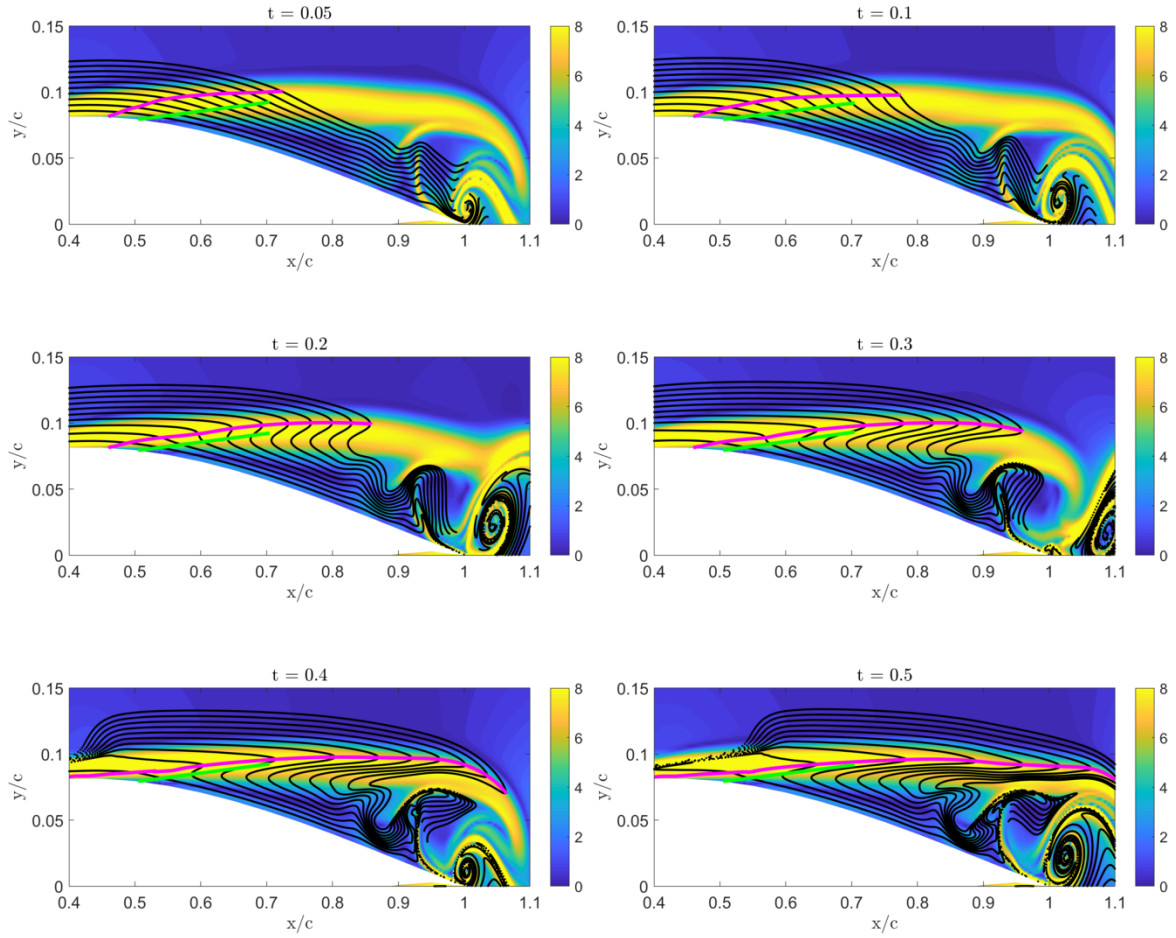

Figure 6.16: Backward-time FTLE field (contour plot) computed from t to $t - T$ over $T = 0.36$. Advected material lines from 0 to t in black and the Lagrangian backbone of separation in magenta. Asymptotic separation profile in green. Y-axis stretched.

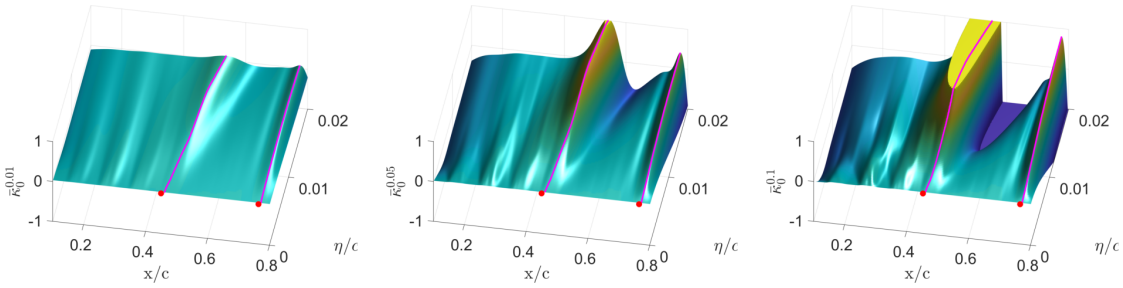

Figure 6.17: Surface plot of the curvature scalar field $\bar{\kappa}_{t_0}^{t_0+T}$ for $T = 0.01$, 0.05, and 0.10. Wall-normal coordinate on y-axis. Backbone in magenta, spiking point in red.

tation (dashed line) that is inherent to the cubic spline boundary representation used for the design of the airfoil. The three ridges are hence a geometric artifact and should not be interpreted as significant spiking events.

We can reduce the oscillatory trend from the spline parametrization by filtering the function $\int_{t_0}^{t_0+T} \partial_{\eta\eta ss}\hat{v}dt$ with a kernel width based on the approximate distance between two spline segments. The filtered solution (red line) successfully recovers the underlying correct function and identifies a single spiking point at $x/c = 0.45$ (red circle) upstream of the separation point.

Figure 6.18 (b) shows the curvature scalar field $\bar{\kappa}_0^{0.25}$ at t_0 in x and y coordinates with the ridge highlighted in magenta and the spiking point from Eulerian on-wall quantities in red. With the close match of the backbone-wall intersection at $x/c = 0.46$ and the Eulerian criterion at $x/c = 0.45$, we demonstrate that the spiking point can be extracted from on-wall based quantities even with approximate parametrization of the boundary, as used in engineering applications.

In Figure 6.14 and 6.15, we show that the global separation of fluid particles traces back to the formation of an initial material spike at mid-cord, shortly upstream of the asymptotic separation point. For larger integration time intervals, however, an additional curvature ridge with an origin at the leading edge is detected (see Figure

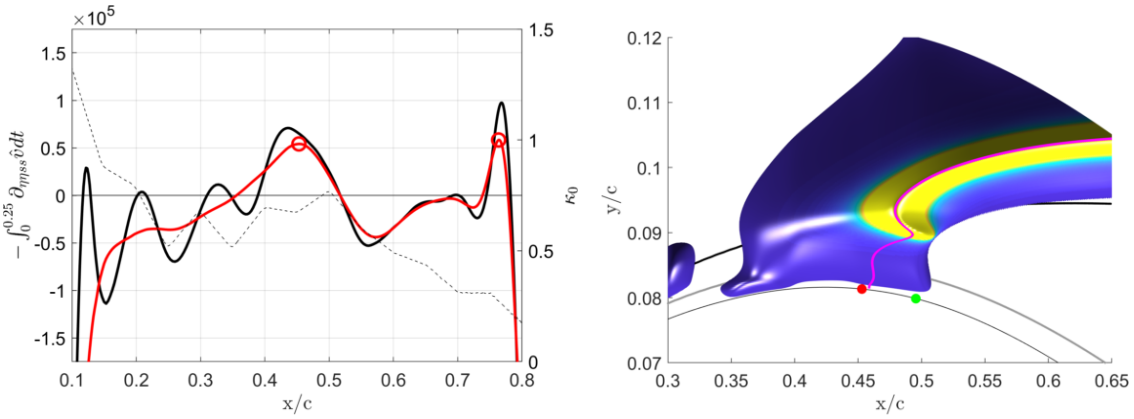

(a) (b)

Figure 6.18: (a) $-\int_0^{0.25}\partial_{\eta\eta ss}\hat{v}dt$ in black. Filtered results and Spiking points in red. Surface curvature κ_0 as dashed line. (b) Curvature change field $log(\bar{\kappa}_0^{0.25})$ at $\mathbf{x}_0$ with backbone (magenta) and Lagrangian spiking point (red) identified from Eulerian on-wall quantities. Displacement thickness in black and momentum thickness in grey. Zero-skin-friction point in green.

6.15). This sharp spike in the material line occurs only in the vicinity of the wall and has no direct connection to the global separation event at mid-cord. Of course, when the leading edge ridge advects to the location of the asymptotic separation manifold, the particles do follow this manifold.

Figure 6.19 shows the advection of a Lagrangian particle sheet at the leading edge to visualize the Lagrangian flow behavior at the stagnation point in more detail: the local contraction of the streamlines forces the fluid to accelerate and the particles closer to the leading edge are initialized on streamlines with higher velocity, leading to upwelling and folding of the material line. Consequently, the spike is rather the result of the displacement of streamlines by the growing boundary layer and the associated normal velocity, than an event associated with separating flow. We conclude that the leading edge spike formation is an artifact from the stagnation point flow and is not an indication of flow separation in this case. A more detailed analysis of this phenomenon will be subject to future studies.

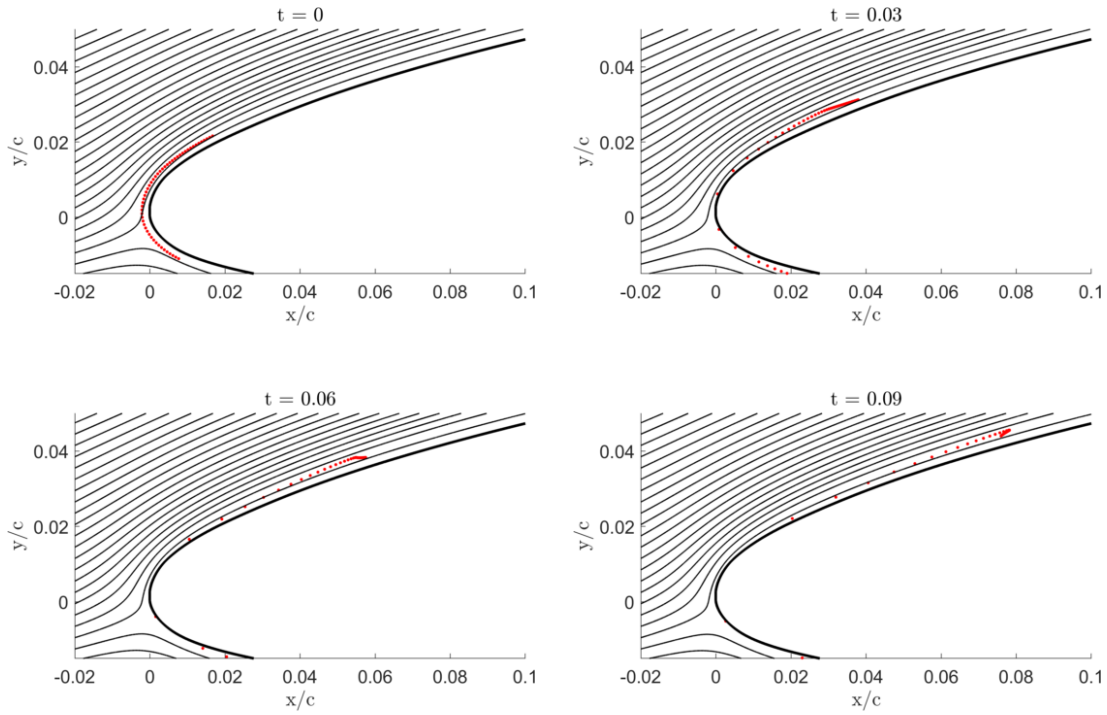

Figure 6.19: Advection of a set of particles at the leading edge. Streamlines shown in black.

6.4 Summary of Results

Kinematic aspects of flow separation have been investigated in external aerodynamics by extracting the initial motion of upwelling fluid material from the wall and its relation to the long-term attracting manifolds in the flow field. Although the wall-bounded kinematics are governed by the formation of a material spike upstream of the asymptotic separation point and ejection of particles in direction of the separation line, it was shown that the off-wall trajectories of the fluid tracers are driven by attracting ridges in the finite-time Lyapunov exponents. Therefore, the complete pathway of Lagrangian flow separation was obtained: from the initial upwelling at the spiking point over the ejection of particles along the asymptotic separation profile to the attracting LCSs.

For the flow around a circular cylinder and a cambered NACA 65(1)-412 airfoil,

the footprint of the initial material upwelling, i.e. the spiking point, was determined by evaluating the curvature of Lagrangian fluid tracers and by extracting high-order on-wall derivatives of the normal velocity as proposed in [43]. An exact match of the Lagrangian and Eulerian criterion for the start of material line spiking verifies the Eulerian criterion and associated the principal location of material upwelling for the first time in two test cases, i.e., the cylinder flow and the flow over an airfoil. For the latter, the spiking point was recovered by appropriately filtering the spurious oscillations in the velocity derivative induced by the spline-based boundary parametrization of the NACA profile, thereby showing that this method is robust to noise. Determining the spiking points requires the extraction of high-order velocity derivatives, which is challenging for general geometries and in experimental settings because it requires very high-resolution data and an accurate representation of the geometry.

With the ability to compute the birth of separation instantaneously from Eulerian on-wall data, the Lagrangian pathway from the spiking point to the asymptotic separation profile can be used as input parameters for dynamic flow controllers.

6.5 Acknowledgements

Sections 6.2 through 6.4, in full, are a reprint of the material as it appears in "Kinematics of Lagrangian Flow Separation in External Aerodynamics", B. F. Klose, M. Serra and G. B. Jacobs, *AIAA Journal*, 2020. B. F. Klose: investigation, visualization, original draft preparation. M. Serra: support with theory and curvature routines, editing. G. B. Jacobs: supervision, review & editing.

Chapter 7

Objective early identification of kinematic instabilities in shear flows

7.1 Overview and Summary

In this chapter, we present an objective diagnostic for the early identification of instabilities based on the maxima in finite-time changes of the curvature of material lines. The maxima are precursors of significant wrinkling of material lines as illustrated for a shear flow in figure 7.1(a–d): a line of Lagrangian fluid tracers initialized along an unstable shear layer undergoes an oscillatory motion induced by an underlying velocity mode and rolls up along the forming vortices as the flow develops. Strong bending locations of material lines point to potential break-up locations of the laminar flow field. These can be visualized and identified through curvature changes. Figure 7.1 also illustrates that the instability definition as a *non-wall-bounded wrinkling* is distinct from the theory of the backbone of separation [43]. While the latter is based on material curvature also, the separation theory considers a *wall-bounded* flow and, moreover, it identifies a *one-sided, upwelling* instead of wrinkling of the material line.

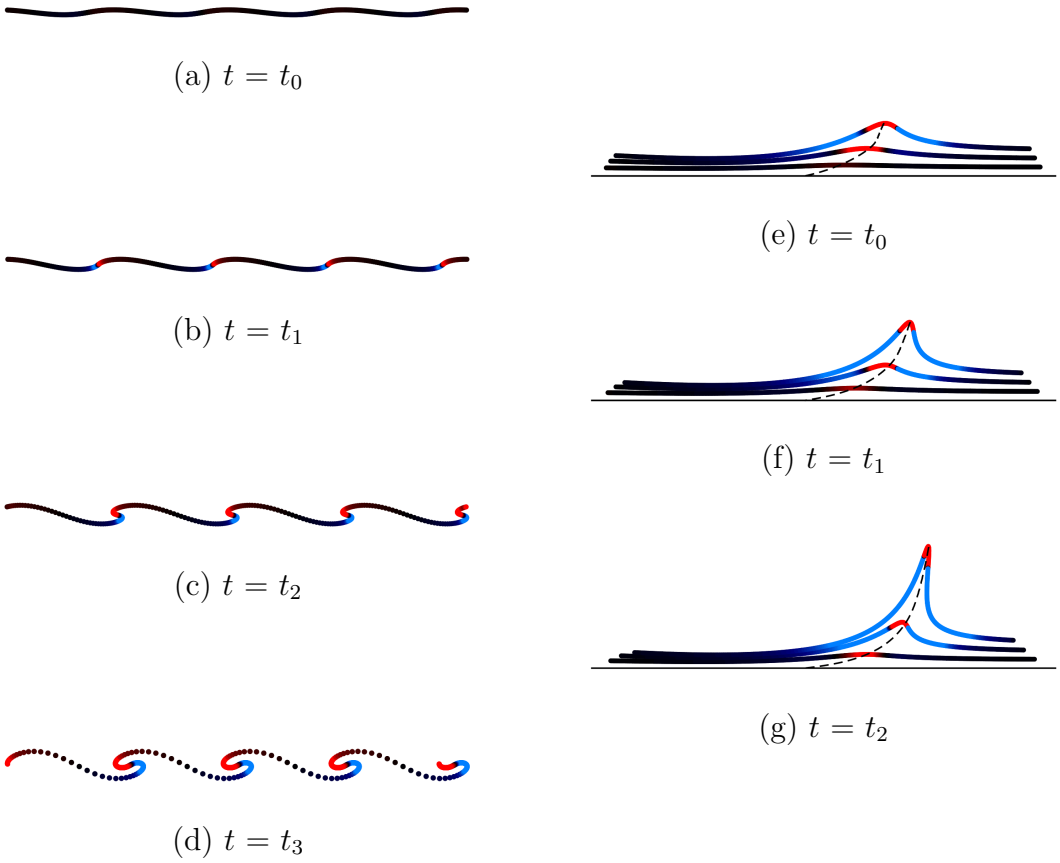

Figure 7.1: Temporal development of a material line in an unstable shear layer (a – d). Time development of material lines and backbone of separation (dashed) in a separated flow in the vicinity of a no-slip wall (e – g) . Coloring by material line curvature from blue (negative) to red (positive).

The kinematic instability identification approach does not rely on assumptions or knowledge of the averaged solution of the flow, as the diagnostic only depends on the kinematics of the material lines. The finite-time approach has practical benefits since in experiments only limited data are available. In addition to being objective, the finite-time integration of Lagrangian particles can prove beneficial in the detection of intermittent instabilities, such as turbulent burst in a sub-critical Poiseuille flow, which will leave a footprint in the Lagrangian deformations even if the flow relaminarizes. More generally, our approach can capture non-normal growths [53], an essential trigger for nonlinear behavior, which remain hidden to LSA.

We first provide analytic formulas connecting characteristic quantities used in LSA of perturbed shear flow with the induced flow map and Lagrangian curvature change. Then, we illustrate and verify the performance of the Lagrangian instability identifier on three two-dimensional Navier-Stokes flows. In a temporally developing jet flow, it is shown that maximum curvature growth rates recover the linear growth rates of several unstable modes as predicted by LSA theory. The unsteady, separated flow over a cambered airfoil at a moderate Reynolds number of 20,000 shows that the curvature modes capture instability in the separated shear layer promptly over finite time without knowledge of a mean or base flow. Finally, the approach is shown to identify instabilities in a flow without a mean during the onset of wake instability in the growing wake behind a circular cylinder at low Reynolds number. In the following sections, the governing equations and the numerical setup of the three cases are presented first (Section 7.2). Then, the results are discussed in Section 7.3. Conclusions are reserved for Section 7.4.

7.2 Methodology and Setup

7.2.1 The curvature scalar

Following Serra et al. [43], we consider a smooth material curve $\gamma \in \mathbb{R}^2$, parametrized at t_0 in the form $\mathbf{r}(s)$, $s \in [s_1, s_2] \subset \mathbb{R}$, and denote its local tangent vector by $\mathbf{r}'(s)$ and curvature scalar by $\kappa_0(s) = \frac{\langle \mathbf{r}''(s), \mathbf{R}\mathbf{r}'(s) \rangle}{\sqrt{\langle \mathbf{r}'(s), \mathbf{r}'(s) \rangle}^3}$ (see figure 7.2). The curvature change (or folding) $\bar{\kappa}_{t_0}^{t_0+T} := \kappa_{t_0}^{t_0+T}$ - κ_0 of γ under the action of $\mathbf{\Phi}_{t_0}^{t}$ can then be computed as

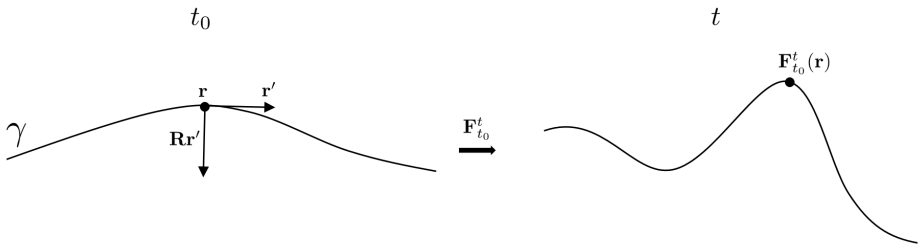

Figure 7.2: Sketch of a material line γ parametrized at t_0 in the form $\mathbf{r}(s)$, $s \in [s_1, s_2] \subset \mathbb{R}$, transported and deformed by the flow map $\mathbf{\Phi}^t_{t_0}$. At any point $\mathbf{r}(s)$, the Lagrangian folding $\bar{\kappa}^{t_0+T}_{t_0} = \kappa^{t_0+T}_{t_0}$ - κ_0 of γ can be computed from equation (7.1).

$$\bar{\kappa}^{t_0+T}_{t_0} = \frac{\left\langle \left(\nabla^2 \mathbf{\Phi}^{t_0+T}_{t_0}(\mathbf{r})\mathbf{r}'\right)\mathbf{r}', \mathbf{R}\nabla\mathbf{\Phi}^{t_0+T}_{t_0}(\mathbf{r})\mathbf{r}'\right\rangle}{\left\langle \mathbf{r}', \mathbf{C}^{t_0+T}_{t_0}(\mathbf{r})\mathbf{r}'\right\rangle^{3/2}} + \kappa_0 \left[\frac{\det\left(\nabla\mathbf{\Phi}^{t_0+T}_{t_0}(\mathbf{r})\right)\left\langle \mathbf{r}', \mathbf{r}'\right\rangle^{3/2}}{\left\langle \mathbf{r}', \mathbf{C}^{t_0+T}_{t_0}(\mathbf{r})\mathbf{r}'\right\rangle^{3/2}} - 1\right], \tag{7.1}$$

where $\langle\cdot,\cdot\rangle$ denotes the inner product; $(\nabla^2\mathbf{\Phi}^t_{t_0}(\mathbf{r})\mathbf{r}')_{ij} = \sum_{k=1}^{2} \partial_{jk}\Phi^t_{t_0 i}(\mathbf{r})r'_k,\ i,j \in \{1,2\}$, $\mathbf{R}$ is a clockwise ninety-degree rotation matrix defined as

$$\mathbf{R} := \begin{bmatrix} 0 & 1 \\ -1 & 0 \end{bmatrix}, \tag{7.2}$$

and $\mathbf{C}^t_{t_0} = [\nabla\mathbf{\Phi}^t_{t_0}]^\top \nabla\mathbf{\Phi}^t_{t_0}$ is the right Cauchy-Green strain tensor. Equation 7.1 shows that the Lagrangian folding depends on spatial inhomogeneities of $\mathbf{\Phi}^t_{t_0}$, the curve stretching encoded by $\mathbf{C}^t_{t_0}$, the initial curvature and the compressibility of the flow described by $\det\left(\nabla\mathbf{\Phi}^t_{t_0}\right)$. See Serra et al. [43] for a more detailed description.

7.2.2 Linear stability analysis

Instabilities in shear flows are commonly analyzed by the growth of a perturbation to a base flow. The incompressible flow field described by u, v, and p is decomposed into a base with a perturbation as $u = U + u'$, $v = V + v'$, and $p = P + p'$, which

is then substituted into the Navier-Stokes equations. Assuming small, exponentially growing perturbations of the form

$$[u', v', p'] = \mathrm{Re}\left([\hat{u}(y), \hat{v}(y), \hat{p}(y)]e^{i(kx-\omega t)}\right), \tag{7.3}$$

the governing equations can be linearized and solved as an eigenvalue problem (see Drazin and Reid [47] for details). In (7.3), the quantities $\hat{u}(y)$, $\hat{v}(y)$, and $\hat{p}(y)$ are the complex amplitudes of the perturbations and k and ω are the real wavenumber and complex frequency. For the analysis of a temporal developing flow, we consider temporal growth governed by the imaginary part ω_i of the complex frequency. An eigenvalue solver determines the frequencies ω_i and corresponding eigenmodes $\hat{u}$, $\hat{v}$, and $\hat{p}$ for a given wavenumber k.

7.2.3 Lagrangian Curvature growth

A theoretical connection between linear stability analysis and the curvature analysis can be made for material lines initialized along the x-axis such that $\mathbf{r}' = [1, 0]^\top$. For these lines, the material time derivative of $\bar{\kappa}_{t_0}^{t_0+T}$ relates to the lateral velocity as $\dot{\kappa}_{t_0} = -\partial_{xx}v$ as proven in appendix B.1. Decomposition of v into a base flow V and fluctuating component v' yields $\dot{\kappa}_{t_0} = -(\partial_{xx}v' + \partial_{xx}V)$. With the base flow $V = 0$ for the planar jet flow, the y-velocity component is $v = v' = \hat{v}(y)e^{ikx-i\omega t}$ and substitution results in

$$\dot{\kappa}_t = -\partial_{xx}v' = -\hat{v}(y)\partial_{xx}e^{ikx-i\omega t} = k^2\hat{v}(y)e^{ikx-i\omega t} = k^2v', \tag{7.4}$$

showing that the rate-of-change of κ scales with v' by the square of the wavenumber. This connection, however, is valid only instantaneously and hence lacks the memory trace, or Lagrangian history, of fluid flows.

To understand how perturbations of a base flow in the infinite-dimensional space leave a footprint on the physical phase space of fluid particles, we derive an analytic

expression relating the Eulerian growth rate and wavenumber of the perturbation and the induced Lagrangian folding of fluid. We focus our analysis on general parallel shear flows perturbed with small perturbations of the form $\mathbf{u}_\epsilon = \mathbf{u_0} + \epsilon\mathbf{u}'$, $0 < \epsilon \ll 1$, where $\mathbf{u_0} = [U(y), 0]^\top$ is the base flow and $\mathbf{u}' = \mathrm{Re}([\hat{u}(y), \hat{v}(y)]e^{i(kx-\omega t)})$ the perturbation . Because there are no analytic flow maps $\mathbf{\Phi}_\epsilon$ induced by $\mathbf{u}_\epsilon$, we first find an analytical approximation of $\mathbf{\Phi}_\epsilon$ neglecting $\mathcal{O}(\epsilon^2)$ terms. We then use the approximated $\mathbf{\Phi}_\epsilon$ and equation (7.1) to compute an analytical expression of the Lagrangian curvature change for initially straight material lines. Using the formulas derived in appendix B.2, we obtain the following result.

Theorem 1 *Consider a planar parallel shear flow of the form* $\mathbf{u}_\epsilon = \mathbf{u_0} + \epsilon\mathbf{u}'$, $0 < \epsilon \ll 1$, *where* $\mathbf{u_0} = [U(y), 0]^\top$ *is the base flow and* $\epsilon\mathbf{u}' = \epsilon\,\mathrm{Re}([\hat{u}(y), \hat{v}(y)]^\top e^{i(kx-\omega t)})$ *the perturbation. The flow map* ${}_\epsilon\mathbf{\Phi}_{t_0}^{t_0+T}(\mathbf{x_0})$ *induced by* $\mathbf{u}_\epsilon$ *admits an analytic solution at leading order, of the form*

$$ {}_\epsilon\mathbf{\Phi}_{t_0}^{t_0+T}(\mathbf{x_0}) = {}_\mathbf{0}\mathbf{\Phi}_{t_0}^{t_0+T}(\mathbf{x_0}) + \mathbf{A}_{t_0}^{t_0+T}(\mathbf{x_0})\epsilon + \mathcal{O}(\epsilon^2), \tag{7.5} $$

where $\mathbf{A}_{t_0}^{t_0+T}(\mathbf{x_0})$ *satisfies the following initial value problem*

$$ \begin{cases} \dot{\overline{\mathbf{A}_{t_0}^t}}(\mathbf{x_0}) = \nabla\mathbf{u_0}({}_\mathbf{0}\mathbf{\Phi}_{t_0}^t(\mathbf{x_0}))\mathbf{A}_{t_0}^t(\mathbf{x_0}) + \mathbf{u}'({}_\mathbf{0}\mathbf{\Phi}_{t_0}^t(\mathbf{x_0}), t) \\ \mathbf{A}_{t_0}^{t_0}(\mathbf{x_0}) = \mathbf{0} \\ {}_\mathbf{0}\mathbf{\Phi}_{t_0}^t(\mathbf{x_0}) = \mathbf{x_0} + \mathbf{u_0}(\mathbf{x_0})(t - t_0). \end{cases} \tag{7.6} $$

We provide the explicit formula for ${}_\epsilon\mathbf{\Phi}_{t_0}^{t_0+T}(\mathbf{x_0})$ *in equation* (B.19).

The curvature change induced by $\mathbf{u}_\epsilon$ *during* $[t_0, t_0 + T]$ *on an initially straight* ($\kappa_0 = 0$) *material line located at* $\mathbf{x_0} = [x_0, y_0]^\top$ *and aligned with the stream-wise direc-*

tion $\mathbf{r}' = [1, 0]^\top$*, can be computed as*

$$\begin{aligned}\bar{\kappa}_{t_0}^{t_0+T}(\mathbf{x_0}) = \frac{k^2}{\omega_i^2 + \omega_r^2 - 2\omega_r k U(y_0) + k^2 U^2(y_0)} \Bigg[\\ e^{\omega_i t_0} \Big(\Big(-\omega_i \hat{v}_r(y_0) + (\omega_r - kU(y_0))\hat{v}_i(y_0) \Big) \cos(kx_0 - \omega_r t_0) \\ + \Big(\omega_i \hat{v}_i(y_0) + (\omega_r - kU(y_0))\hat{v}_r(y_0) \Big) \sin(kx_0 - \omega_r t_0) \Big) \\ + e^{\omega_i (t_0+T)} \Big(\Big(\omega_i \hat{v}_r(y_0) - (\omega_r - kU(y_0))\hat{v}_i(y_0) \Big) \cos(kx_0 - \omega_r(t_0+T) + kU(y_0)T) \\ - \Big(\omega_i \hat{v}_i(y_0) + (\omega_r - kU(y_0))\hat{v}_r(y_0) \Big) \sin(kx_0 - \omega_r(t_0+T) + kU(y_0)T) \Big) \Bigg] + \mathcal{O}(\epsilon^2),\end{aligned} \tag{7.7}$$

where $\hat{u} = \hat{u}_r + i\hat{u}_i$*,* $\hat{v} = \hat{v}_r + i\hat{v}_i$ *are complex amplitudes,* $\omega = \omega_r + i\omega_i$ *is the complex frequency and* k *the real wave number.*

Proof. See appendix B.2. □

Properties of Lagrangian Curvature growth

Equation (7.7) provides an analytic relation between a velocity field composed of normal modes and the Lagrangian curvature change and therefore directly connects LSA-based quantities with fluid material wrinkling, which is objective under (1.1). Several essential properties of the curvature change in unstable flows given by equation (7.7) follow:

(i) First and foremost, *the curvature change grows exponentially at a rate* ω_i *according to LSA* after adjusting from the initial, zero $\bar{\kappa}$. This theoretical proof solidifies the validity of the definition of the instability through curvature modes and connects it with the LSA for velocity fields which is not frame-invariant.

(ii) For $\omega_i < 0$ (ceasing perturbation), the $\bar{\kappa}$ converges to a finite value because the initial perturbation is retained in the fluid deformation (cf. figure B.2). This

memory trace of fluid history is particularly relevant in the context of non-normal growth.

(iii) The curvature and the velocity field are phase shifted if the fluid particles move relative to the velocity perturbation mode. Along the *critical layer* [47], i.e. where $U = c_r = \omega_r/k$, the curvature maxima of material lines travel in phase with the perturbation and are therefore material.

We note that if no reference flow direction is available, the placement of material lines is not trivial, but could be based on flow structures such as zero-mass-flux lines or Lagrangian coherent structures (LCS) [42, 41, 56].

7.2.4 Test cases

Solutions to the two-dimensional compressible Navier-Stokes equations for conservation of mass, momentum and energy in non-dimensional form are obtained using a discontinuous Galerkin spectral element method for spatial approximation and a 4^{th}-order explicit Runge-Kutta scheme for temporal integration. For a description of the method and validation of the solver we refer the interested reader to Kopriva [112], Nelson and Jacobs [64] and references therein. Lagrangian fluid particles are traced with a 3^{rd} order Adam-Bashfort scheme in time according to Mittal et al. [108].

Temporarily developing jet

The temporal stability of a top-hat jet profile is investigated computationally in a periodic domain. The characteristic scales of the problem are the jet width h and the velocity difference ΔU between center flow U_1 and coflow U_2. The field is initialized

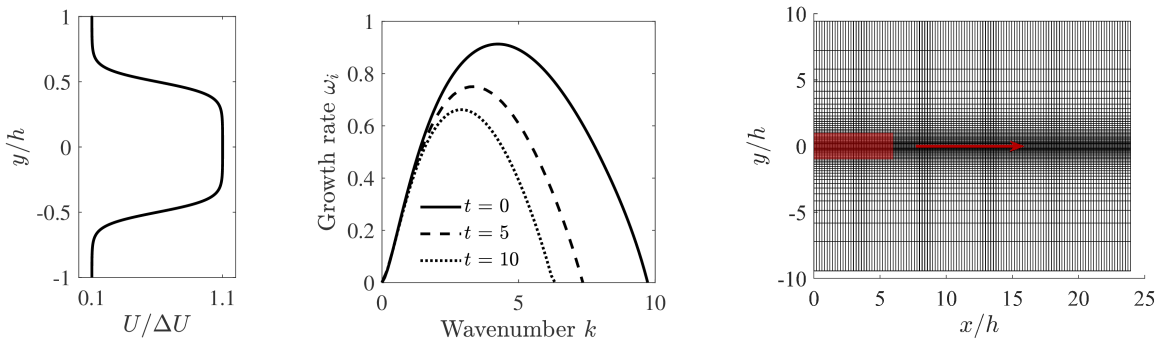

(a) Velocity profile (b) Dispersion relation (c) Computational domain

Figure 7.3: (a) Hyperbolic tangent, jet flow velocity profile normalized by the velocity difference ΔU between center and coflow. (b) Dispersion relation, i.e. temporal growth rates $\omega_i(t)$ versus wavenumbers k, determined with LSA for viscous jet velocity profiles at $t = 0$, 5, and 10. (c) Computational domain and grid in normalized coordinates with initial particle positions (shaded red area) and flow direction (red arrow).

with a hyperbolic tangent function velocity profile (see figure 7.3a),

$$U = \frac{U_1 - U_2}{2}\left(\tanh\frac{y+\frac{1}{2}h}{2\theta} - \tanh\frac{y-\frac{1}{2}h}{2\theta}\right) + U_2, \tag{7.8}$$

where the lateral velocity component is $V = 0$. The center and coflow velocities are $U_1/\Delta U = 1.1$ and $U_2/\Delta U = 0.1$, respectively.

Following Stanley et al. [80], the shear layer momentum thickness is set to $\theta/h = 1/20$ and the Reynolds number based on the jet width h and velocity difference ΔU to $Re_h = \Delta U h/\nu = 3000$. A free-stream Mach number of $M = 0.1$, based on a characteristic velocity of unity ($M = 0.11$ if based on the center flow and $M = 0.01$ if based on the outer flow), ensures that flow has negligible compressibility effects. This is verified by a comparison of a simulation at $M = 0.05$ which shows no discernible changes in the results presented below.

Using LSA, the dispersion relation is determined for the incompressible jet flow profile. It is plotted in figure 7.3(b) and peaks at a wavenumber of $k_{max} = 4.2$. The eigenmodes corresponding to wavenumbers $k = 2.1$, $k = 4.2$ and $k = 8.4$ are visual-

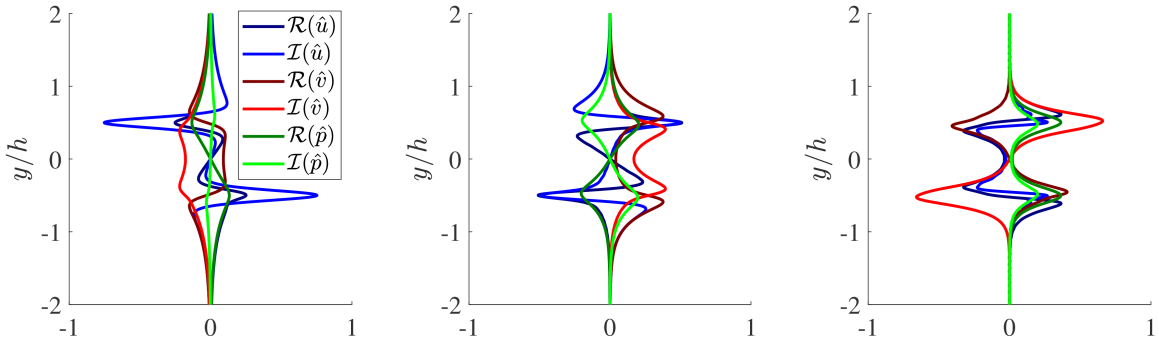

(a) $k = 2.1$ (b) $k = 4.2$ (c) $k = 8.4$

Figure 7.4: Real and imaginary components of the unstable eigenmodes of u, v, and p obtained from LSA for wavenumbers $k = 2.1$ (a), $k = 4.2$ (b), and $k = 8.4$ (c).

ized in figure 7.4(a–c). Note that the temporarily developing viscous jet flow does not have a time-independent base flow state and diffuses in time. The dipersion relation as shown in figure 7.3(b) is therefore time-dependent also. Based on the wavelength of this most unstable mode $\lambda_{max} = 2\pi/k_{max}$ at t=0, the computational domain is sized to fit 16 waves in x-direction ($x \in [0,\ 16\lambda_{max}]$) and is large enough in y-direction ($y/h \in [-3\pi,\ 3\pi]$) for the eigenmodes (see figure 7.4) to reduce to machine precision zero. To avoid grid resolution issues, an unnecessarily high number of 7200 quadrilateral elements clustered around the center line is used with the solution approximated with a 9^{th} order polynomial within each element (see figure 7.3c). Periodic boundary conditions are specified in x-direction and Riemannian free-stream boundary conditions [81] are imposed in y-direction. The velocity field is initialized according to (7.8). The real part of the eigenmodes corresponding to $k_{pert} = 2.1$, $k_{pert} = k_{max} = 4.2$, and $k_{pert} = 8.4$ (see figure 7.4) are scaled with a factor of 10^{-3} and superimposed onto the base flow as initial perturbation. Additionally, we also consider random noise perturbations. A sheet of 501×251 Lagrangian fluid tracers is initialized in the region $x_p \in [0,\ 4\lambda_{max}]$ and $y_p \in [-h,\ h]$ for cases using LSA eigenmodes and 2001×251 ($x_p \in [0,\ 16\lambda_{max}]$) tracers are initialized for computations with random noise perturbations.

NACA 65(1)-412 airfoil flow

To test the kinematic approach for an unstable flow without an analytical base field, we consider the stability of a separated and unstable shear layer in the flow field over a cambered NACA 65(1)-412 airfoil at 7° incidence for a chord-based Reynolds number of $Re_c = 20{,}000$ and a free-stream Mach number of $M = 0.3$. The parameter c refers to the chord length of the wing. We have studied flow separation and Lagrangian wake dynamics extensively for this geometry in previous work (e.g. [76, 84, 35]) and use the setup that yields a grid-independent solution with negligible blockage effects of these investigations here.

The computational domain (C-grid) consists of 23,400 quadrilateral elements and, within each element, the solution is approximated by 6^{th} order Legendre-Gauss polynomials. The in- and outflow boundaries of the domain are 30 chord lengths away from the airfoil, yielding a blockage effect of 1% by the computational domain. A damping layer at the outflow boundary reduces pressure reflections from outflow boundary [81]. The mesh is refined around the airfoil (see figure 7.5a), with first grid point away from the wall at approximately $y_g^+ = 0.2$. where, y^+ refers to the dimensionless wall coordinate. Figure 7.5(a) further illustrates the location of the 4001×300 Lagrangian fluid tracers that are initialized in wall-parallel lines along the upper surface of the airfoil.

Circular cylinder

In a final test, the origin and onset of vortex shedding in the wake behind circular cylinder at $Re_d = 200$ is considered with the goal of illustrating the objective nature of the kinematic approach. Strykowski and Sreenivasan [50] show that the vortex shedding behind a circular cylinder has its origin in unstable modes in the growing cylinder wake region. Control of those modes can delay or prevent shedding

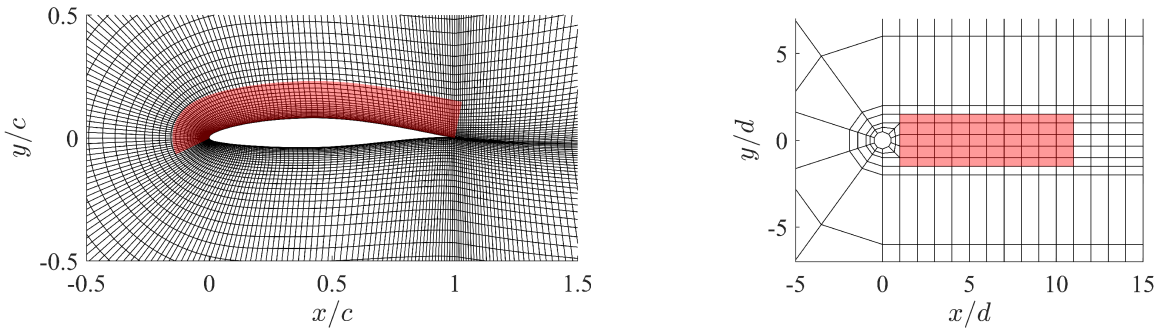

(a) NACA 65(1)-412 (b) Circular cylinder

Figure 7.5: Computational domain and grid used for simulations of the flows over (a) a NACA 65(1)-412 airfoil and (b) a circular cylinder. Only elements edges (no quadrature grid points within the element) are shown. Fluid particle tracers are initialized in the element colored in red.

from occurring. Because the instability is associated with temporal growth of the wake, a steady base velocity and a corresponding velocity perturbation cannot be defined. The finite-time material line curvature change can be.

Following the problem setup in Klose et al. [62] that was used for the analysis of kinematic aspects of Lagrangian separation, a free-stream Mach number of $M = 0.1$ is specified. The grid-independent solution [62] is approximated with a high, 18^{th} order polynomial approximation on 347 quadrilateral elements (see figure 7.5 b). Riemannian free-stream conditions are prescribed at all outer boundaries and the vertical domain size $y/d \in [-20, 20]$ yields a blockage of 2.5%. A sheet of 501×251 Lagrangian fluid tracers is initialized half a diameter downstream from the cylinder in the region $x_p \in [1d, 11d]$ and $y_p \in [-1.5d, 1.5d]$, as shown in figure 7.5(b).

7.3 Results and Discussion

7.3.1 Temporarily developing jet

Finite-time instabilities are extracted from Lagrangian particles by integrating fluid tracers from some time t_0 over the interval T until the time $t = t_0 + T$. Given that the curvature change depends on both, t_0 and T, two cases are considered for the computation of $\bar{\kappa}_{t_0}^{t_0+T}$ based on (7.1): (a) the reference state is set at $t_0 = 0$ and we calculate $\bar{\kappa}_0^t$ based on a single particle trace or (b) the integration interval T is kept constant and the curvature follows as $\bar{\kappa}_{t-T}^t$ with the particle trace re-initialized every interval T. In both cases, the tangent vector is $\mathbf{r}' = [1, 0]^T$ and $\kappa_0 = 0$, such that only the first term of (7.1) contributes to the curvature change. The resulting curvature scalar field $\bar{\kappa}_{t_0}^{t_0+T}$ is plotted over the advected particle positions in figures 7.6 and 7.7.

Consistent with figure 7.1, the time series (a) – (c) shows how the initial waviness in the curvature field and associated early wrinkles in the material line are precursors of regions with increased and concentrated curvature change magnitudes associated with vortex roll-up at later times. Local extrema in the curvature fields (green and orange markers in figures 7.6 and 7.7), as well as the point in between with a maximum gradient (yellow marker), represent point identifiers of significant material wrinkling and vortex formation at later times. Per the property (iii) described in section 7.2.3, local maxima of the Lagrangian curvature change in unstable, parallel shear layers are only material along the critical layer where $U(y) = c$ and can shift elsewhere in regions where the unstable mode has a different phase velocity as compared to the flow's convection velocity. The yellow point markers are located exactly on the critical lines at $y = \pm 0.51h$ and $y = \pm 0.50h$ for $k_{pert} = 2.1$ and $k_{pert} = 4.2$ and can be considered critical points in the Lagrangian analysis.

The shift between the vertical curvature change bands visualized in Figure 7.6

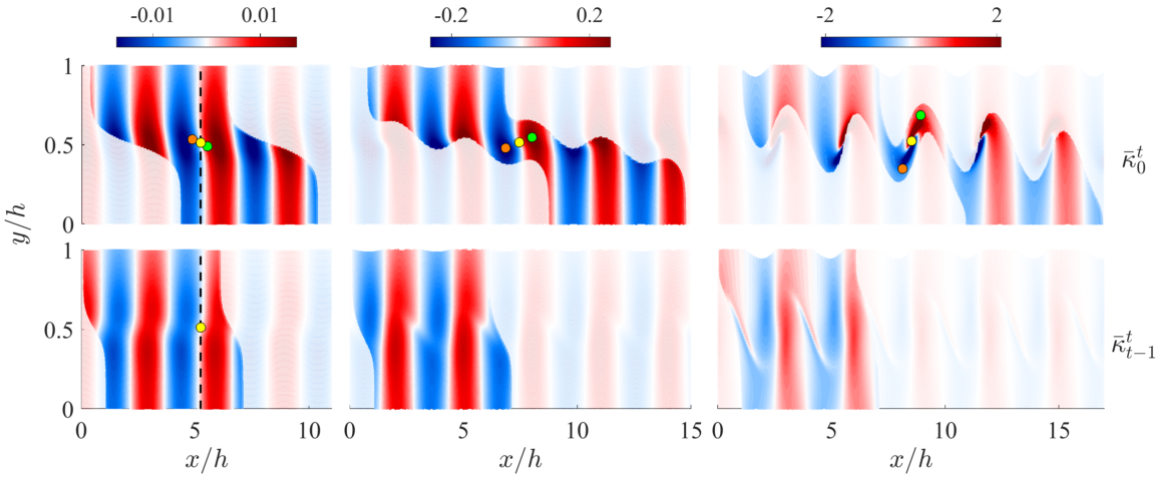

(a) $t = 4.0$ (b) $t = 8.0$ (c) $t = 10.0$

Figure 7.6: Contours of the curvature scalar field $\bar{\kappa}_0^t$ (upper figures) and $\bar{\kappa}_{t-1}^t$ (lower figures) at $t = 4.0$ (a), $t = 8.0$ (b) and $t = 10.0$ (c) for a jet flow computation with initial velocity perturbation according to eigenmodes with a wavenumber $k_{pert} = 2.1$. Only the upper half of the jet is shown. Time units are scaled by $h/\Delta U$. Bright visualizations are for directly computed fields. The faded contours are copies of the bright contours. Color-coded tracers: $\max(|\nabla\bar{\kappa}_0^8|)$ in yellow, $\max(\bar{\kappa}_0^8)$ in green, and $\min(\bar{\kappa}_0^8)$ in orange, based on the scalar field in (b). Material position of color-coded tracers at earlier and later times indicated in (a) and (c). Dashed line indicates indicates location of center marker in upper figure and is duplicated in lower figure, together with yellow marker.

and 7.7 for long and short integration intervals, i.e. $\bar{\kappa}_0^t$ and $\bar{\kappa}_{t-1}^t$, respectively, is also explained by the relative velocity difference of the modes and the fluid. Because the phase shift between the finite-time curvature change and the velocity mode depends on the integration interval T of the particle trace (cf. equation (7.7)), different initial times $(t - T)$ of $\bar{\kappa}_{t-T}^t$ yield a different phase in the curvature field. Along the critical layer, particles are not subjected to passing unstable wave modes, and the short and long time-integrated curvature contours have their maxima and minima at the same location. Above and below, the fluid particles move at a different speed as compared to the velocity mode such that the bands are slightly shifted with respect to each other. An analysis of the phase shift for a simple traveling mode is presented with additional

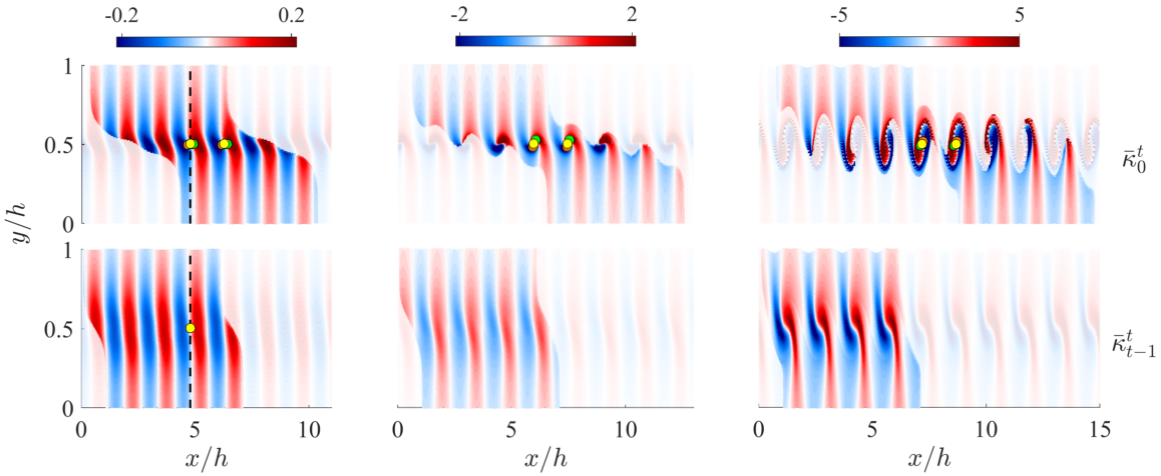

(a) $t = 4.0$ (b) $t = 6.0$ (c) $t = 8.0$

Figure 7.7: Contours of the curvature scalar field $\bar{\kappa}_0^t$ (upper figures) and $\bar{\kappa}_{t-1}^t$ (lower figures) for $t = 4.0$ (a), $t = 6.0$ (b) and $t = 8.0$ (c) for a jet flow computation with initial velocity perturbation according to eigenmodes with a wavenumber $k_{pert} = 4.2$. Only the upper half of the jet is shown. Time units are scaled by $h/\Delta U$. Bright visualizations are for directly computed fields. The faded contours are copies of the bright contours. Color-coded tracers: $\max(|\nabla\bar{\kappa}_0^6|)$ in yellow, $\max(\bar{\kappa}_0^6)$ in green, and $\min(\bar{\kappa}_0^6)$ in orange, based on the scalar field in (b). Material position of color-coded tracers at earlier and later times indicated in (a) and (c). Dashed line indicates indicates location of center marker in upper figure and is duplicated in lower figure, together with yellow marker.

visualizations in appendix B.3 to provide a theoretical basis for the phase shift.

To determine the growth of the maximum curvature change in the temporally developing jet flow, we consider the material line with a local maximum curvature gradient $|\nabla\bar{\kappa}_0^8|$ and $|\nabla\bar{\kappa}_0^6|$ according to the yellow markers in figures 7.6 and 7.7 respectively. Along these lines, we evaluate the Fourier transform $\mathcal{F}(k)$ of $\bar{\kappa}_0^t$ and $\bar{\kappa}_{t-1}^t$ at every time step and record its amplitude, as shown in figure 7.8(a–b) where surfaces of $|\mathcal{F}|$ are plotted over the wavenumber space and time. Similarly, the v' velocity amplitude is determined along the critical layer ($y/h = 0.5$) and is added for reference in figure 7.8(c).

All surface plots in figure 7.8 have a ridge of local maximum $|\mathcal{F}|$ at the respective perturbation wavenumber k_{pert} (indicated as red line). Additional ridges emerge over time in figure 7.8(a–c). These are an indication of non-linear energy transfer to modes at other frequencies as the base profile diffuses over time.

A direct comparison of of v', $\bar{\kappa}_0^t$, and $\bar{\kappa}_{t-1}^t$ at the perturbation wavenumber is presented in figure 7.8(d), where the time-dependent Fourier transform amplitudes are plotted versus time. The slope of the dotted straight line, which is plotted for reference, is according to the exponential growth rate obtained from LSA, $e^{\omega_i(t_0)t}$. The v' velocity initially grows according to the rate predicted by LSA (dashed lines), but departs from the linear growth trend when the shear layer diffuses significantly over time. While the v' velocity growth starts from the imposed perturbation, the material lines have zero curvature change at the initial time. Because of this the growth of the material line's curvature change follows the growth predicted by LSA (dashed lines in figure 7.8d) only after an initial adjustment phase. This characteristic is confirmed by the analytic form of the curvature scalar equation (7.7). An initial curvature can be added to the material line in the form of a sinuous perturbation (denoted by ϵ) with the wavelength set to the LSA eigenmodes. In that case, the curvature change follows the growth

predicted by LSA without the adjustment phase as shown in figure 7.9.

The Lagrangian curvature change for relatively short integration intervals, $\bar{\kappa}^t_{t-1}$, (green) in figure 7.8(d) closely follows the trends of the v' velocity (red). This is consistent with the relation between $\bar{\kappa}^t_{t-1}$ and v' as derived in (7.4), as it can be expected that the short time curvature change follows the infinitesimally small curvature change, $\dot{\kappa}_t$, and thus also scales with the transverse velocity perturbation.

For larger time intervals, T, however, this reasoning no longer applies because non-linearities lead to coupling with and excitation of other modes, and so (7.4) which is derived for a single mode perturbation equation (7.7) becomes invalid. For perturbations at higher wave number (figure 7.8), this mode coupling occurs at an earlier time as compared to cases with the lower wave number perturbations. For example, in the case of perturbation with symmetric eigenmodes at $k_{pert} = 8.4$ (see figure 7.8d), $\bar{\kappa}^t_0$ grows whereas the v' and $\bar{\kappa}^t_{t-1}$ reduce after a short initial growth, i.e. the perturbation is ceasing and the flow becomes stable. Owing to the low Reynolds number, the shear layer diffuses leading to changes in the stability properties over time and as a result the mode at $k = 8.4$ moves outside the unstable regime (see figure 7.3b). In the kinematic analysis, however, the initial perturbation of the fluid particles is carried on (unless the tracers are re-inialized) yielding a continuously growing deformation of the material lines within the layer $0.47 < |y/h| < 0.53$, as shown in figure 7.10. Notably, the curvature $\bar{\kappa}^t_0$ of the material line at $y/h = 0.5$ follows the growth rate given by LSA (see figure 7.8d). This continuous growth of the deformation in the Lagrangian frame showcases how the footprint of a temporary instability persists. This curvature persistence is a very useful feature in practice as one necessarily has to identify instabilities over a finite time in experiments, while the LSA and the instantaneous growth rate of v' are generally unavailable.

To asses the ability of the kinematic approach to identify emerging unstable

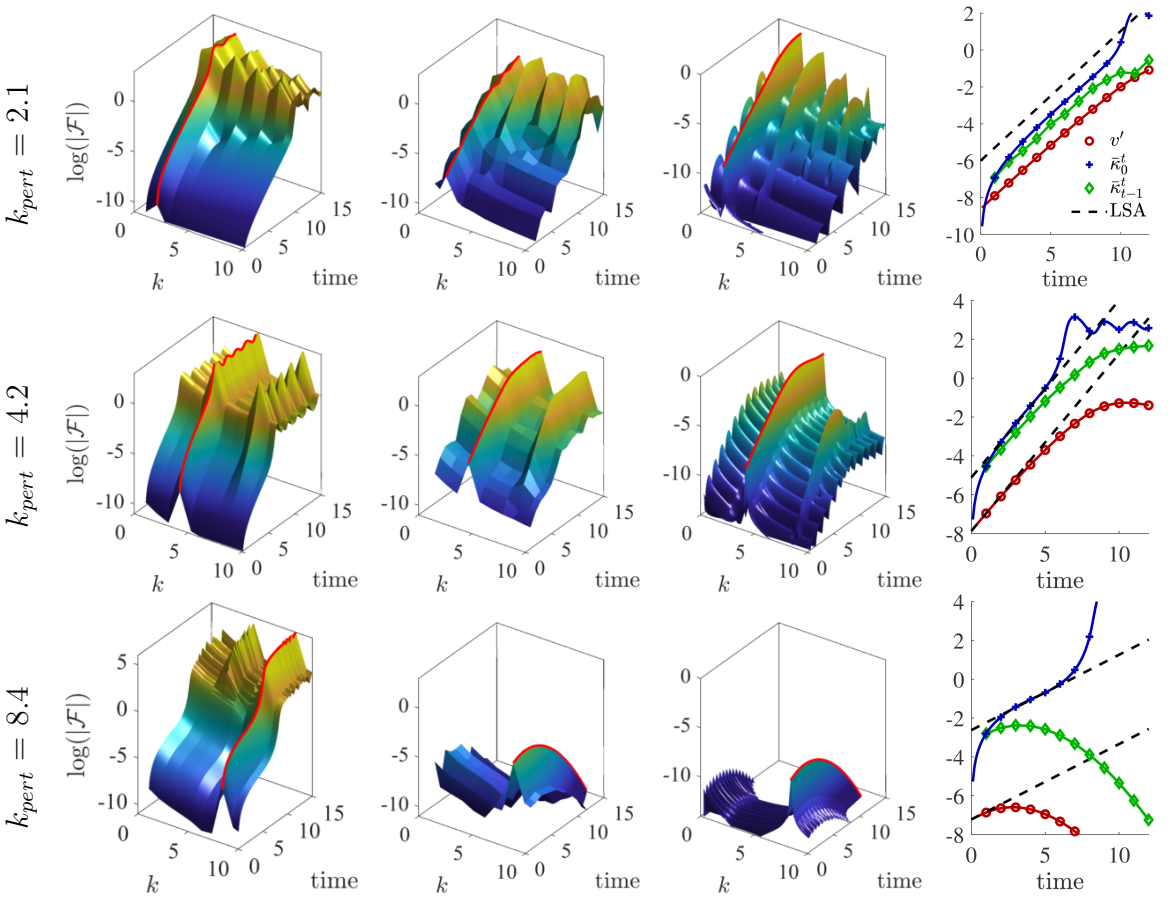

(a) $\bar{\kappa}_0^t$ (b) $\bar{\kappa}_{t-1}^t$ (c) v' (d) $\log(|\mathcal{F}(k_{pert})|)$

Figure 7.8: Columns (a–c): amplitude of the Fourier transform $\mathcal{F}$ of v' (a), $\bar{\kappa}_0^t$ (b), and $\bar{\kappa}_{t-1}^t$ (c) plotted versus wavenumber and time. The temporal development of maxima in $|\mathcal{F}|$ at is highlighted with a red line. (d) Comparison of the amplitude of the Fourier transforms over time with the LSA growth rate (dashed lines). The rows correspond to the wavenumbers of the initial perturbation mode with $k_{pert} = 2.1$, 4.2, and 8.4.

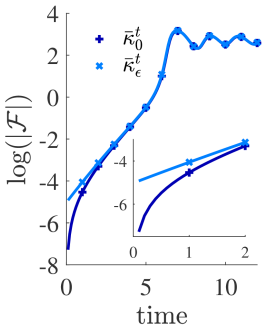

Figure 7.9: Comparison of the temporal development of the maximum amplitude of the Fourier transform $\mathcal{F}$ of $\bar{\kappa}_0^t$ and $\bar{\kappa}_\epsilon^t$ for $k_{pert} = 4.2$, where ϵ is an initial perturbation of the material line.

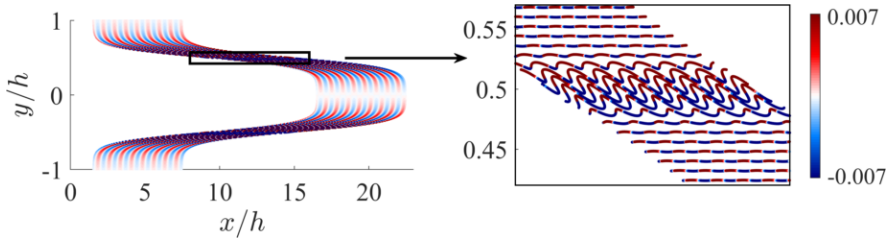

Figure 7.10: Curvature scalar field $\bar{\kappa}_0^{15.0}$ plotted along advected particle positions at $t = 15.0$ for an initial perturbation mode with wavenumber k_{pert} = 8.4. The right figure is a zoomed in visualization of the box identified in the left figure.

modes in a flow subject to perturbations with multiple modes, the jet flow is simulated with an initial random mode perturbation. Following Kraichnan [113], the velocity perturbation is initialized by superposition of fifty Fourier modes with random coefficients and amplitude as follows:

$$\mathbf{u}' = 2 \sum_{n=1}^{N=50} \tilde{u}_n \boldsymbol{\sigma}_n \cos\left(\mathbf{k}_n \cdot \mathbf{x} + \psi_n\right). \tag{7.9}$$

Here, $\tilde{u}_n$ is the randomized amplitude function, $\mathbf{k}_n$ the wavenumber vector and ψ_n a random phase shift. By imposing a solenoidal velocity field, the condition $\mathbf{k}_n \cdot \boldsymbol{\sigma}_n = 0$ determines the components of the unit vector $\boldsymbol{\sigma}$. Only multiples of the smallest possible wavenumber in the domain, i.e. $k_{x,y;n} = nk_{min}$, where n is a random integer in the range $1 \leq n \leq N$, are considered to ensure periodicity. The flow is simulated at a higher Reynolds number of $Re_h = 300{,}000$ as compared to the cases above, which reduces the impact of the shear layer growth and the associated shifting of the stability properties of the flow (see figure 7.3b).

Snapshots of the particle trace colored by the curvature $\bar{\kappa}_0^t$ are presented in figure 7.11 for integration times $T = 7$ (a) and $T = 11$ (b). The random modes leave a footprint in the particle trace and high frequency content is still visible at $t = 7$. At this time, however, the dominant modes driving the fluid deformation have emerged in the curvature field and are decisive in the the topology of the material lines at $t = 11$ (see figure 7.11b). To understand the connection between the curvature field at $t = 7$ and $t = 11$, fluid tracers are initialized at local curvature maxima at $t = 7$ (see green markers). At $t = 11$, the material lines have deformed significantly along the shear layers, leading to increased local magnitudes of the maximum curvature. Figure 7.11(b) shows that the green tracers initialized at $t = 7$ are located at the maximum fluid wrinkling and curvature locations of the forming vortices at $t = 11$, underscoring that local curvature maxima can identify locations of vortex roll-up at early times.

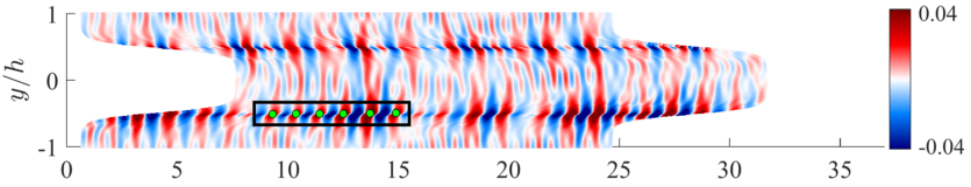

(a) $t = 7.0$

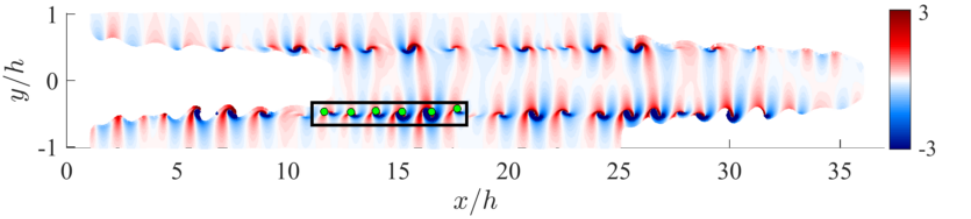

(b) $t = 11.0$

Figure 7.11: Contours of the curvature scalar field $\bar{\kappa}_0^{7.0}$ (a) and $\bar{\kappa}_0^{11.0}$ (b) for perturbation with random modes. Green tracers: $\max(\bar{\kappa}_0^{7})$ of the scalar field within the lower half of the jet shown in (a) and advected positions at $t = 11$ in (b).

7.3.2 NACA 65(1)-412 airfoil flow

The transitional flow over a NACA 65(1)-412 airfoil at 7° incidence and chord-based Reynolds number $Re_c = 20{,}000$ is characterized by a laminar separation bubble (LSB) as shown by the time averaged velocity field and streamlines in figure 7.12. Upstream of the separation bubble, fluid particles well up as discussed in the introduction and depicted in figure 7.1(e-g). They consequently move towards an asymptotic manifold that has its origin at the averaged zero skin friction point (figure 7.12) where the streamlines break away from the wall.

Upon flow separation, a shear layer forms that is unstable as plots of the instantaneous Lagrangian curvature change field $\bar{\kappa}_{55.0}^{55.01}$ and $\bar{\kappa}_{55.0}^{55.1}$ (based on wall-parallel material lines) in figure 7.13(a–b) show. In the figure, the y coordinate is independently scaled from the x-coordinate to obtain a clearer visualization of the flow phenomena that occur in a thin region close to the airfoil. Kelvin-Helmholtz instabilities along

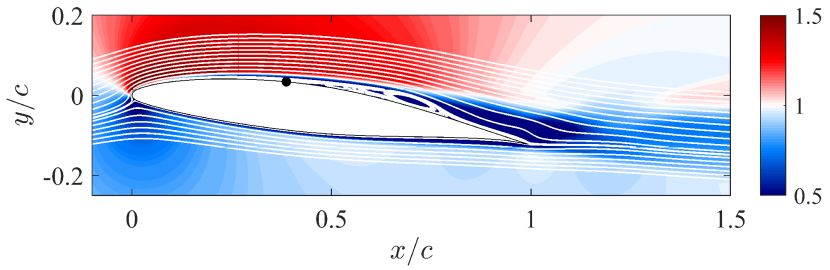

Figure 7.12: Contours of time-averaged velocity magnitude and streamlines (white) for a two-dimensional Navier-Stokes flow over the NACA-65(1)412 airfoil at 7° incidence. The black circle identifies the time-averaged zero skin friction point. Plot shows rotated field with horizontally aligned inflow velocity vector.

the spatially developing, separated shear layer lead to vortex formation upstream of the location where the LSB reattaches. Further downstream, the flow transitions to a wall-bounded, vortex dominated pattern. The curvature fields $\bar{\kappa}_{55.0}^{55.01}$ and $\bar{\kappa}_{55.0}^{55.1}$ show the wrinkling modes associated with the Kelvin-Helmholtz instabilities. These modes are visible through bands of positive and negative curvatures in the vicinity the separated shear layer similar to the temporally developing jet.

The bands in the Lagrangian curvature fields in figure 7.13(a) and (b) upstream of the vortex roll-up at $x/c = 0.7$ identify the process of off-wall material line folding associated with the Kelvin-Helmholtz instability in the shear layer. The green, circular markers identify the locations of the local maxima of $\bar{\kappa}_{55.0}^{55.01}$ on these curvature bands in figure 7.13(a) and their advected locations at $t = 55.1$ in figure 7.13(b). The advected Lagrangian grids (grey) based on the tracers initialized according to figure 7.5(a) are also plotted for reference. Similar to the jet flow, the maximum wrinkling occurs in the vicinity of the curvature extrema. These curvature peaks are also nearly material and remain close to the local maxima of the curvature computed over a longer integration interval, $\bar{\kappa}_{55.0}^{55.1}$ (see green, diamond-shaped markers). The strongly increasing magnitude of the curvature maxima along the spatially developing unstable shear flow provides evidence that curvature changes identify instabilities and the material wrinkling at the

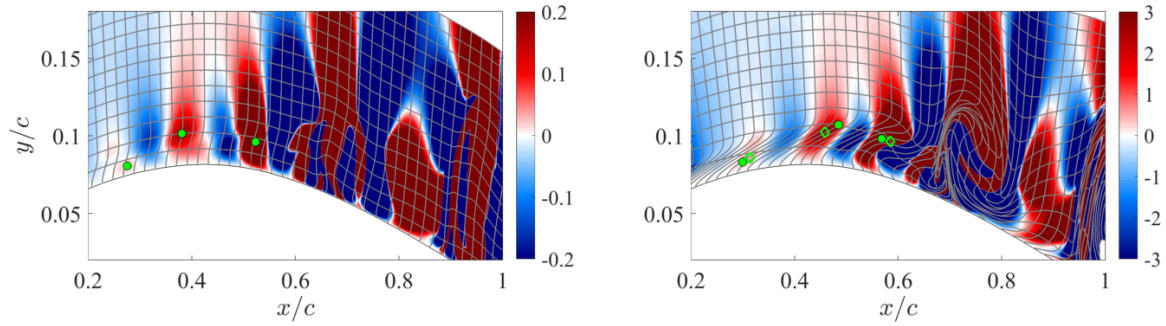

(a) $\bar{\kappa}_{55.0}^{55.01}$ (b) $\bar{\kappa}_{55.0}^{55.1}$

Figure 7.13: Contour plots of the curvature scalar $\bar{\kappa}_{55.0}^{55.01}$ (a) and $\bar{\kappa}_{55.0}^{55.1}$ (b) with advected Lagrangian grid in gray. Local maxima of the curvature scalar in green: $\max(\bar{\kappa}_{55.0}^{55.01})$ (circles) are based on the scalar field in (a) and their advected positions plotted in (b). $\max(\bar{\kappa}_{55.0}^{55.1})$ (diamonds) are based on the scalar field in (b). The y-axis is stretched.

onset of vortex formation.

7.3.3 Wake behind a circular cylinder

To understand the material wrinkling and its curvature field related to the emergence of an unstable mode in the growing wake of a circular cylinder, horizontal material lines are initialized half a diameter downstream of the cylinder and advected for one convective time unit. The Lagrangian curvature change ($\bar{\kappa}_{t-1}^{t}$) and curvature rate ($\dot{\kappa}_t$) are extracted from the material lines and contours fields thereof are plotted in figure 7.14 at times $t = 105$ and $t = 160$, together with common Eulerian quantities such as the transverse velocity component, vorticity and the Q-criterion. Also visualized for reference are the advected and deformed Lagrangian grids, which are overlayed to the $\bar{\kappa}_{t-1}^{t}$ fields.

Up to $t = 105$, the recirculation region is growing with time. No steady time-averaged solution is hence available that would allow for the computation of perturbation quantities. While all (frame-dependent) Eulerian quantities in figure 7.14 show a

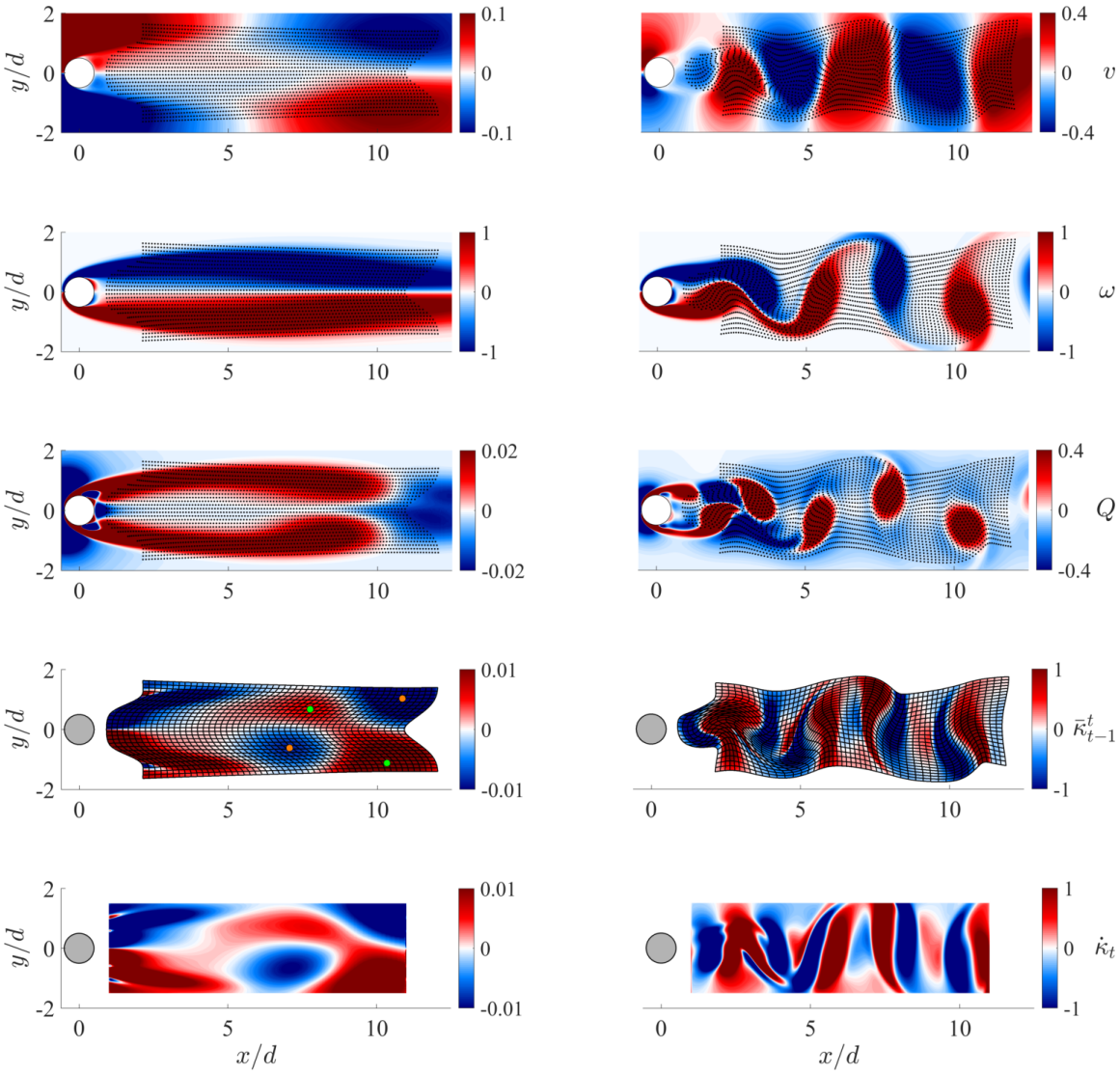

(a) $t = 105$ (b) $t = 160$

Figure 7.14: Comparison of Eulerian and Lagrangian quantities for the circular cylinder. From top to bottom: v velocity, vorticity, Q-criterion, Lagrangian curvature scalar field $\bar{\kappa}^t_{t-1}$ (with deformed Lagrangian grid) and Lagrangian curvature rate $\dot{\kappa}_t$ at times $t = 105$ (a) and $t = 160$ (b). Local minima and maxima of $\bar{\kappa}^{105}_{104}$ indicated by orange and green markers in (a). The particle trace is added to the plots of Eulerian quantities for orientation. Note that the range of the color map changes with t.

symmetric topology with respect to the x axis at $t = 105$, the curvature scalars $\bar{\kappa}_{104}^{105}$ and $\dot{\kappa}_{105}$ show an asymmetric fluid deformation at this early stage. This asymmetry is the early indicator of the development of the wake instability that remains hidden to the other fields.

At a later time ($t = 160$), the wake is unstable and has developed the characteristic Von-Karman vortex street, where the strongly increased transverse fluid motion results in significant bending of the material lines visualized through the deformed material grid along with $\bar{\kappa}_{159}^{160}$. While vortices in the wake are identified by regions of large vorticity or positive values of the Q-criterion, their rotating motion induces pairs of negative and positive curvature that resemble the *yin-yang* symbol in the $\bar{\kappa}_{159}^{160}$ field. Connectors between vortices are identified as slender curvature ridges and positive and negative values provide directional information about the fluid motion and deformations.

7.4 Summary of Results

A finite-time curvature change diagnostic is introduced to identify instabilities in material lines in the Lagrangian frame. By defining a flow instability in the Lagrangian frame as the increased folding of lines of fluid particles, the identification does not require knowledge of the base flow profile or averaged flow fields but only the flow map of particle traces. Material lines are sensitive to fluid deformation and can therefore locate unstable modes in the particle phase early on. Because the transient short-term instabilities leave a footprint in the advected fluid material line's curvature change over finite time, a convenient time interval would be available in practice to capture instabilities. The material curvature is objective, independent of the parametrization, and so the identification applies to a broad variety of flows, including those over general

complex geometries, rotating frames, and experimental setups with particle tracers.

Analytic formulas for the approximation of the flow map and curvature change are provided for perturbed parallel shear flows. These formulas connect relevant Eulerian quantities used in LSA characterizing the dynamics of perturbations in the infinite-dimensional space of velocities with their induced effects in the physical space of fluid flows. The workings of the diagnostic are illustrated conceptually for the case of the hyperbolic tangent jet in a periodic domain for perturbations with eigenmodes of three different wavenumbers and random noise. It is shown that the material curvature change accurately captures the unstable modes early in the jet flow. Exponential growth rates of Lagrangian curvature match the values predicted by linear stability analysis, as we predict analytically. In a jet flow with random initial mode perturbations, the curvature field captures the emerging unstable mode.

Tests of the flows over a cambered airfoil at incidence and the wake behind a circular cylinder demonstrate the ability of the kinematic approach to identify instabilities without the requirement of an analytical mean or a frame of reference. The curvature field identifies the early onset of vortex formation that remains hidden to typical Eulerian diagnostics.

7.5 Acknowledgements

Chapter 7, in full, is currently being prepared for submission for publication of the material, B. F. Klose, M. Serra and G. B. Jacobs. B. F. Klose: development of theory, data acquisition, original draft preparation. M. Serra: development of theory (Theorem 1), editing. G. B. Jacobs: development of theory, supervision, review & editing.

Chapter 8

Conclusions

A comprehensive account of the transitional flow over a cambered airfoil is given to enhance the general understanding of boundary layer separation and instabilities encountered in low-Reynolds number airfoil aerodynamics. The airfoil flow is analyzed for a series of angles of attack through a combination of highly accurate three-dimensional simulations and Lagrangian particle dynamics. Additionally, a definition of kinematic instabilities is introduced based on the finite-time wrinkling of Lagrangian material lines and is shown to capture unstable modes in shear flows early. The diagnostic is based on the curvature change of material lines, is objective, and can be applied to flow problems of general complexity.

8.1 Low-Reynolds number airfoil flow

Boundary layer separation and the corresponding three-dimensional structures in the transitional flow over a cambered airfoil are analyzed through a series of high-fidelity simulations at various flow angles and a chord-based Reynolds number of $Re = 2 \times 10^4$. The flow topology, wake structure, aerodynamic forces, and statistics are

governed by the transition location of the separated shear layer on the suction side of the profile, which divides the flow into two dynamical regimes: at angles of attack smaller than 7°, the upper boundary layer separates around mid-chord and remains laminar until it interacts with the trailing edge vortex, which forms from the roll-up of the bottom-side boundary layer. As a result, a transitional Von-Karman-type vortex street is established in the wake. For angles larger than 7°, the separation point moves to the leading edge of the airfoil and the shear layer transitions to turbulence and reattaches, resulting in a laminar separation bubble at the leading edge and a turbulent wake. The bifurcation of the flow is accompanied by a rapid increase of the aerodynamic lift and decrease of drag, which is attributed to the recovery of the free-stream pressure at the trailing edge. An intermediate state is shown to exist at 7° incidence, where a LSB forms at the rear side of the airfoil. Here, the flow reattachment occurs just upstream of the trailing edge ($0.92c$) such that the breaking vortices do not transition into a fully developed turbulent boundary layer, but shed off in large patches or "puffs" of turbulent motion.

Because the NACA 65(1)-412 is designed to maximize the laminar flow region over the wing, the absence of an early transition to turbulence at low Reynolds number prevents the reattachment of the separated boundary layer on the airfoil's rear side at lower angles of attack and results in a significant loss of the lifting force, which is even negative at AOA = 0°. With the rapid increase in the lifting force upon bifurcation of the flow, the efficient operation of laminar airfoils in low-Reynolds number flow conditions can be challenging and difficult to predict. The use of active or passive flow controllers to induce transition early should therefore be considered in order to alleviate these drawbacks.

In a preceding study of marginally resolved Navier-Stokes simulations, the performance of the underlying DGSEM code is evaluated. It is shown that the implemen-

tation of kinetic energy conserving volume fluxes into the scheme results in a stabilization of the oftentimes temperamental numerical method without the use of filters or artificial viscosity.

8.2 The kinematics of flow separation

Kinematic aspects of flow separation have been investigated in external aerodynamics by extracting the initial motion of upwelling fluid material from the wall and its relation to the long-term attracting manifolds in the flow field. Although the wall-bounded kinematics are governed by the formation of a material spike upstream of the asymptotic separation point and ejection of particles in direction of the separation line, it was shown that the off-wall trajectories of the fluid tracers are driven by attracting ridges in the finite-time Lyapunov exponents. Therefore, the complete pathway of Lagrangian flow separation was obtained: from the initial upwelling at the spiking point over the ejection of particles along the asymptotic separation profile to the attracting LCSs.

For the flow around a circular cylinder and a cambered NACA 65(1)-412 airfoil, the footprint of the initial material upwelling, i.e. the spiking point, was determined by evaluating the curvature of Lagrangian fluid tracers and by extracting high-order on-wall derivatives of the normal velocity as proposed in [43]. An exact match of the Lagrangian and Eulerian criterion for the start of material line spiking verifies the Eulerian criterion and associated the principal location of material upwelling for the first time in two test cases, i.e., the cylinder flow and the flow over an airfoil. For the latter, the spiking point was recovered by appropriately filtering the spurious oscillations in the velocity derivative induced by the spline-based boundary parametrization of the NACA profile, thereby showing that this method is robust to noise. Determining the

spiking points requires the extraction of high-order velocity derivatives, which is challenging for general geometries and in experimental settings because it requires very high-resolution data and an accurate representation of the geometry.

With the ability to compute the birth of separation instantaneously from Eulerian on-wall data, the Lagrangian pathway from the spiking point to the asymptotic separation profile can be used as input parameters for dynamic flow controllers.

8.3 Objective identification of kinematic instabilities

A finite-time curvature change diagnostic is introduced to identify instabilities in material lines in the Lagrangian frame. By defining a flow instability in the Lagrangian frame as the increased folding of lines of fluid particles, the identification does not require knowledge of the base flow profile or averaged flow fields but only the flow map of particle traces. Material lines are sensitive to fluid deformation and can therefore locate unstable modes in the particle phase early on. Because the transient short-term instabilities leave a footprint in the advected fluid material line's curvature change over finite time, a convenient time interval would be available in practice to capture instabilities. The material curvature is objective, independent of the parametrization, and so the identification applies to a broad variety of flows, including those over general complex geometries, rotating frames, and experimental setups with particle tracers.

Analytic formulas for the approximation of the flow map and curvature change are provided for perturbed parallel shear flows. These formulas connect relevant Eulerian quantities used in LSA characterizing the dynamics of perturbations in the infinite-dimensional space of velocities with their induced effects in the physical space of fluid flows. The workings of the diagnostic are illustrated conceptually for the case of the

hyperbolic tangent jet in a periodic domain for perturbations with eigenmodes of three different wavenumbers and random noise. It is shown that the material curvature change accurately captures the unstable modes early in the jet flow. Exponential growth rates of Lagrangian curvature match the values predicted by linear stability analysis, as we predict analytically. In a jet flow with random initial mode perturbations, the curvature field captures the emerging unstable mode.

Tests of the flows over a cambered airfoil at incidence and the wake behind a circular cylinder demonstrate the ability of the kinematic approach to identify instabilities without the requirement of an analytical mean or a frame of reference. The curvature field identifies the early onset of vortex formation that remains hidden to typical Eulerian diagnostics.

8.4 Future work

The analysis of low-Reynolds number airfoil aerodynamics, the kinematics of Lagrangian structures in boundary layer separation, and the stability analysis based on material line wrinkling are generalizable to other flow problems and Reynolds numbers and provide the foundation to make informed decisions on the design, operation, and control of aerodynamic devices in the transitional flow regime. The application of active flow control concepts that take advantage of the three-dimensional instabilities should therefore be explored in future research. Additionally, analysis of geometric variations in this airfoil flow, for example endplates and/or slits at the wing tips, and their effect on the boundary layer separation and the critical angle could enhance our understanding of the differences observed in computations and experiments.

The extension of the kinematics of flow separation and the identification of kinematic finite-time instabilities to three-dimensional flows would make those concepts

available to a large number of complex applications. The effect of turbulence modeling on the Lagrangian separation dynamics and the application of the fluid spike extraction in time-averaged flows at high Reynolds numbers are also unknown. Such research could open these concepts to the broader computational fluid dynamics community, as well as commercial software applications.

Appendix A

The multitude of flow regimes in cambered airfoil aerodynamics at Re = 20,000: a two-sided story

A.1 Parameter study: 2D simulations

In this section we present results of two-dimensional Navier-Stokes simulations of the NACA 65(1)-412 and elaborate on the effect of resolution, domain size, and Mach number. Although the physical meaning of these results is limited because vortex stretching is absent in two-dimensional approximation, they are relevant for assessing conditions in numerical experiment through parametric studies.

A.1.1 Effect of Mach number

Although low-Reynolds number flows also typically operate at low Mach numbers, some applications (e.g. UAV at high altitude) may encounter compressibility effects [2]. The Prandtl-Glauert correction rule to estimate the compressibility effects

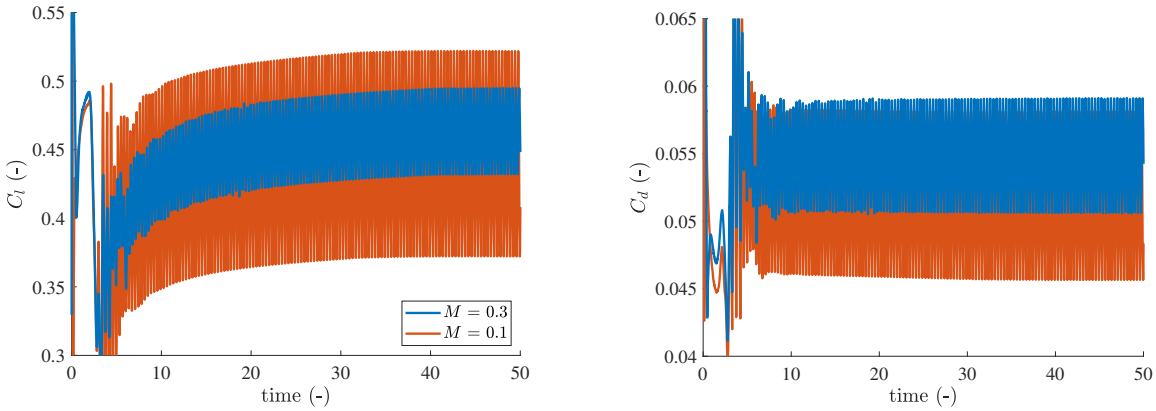

(a) Lift coefficient

(b) Drag coefficient

Figure A.1: Lift and drag coefficients at AOA = 4° over time for different Mach numbers. Domain radius $R = 30c$.

Table A.1: Lift and drag forces for AOA = 4° and different Mach numbers.

M	C_l	$C_{l,p}$	$C_{l,f}$	C_d	$C_{d,p}$	$C_{d,f}$
0.1	0.444	0.443	0.001	0.051	0.033	0.019
0.3	0.463	0.462	0.001	0.054	0.036	0.019

of the flow is $C_{p,M}/C_{p,i} = 1/\sqrt{1-M^2}$. For Mach numbers $M = 0.1$ and $M = 0.3$, the correction factors are $C_{p,M=0.1}/C_{p,i} = 1.005$ and $C_{p,M=0.3}/C_{p,i} = 1.048$ respectively and hence we expect deviations of around 4% – 5%.

At 4° angle of attack, the lower compressibility at $M = 0.1$ results in a larger amplitude of the lift and drag force oscillations, as well as an offset of the time-averaged values by 4% and 6% respectively (see table A.1). These values are in very good agreement with the predicted deviations based on the Prandtl-Glauert correction. Time-averaged profiles of the the pressure and skin friction coefficients in figure A.2 show that the differences in compressibility effect mainly the pressure distribution on the suction side of the airfoil and have a negligible impact on the skin friction distribution.

At 8° incidence, a slender LSB stretches from the leading until $x_r/c = 0.45$, 0.41, and 0.49 for $M = 0.05$, 0.1, and 0.3 respectively. The profiles of the pressure and skin

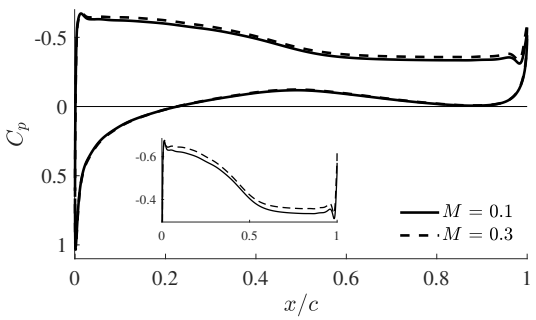

(a) Pressure coefficient

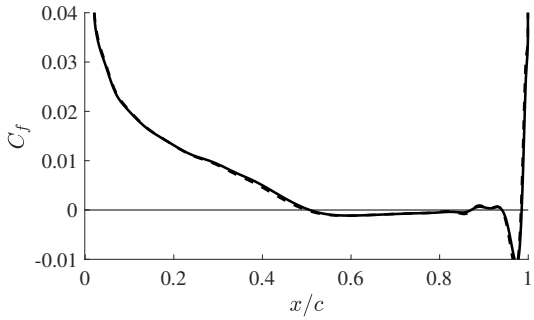

(b) Skin friction coefficient

Figure A.2: Time-averaged pressure and skin friction coefficients for $M = 0.1$ and $M = 0.3$ at AOA $= 4°$, $R = 30c$.

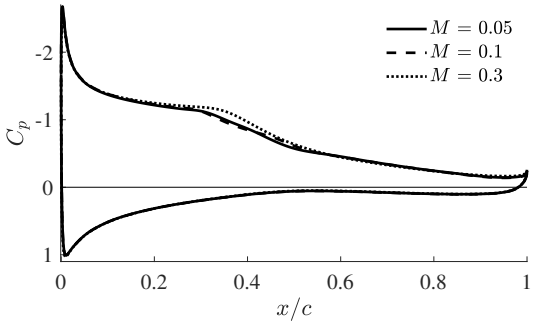

(a) Pressure coefficient

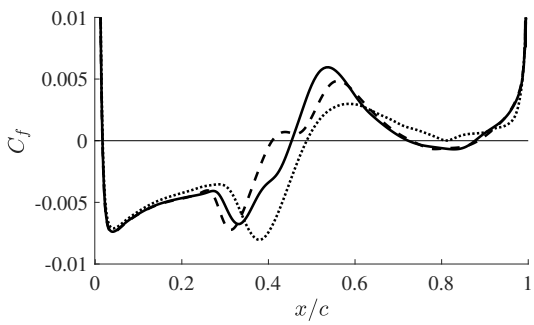

(b) Skin friction coefficient

Figure A.3: Time-averaged pressure and skin friction coefficients for different Mach numbers at AOA $= 8°$, $R = 30c$.

friction coefficients are given in figure A.3 and show that the higher compressibility in case of $M = 0.3$ results in a more distinct pressure plateau and elongated separation bubble with downstream reattachment compared to the lower-Mach number cases. Streamlines of the time-averaged recirculating flow within the LSB are plotted in figure A.5 and illustrate the difference in bubble sizes. The lift and drag coefficient averages differ by 2% and 12% respectively (see table A.2) and can be attributed to the modified pressure distribution caused by the different LSB sizes.

In addition to assessing compressibility effects by computing the flow at different Mach numbers with the compressible DGSEM solver, we also compare our results

Table A.2: Lift and drag forces for AOA = 8° and different Mach numbers.

M	C_l	$C_{l,p}$	$C_{l,f}$	C_d	$C_{d,p}$	$C_{d,f}$
0.05	0.941	0.940	0.002	0.052	0.041	0.010
0.1	0.946	0.944	0.002	0.052	0.042	0.011
0.3	0.965	0.964	0.002	0.058	0.048	0.010

with incompressible flow simulations performed with ANSYS FLUENT. Transient, incompressible computations are conducted with a pressure-based solver, second-order upwind for the spatial discretization, and second-order implicit time-stepping. No turbulence model is applied such that only source for artificial viscosity is through numerical dissipation from the upwinding scheme. A C-type domain with radius and wake length of 30 chords and consisting of 802,300 quadrilateral elements is used. The outer boundaries treated as velocity inflow (left, lower, and upper) and pressure outflow conditions (right) and a no-slip condition is applied at airfoil surface.

Figure A.4 shows the history of the lift and drag coefficients obtained from compressible DGSEM computations at a Mach number of $M = 0.05$ and sixth order polynomial representation and incompressible simulations with FLUENT. The results are in remarkably good agreement and confirm that the solution to this particular flow has converged across different numerical solvers. The case also shows that compresibility effects are not the cause for the disagreement with the USC wind tunnel experiments at AOA = 8° as all simulations show the transitioned state regardless of the Mach number.

A comparison of the streamlines inside the LSB (see figure A.5) indicates that the bubble size in the FLUENT computations is nearly identical with the DGSEM results at $M = 0.3$, but deviates from the topology found at $M = 0.05$. While the differences between the DGSEM results are solely related to the compressibility effects, results from the FLUENT simulation are also affected by the lower order accuracy of

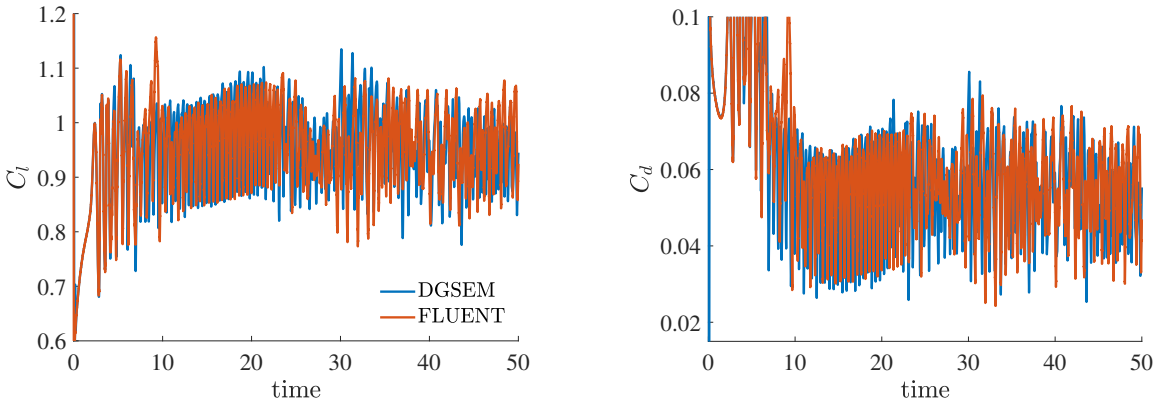

(a) Lift coefficient

(b) Drag coefficient

Figure A.4: Lift and drag coefficients at AOA = 8° over time DGSEM ($M = 0.05$) and FLUENT (incompressible) computations.

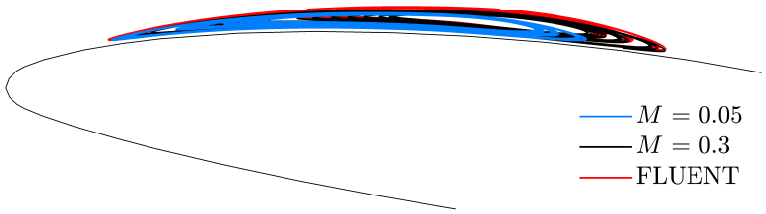

Figure A.5: Laminar separation bubble for $M = 0.05$ and $M = 0.3$ (DGSEM) and incompressible (FLUENT) at AOA = 8°, $R = 30c$.

the spatial and temporal discretization and the increased numerical dissipation of the upwind scheme.

A.1.2 Resolution – is it DNS?

The resolution in spectral element methods can be adjusted either through mesh refinement (h) or by increasing the polynomial order per element (p). The two meshes employed in this paper, *Grid 1* and *Grid 2*, are based on very different element sizes and polynomial orders (cf. 5.1). For 4° incidence, Nelson et al. [76] reports a grid-converged solution for a polynomial order of $P = 12$ on *Grid 1*. Because the flow transitions to turbulence at higher angles of attack, we compare time-averaged results of the coarser

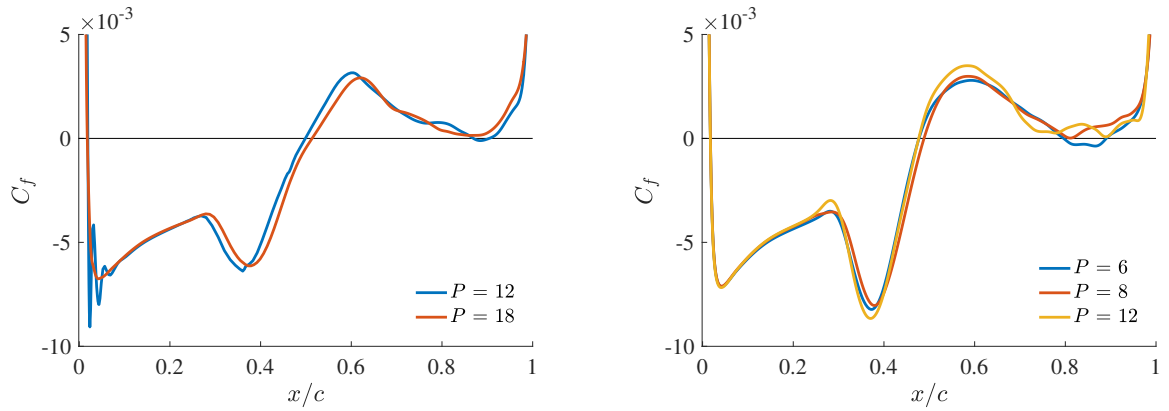

(a) *Grid 1* (b) *Grid 2*

Figure A.6: Time-averaged leading-edge skin friction for *Grid 1* and *Grid 2* at different polynomial orders. $Re_c = 20{,}000$, AOA $= 8°$.

Grid 1 and the refined *Grid 2* at different polynomial orders for 8° incidence. At this angle, the wind tunnel experiments at USC and the computations deviate considerably as the experiment is still in the laminar regime below α_{crit} while the DNS simulations has already become turbulent.

We assess the fidelity of the numerical results by comparison of the skin friction coefficient for different resolutions. Figure A.6(a) shows that at a polynomial order of $N = 12$, resolution at the airfoil's leading edge is insufficient and causes spurious, numerical oscillations in the solution. Although of considerable amplitude, these oscillations remain a local artifact and do not affect the results significantly in comparison to the converged solution at $N = 18$. The higher mesh refinement of *Grid 2* requires lower polynomial orders to reach a converged solution and the skin friction coefficients plotted in figure A.6(b) show good agreement for polynomial orders $N = 4$ – $N = 8$. The minor deviations can be attributed to the finite number of samples collected for temporal statistics. Note that differences between figure A.6(a) and (b) stem from a larger buffer layer region in *Grid 1* that results in reduced feedback of waves from the wake.

Table A.3: Lift and drag coefficients for AOA = 4° and different domain sizes.

Domain radius	C_l	$C_{l,p}$	$C_{l,f}$	C_d	$C_{d,p}$	$C_{d,f}$
$3.5c$	0.434	0.433	0.001	0.055	0.036	0.019
$30c$	0.463	0.462	0.001	0.054	0.036	0.019

Given that no filter is employed in either of the simulations and the solution shows convergence, we consider the results presented in this paper DNS with the exception of the case at 10°, which show some under-resolution at the leading edge and should therefore be considered implicit LES.

A.1.3 Domain size

We assess the effect of the Riemannian free-stream boundaries on the solution by comparing the aerodynamic forces, pressure and skin friction coefficients for different sizes of the computational domain for several angles of attack.

Figure A.7 illustrates the lift and drag coefficient for the flow at 4° incidence and domain radii from $R = 3.5c$ to $R = 50c$. Corresponding pressure and skin friction distributions over the wing are plotted in figure A.8 for $R = 3.5c$ and $30c$. The free-stream boundaries show a strong impact on the pressure coefficient at the leading edge, which is significantly lower for the larger domain and indicates that the proximity of the boundaries for $R = 3.5c$ forces the flow in this region. The pressure deviation is reflected in the trend of the lifting force with deviations of the time-averaged solution of 6% between small and large domains (see table A.3). As the discrepancies are mainly caused by the differences in the pressure distribution, the drag force shows only minor variations between the cases and converges more quickly. The strongly sinusoidal time dependency of the forces is maintained for all domain radii.

Because the magnitude of the pressure and friction forces increases with the

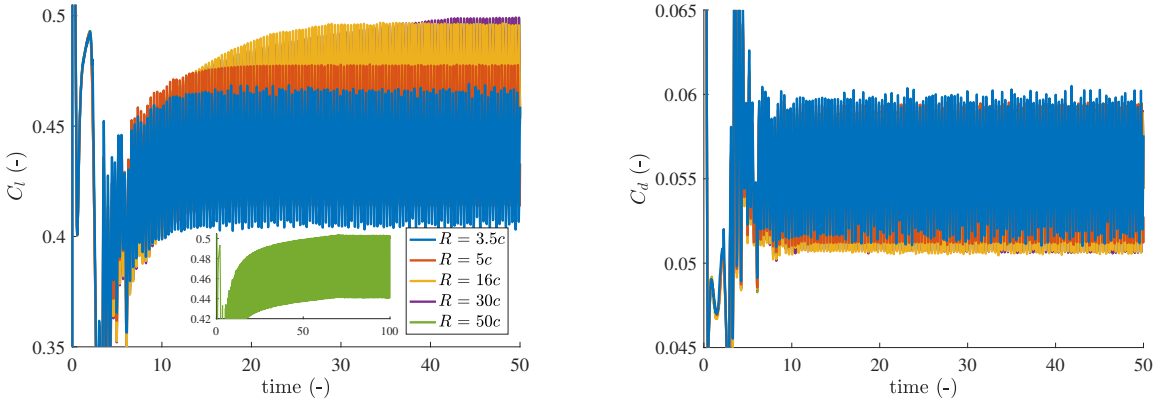

(a) Lift coefficient (b) Drag coefficient

Figure A.7: Lift and drag coefficients over time for different computational domain sizes and AOA = 4°, $M = 0.3$.

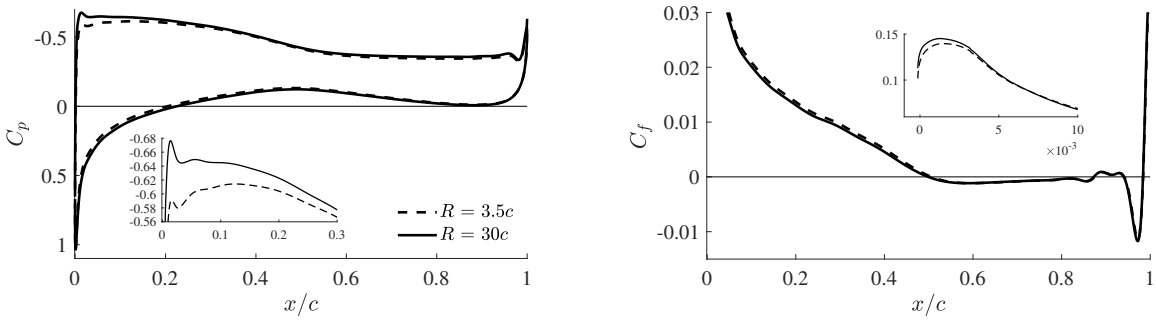

(a) Pressure coefficient (b) Skin friction coefficient

Figure A.8: Time-averaged pressure and skin friction coefficients for $R = 3.5c$ and $R = 30c$ at AOA = 4°, $M = 0.3$.

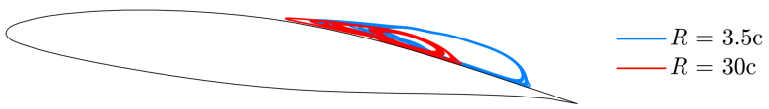

Figure A.9: Laminar separation bubble for domain radii $R = 3.5c$ and $R = 30c$ at AOA $= 7°$, $M = 0.3$.

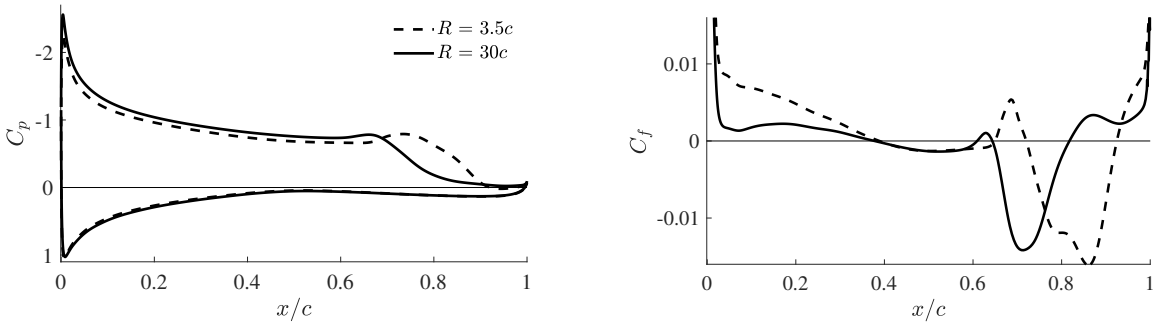

(a) Pressure coefficient

(b) Skin friction coefficient

Figure A.10: Time-averaged pressure and skin friction coefficients for $R = 3.5c$ and $R = 30c$ at AOA $= 7°$, $M = 0.3$.

flow angle, the influence of the free-stream boundaries also becomes more distinct. For 7° incidence, the separated boundary layer reattaches at the rear of the airfoil and forms a local LSB. Streamlines of the time-averaged solution within the separation bubble are plotted in figure A.9 for domain sizes of $R = 3.5c$ and $R = 30c$. The LSB is significantly larger in the smaller domain where the free-stream boundaries impact the solution stronger by forcing the flow. The difference in LSB sizes is distinctly visible in the time-averaged profiles of the surface pressure and skin friction coefficients, where both, C_p and C_f, show the shift of the reattachment point of the LSB (see figure A.10). Despite these significant differences in the flow topology, the time-averaged lift coefficient deviates only by 1.5%, while the drag force differs by more than 40% (see table A.4). Note that the magnitude of the drag is only about 5% of the lift force and hence is more susceptible to such changes.

The effect of free-stream boundaries on the flow topology is even more pro-

Table A.4: Lift and drag coefficients for AOA = 7° and different domain sizes.

Domain radius	C_l	$C_{l,p}$	$C_{l,f}$	C_d	$C_{d,p}$	$C_{d,f}$
$3.5c$	0.931	0.928	0.002	0.074	0.062	0.012
$30c$	0.946	0.944	0.002	0.052	0.041	0.011

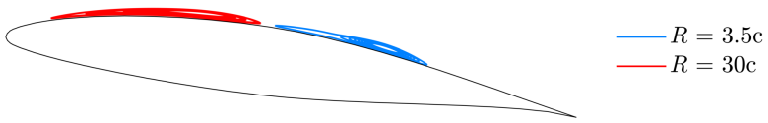

Figure A.11: Laminar separation bubble for domain radii $R = 3.5c$ and $R = 30c$ at AOA = 8°, $M = 0.3$.

nounced at 8° incidence, where the location of the LSB completely shifts between the front and the rear side of the airfoil (see figure A.11). This, again, is reflected in the surface pressure and the skin friction coefficient (see figure A.12), but curiously does not translate into a significant change in the integrated lift or the drag force, as summarized in table A.5. The reason is that the bubble height is small and hence only slightly changes the pressure distribution, which remains approximately constant throughout separated flow regions. Given that both lift and drag coefficients are dominated by the pressure force (see table A.5), the location of the LSB has only a limited affect on the lift as long as the bubble remains slender.

The parametric study of two-dimensional Navier-Stokes simulations show that although the LSB location can be notably affected by changes in domain size, resolution, and Mach number, the results do not indicate that any of the tested parameters move the critical angle of attack to higher values. Particularly, the good agreement

Table A.5: Lift and drag coefficients for AOA = 8° and different domain sizes.

Domain radius	C_l	$C_{l,p}$	$C_{l,f}$	C_d	$C_{d,p}$	$C_{d,f}$
$3.5c$	0.989	0.987	0.002	0.064	0.053	0.011
$30c$	0.962	0.961	0.002	0.058	0.047	0.010

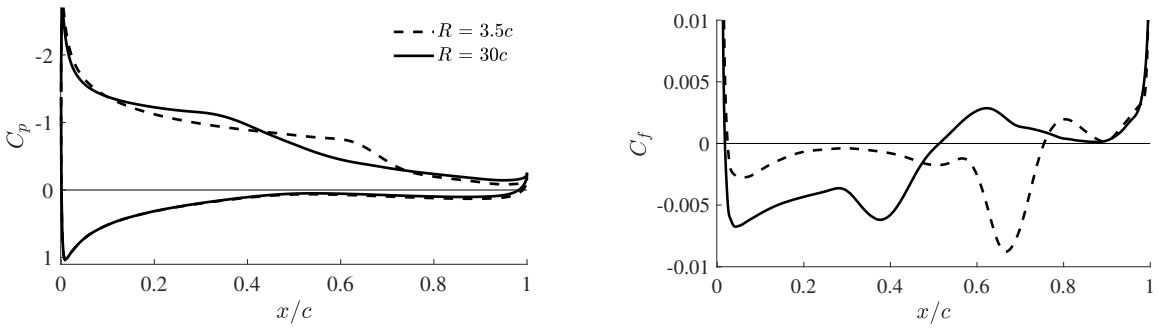

(a) Pressure coefficient

(b) Skin friction coefficient

Figure A.12: Time-averaged pressure and skin friction coefficients for $R = 3.5c$ and $R = 30c$ at AOA = 8°, $M = 0.3$.

between DGSEM and FLUENT simulations imply that the flow at 8° incidence has converged to a reasonable level across different numerical solvers. We therefore consider the high-order results presented in this paper to be high-fidelity DNS.

Appendix B

Objective early identification of kinematic instabilities in shear flows

B.1 Proof of $\dot{\kappa}_t = -\partial_{xx} v$

Following Serra et al. [43], the material curvature rate of material lines parametrized by arc-length is

$$\dot{\kappa}_t = \langle (\nabla \mathbf{S}\mathbf{r}')\mathbf{r}', \mathbf{R}\mathbf{r}' \rangle - \frac{1}{2}\langle \nabla\omega, \mathbf{r}' \rangle - 3\kappa_0 \langle \mathbf{r}', \mathbf{S}\mathbf{r}' \rangle, \tag{B.1}$$

with the rate-of-strain tensor $\mathbf{S} = \frac{1}{2}(\nabla\mathbf{u} + \nabla\mathbf{u}^\top)$, the local tangent vector $\mathbf{r}', |\mathbf{r}'| = 1$, and $\mathbf{R}$ is a rotation matrix defined according to (7.2).

We now separate the right-hand side of (B.1) into 3 parts and simplify each term separately under the assumption $\mathbf{r}' = [1, 0]^\top$.

Evaluation of the first term: $\langle (\nabla \mathbf{S}\mathbf{r}')\mathbf{r}', \mathbf{R}\mathbf{r}' \rangle$

$$
\begin{aligned}
\nabla \mathbf{S}\mathbf{r}' &= \partial_x \mathbf{S} r'_x + \partial_y \mathbf{S} r'_y \\
&= \partial_x \begin{bmatrix} \partial_x u & (\partial_y u + \partial_x v)/2 \\ (\partial_x v + \partial_y u)/2 & \partial_y v \end{bmatrix} r'_x + \partial_y \begin{bmatrix} \partial_x u & (\partial_y u + \partial_x v)/2 \\ (\partial_x v + \partial_y u)/2 & \partial_y v \end{bmatrix} r'_y \\
&= \begin{bmatrix} \partial_{xx} u r'_x & r'_x(\partial_{yx} u + \partial_{xx} v)/2 \\ r'_x(\partial_{xx} v + \partial_{yx} u)/2 & \partial_{yx} v r'_x \end{bmatrix} + \begin{bmatrix} \partial_{xy} u r'_y & r'_y(\partial_{yy} u + \partial_{xy} v)/2 \\ r'_y(\partial_{xy} v + \partial_{yy} u)/2 & \partial_{yy} v r'_y \end{bmatrix}
\end{aligned} \tag{B.2}
$$

$$
\begin{aligned}
(\nabla \mathbf{S}\mathbf{r}')\mathbf{r}' &= \begin{bmatrix} \partial_{xx} u r'^2_x + r'_x r'_y(\partial_{yx} u + \partial_{xx} v)/2 \\ r'^2_x(\partial_{xx} v + \partial_{yx} u)/2 + \partial_{yx} v r'_x r'_y \end{bmatrix} + \begin{bmatrix} \partial_{xy} u r'_y r'_x + r'^2_y(\partial_{yy} u + \partial_{xy} v)/2 \\ r'_y r'_x(\partial_{xy} v + \partial_{yy} u)/2 + \partial_{yy} v r'^2_y \end{bmatrix} \\
&= \begin{bmatrix} \partial_{xx} u r'^2_x + r'_x r'_y(\partial_{yx} u + \partial_{xx} v)/2 + \partial_{xy} u r'_y r'_x + r'^2_y(\partial_{yy} u + \partial_{xy} v)/2 \\ r'^2_x(\partial_{xx} v + \partial_{yx} u)/2 + \partial_{yx} v r'_x r'_y + r'_y r'_x(\partial_{xy} v + \partial_{yy} u)/2 + \partial_{yy} v r'^2_y \end{bmatrix}
\end{aligned} \tag{B.3}
$$

$$
\begin{aligned}
\langle (\nabla \mathbf{S}\mathbf{r}')\mathbf{r}', \mathbf{R}\mathbf{r}' \rangle = {} & \partial_{xx} u r'^2_x r'_y + r'_x r'^2_y(\partial_{yx} u + \partial_{xx} v)/2 + \partial_{xy} u r'^2_y r'_x + r'^3_y(\partial_{yy} u + \partial_{xy} v)/2 \\
& - r'^3_x(\partial_{xx} v + \partial_{yx} u)/2 - \partial_{yx} v r'^2_x r'_y - r'_y r'^2_x(\partial_{xy} v + \partial_{yy} u)/2 - \partial_{yy} v r'^2_y r'_x
\end{aligned} \tag{B.4}
$$

For a tangent vector $\mathbf{r}' = [1, 0]^\top$, (B.4) can be rewritten as

$$
\langle (\nabla \mathbf{S}\mathbf{r}')\mathbf{r}', \mathbf{R}\mathbf{r}' \rangle = -(\partial_{xx} v + \partial_{yx} u)/2. \tag{B.5}
$$

Evaluation of the second term: $-\frac{1}{2}\langle \nabla\omega, \mathbf{r}' \rangle$

$$
-\frac{1}{2}\langle \nabla\omega, \mathbf{r}' \rangle = -(\partial_x \omega r'_x + \partial_y \omega r'_y)/2 \tag{B.6}
$$

Again, we assume a tangent vector $\mathbf{r}' = [1, 0]^\top$, which simplifies (B.6) to

$$
-\frac{1}{2}\langle \nabla\omega, \mathbf{r}' \rangle = -\partial_x \omega/2. \tag{B.7}
$$

Evaluation of the third term: $-3\kappa_0\langle \mathbf{r}', \mathbf{S}\mathbf{r}'\rangle$

$$\mathbf{S}\mathbf{r}' = \begin{bmatrix} \partial_x u r'_x + r'_y(\partial_y u + \partial_x v)/2 \\ r'_x(\partial_x v + \partial_y u)/2 + \partial_y v r'_y \end{bmatrix} \tag{B.8}$$

$$-3\kappa_0\langle \mathbf{r}', \mathbf{S}\mathbf{r}'\rangle = -3\kappa_0(\partial_x u r'^2_x + r'_y r'_x(\partial_y u + \partial_x v)/2 + r'_x r'_y(\partial_x v + \partial_y u)/2 + \partial_y v r'^2_y) \tag{B.9}$$

Again, simplification with $\mathbf{r}' = [1, 0]^\top$ leads to

$$-3\kappa_0\langle \mathbf{r}', \mathbf{S}\mathbf{r}'\rangle = -3\kappa_0\partial_x u, \tag{B.10}$$

where the initial curvature κ_0 is also zero so that

$$-3\kappa_0\langle \mathbf{r}', \mathbf{S}\mathbf{r}'\rangle = 0. \tag{B.11}$$

Substituting the three simplified terms back into (B.1) yields

$$\dot{\kappa}_t = \langle(\nabla \mathbf{S}\mathbf{r}')\mathbf{r}', \mathbf{R}\mathbf{r}'\rangle - \frac{1}{2}\langle \nabla\omega, \mathbf{r}'\rangle - 3\kappa_0\langle \mathbf{r}', \mathbf{S}\mathbf{r}'\rangle = -\frac{1}{2}(\partial_{xx} v + \partial_{yx} u + \partial_x \omega), \tag{B.12}$$

and with $\omega = \partial_x v - \partial_y u$ it follows that

$$\dot{\kappa}_t = -\frac{1}{2}\partial_x(\partial_x v + \partial_y u + \omega) = -\frac{1}{2}\partial_x(\partial_x v + \partial_y u + \partial_x v - \partial_y u) = -\partial_{xx} v. \tag{B.13}$$

B.2 Proof of Theorem 1

Here we derive an analytic expression for the curvature change $\bar{\kappa}_{t_0}^{t_0+T}$ in perturbed parallel shear flows of the form

$$\mathbf{u}_\epsilon = \mathbf{u_0} + \epsilon \mathbf{u}', \quad 0 < \epsilon \ll 1, \tag{B.14}$$

where $\mathbf{u_0} = [U(y), 0]^\top$ is the base flow and $\mathbf{u}' = \mathrm{Re}([\hat{u}(y), \hat{v}(y)]e^{i(kx-\omega t)})$ is the perturbation, whose components are

$$\begin{aligned} u' &= e^{\omega_i t}\left[\hat{u}_r \cos(kx - \omega_r t) - \hat{u}_i \sin(kx - \omega_r t)\right], \\ v' &= e^{\omega_i t}\left[\hat{v}_r \cos(kx - \omega_r t) - \hat{v}_i \sin(kx - \omega_r t)\right]. \end{aligned} \tag{B.15}$$

Here, $\hat{u} = \hat{u}_r + i\hat{u}_i,\ \hat{v} = \hat{v}_r + i\hat{v}_i$ are complex amplitudes, $\omega = \omega_r + i\omega_i$ is the complex frequency and k the real wave number. Because analytic solutions of of the flow map ${}_\epsilon\mathbf{\Phi}$ induced by $\mathbf{u}_\epsilon$ are not available, we first seek an analytic approximation of ${}_\epsilon\mathbf{\Phi}$ by neglecting $\mathcal{O}(\epsilon^2)$ terms. We define the flow map of the base flow and the perturbed flows as

$$\begin{aligned} {}_{\mathbf{0}}\mathbf{\Phi}_{t_0}^{t_0+T}(\mathbf{x_0}) &= \mathbf{x}_0 + \int_{t_0}^{t_0+T} \mathbf{u_0}\left({}_{\mathbf{0}}\mathbf{\Phi}_{t_0}^{\tau}(\mathbf{x_0}), \tau\right) \mathrm{d}\tau, \\ {}_{\epsilon}\mathbf{\Phi}_{t_0}^{t_0+T}(\mathbf{x_0}) &= \mathbf{x}_0 + \int_{t_0}^{t_0+T} \mathbf{u}_\epsilon\left({}_{\epsilon}\mathbf{\Phi}_{t_0}^{\tau}(\mathbf{x_0}), \tau\right) \mathrm{d}\tau. \end{aligned} \tag{B.16}$$

Computing a Taylor expansion of ${}_\epsilon\mathbf{\Phi}$ with respect to ϵ, we obtain

$${}_{\epsilon}\mathbf{\Phi}_{t_0}^{t_0+T}(\mathbf{x_0}) - {}_{\mathbf{0}}\mathbf{\Phi}_{t_0}^{t_0+T}(\mathbf{x_0}) = \underbrace{\frac{d}{d\epsilon}{}_{\epsilon}\mathbf{\Phi}_{t_0}^{t_0+T}(\mathbf{x_0})|_{\epsilon=0}}_{\mathbf{A}_{t_0}^{t_0+T}(\mathbf{x_0})}\epsilon + \mathcal{O}(\epsilon^2), \tag{B.17}$$

where $\mathbf{A}_{t_0}^{t_0+T}(\mathbf{x_0})$ is a vector governing the leading order deviations between trajectories of the base flow and the perturbed flow. From equations (B.16-B.17), we find that $\mathbf{A}_{t_0}^{t_0+T}(\mathbf{x_0})$ satisfies the linear non-autonomous vectorial differential equation

$$\begin{cases} \dot{\mathbf{A}}_{t_0}^{t}(\mathbf{x_0}) = \nabla\mathbf{u_0}({}_{\mathbf{0}}\mathbf{\Phi}_{t_0}^{t}(\mathbf{x_0}))\mathbf{A}_{t_0}^{t}(\mathbf{x_0}) + \mathbf{u}'({}_{\mathbf{0}}\mathbf{\Phi}_{t_0}^{t}(\mathbf{x_0}), t) \\ \mathbf{A}_{t_0}^{t_0}(\mathbf{x_0}) = \mathbf{0} \\ {}_{\mathbf{0}}\mathbf{\Phi}_{t_0}^{t}(\mathbf{x_0}) = \mathbf{x_0} + \mathbf{u_0}(\mathbf{x_0})(t - t_0). \end{cases} \tag{B.18}$$

The dynamic matrix of equation (B.18) is the Jacobian of the base flow, while the forcing term is the perturbation, both of which evaluated along trajectories of the base flow. These terms as well as (B.18) admit analytic solutions, hence providing the

following analytic leading order approximation of the perturbed flow map

$$
\begin{aligned}
{}_{\epsilon}\mathbf{\Phi}_{t_0}^{t_0+T}(\mathbf{x_0}) &= {}_{\mathbf{0}}\mathbf{\Phi}_{t_0}^{t_0+T}(\mathbf{x_0}) + \mathbf{A}_{t_0}^{t_0+T}(\mathbf{x_0})\epsilon + \mathcal{O}(\epsilon^2) \\
&= \begin{bmatrix} x_0 + U(y_0)T + \epsilon\left(f_1(y_0)\hat{u}_r(y_0) + f_2(y_0)\hat{u}_i(y_0)\right)/g(y_0) \\ y_0 + \epsilon\left(f_5(y_0)\hat{v}_r(y_0) + f_6(y_0)\hat{v}_i(y_0)\right)/g(y_0) \end{bmatrix} \\
&+ \begin{bmatrix} \epsilon\left(f_3(y_0)\hat{v}_r(y_0)\,\partial_y U(y_0) + f_4(y_0)\hat{v}_i(y_0)\,\partial_y U(y_0)\right)/g^2(y_0) \\ 0 \end{bmatrix} + \mathcal{O}(\epsilon^2),
\end{aligned}
\tag{B.19}
$$

where

$$
\begin{aligned}
f_1 &= -e^{\omega_i t_0}\omega_i \cos(kx_0 - \omega_r t_0) + e^{\omega_i t_0}\Big(\omega_r - kU(y_0)\Big)\sin(kx_0 - \omega_r t_0) \\
&+ e^{\omega_i(t_0+T)}\omega_i \cos(kx_0 - \omega_r(t_0+T) + kU(y_0)T) \\
&- e^{\omega_i(t_0+T)}\Big(\omega_r - kU(y_0)\Big)\sin(kx_0 - \omega_r(t_0+T) + kU(y_0)T),
\end{aligned}
\tag{B.20}
$$

$$
\begin{aligned}
f_2 &= e^{\omega_i t_0}\omega_i \sin(kx_0 - \omega_r t_0) + e^{\omega_i t_0}\Big(\omega_r - kU(y_0)\Big)\cos(kx_0 - \omega_r t_0) \\
&- e^{\omega_i(t_0+T)}\omega_i \sin(kx_0 - \omega_r(t_0+T) + kU(y_0)T) \\
&- e^{\omega_i(t_0+T)}\Big(\omega_r - kU(y_0)\Big)\cos(kx_0 - \omega_r(t_0+T) + kU(y_0)T),
\end{aligned}
\tag{B.21}
$$

$$
\begin{aligned}
f_3 &= -e^{\omega_i t_0}\Big(\omega_i^2 + \omega_i^3 T - \omega_r^2 + \omega_i\omega_r^2 T - k^2U^2(y_0) + \omega_i k^2 U^2(y_0)T \\
&+ 2\omega_r kU(y_0) - 2\omega_i\omega_r kU(y_0)T\Big)\cos(kx_0 - \omega_r t_0) \\
&+ e^{\omega_i t_0}\Big(2\omega_i\omega_r + \omega_i^2\omega_r T + \omega_r^3 T - k^3U^3(y_0)T + 3\omega_r k^2U^2(y_0)T - 2\omega_i kU(y_0) \\
&- \omega_i^2 kU(y_0)T - 3\omega_r^2 kU(y_0)T\Big)\sin(kx_0 - \omega_r t_0) \\
&+ e^{\omega_i(t_0+T)}\Big(\omega_i^2 - \omega_r^2 - k^2U^2(y_0) + 2\omega_r kU(y_0)\Big)\cos(kx_0 - \omega_r(t_0+T) + kU(y_0)T) \\
&- e^{\omega_i(t_0+T)}\Big(2\omega_i\omega_r - 2\omega_i kU(y_0)\Big)\sin(kx_0 - \omega_r(t_0+T) + kU(y_0)T),
\end{aligned}
\tag{B.22}
$$

$$
\begin{aligned}
f_4 = {} & e^{\omega_i t_0}\Big(\omega_i^2 + \omega_i^3 T - \omega_r^2 + \omega_i \omega_r^2 T - k^2 U^2(y_0) + \omega_i k^2 U^2(y_0) T \\
& + 2\omega_r k U(y_0) - 2\omega_i \omega_r k U(y_0) T\Big) \sin(kx_0 - \omega_r t_0) \\
& + e^{\omega_i t_0}\Big(2\omega_i \omega_r + \omega_i^2 \omega_r T + \omega_r^3 T - k^3 U^3(y_0) T + 3\omega_r k^2 U^2(y_0) T - 2\omega_i k U(y_0) \\
& - \omega_i^2 k U(y_0) T - 3\omega_r^2 k U(y_0) T\Big) \cos(kx_0 - \omega_r t_0) \\
& - e^{\omega_i (t_0+T)}\Big(\omega_i^2 - \omega_r^2 - k^2 U^2(y_0) + 2\omega_r k U(y_0)\Big) \sin(kx_0 - \omega_r(t_0+T) + kU(y_0)T) \\
& - e^{\omega_i (t_0+T)}\Big(2\omega_i \omega_r - 2\omega_i k U(y_0)\Big) \cos(kx_0 - \omega_r(t_0+T) + kU(y_0)T),
\end{aligned}
\tag{B.23}
$$

$$
\begin{aligned}
f_5 = {} & -e^{\omega_i t_0}\omega_i \cos(kx_0 - \omega_r t_0) + e^{\omega_i t_0}\Big(\omega_r - kU(y_0)\Big) \sin(kx_0 - \omega_r t_0) \\
& + e^{\omega_i (t_0+T)}\omega_i \cos(kx_0 - \omega_r(t_0+T) + kU(y_0)T) \\
& - e^{\omega_i (t_0+T)}\Big(\omega_r - kU(y_0)\Big) \sin(kx_0 - \omega_r(t_0+T) + kU(y_0)T),
\end{aligned}
\tag{B.24}
$$

$$
\begin{aligned}
f_6 = {} & e^{\omega_i t_0}\omega_i \sin(kx_0 - \omega_r t_0) + e^{\omega_i t_0}\Big(\omega_r - kU(y_0)\Big) \cos(kx_0 - \omega_r t_0) \\
& - e^{\omega_i (t_0+T)}\omega_i \sin(kx_0 - \omega_r(t_0+T) + kU(y_0)T) \\
& - e^{\omega_i (t_0+T)}\Big(\omega_r - kU(y_0)\Big) \cos(kx_0 - \omega_r(t_0+T) + kU(y_0)T),
\end{aligned}
\tag{B.25}
$$

$$
g = \omega_i^2 + \omega_r^2 - 2\omega_r k U(y_0) + k^2 U^2(y_0). \tag{B.26}
$$

The baseflow profile $U = U(y_0)$ and the perturbation modes $\hat{u}(y_0)$ and $\hat{v}(y_0)$ are functions of the initial y-location of the tracers.

With the flow map of the perturbed flow available, we can compute the deformation gradient and Cauchy-Green strain tensor and apply (7.1) to calculate the Lagrangian curvature change. We determine the leading order terms of $\bar{\kappa}_{t_0}^{t_0+T}$, for the case of $\mathbf{r}' = [1,\, 0]^\top$ and $\kappa_0 = 0$, by performing a Taylor series expansion in the perturbation ϵ and collecting the first-order terms. To the first order, the curvature change

for horizontal material lines in a perturbed parallel shear flow can be computed as

$$\bar{\kappa}_{t_0}^{t_0+T} = \frac{k^2}{\omega_i^2+\omega_r^2-2\omega_r kU(y_0)+k^2U^2(y_0)}\Bigg[\\ e^{\omega_i t_0}\Big(\Big(-\omega_i\hat{v}_r(y_0)+(\omega_r-kU(y_0))\hat{v}_i(y_0)\Big)\cos(kx_0-\omega_r t_0) \\ +\Big(\omega_i\hat{v}_i(y_0)+(\omega_r-kU(y_0))\hat{v}_r(y_0)\Big)\sin(kx_0-\omega_r t_0)\Big) \\ +e^{\omega_i(t_0+T)}\Big(\Big(\omega_i\hat{v}_r(y_0)-(\omega_r-kU(y_0))\hat{v}_i(y_0)\Big)\cos(kx_0-\omega_r(t_0+T)+kU(y_0)T) \\ -\Big(\omega_i\hat{v}_i(y_0)+(\omega_r-kU(y_0))\hat{v}_r(y_0)\Big)\sin(kx_0-\omega_r(t_0+T)+kU(y_0)T)\Big)\Bigg]\epsilon+\mathcal{O}(\epsilon^2). \tag{B.27}$$

This completes the proof of Theorem 1.

We check the analytic solutions of the flow map (B.19) and the curvature scalar (B.27) for a material line advected under $\mathbf{u_0} = [(1+\tanh(y))/2, 0]^\top$ (hyperbolic tangent shear profile) and time-dependent perturbations of the form $\mathbf{u}' = \mathrm{Re}([\hat{u}(y), \hat{v}(y)]e^{i(kx-\omega t)})$. The tracers are initialized at $y_0 = 0$ and $x_0 \in [0, 10]$ and the parameters are chosen to be $k = 1$, $\omega_r = 2$, $\omega_i = 0.1$, $\epsilon = 1\%$, and $T = 20$. The eigenmode shape functions are set to $\hat{u}_r(y) = \hat{u}_i(y) = -\tanh(y)\,\mathrm{sech}(y)/k$ and $\hat{v}_r(y) = -\hat{v}_i(y) = \mathrm{sech}(y)$, such that a solenoidal velocity field is constructed. In figure B.1, the analytic solutions from (B.19) and (B.27) are compared to their numerical results from integrating $\mathbf{u}_\epsilon = \mathbf{u_0} + \epsilon\mathbf{u}'$ described above. The deviations are small confirming the validity of our analytical approximation.

The temporal development of the curvature scalar (B.27) is illustrated in figure B.2 together with the velocity $v = \mathrm{Re}(\hat{v}(y)e^{i(kx-\omega t)})$ for positive (growing perturbation) and negative (ceasing perturbation) temporal growth rates. The set of parameters is the same as introduced above, but for a single point $[x_0, y_0] = [1, 0]$ instead of a material line.

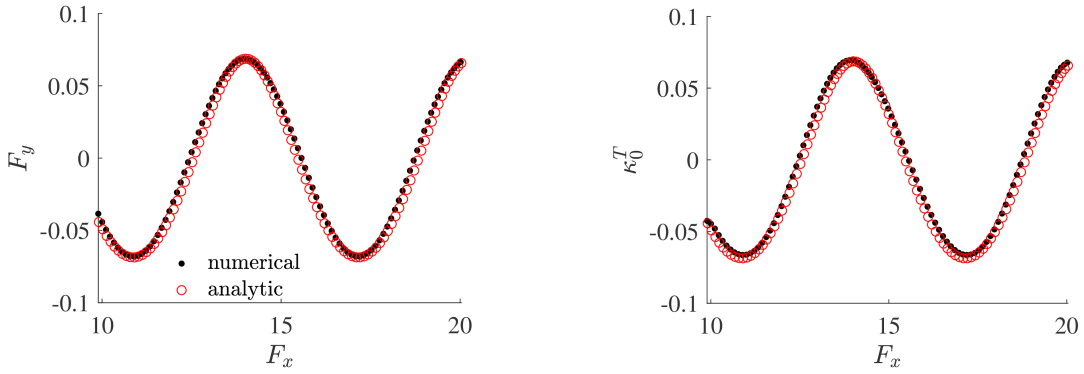

(a) Flow map (b) Curvature scalar

Figure B.1: Comparison of analytic and numerical approximations of the flow map ${}_\epsilon\mathbf{\Phi}_0^{20}$ and the curvature scalar for $\bar{\kappa}_0^{20}$. F_x and F_y are the x and y components of the flow map $\mathbf{\Phi}$. Parameters: $\mathbf{u_0} = [(1+\tanh(y))/2, 0]^\top$, $y_0 = 0$, $k = 1$, $\omega_r = 2$, $\omega_i = 0.1$, $\epsilon = 1\%$, and $T = 20$.

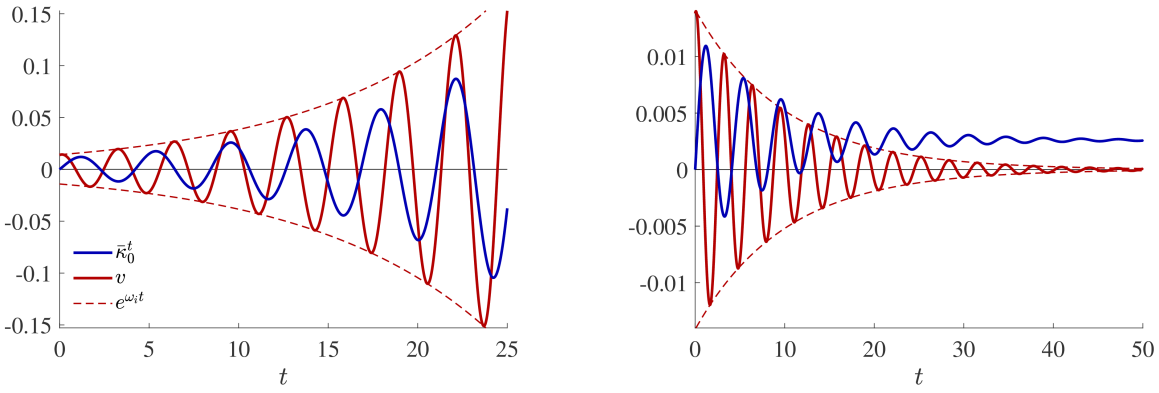

(a) $\omega_i > 0$ (b) $\omega_i < 0$

Figure B.2: Comparison of analytic curvature scalar (B.27), the velocity $v = \mathrm{Re}(\hat{v}(y)e^{i(kx-\omega t)})$, and the envelope function $e^{\omega_i t}$. Parameters: $\mathbf{u_0} = [(1+\tanh(y))/2, 0]^\top$, $y_0 = 0$, $k = 1$, $\omega_r = 2$, $|\omega_i| = 0.1$, $\epsilon = 1\%$.

B.3 Material response to a traveling wave

B.3.1 Model problem: traveling sine wave

To understand the kinematic response of fluid material to a traveling wave in general, the exponentially growing velocity field of a traveling sine wave is considered and as given by $[u, v]^\top = [0, Ae^{\omega_i t} \sin(kc_r t - kx)]$. The wave amplitude, speed and wave number are set to $A = 0.01$, $c_r = 0.5$ and $k = 4.2$, respectively.

Integration of the kinematic equation yields the particle coordinates $x_p = \int_{t_0}^{t_1} u dt$ and $y_p = \int_{t_0}^{t_1} v dt$. Because $u = 0$ there is no motion of the fluid material in x-direction. If the velocity amplitude is constant ($\omega_i = 0$), then the y-location of a material line initialized at $y_p(t_0{=}0) = 0$ is

$$y_p(x,t) = \frac{A}{kc_r} \left[\cos(kx) - \cos(kc_r t - kx)\right]. \tag{B.28}$$

Hence, the wave length of this traveling material wave is the same as that of the velocity wave. The former, however, travels at half the phase speed as compared to the latter. This can be understand by inspecting the x-location of the particle mode evaluated at $y_p = 0$ from (B.28)

$$x\big|_{y_p=0} = \frac{1}{2} c_r t. \tag{B.29}$$

For an exponentially increasing velocity field ($\omega_i = 0.9$), the y-location of a material line initialized at $y_p(t_0{=}0) = 0$ is

$$y_p(x,t) = \frac{A}{\omega_i^2 + (kc_r)^2} \left[\omega_i \sin(kx) + kc_r \cos(kx) + \right. \tag{B.30}$$

$$\left. e^{\omega_i t}(\omega_i \sin(kc_r t - kx) - kc_r \cos(kc_r t - kx))\right]. \tag{B.31}$$

Asymptotically for $t \to \infty$, the material mode locks on to the velocity mode as is again

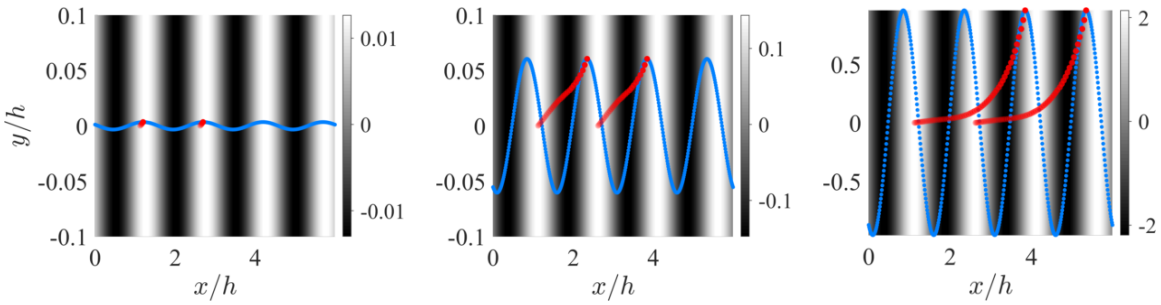

(a) $t = 0.3$ (b) $t = 3.0$ (c) $t = 6.0$

Figure B.3: (a–c) Development of a material line (blue) under the velocity field $[u, v]^\top = [0, Ae^{\omega_i t} \sin(kc_r t - kx)]$ (black-white) over time. Location history of Lagrangian curvature peaks in red.

understood by inspecting x evaluated at y_p=0.

$$\lim_{t\to\infty} x|_{y_p=0} = c_r t - \frac{1}{k} \arctan\left(\frac{kc_r}{\omega_i}\right). \tag{B.32}$$

Figure B.3(a–c) shows the development of a material line (blue) subject to an exponentially growing velocity mode (black-white), with the location history of curvature peaks in red. The x-location of the first curvature peak over time is shown in figure B.4, where the slope confirms that the curvature mode initially travels at half the phase speed of the velocity mode but accelerates until they move uniformly. The plots in (a) to (c) confirm the locking of the modes and shows that curvature and velocity peaks travel separated by the phase shift introduced in (B.32). If wavenumber and phase speed are known, the growth rate ω_i can therefore be computed solely based on the shift between the curvature and the velocity mode.

B.3.2 Traveling mode in the jet flow

The shifting of velocity and curvature modes for the jet flow is visualized in figure B.5. For a very short integration interval, the Lagrangian curvature field is approximately equal to $\dot{\kappa}_t$ and directly matches the pattern of the Eulerian transverse

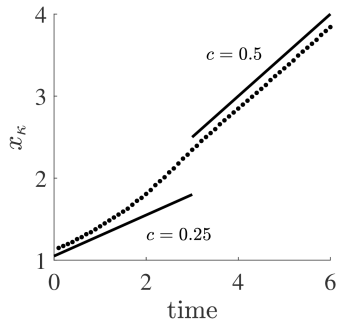

Figure B.4: X-locations of the first Lagrangian curvature peak (see figure B.3) over time. Phase velocity c (slopes) indicated as solid lines in black.

velocity. While the material line motion initially corresponds to v' (see figure B.5a), the modes develop a phase shift in the jet core and the outer region as the velocity modes travel relative to the Lagrangian particle trace (see figure B.5b). Only along the shear layer, where the phase speed closely matches the advection velocity of the fluid, extrema of $\bar{\kappa}_{t_0}^{t_0+T}$ and v' move together and result in much larger deformations of the particle trace than in the core flow (compare right plots of figure B.5b). From a Lagrangian perspective, the fluid particles in the shear layer see the perturbation mode as standing wave and therefore diverge faster than particles outside or inside the jet.

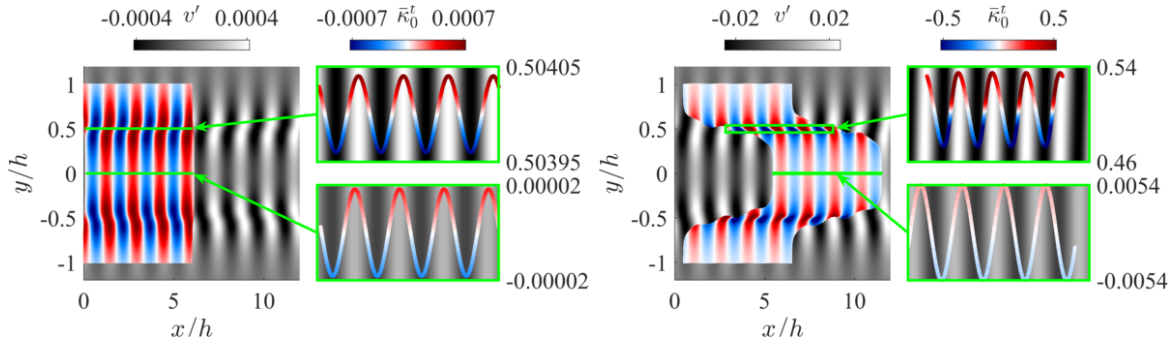

(a) $t = 0.1$ (b) $t = 5.0$

Figure B.5: Curvature scalar field $\bar{\kappa}_0^t$ (blue-white-red) graphed over transverse velocity perturbation field v' (black-white) at times $t = 0.1$ (a) and $t = 5.0$ (b). Initial perturbation with eigenmodes for wavenumber $k_{pert} = 4.2$. (a) and (b) each have an overview plot on the left and detail plots of material lines along the shear layer and center line on the right. Location of material lines and detail plots pointed out by green arrows and boxes. Y-axis of detail plots is strongly stretched to show fluid particle motion (see green boxes). Note that the color maps are adjusted at each time step.

Bibliography

[1] M. Drela. XFOIL: An analysis and design system for low Reynolds number airfoils. In T. J. Mueller, editor, *Low Reynolds Number Aerodynamics*, pages 1–12, Berlin, Heidelberg, 1989. Springer Berlin Heidelberg. ISBN 978-3-642-84010-4.

[2] P. B. S. Lissaman. Low-Reynolds-number airfoils. *Annual Review of Fluid Mechanics*, 15(1):223–239, 1983. doi: 10.1146/annurev.fl.15.010183.001255.

[3] H. Schlichting and K. Gersten. *Boundary-Layer Theory*. Springer-Verlag, New York, 1999.

[4] Michael Amitay, Barton Smith, and Ari Glezer. Aerodynamic flow control using synthetic jet technology. *36th AIAA Aerospace Sciences Meeting and Exhibit*, 1998.

[5] Michael Amitay, Douglas R. Smith, Valdis Kibens, David E. Parekh, and Ari Glezer. Aerodynamic Flow Control over an Unconventional Airfoil Using Synthetic Jet Actuators. *AIAA Journal*, 39(3), March 2001.

[6] Ari Glezer and Michael Amitay. Synthetic Jets. *Annual review of fuid mechanics*, 34(1), 2002.

[7] A. Uranga, P.-O. Persson, M. Drela, and J. Peraire. Implicit large eddy simulation of transition to turbulence at low reynolds numbers using a discontinuous galerkin method. *International Journal for Numerical Methods in Engineering*, 87:232–261, 2011.

[8] P. A. Durbin. Some recent developments in turbulence closure modeling. *Annual Review of Fluid Mechanics*, 50(1):77–103, 2018. doi: 10.1146/annurev-fluid-122316-045020.

[9] D. Lee, T. Nonomura, A. Oyama, and K. Fujii. Comparison of numerical methods evaluating airfoil aerodynamic characteristics at low Reynolds number. *Journal of Aircraft*, 52(1):296–306, 2015. doi: 10.2514/1.C032721.

[10] R. S. Rogallo and P. Moin. Numerical simulation of turbulent flow. *Ann. Rev. Fluid Mech.*, 16:99–137, 1984.

[11] P. R. Spalart. Detached-eddy simulation. *Annual Review of Fluid Mechanics*, 41 (1):181–202, 2009. doi: 10.1146/annurev.fluid.010908.165130.

[12] P. Moin and K. Mahesh. Direct numerical simulation: a tool in turbulence research. *Ann. Rev. Fluid Mech.*, 30:539–578, 1998.

[13] David A. Kopriva. *Implementing Spectral Methods for Partial Differential Equations*. Springer, New York, 2009.

[14] J.S. Hesthaven and T. Warburton. *Nodal discontinuous Galerkin methods: algorithms, analysis, and applications*. Springer-Verlag, Berlin, 2008.

[15] A. Chaudhuri, G.B. Jacobs, W.S. Don, H. Abbassi, and F. Mashayek. Explicit discontinuous spectral element method with entropy generation based artificial viscosity for shocked viscous flows. *J. Comp. Phys.*, 32:99–117, 2017.

[16] G. J. Gassner, A. R. Winters, and D. A. Kopriva. Split form nodal discontinuous Galerkin schemes with summation-by-parts property for the compressible Euler equations. *Journal of Computational Physics*, 327:39–66, 2016.

[17] Bjoern F. Klose, Gustaaf B. Jacobs, and David A. Kopriva. Assessing standard and kinetic energy conserving volume fluxes in discontinuous Galerkin formulations for marginally resolved navier-stokes flows. *Computers & Fluids*, 205: 104557, 2020. ISSN 0045-7930. doi: https://doi.org/10.1016/j.compfluid.2020.104557.

[18] H. Shan, L. Jiang, and L. Chaoqun. Direct simulation of flow separation around NACA 0012 airfoil. *Computers & Fluids*, 34:1096–1114, 2005.

[19] L. E. Jones, R. D. Sandberg, and N. D. Sandham. Direct numerical simulations of forced and unforced separation bubbles on an airfoil at incidence. *Journal of Fluid Mechanics*, 602:175–207, 2008.

[20] L. E. Jones, R. D. Sandberg, and N. D. Sandham. Stability and receptivity characteristics of a laminar separation bubble on an aerofoil. *Journal of Fluid Mechanics*, 648:257–296, 2010.

[21] Wei Zhang, Wan Cheng, Wei Gao, Adnan Qamar, and Ravi Samtaney. Geometrical effects on the airfoil flow separation and transition. *Computers & Fluids*, 116:60 – 73, 2015.

[22] L. E. Jones and R. D. Sandberg. Numerical analysis of tonal airfoil self-noise and acoustic feedback-loops. *Journal of Sound and Vibration*, 330(25):6137 – 6152, 2011. doi: https://doi.org/10.1016/j.jsv.2011.07.009.

[23] R. D. Sandberg and L. E. Jones. Direct numerical simulations of low reynolds number flow over airfoils with trailing-edge serrations. *Journal of Sound and Vibration*, 330(16):3818 – 3831, 2011. doi: https://doi.org/10.1016/j.jsv.2011.02.005.

[24] J. H. Almutairi, L. E. Jones, and N. D. Sandham. Intermittent bursting of a laminar separation bubble on an airfoil. *AIAA Journal*, 48(2):414–426, 2010.

[25] Ponnampalam Balakumar. Direct numerical simulation of flows over an NACA-0012 airfoil at low and moderate reynolds numbers. *AIAA Fluid Dynamics Conference*, 47, June 2017.

[26] Douglas Serson, Julio R. Meneghini, and Spencer J. Sherwin. Direct numerical simulations of the flow around wings with spanwise waviness. *Journal of Fluid Mechanics*, 826:714–731, 2017. doi: 10.1017/jfm.2017.475.

[27] Miguel R. Visbal and Daniel J. Garmann. Dynamic stall of a finite-aspect-ratio wing. *AIAA Journal*, 57(3):962–977, 2019.

[28] M. Galbraith and M. Visbal. *Implicit Large Eddy Simulation of Low-Reynolds-Number Transitional Flow Past the SD7003 Airfoil*. 2010. doi: 10.2514/6.2010-4737.

[29] Miguel R. Visbal. Numerical investigation of deep dynamic stall of a plunging airfoil. *AIAA Journal*, 49(10):2152–2170, 2011.

[30] A. D. Beck, T. Bolemann, D. Flad, H. Frank, G. J. Gassner, F. Hindenlang, and C.-D. Munz. High-order discontinuous Galerkin spectral element methods for transitional and turbulent flow simulations. *International Journal for Numerical Methods in Fluids*, 76(8):522–548, 2014.

[31] Tamer A. Zaki, Jan G. Wissink, Wolfgang Rodi, and Paul A. Durbin. Direct numerical simulations of transition in a compressor cascade: the influence of free-stream turbulence. *Journal of Fluid Mechanics*, 665:57–98, 2010.

[32] Richard D. Sandberg, Vittorio Michelassi, Richard Pichler, Liwei Chen, and Roderick Johnstone. Compressible Direct Numerical Simulation of Low-Pressure Turbines – Part I: Methodology. *Journal of Turbomachinery*, 137(5), 05 2015. ISSN 0889-504X. doi: 10.1115/1.4028731.

[33] L. Joseph Herrig, James C. Emery, and John R. Erwin. Systematic two-dimensional cascade tests of naca 65-series compressor blades at low speeds. Naca technical note 3916, 1951.

[34] L. C. Wright. Blade selection for a modern axial-flow compressor. Nasa conference proceedings, 1974.

[35] J. Tank, B. F. Klose, G. Jacobs, and G. R. Spedding. Computer and laboratory studies on the aerodynamics of the NACA 65(1)-412 at Reynolds number 20 000. AIAA scitech 2019 forum, 2019.

[36] G Haller. Exact theory of unsteady separation for two-dimensional flows. *J. Fluid Mech.*, 512:357–311, 2004.

[37] M. Weldon, T. Peacock, G.B. Jacobs, M. Helu, and G. Haller. Experimental and numerical investigation of the kinematic theory of unsteady separation. *J. Fluid Mech.*, 611:1–11, 2008.

[38] G. Haller. Distinguished material surfaces and coherent structures in 3D fluid flows. *Physica D*, 149:248–277, 2001.

[39] G. Haller. Finding finite-time invariant manifolds in two-dimensional velocity fields. *Chaos*, 10:99, 2000.

[40] G. Haller. Lagrangian coherent stuctures from approximate velocity data. *Phys. Fluids*, 14:1851, 2006.

[41] George Haller. A variational theory of hyperbolic Lagrangian Coherent Structures. *Physica D*, 240(7), March 2011.

[42] S. C. Shadden, F. Lekien, and J. E. Marsden. Definition and properties of Lagrangian coherent structures from finite-time Lyapunov exponents in two-dimensional aperiodic flows. *Physica D*, 212:271–305, 2005.

[43] M. Serra, J. Vetel, and G. Haller. Exact theory of material spike formation in flow separation. *Journal of Fluids Mechanics*, 845:51–92, June 25 2018.

[44] J. H. Seo, F. Cadieux, R. Mittal, E. Deem, and L. Cattafesta. Effect of synthetic jet modulation schemes on the reduction of a laminar separation bubble. *Phys. Rev. Fluids*, 3(3), March 2018.

[45] P. Huerre and P. A. Monkewitz. Local and global instabilities in spatially developing flows. *Annual Review of Fluid Mechanics*, 22:473–537, January 1990.

[46] B. J. Bayly, S. A. Orszag, and T. Herbert. Instability mechanisms in shear-flow transition. *Annual Review of Fluid Mechanics*, 20(1):359–391, 1988.

[47] P. G. Drazin and W. H. Reid. *Hydrodynamic Stability*. Cambridge Monographs on Mechanics and Applied Mathematics. Cambridge University Press, Cambridge, second edition, 2003.

[48] P. J. Schmid. Nonmodal stability theory. *Annual Review of Fluid Mechanics*, 39 (1):129–162, 2007. doi: 10.1146/annurev.fluid.38.050304.092139.

[49] V. Theofilis. Global linear instability. *Annual Review of Fluid Mechanics*, 43: 319–352, 2011.

[50] P. J. Strykowski and K. R. Sreenivasan. On the formation and suppression of vortex 'shedding' at low Reynolds numbers. *Journal of Fluid Mechanics*, 218: 71–107, 1990.

[51] A. J. Bergou, S. Xu, and Z. J. Wang. Passive wing pitch reversal in insect flight. *Journal of Fluid Mechanics*, 591:321–337, 2007. doi: 10.1017/S0022112007008440.

[52] R. Ranjan, S. Unnikrishnan, and D. Gaitonde. A robust approach for stability analysis of complex flows using high-order Navier-Stokes solvers. *Journal of Computational Physics*, 403:109076, 2020. ISSN 0021-9991. doi: https://doi.org/10.1016/j.jcp.2019.109076.

[53] P. J. Schmid and D. S. Henningson. *Stability and Transition in Shear Flows*, volume 142 of *Applied Mathematical Sciences*. Springer, New York, NY, 2001.

[54] J. C. R. Hunt, A. A. Wray, and P. Moin, editors. *Eddies, stream, and convergence zones in turbulent flows*, Stanford University, Stanford, CA, 1987. Center for Turbulence Research. Report CTR-S88.

[55] J. Jeong and F. Hussain. On the identification of a vortex. *Journal of Fluid Mechanics*, 285:69–94, 1995.

[56] G. Haller. Lagrangian Coherent Structures. *Annual Review of Fluid Mechanics*, 47:137–162, August 28 2014.

[57] M. Serra and G. Haller. Objective Eulerian coherent structures. *Chaos*, 26(5): 053110, 2016.

[58] G. Haller, A. Hadjighasem, M. Farazmand, and F. Huhn. Defining coherent vortices objectively from the vorticity. *Journal of Fluid Mechanics*, 795:136–173, 2016.

[59] H. Babaee, M. Farazmand, G. Haller, and T. P. Sapsis. Reduced-order description of transient instabilities and computation of finite-time Lyapunov exponents. *Chaos*, 27(6):063103, 2017.

[60] H. Babaee and T. P. Sapsis. A minimization principle for the description of modes associated with finite-time instabilities. *Proceedings of the Royal Society A: Mathematical, Physical and Engineering Sciences*, 472(2186):20150779, 2016. doi: 10.1098/rspa.2015.0779.

[61] M. Serra, S. Crouzat, G. Simon, J. Vétel, and G. Haller. Material spike formation in highly unsteady separated flows. *Journal of Fluid Mechanics*, 883:A30, 2020. doi: 10.1017/jfm.2019.876.

[62] B. F. Klose, M. Serra, and G. B. Jacobs. Kinematics of Lagrangian flow separation in external aerodynamics. *AIAA Journal*, 58(5):1926–1938, 2020.

[63] M. Alam and N. D. Sandham. Direct numerical simulation of 'short' laminar separation bubbles with turbulent reattachment. *Journal of Fluid Mechanics*, 410:1–28, 2000. doi: 10.1017/S0022112099008976.

[64] D. A. Nelson and G. B. Jacobs. DG-FTLE: Lagrangian coherent structures with high-order discontinuous-Galerkin methods. *Journal of Computational Physics*, 295:65–86, August 2015.

[65] Gregor J. Gassner, Andrew R. Winters, Florian J. Hindenlang, and David A. Kopriva. The BR1 scheme is stable for the compressible Navier–Stokes equations. *Journal of Scientific Computing*, Apr 2018. ISSN 1573-7691. doi: 10.1007/s10915-018-0702-1.

[66] P. Roe. Approximate Riemann solvers, parameter vectors, and difference schemes. *Journal of Computational Physics*, 135(2):250–258, 1997.

[67] G. Gassner and D. A. Kopriva. A comparison of the dispersion and dissipation errors of Gauss and Gauss–Lobatto discontinuous Galerkin spectral element methods. *Society for Industrial and Applied Mathematics*, 33(5):2560–2579, 2011.

[68] D. A. Kopriva and G. Gassner. On the quadrature and weak form choices in collocation type discontinuous Galerkin spectral element methods. *Journal of Scientific Computing*, 44(2):136–155, 2010.

[69] Sergio Pirozzoli. Numerical Methods for High-Speed Flows. *Annual Review of Fluid Mechanics*, 43:163–194, 2011.

[70] David Flad and Gregor Gassner. On the use of kinetic energy preserving DG-schemes for large eddy simulation. *Journal of Computational Physics*, 350:782–795, 2017.

[71] Stephen B. Pope. *Turbulent Flows*. Cambridge University Press, New York, 2000.

[72] Atsushi Okajima. Strouhal numbers of rectangular cylinders. *Journal of Fluid Mechanics*, 123:379–398, October 1982.

[73] A. Sohankar, C. Norberg, and L. Davidson. Low-Reynolds-number flow around a square cylinder at incidence: study of blockage, onset of vortex shedding and outlet boundary condition. *International Journal for Numerical Methods in Fluids*, 26:39–56, December 4 1998.

[74] Rupad .M. Darekar and Spencer J. Sherwin. Flow past a square-section cylinder with a wavy stagnation face. *Journal of Fluid Mechanics*, 426:263–295, January 10 2001.

[75] Khosro Shahbazi, Paul F. Fischer, and C. Ross Ethier. high-order discontinuous Galerkin method for the unsteady incompressible Navier–Stokes equations. *Journal of Computational Physics*, 222:391–407, March 1 2007.

[76] D. A. Nelson, G. B. Jacobs, and D. A. Kopriva. Effect of Boundary Representation on Viscous, Separated Flows in a Discontinuous-Galerkin Navier-Stokes Solver. *Theoretical Computational Fluid Dynamics*, 30:363–385, March 30 2016.

[77] D. Stanescu and W.G. Habashi. 2N-storage low dissipation and dispersion Runge-Kutta schemes for computational acoustics. *Journal of Computational Physics*, 143(2):674 – 681, 1998.

[78] R. C. Moura, G. Mengaldo, J. Peiro, and S. J. Sherwin. On the eddy-resolving capability of high-order discontinuous Galerkin approaches to implicit LES / under-resolved DNS of Euler turbulence. *Journal of Computational Physics*, 330: 615–623, February 2017.

[79] Andrew R. Winters, Rodrigo C. Moura, Gianmarco Mengaldo, Gregor J. Gassner, Stefanie Walch, Joaquim Peiro, and Spencer J. Sherwin. A comparative study on polynomial dealiasing and split form discontinuous Galerkin schemes for under-resolved turbulence computations. *Journal of Computational Physics*, 372:1–21, November 1 2018.

[80] S. A. Stanley, S. Sarkar, and J. P. Mellado. A study of the flow-field evolution and mixing in a planar turbulent jet using direct numerical simulation. *Journal of Fluid Mechanics*, 450:377–407, January 2002.

[81] G. B. Jacobs, D. A. Kopriva, and F. Mashayek. A comparison of outflow boundary conditions for the multidomain staggered-grid spectral method. *Numerical Heat Transfer, Part B: Fundamentals*, 44:225–251, 2003.

[82] D. Stanescu, D. Ait-Ali-Yahia, W. G. Habashi, and M. P. Robichaud. Multidomain spectral computations of sound radiation from ducted fans. *AIAA Journal*, 37(6):296—-302, 1999.

[83] P. Rasetarinera, D.A. Kopriva, and M.Y. Hussaini. Discontinuous spectral element solution of acoustic radiation from thin airfoils. *AIAA J.*, 39(11):2070–2075, 2001.

[84] B. F. Klose, G. B. Jacobs, J. Tank, and G. Spedding. Low Reynolds number airfoil aerodynamics: three different flow patterns within an angle of attack range of four degrees. AIAA aviation 2018 forum, 2018.

[85] M. H. Carpenter and C. A. Kennedy. A fourth-order 2N-storage Runge-Kutta scheme. NASA TM 109112, June 1994.

[86] Daniel Alan Nelson. *High-fidelty Lagrangian coherent structures analysis and DNS with discontinuous-Galerkin methods*. PhD Thesis, University of California, San Diego in conjuction with San Diego State University, San Diego, CA, Month unknown 2015. http://escholarship.org/uc/item/2cv4f732.

[87] Shutian Deng, Li Jiang, and Chaoqun Liu. DNS for flow separation control around an airfoil by pulsed jets. *Computers & Fluids*, 36(6):1040–1060, July 2007.

[88] Nicholas J. Georgiadis, Donald P. Rizzetta, and Christer Fureby. Large-eddy simulation: Current capabilities, recommended practices, and future research. *AIAA Journal*, 48(8), August 2010.

[89] D. A. Choi. Wind tunnel experiments on the flow over a NACA 65(1)-412 airfoil at a Reynolds number of 20,000. Master thesis, San Diego State University, San Diego, CA, Fall 2020.

[90] F. M. White. *Viscous Fluid Flow*. McGraw-Hill, New York, NY, 1991.

[91] T. Wei and C. R. Smith. Secondary vortices in the wake of circular cylinders. *Journal of Fluid Mechanics*, 169:513–533, 1986. doi: 10.1017/S0022112086000733.

[92] C. Williamson. Vortex dynamics in the cylinder wake. *Ann. Rev. Fluid Mech.*, 28:477–539, 1996.

[93] C. H. K. Williamson. Three-dimensional wake transition. *Journal of Fluid Mechanics*, 328:345–407, 1996. doi: 10.1017/S0022112096008750.

[94] T. Leweke and C. H. K. Williamson. Three-dimensional instabilities in wake transition. *European Journal of Mechanics - B/Fluids*, 17(4):571 – 586, 1998. ISSN 0997-7546. doi: https://doi.org/10.1016/S0997-7546(98)80012-5. Special Issue Dynamics and Statistics of Concentrated Vortices in Turbulent Flow (Euromech Colloquium 364).

[95] M. J. Lighthill. Introduction. boundary layer theory. In L. Rosenhead, editor, *Laminar Boundary Layer Theory*, pages 46–113. Oxford University Press, Oxford, England, 1963.

[96] B. R. Morton. The generation and decay of vorticity. *Geophysical & Astrophysical Fluid Dynamics*, 28(3-4):277–308, 1984. doi: 10.1080/03091928408230368.

[97] Hans Hornung. Vorticity generation and transport. In *10th Australasian Fluid Mechanics Conference, Volume 1*, volume 1, pages KS3.1–KS3, January 1989.

[98] J. Spurk and N. Aksel. *Fluid Mechanics*. Springer-Verlag, Berlin Heidelberg, 2008.

[99] R. R. Kerswell. Elliptical instability. *Annual Review of Fluid Mechanics*, 34(1): 83–113, 2002. doi: 10.1146/annurev.fluid.34.081701.171829.

[100] A. H. Haidari and C. R. Smith. The generation and regeneration of single hairpin vortices. *Journal of Fluid Mechanics*, 277:135–162, 1994. doi: 10.1017/S0022112094002715.

[101] T. Sakai, P. J. Diamessis, and G. B. Jacobs. Self-sustained instability, transition, and turbulence induced by a long separation bubble in the footprint of an internal solitary wave. I. Flow topology. *Physical Review Fluids*, 2020. accepted for publication.

[102] M Tobak and D J Peake. Topology of three-dimensional separated flows. *Annual Review of Fluid Mechanics*, 14(1):61–85, 1982. doi: 10.1146/annurev.fl.14.010182.000425.

[103] D. Rodríguez and V. Theofilis. On the birth of stall cells on airfoils. *Theoretical and Computational Fluid Dynamics*, 25:105–117, 2011.

[104] P. Moin and P. R. Spalart. Contributions of numerical simulation data bases to the physics, modeling and measurement of turbulence. NASA TM 100022, NASA, 1987.

[105] P. G. Huang, G.N. Coleman, and P. Bradshaw. Compressible turbulent channel flows: DNS results and modelling. *J. Fluid Mech.*, 305:185–218, 1995.

[106] X. Wu and P. Moin. Direct numerical simulation of turbulence in a nominally zero-pressure-gradient flat-plate boundary layer. *Journal of Fluid Mechanics*, 630:5–41, 2009. doi: 10.1017/S0022112009006624.

[107] D. A. Kopriva. A staggered-grid multidomain spectral method for the compressible Navier-Stokes equations. *Journal of Computational Physics*, 143:125–158, 1998.

[108] K. Mittal, S. Dutta, and P.F. Fischer. Nonconforming Schwarz-spectral element methods for incompressible flow. *Computers and Fluids*, 191:104237, 2019.

[109] M. P. Rockwood and M.A. Green. Real-time identification of vortex shedding in the wake of a circular cylinder. *AIAA J.*, 57(1):223–238, 2019.

[110] Kamran Mohseni, Doug Lipinski, and Blake Cardwell. A Lagrangian Analysis of a Two-Dimensional Airfoil with Vortex Shedding. *Journal of Physics A: Mathematical and Theoretical*, 41(34):1–22, August 11 2008.

[111] Martin H. Kamphuis, Gustaaf B. Jacobs, Kevin K. Chen, Geoffrey Spedding, and Harry W. M. Hoeijmakers. Pulse Actuation And Its Effects On Separated Lagrangian Coherent Structures For Flows Over A Cambered Airfoil. *Proceedings of the ASME 2017 International Design Engineering Technical Conferences & Computers and Information in Engineering Conference*, November 2017.

[112] D.A. Kopriva. *Implementing Spectral Methods for Partial Differential Equations*. Springer-Verlag, Berlin, 2009.

[113] R. H. Kraichnan. Diffusion by a random velocity field. *Physics of Fluids*, 13: 22–31, 1970.